Quantum Monte Carlo methods and strongly correlated electrons on honeycomb structures

Thomas C. Lang

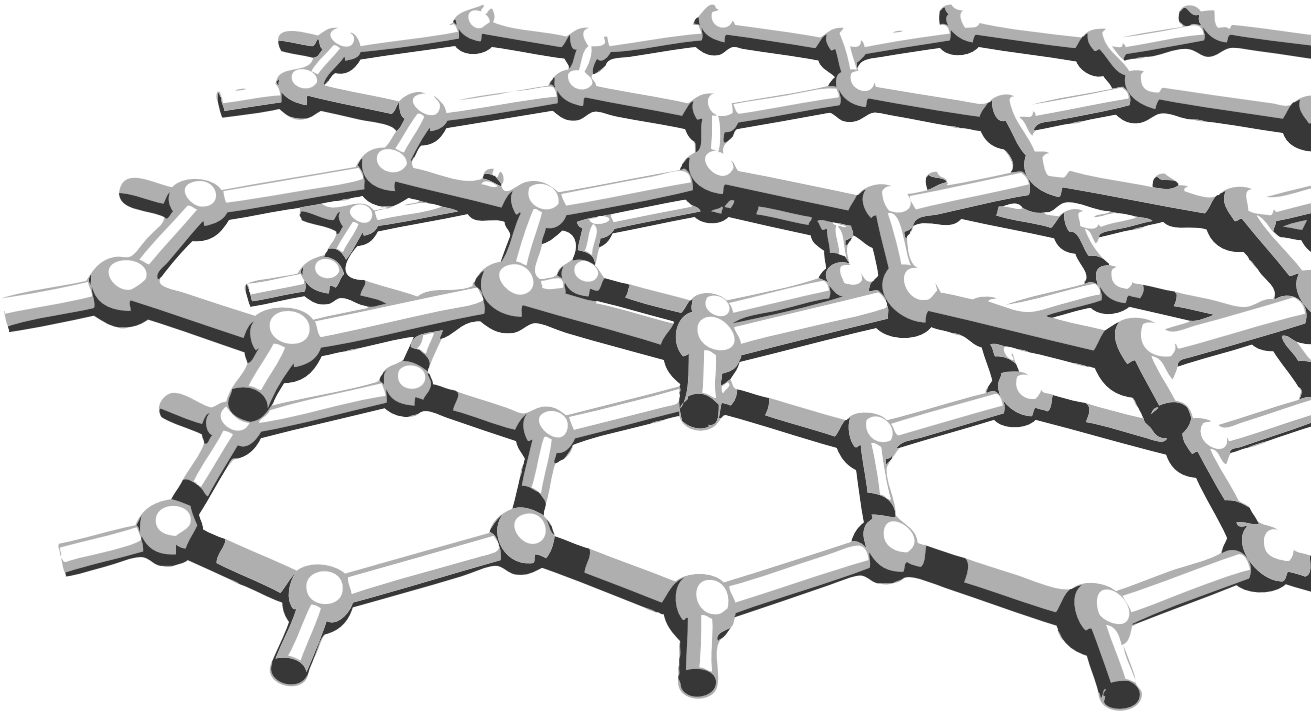

Dissertation zur Erlangung des naturwissenschaftlichen Doktorgrades
der Bayerischen Julius-Maximilians-Universität Würzburg
vorgelegt von Thomas C. Lang aus Graz, Österreich

Betreut von Prof. Dr. Fakher F. Assaad
Institut für Theoretische Physik und Astrophysik

Würzburg 2010

...
Eingereicht am: 29.09.2010
bei der Fakultät für Physik und Astronomie

1. Gutachter: Prof. Dr. Fakher F. Assaad
2. Gutachter: Prof. Dr. Ralph Claessen
3. Gutachter: Prof. Dr. Sylvain Capponi
der Dissertation.

1. Prüfer: Prof. Dr. Fakher F. Assaad
2. Prüfer: Prof. Dr. Ralph Claessen
3. Prüfer: Prof. Dr. Björn Trauzettel
im Promotionskolloquium.

Tag des Promotionskolloquiums: 16.12.2010

Doktorurkunde ausgehändigt am: _____

Abstract

In this thesis we apply recently developed, as well as sophisticated quantum Monte Carlo methods to numerically investigate models of strongly correlated electron systems on honeycomb structures. The latter are of particular interest owing to their unique properties when simulating electrons on them, like the relativistic dispersion, strong quantum fluctuations and their resistance against instabilities. This work covers several projects including the advancement of the weak-coupling continuous time quantum Monte Carlo and its application to zero temperature and phonons, quantum phase transitions of valence bond solids in spin-1/2 Heisenberg systems using projector quantum Monte Carlo in the valence bond basis, and the magnetic field induced transition to a canted antiferromagnet of the Hubbard model on the honeycomb lattice. The emphasis lies on two projects investigating the phase diagram of the SU(2) and the SU(N)-symmetric Hubbard model on the hexagonal lattice.

At sufficiently low temperatures, condensed-matter systems tend to develop order. An exception are quantum spin-liquids, where fluctuations prevent a transition to an ordered state down to the lowest temperatures. Previously elusive in experimentally relevant microscopic two-dimensional models, we show by means of large-scale quantum Monte Carlo simulations of the SU(2) Hubbard model on the honeycomb lattice, that a quantum spin-liquid emerges between the state described by massless Dirac fermions and an antiferromagnetically ordered Mott insulator. This unexpected quantum-disordered state is found to be a short-range resonating valence bond liquid, akin to the one proposed for high temperature superconductors.

Inspired by the rich phase diagrams of SU(N) models we study the SU(N)-symmetric Hubbard Heisenberg quantum antiferromagnet on the honeycomb lattice to investigate the reliability of $1/N$ corrections to large-N results by means of numerically exact QMC simulations. We study the melting of phases as correlations increase with decreasing N and determine whether the quantum spin liquid found in the SU(2) Hubbard model at intermediate coupling is a specific feature, or also exists in the unconstrained t-J model and higher symmetries.

Kurzbeschreibung

Wir untersuchen mit Hilfe von neu entwickelten sowie technisch ausgereiften Quanten-Monte-Carlo Methoden Modelle stark korrelierter Elektronen auf hexagonalen Gittern. Letztere zeichnen sich durch die einzigartigen Eigenschaften der auf ihnen simulierten Elektronen aus, wie zum Beispiel deren relativistische Dispersionsrelation, die starken Quantenfluktuationen und deren Beständigkeit gegenüber Instabilitäten. Diese Arbeit umfasst mehrere Projekte, einschließlich der Erweiterung des weak-coupling continuous time Quanten-Monte-Carlo Verfahrens und dessen Anwendung auf Phononen-Systeme und den Null-Temperatur Grundzustand, der Studie eines Quanten Phasen Übergangs in einem Kristall mit dominanter Valenzbindung in einem Spin-1/2 Heisenberg model mit vier-Spin Wechselwirkung, und der Untersuchung eines gekippten Antiferromagneten im Hubbard Model, induziert durch ein externes Magnetfeld. Die Schwerpunkte dieser Arbeit liegen bei zwei Studien der Phasendiagramme des SU(2) und SU(N)-symmetrischen Hubbard Models auf dem hexagonalen Gitter.

Bei niedrigen Temperaturen haben Elektronen in Festkörpern die Tendenz, Ordnung zu entwickeln. Eine Ausnahme sind Quanten Spinflüssigkeiten, in denen Fluktuationen Ordnung selbst bei niedrigsten Temperaturen verhindern. Bislang war es nahezu unmöglich, diese in experimentell realistischen mikroskopischen Modellen zu finden und zu simulieren. In aufwändigen Quanten-Monte-Carlo Simulationen des SU(2) Hubbard Models konnten wir das Auftreten einer solchen Quanten Spinflüssigkeit zeigen, welche die Phasen der masselosen Dirac-Fermionen und eines antiferromagnetischem Isolators trennt. Dieser unerwartete, ungeordnete Quantenzustand weist kurzreichweitige Korrleationen ähnlich einer Resonanz Valenzbond Flüssigkeit auf, welche in Zusammenhang mit Hochtemperatur-Spuraleitung steht.

Motiviert durch die reichhaltigen Phasendiagramme von SU(N)-symmetrischen Modellen, untersuchen wir mit Hilfe von Quanten-Monte Carlo-Simulationen den SU(N)-Hubbard-Heisenberg-Antiferromagneten auf dem hexagonalen Gitter in Bezug auf die Verlässlichkeit von $1/N$ Korrekturen von Molekularfeldnäherungen. Wir untersuchen das Schmelzen von Phasen als Funktion von abnehmendem N und bestimmen, ob die im SU(2)-Hubbard-Model gefundene Quanten Spinflüssigkeit eine spezielle Eigenschaft dieses Modells ist, oder ob diese auch im erweiterten t-J Modell bei höheren Symmetrien gefunden werden kann.

Contents

1 Introduction

The fundamental concepts of symmetry and emergence lie at the heart of physics. Emergence paraphrases the fact that seemingly trivial properties and interactions can be the source for mind boggling complexity, a fact that can be found in all fields of physics, be it classical-, or quantum-physics. Applied to the domain of condensed matter physics this can be the spontaneous formation of order or the creation of new (quasi-)particles which mediate interactions. All are nontrivial phenomena which could not have been predicted from their constituents alone.

Inseparably linked to emergence is symmetry, the concept of balance or patterned self-similarity and often equated with beauty. Classifying states, excitations and their constituents according to their symmetry allows to greatly simplify complex problems and relate them to larger categories of problems. In this thesis several different quantum systems are investigated and the two keystones of physics, symmetry and emergence, will be encountered repeatedly. Quantum systems could be expected to be somehow more complicated, more confusing and outlandish than the everyday world that we are familiar with. And although often counterintuitive, yet every system that we have studied has turned out to be elegant in its own way. Beauty lies at the heart of (condensed) matter.

This thesis is organized in seven chapters: This very first chapter gives a general overview of the model, the lattice and the projector quantum Monte Carlo which you will encounter repeatedly throughout this script. The following chapters discuss the projects investigated in this dissertation. In particular, Chapter 2 describes technical details of the extension of the weak-coupling continuous-time quantum Monte Carlo algorithm and its application to the Hubbard-Holstein model. Chapter 3 treats the JQ-model, a quantum Heisenberg model with multi-spin exchange, and the formation and breakdown of valence bond solid states. In Ch. 4 and Ch. 5 we switch over to itinerant electrons and discuss the two major investigations of this thesis: the SU(2) and SU(N) Hubbard Heisenberg model on the honeycomb lattice, where we study the rich variety of semi-metal to insulator quantum phase transitions and the emergence of a quantum spin liquid state. Chapter 6 gives a brief overview of the Hubbard model subjected to an external magnetic field. All projects conclude with discussions and a summary of the

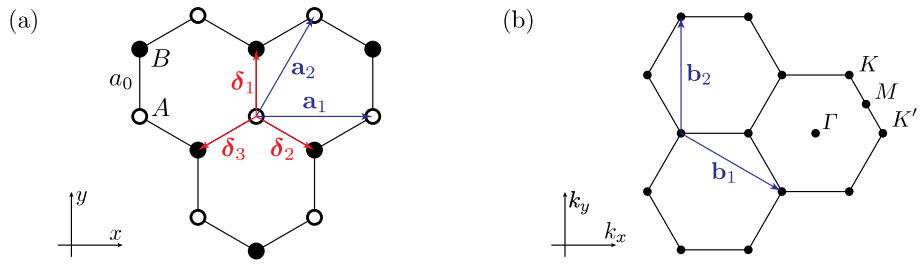

Fig. 1.1.: Real (a) and reciprocal (b) lattice and their primitive vectors.

results. The thesis ends with an overall conclusion, followed by the appendix dealing with technical details.

In this thesis I try to emphasize facts I found essential, or especially helpful to understand the subject at hand. Many topics mentioned in this work are vast fields on their own, whose surface can only be scratched here. For these I try to give the most important references in order to provide a starting point for further reading.

1.1. The honeycomb lattice

A common theme in this thesis (with the exception of Ch. 2) is the honeycomb lattice. Its structure, properties and their implications are outlined in this section.

1.1.1. Structure and symmetry

In geometry and crystallography, a Bravais lattice (named after Auguste Bravais (1850)) is an infinite set of unit cells at the points generated by discrete translation operations

$$\mathbf{R} = n_1\mathbf{a}_1 + n_2\mathbf{a}_2 + n_3\mathbf{a}_3 \,, \qquad n_i \in \mathbb{Z} \,. \tag{1.1}$$

In two dimensions, there are five Bravais lattices which can be distinguished by the relative length of their primitive vectors $r = |\mathbf{a}_1|/|\mathbf{a}_2|$ and their enclosed angle $\phi = \measuredangle(\mathbf{a}_1, \mathbf{a}_2)$: oblique ($r \neq 1$, $\phi \neq 90°$), rectangular ($r \neq 1$, $\phi = 90°$), centered rectangular ($r \neq 1$, $\phi = 45°$), hexagonal ($r = 1$, $\phi = 60°$), and square ($r = 1$, $\phi = 90°$). Actually, the points of the hexagonal Bravais lattice form a triangular lattice. The equilateral triangular lattice with two orbitals per unit cell (at distance a_0) is equivalent to the honeycomb structure or the tiling of hexagons. We set a_0 as the unit length between sites and use the primitive lattice vectors in real space

$$\mathbf{a}_1 = a_0 \left(\sqrt{3}, 0\right) \,, \qquad \mathbf{a}_2 = a_0 \left(\frac{\sqrt{3}}{2}, \frac{3}{2}\right) \,, \tag{1.2}$$

as illustrated in Fig. 1.1a. The primitive vectors reciprocal space can be obtained by matrix inversion $(\mathbf{b}_1\mathbf{b}_2)^T = 2\pi\,(\mathbf{a}_1\mathbf{a}_2)^{-1}$, such that $\mathbf{b}_i\mathbf{a}_j = 2\pi\delta_{ij}$. They read

$$\mathbf{b}_1 = \frac{2\pi}{a_0}\left(\frac{\sqrt{3}}{3}, -\frac{1}{3}\right) , \qquad \mathbf{b}_2 = \frac{2\pi}{a_0}\left(0, \frac{2}{3}\right) . \tag{1.3}$$

The high symmetry points of the first Brillouin zone are $\mathbf{\Gamma} = (0,0)$, $\mathbf{M} = (\sqrt{3}/2, 1/2)/3$, $\mathbf{K} = (1/\sqrt{3}, 1)/3$ and $\mathbf{K}' = (2/\sqrt{3}, 0)/3$ as indicated in Fig. 1.1b. The orbitals can be seen as two sites per unit cell, forming a triangular lattice which manifests itself in reciprocal space in the two nodal points K and K'. This sublattice property is also referred to as *valley degeneracy* in reciprocal space and allows to introduce an additional pseudo-spin degree of freedom when deriving an effective model for the system [1].

The terms hexagonal lattice and honeycomb lattice will be used synonymously to denote the structure depicted in Fig. 1.1. Orbitals A (B) are shown as open (filled) circles. Orbitals of the same kind form a triangular lattice, such that the honeycomb lattice can be interpreted as two interpenetrating triangular sublattices. The orbitals A and B are inequivalent sites, which can be seen from the nearest neighbor bonds either forming an upright, or upside down Y-shape illustrated by the strong red and blue bonds in Fig. 1.2.

The lattice can be divided into three distinct types of plaquettes denoted R,G and B colored red, green and blue, respectively, in Fig. 1.2. Each type of plaquette forms a triangular, or hexagonal pattern with three- or six-fold rotational symmetry, that is a finer lattice relative to the lattice of translational symmetry (of the same color). Additionally, reflections along the symmetry axes of these patterns map to themselves. We will encounter this pattern scheme again in the possible dimer coverings of the lattice. The symmetry of the hexagonal lattice in Schönflies notation is defined by the point group D_{6h} for dihedral, or two-sided group. The subset $6h$ indicates that the group has a six-fold rotation axis, plus a twofold axis perpendicular to that axis, plus a mirror plane perpendicular to the six-fold axis.

1.1.2. Tight binding band structure

In order to distinguish the two orbitals per unit cell one can use the operators $a^\dagger$ (a) and $b^\dagger$ (b) which create (annihilate) electrons with spin σ on sublattice A and B, respectively. In the following we will use the two notations $a^\dagger$, $b^\dagger$, or simply $c^\dagger$ (but respecting the sublattices) interchangeably.

Considering that electrons can hop to the three nearest-neighbor sites given by the real space vectors $\boldsymbol{\delta} = \{\mathbf{0}, -\mathbf{a}_2, \mathbf{a}_1 - \mathbf{a}_2\}$, the tight-binding Hamiltonian for electrons on the honeycomb lattice [2, 3] has the form

$$H_K = \sum_{\mathbf{R}} \sum_{i=1,2,3} \left(t_i\, a^\dagger_{\mathbf{R}} b_{\mathbf{R}+\boldsymbol{\delta}_i} + \text{h.c.} \right) . \tag{1.4}$$

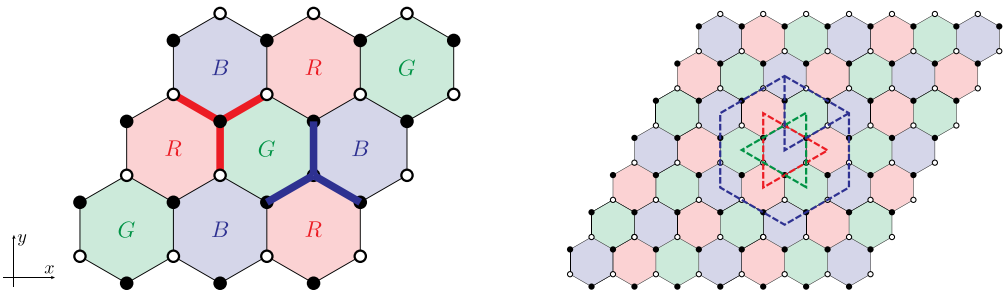

Fig. 1.2.: Colored bonds and plaquettes to illustrate the two inequivalent sites and the symmetries of the honeycomb lattice.

For the number of unit cells N, we define the Fourier transformations

$$a^\dagger_{\mathbf{R}} = \frac{1}{\sqrt{N}} \sum_{\mathbf{R}} \mathrm{e}^{-\mathrm{i}\,\mathbf{k}\cdot\mathbf{R}} a^\dagger_{\mathbf{k}} \,, \qquad a_{\mathbf{R}} = \frac{1}{\sqrt{N}} \sum_{\mathbf{R}} \mathrm{e}^{\mathrm{i}\,\mathbf{k}\cdot\mathbf{R}} a_{\mathbf{k}} \,, \tag{1.5}$$

(for sublattice B, respectively) and insert them into Eq. (1.4) to obtain the Hamiltonian in reciprocal space

$$\begin{aligned} H_K &= \frac{1}{N} \sum_{\mathbf{R}} \sum_{\mathbf{k},\mathbf{k}'} \sum_{i=1,2,3} \Big(t_i \underbrace{\mathrm{e}^{-\mathrm{i}\,\mathbf{R}\cdot(\mathbf{k}-\mathbf{k}')}}_{\delta_{\mathbf{k}\mathbf{k}'}} \mathrm{e}^{-\mathrm{i}\,\mathbf{k}\cdot\boldsymbol{\delta}_i} a^\dagger_{\mathbf{k}} b_{\mathbf{k}} + \mathrm{h.c.} \Big) \\ &= \sum_{\mathbf{k}} \sum_{i=1,2,3} \Big(t_i \, \mathrm{e}^{-\mathrm{i}\,\mathbf{k}\cdot\boldsymbol{\delta}_i} a^\dagger_{\mathbf{k}} b_{\mathbf{k}} + \mathrm{h.c.} \Big) \,. \end{aligned} \tag{1.6}$$

In general we use isotropic hopping such that $t_i = t$. We define $t' = t_i \, \mathrm{e}^{-\mathrm{i}\,\mathbf{k}\cdot\boldsymbol{\delta}_i}$ and diagonalize the Hamiltonian

$$H_K = \sum_{\mathbf{k}} (a^\dagger_{\mathbf{k}} \, b^\dagger_{\mathbf{k}}) \begin{pmatrix} 0 & t' \\ t'^* & 0 \end{pmatrix} \begin{pmatrix} a_{\mathbf{k}} \\ b_{\mathbf{k}} \end{pmatrix} \,, \tag{1.7}$$

which yields two solutions per momentum $\mathbf{k}$ – the two bands of the two site unit-cell

$$\varepsilon(\mathbf{k}) = \sqrt{t' \, t'^*} = \pm\sqrt{3 + 2\cos(\mathbf{k}\cdot(\mathbf{a}_2 - \mathbf{a}_1) + 2\cos(\mathbf{k}\cdot\mathbf{a}_1) + 2\cos(\mathbf{k}\cdot\mathbf{a}_2)} \,. \tag{1.8}$$

The band structure along the high symmetry path Γ-K-M-Γ (cf. Fig. 1.1b) is plotted in Fig. 1.3 next to three dimensional plot of the band structure including the first Brillouin zone. The figure also shows a zoom in of the band structure close to one of the nodal points K or K' at the boundary of the Brillouin zone. It is the characteristic linear dispersion known as Dirac cone which can be obtained by expanding the full band structure in Eq. (1.8) close to the $\mathbf{K}$ or $\mathbf{K}'$ vector. For $|\mathbf{q}| \ll |\mathbf{K}|$, where $\mathbf{q}$ is the momentum measured relatively to the Dirac points, the dispersion is

$$E(\mathbf{q}) \approx \pm v_{\mathrm{F}} |\mathbf{q}| + \mathcal{O}(\frac{q}{K})^2 \,, \tag{1.9}$$

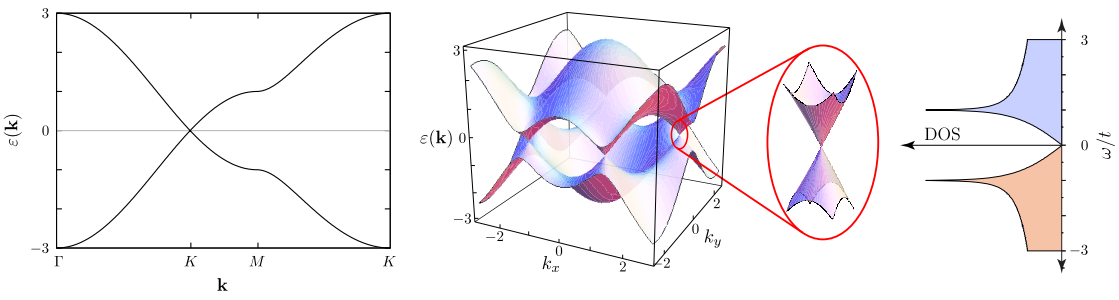

Fig. 1.3.: Band structure along the high symmetry path as well as a 3D plot of the dispersion around the first Brillouin zone with its Dirac cones and the density of states (DOS) of the nearest neighbor tight binding model on the honeycomb lattice.

with the Fermi velocity $v_\mathrm{F} = 3t/2$, [2]. This is in contrast to the usual quadratic dispersion $\varepsilon(\mathbf{q}) = q^2/2m$, where m is the electron mass. While in the usual case the velocity changes with the energy $v = k/m = \sqrt{2E/m}$, the velocity in Eq. (1.9) does not depend on the energy or momentum. Deviations from the linear dispersion set in for large momenta away from the Dirac point. Due to the three symmetry axes of the lattice this is known as *trigonal warping* [1].

The linear dispersion around the nodal points resembles the energy of relativistic particles (see the light-cone in Fig. 1.3) which are described by the massless Dirac equation. Indeed, the expansion of the tight binding structure around K and K' allows to map the low energy effective Hamiltonian to a 2D Dirac equation: The operators in Eq. (1.9) can be restated as a sum of the two terms

$$a_\mathbf{R} = \mathrm{e}^{\mathrm{i}\,\mathbf{K}\cdot\mathbf{R}} a_{1,\mathbf{K}} + \mathrm{e}^{\mathrm{i}\,\mathbf{K}'\cdot\mathbf{R}} a_{2,\mathbf{R}} \,, \tag{1.10}$$

(for sublattice B, respectively), the indices $i = 1, 2$ refer to the K, K' point. In the low energy limit only states near the nodal points contribute to the dynamics. Assuming the $a_{i,\mathbf{R}}, b_{i,\mathbf{R}}$ vary only slowly over the unit cell, the operators may be expanded up to linear order in $\boldsymbol{\delta}$ (the vectors to the nearest neighbors). Since the neighboring sites are symmetrically arranged, the condition $\sum_i \mathrm{e}^{\pm\mathrm{i}\mathbf{K}\cdot\boldsymbol{\delta}_i} = \sum_i \mathrm{e}^{\pm\mathrm{i}\mathbf{K}'\cdot\boldsymbol{\delta}_i} = 0$ holds and allows to formulate the tight binding Hamiltonian as [4]

$$H_K \approx -\mathrm{i}v_\mathrm{F} \int dxdy \left(\mathbf{\Psi}_1^\dagger(\mathbf{R})\boldsymbol{\sigma}\cdot\boldsymbol{\nabla}\mathbf{\Psi}_1 + \mathbf{\Psi}_2^\dagger(\mathbf{R})\boldsymbol{\sigma}\cdot\boldsymbol{\nabla}\mathbf{\Psi}_2 \right) \,, \tag{1.11}$$

with $\boldsymbol{\sigma} = (\sigma_x, \sigma_y)$, $\boldsymbol{\sigma}^* = (\sigma_x, -\sigma_y)$ and $\mathbf{\Psi}_i = (a_i^\dagger, b_i^\dagger)$. In first quantization the two-component wave function $\psi(\mathbf{r})$ obeys the 2D Dirac equation $-\mathrm{i}v_\mathrm{F}\boldsymbol{\sigma}\cdot\boldsymbol{\nabla}\psi(\mathbf{r}) = \psi(\mathbf{r})$. In momentum-space the Hamiltonian takes the form $H_K = v_\mathrm{F}\boldsymbol{\sigma}\cdot\mathbf{k}$ around $\mathbf{K}$ and $H_{K'} = v_\mathrm{F}\boldsymbol{\sigma}^*\cdot\mathbf{k}$ around $\mathbf{K}'$ with energies $E = \pm v_\mathrm{F}k$. Because of these properties the nodal points K or K' are often referred to as Dirac points.

1.1.3. The Stoner criterion

The intriguing consequence of the tight binding band structure is a vanishing density of states (DOS) at the Fermi level (see Fig. 1.3). As mentioned (cf. Eq. (1.9)), the energy increases linearly around the Fermi level with only the nodal points contributing to the DOS at energy $\omega = 0$. In consequence this leads to a linearly vanishing DOS $g(\omega)$ at the Fermi level.

$$g(\omega) = \frac{1}{N}\sum_{\mathbf{k}} \delta(\omega - \varepsilon(\mathbf{k})) \,, \tag{1.12}$$

and in the vicinity of the Fermi level $g(\omega) \propto v_{\mathrm{F}}|\mathbf{q}|$. This fact makes electrons on the honeycomb lattice (fairly) resistant against instabilities. In order to demonstrate that, let us consider the prime example, the Stoner instability for free electrons – many other instabilities have a very similar formal structure. The Stoner criterion essentially states that electrons are prone to a magnetic instability, because the magnetic susceptibility shows a log-divergence as long as there is a finite DOS at the Fermi level.

The (transversal) magnetic susceptibility in the static case $\omega = 0$ reads

$$\chi^{+-}_{\ell,\ell'}(\mathbf{q}) = -\int_0^\beta d\tau \big\langle S^+_\ell(\mathbf{q},\tau) S^-_{\ell'}(-\mathbf{q},0)\big\rangle \quad \text{where} \quad S^\pm_\ell(\tau) = \mathrm{e}^{H\tau} S^\pm_\ell(0) \mathrm{e}^{-H\tau} \,, \tag{1.13}$$

where ℓ, ℓ' denote orbitals on the sublattices A, B and $S^+_\ell(\mathbf{q}) = \frac{1}{\sqrt{N}}\sum_{\mathbf{q}} c^\dagger_{\ell,\mathbf{q},\sigma} c_{\ell,\mathbf{q},\sigma'}$ are the spin raising operators. Operators for the other sublattice and for spin lowering are defined accordingly. The (transversal) magnetization on orbital ℓ upon applying an orbital dependent external magnetic field B^{xy}_μ, amounts to

$$m^{xy}_\ell = \sum_{\mu=\ell,\ell'} \chi^{+-}_{\ell,\mu} B^{xy}_\mu \,. \tag{1.14}$$

Hence, if χ is prone to an instability, an infinitesimal small magnetic field is sufficient to trigger magnetic order. Let's check the formal definition in the free (noninteracting) system: To compute the susceptibility we Wick-expand

$$\begin{aligned}
\chi^{+-}_{\ell,\ell'}(\mathbf{q}) &= -\frac{1}{N}\int_0^\beta d\tau \sum_{\mathbf{k},\mathbf{k}'} \big\langle c^\dagger_{\ell,\mathbf{k},\uparrow}(\tau) c_{\ell,\mathbf{k}+\mathbf{q},\downarrow}(\tau) c^\dagger_{\ell',\mathbf{k}',\downarrow}(0) c_{\ell',\mathbf{k}'-\mathbf{q},\uparrow}(0)\big\rangle \\
&= -\frac{1}{N}\int_0^\beta d\tau \sum_{\mathbf{k},\mathbf{k}'} \delta_{\mathbf{k},\mathbf{k}'} \big\langle c^\dagger_{\ell,\mathbf{k},\uparrow}(\tau) c_{\ell',\mathbf{k}'-\mathbf{q},\uparrow}(0)\big\rangle \big\langle c_{\ell,\mathbf{k}+\mathbf{q},\downarrow}(\tau) c^\dagger_{\ell',\mathbf{k}',\downarrow}(0)\big\rangle \\
&= -\frac{1}{N}\int_0^\beta d\tau \sum_{\mathbf{k}} \big\langle c^\dagger_{\ell,\mathbf{k},\uparrow}(\tau) c_{\ell',\mathbf{k},\uparrow}(0)\big\rangle \big\langle c_{\ell,\mathbf{k}+\mathbf{q},\downarrow}(\tau) c^\dagger_{\ell',\mathbf{k}+\mathbf{q},\downarrow}(0)\big\rangle \,,
\end{aligned} \tag{1.15}$$

where we used $\mathbf{k}' = \mathbf{k} + \mathbf{q}$. For a staggered magnetic field $B^{xy}_A = -B^{xy}_B$ the magnetization $m_{\mathrm{AF}} = \chi^{+-}_{A,A} - \chi^{+-}_{A,B}$ (cf. Eq. (1.14)). The antiferromagnetic and ferromagnetic

susceptibilities actually form the eigenvectors of the susceptibility tensor due to the two sublattices [5]. The antiferromagnetic susceptibility reads

$$\begin{aligned}
\chi_{\mathrm{AF}} &= -\frac{1}{2}{\sum_{\ell,\ell'}}' \chi^{+-}_{\ell,\ell} - \chi^{+-}_{\ell,\ell'} \\
&= -\frac{1}{2N}\int_0^\beta d\tau \sum_{\mathbf{k}} {\sum_{\ell,\ell'}}' \left\langle c^\dagger_\ell(\tau) c_{\ell'}(0)\right\rangle_{\mathbf{k},\uparrow} \left\langle c_\ell(\tau) c^\dagger_{\ell'}(0)\right\rangle_{\mathbf{k}+\mathbf{q},\downarrow} \\
&= -\frac{1}{2N}\int_0^\beta d\tau \sum_{\mathbf{k}} {\sum_{\ell,\ell'}}' \mathrm{e}^{\tau(\varepsilon_\ell(\mathbf{k},\uparrow)-\varepsilon_{\ell'}(\mathbf{k}+\mathbf{q},\downarrow))} \left\langle c^\dagger_\ell c_{\ell'}\right\rangle_{\mathbf{k},\uparrow} \left(1 - \left\langle c^\dagger_\ell c_{\ell'}\right\rangle_{\mathbf{k}+\mathbf{q},\downarrow}\right) \\
&= -\frac{1}{2N} \sum_{\mathbf{k}} {\sum_{\ell,\ell'}}' \frac{\mathrm{e}^{\beta(\varepsilon_\ell(\mathbf{k},\uparrow)-\varepsilon_{\ell'}(\mathbf{k}+\mathbf{q},\downarrow))}-1}{\varepsilon_\ell(\mathbf{k},\uparrow)-\varepsilon_{\ell'}(\mathbf{k}+\mathbf{q},\downarrow)} \left\langle c^\dagger_\ell c_{\ell'}\right\rangle_{\mathbf{k},\uparrow} \mathrm{e}^{\beta\varepsilon_{\ell'}(\mathbf{k}+\mathbf{q},\downarrow)} \left\langle c^\dagger_\ell c_{\ell'}\right\rangle_{\mathbf{k}+\mathbf{q},\downarrow} \\
&= -\frac{1}{2N} \sum_{\mathbf{k}} {\sum_{\ell,\ell'}}' \frac{n_{\mathrm{F},\ell'}(\mathbf{k}+\mathbf{q},\downarrow) - n_{\mathrm{F},\ell}(\mathbf{k},\uparrow)}{\varepsilon_\ell(\mathbf{k},\uparrow)-\varepsilon_{\ell'}(\mathbf{k}+\mathbf{q},\downarrow)} \,, \qquad (1.16)
\end{aligned}$$

where $n_{\mathrm{F},\ell}(\mathbf{k}) = 1/(\mathrm{e}^{\beta\varepsilon_\ell(\mathbf{k})}+1)$ is the Fermi-function and the sum runs over the elements $\ell \neq \ell'$, only. This general form of the susceptibility is independent of whether we start from the longitudinal-, or the transversal magnetic susceptibility. We can see that any imbalance in the spin population would be enhanced by a small denominator – under an integral the log-divergence is obvious. The necessary condition of the denominator is called the *nesting condition*

$$\varepsilon(\mathbf{k}+\mathbf{Q}) = -\varepsilon(\mathbf{k}) \,, \qquad (1.17)$$

where $\mathbf{Q}$ is the nesting vector. In general, nearest neighbor hopping tight binding models fulfill this condition on bipartite lattices, since there is a finite portion of the Fermi surface which can be connected to another part by the same vector $\mathbf{Q}$. Because of the two orbitals in the honeycomb lattice antiferromagnetic order is established within the unit cell such that $\mathbf{Q} = (0,0)$. In the case discussed here, the nesting condition reads $\varepsilon_\ell(\mathbf{k},\uparrow) = -\varepsilon_{\ell'}(\mathbf{k},\downarrow)$, such that we can write the enumerator as

$$n_{\mathrm{F},\ell'}(\mathbf{k}) - n_{\mathrm{F},\ell}(\mathbf{k}) = \frac{1}{\mathrm{e}^{-\beta\varepsilon_\ell(\mathbf{k})}+1} - \frac{1}{\mathrm{e}^{\beta\varepsilon_\ell(\mathbf{k})}+1} = \frac{\mathrm{e}^{\beta\varepsilon_\ell(\mathbf{k})}-1}{\mathrm{e}^{\beta\varepsilon_\ell(\mathbf{k})}+1} = \tanh\left(\frac{\beta\varepsilon_\ell(\mathbf{k})}{2}\right) \,, \qquad (1.18)$$

and use $d\varepsilon\, g(\varepsilon) = d\mathbf{k}\, n(\mathbf{k})$, $\int d\varepsilon\, g(\varepsilon) = N$ to restate the antiferromagnetic susceptibility:

$$\begin{aligned}
\chi_{\mathrm{AF}} &= -\frac{1}{2N} \sum_{\mathbf{k}} \sum_{\ell} \tanh\left(\frac{\beta\varepsilon_\ell(\mathbf{k})}{2}\right) \frac{1}{2\varepsilon_\ell(\mathbf{k})} \\
&= -\frac{1}{2} \sum_{\ell} \int d\varepsilon_\ell\, g(\varepsilon_\ell) \tanh\left(\frac{\beta\varepsilon_\ell}{2}\right) \frac{1}{2\varepsilon_\ell} \,. \qquad (1.19)
\end{aligned}$$

To evaluate the integral we linearize the tanh, such that $\tanh \sim x$ around zero and 1 (-1) for $x > 1$ $(x < 1)$, and approximated the DOS with the DOS at the Fermi level E_F

$$\begin{aligned}
\chi_{\text{AF}} &= -\frac{1}{2}\sum_{\ell}\left[-\int_{-W}^{-2/\beta} d\varepsilon_\ell + \int_{-2/\beta}^{2/\beta} d\varepsilon_\ell + \int_{2/\beta}^{W} d\varepsilon_\ell\right] g(\varepsilon_\ell)\frac{1}{2\varepsilon_\ell} \\
&\approx -\frac{1}{2}\sum_{\ell} g(E_{F,\ell})\left[\int_{2/\beta}^{W} d\varepsilon_\ell - \int_{-W}^{-2/\beta} d\varepsilon_\ell\right]\frac{1}{2\varepsilon_\ell} \\
&= -\frac{1}{2}\sum_{\ell} g(E_{F,\ell}) \ln\left(\frac{W}{2T}\right) \,, \qquad (1.20)
\end{aligned}$$

where W is the bandwidth. The susceptibility diverges logarithmically as the temperature $T = 1/\beta$ goes to zero, but it also is proportional to the DOS. For the honeycomb lattice the DOS vanishes at the Fermi level at half-filling ($g(\varepsilon) \propto \varepsilon$) and hence cuts off the log-divergence. Although in principle susceptible to an external field, there are no states to trigger the instability. However, interactions might dynamically generate states at and close to the Fermi level such that the instability is set off, eventually.

On the square lattice, a van Hove singularity at $\omega = 0$ creates a divergence of the DOS, $g(\varepsilon) \propto \log(\varepsilon)$, and hence there is a log-square singularity in χ_{AF}. For the Hubbard model on the square lattice this implies that any infinitesimal small value of U will lead to spontaneous antiferromagnetic order ($U_c = 0^+$). In contrast, the fact that sufficiently strong interactions are necessary to trigger instabilities on the honeycomb allows to study the semi-metal to insulator transition at a finite U_c. Additionally, the low coordination number $Z = 3$ suggests fluctuations to be important. Together this makes the Hubbard model on the honeycomb lattice a promising candidate for interesting physics.

Outlook – Bilayer graphene and Carbon nano ribbons

Adding a second honeycomb layer can significantly change the free dispersion: Stacking the two layers such that sublattice A of one layer is on top of sublattice B of the other (AB-, or Bernal-staking [1]) is illustrated along the dispersion relation of the corresponding tight-binding model below. This is the natural stacking order of carbon bilayers. In the tight-binding approximation we reduced possible interlayer hopping to the AB connection indicated by the vertical (gray) lines connecting the layers with matrix element $t_\perp$. The interlayer hopping leads to a quadratic dispersion $\varepsilon(\mathbf{k})$ near the K-point which results in a finite density of states and makes the bilayer system more susceptible to instabilities like superconductivity.

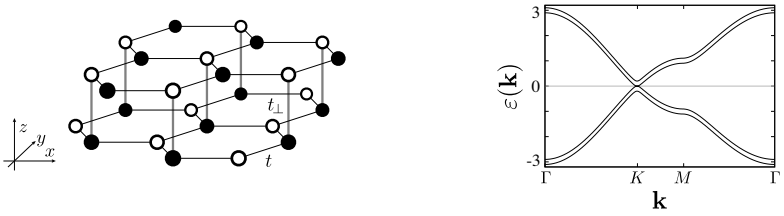

A ribbon structure can be obtained by imposing open boundary conditions along one of the lattice dimensions. Depending on the type of the termination along the ribbon, either forming a zig-zag or armchair edge, the free dispersion shows significant differences. For the zig-zag ribbon illustrated in panel (a) below, sites of different sublattices are exposed at the edge which leads to localized states which manifest themselves in the dispersion-less section of the lowest band around $\mathbf{k} = \pm\pi$. In finite length ribbons weak Coulomb repulsion induces edge ferromagnetism. In armchair ribbons the spectrum is either gapped or ungapped (panel (b) left and right), depending on the even or odd number of unit cells perpendicular to the extension of the ribbon (here, in-/excluding the blue sites in panel (b)).

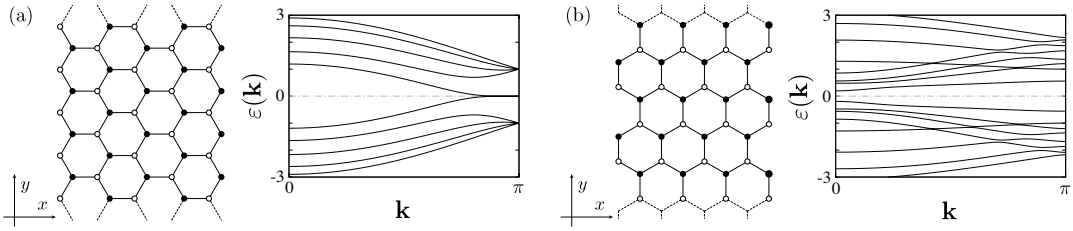

Investigations of the stability of the magnetic properties of the ribbons and instabilities in the bilayer structure are under way.

1.2. Projector Quantum Monte Carlo

The basic idea of the Monte Carlo (MC) method is to construct a Markov sequence of configurations, which represent the equilibrium distribution of a system's degrees of freedom. This is achieved by updating an existing configuration according to a probability distribution, which respects to the detailed balance condition, as introduced by Metropolis and others [6]. In general, this allows to compute eigenvalues for problems whose complexity increases exponentially in configuration space, with polynomial time effort. For a comprehensive overview we refer the reader to the book by Landau and Binder [7].

Quantum Monte Carlo (QMC) is the natural generalization of classical MC, introducing an extra dimension – the imaginary (Euclidean) time axis. The Projector quantum Monte Carlo (PQMC) is a zero temperature version of the Auxiliary Field QMC (or Determinantal QMC) introduced by Blankenbecler, Scalapino and Sugar (BSS) in 1981 [8, 9]. In this section we will outline the method described detailed in [10, 11].

1.2.1. Basic formulation

The objective is to calculate quantum mechanical expectation values of the form

$$\langle O \rangle = \frac{1}{Z} \mathrm{Tr} \left[O \mathrm{e}^{-\beta H} \right] = \frac{1}{Z} \int \mathcal{D}[\phi(i,\tau)] \, \mathrm{e}^{-S[\phi(i,\tau)]} \, O(\phi(i,\tau)) \, , \tag{1.21}$$

where the partition function Z is given by

$$Z = \mathrm{Tr} \left[\mathrm{e}^{-\beta H} \right] = \int \mathcal{D}[\phi(i,\tau)] \, \mathrm{e}^{-S[\phi(i,\tau)]} \, . \tag{1.22}$$

Here $S[\phi]$ denotes the Euclidean action for all possible configurations of the classical fields ϕ, $\beta = 1/k_\mathrm{B}T = \mathrm{i}\, t/\hbar$ is the inverse temperature (imaginary time) and k_B denotes Boltzmann's constant.

In the following we will concentrate on the half-filled Hubbard model, which reads $H = H_t + H_U$, with $H_t = -t \sum_{\langle ij \rangle, \sigma} c^\dagger_{i\sigma} c_{j\sigma}$ and $H_U = \sum_i (n_{i\uparrow} - \frac{1}{2})(n_{i\downarrow} - \frac{1}{2})$, described in Sec. 1.3. In the limit $\beta \to \infty$ the ground state is obtained. If one is interested in ground state properties, it is convenient and more efficient to adopt a projective scheme, where an observable O is obtained by projecting a trial wave function $\big|\Psi_T\big\rangle = \sum_n \big|\Psi_n\big\rangle\big\langle\Psi_n\big|\Psi_0\big\rangle$ along the imaginary time axis

$$\frac{\big\langle\Psi_0\big|O\big|\Psi_0\big\rangle}{\big\langle\Psi_0\big|\Psi_0\big\rangle} = \lim_{\Theta\to\infty} \frac{\big\langle\Psi_T\big|\mathrm{e}^{-\Theta H} O \mathrm{e}^{-\Theta H}\big|\Psi_T\big\rangle}{\big\langle\Psi_T\big|\mathrm{e}^{-2\Theta}\big|\Psi_T\big\rangle} \, . \tag{1.23}$$

Under the assumption of a finite overlap of the trial wave function with the ground state ($\big\langle\Psi_T\big|\Psi_0\big\rangle \neq 0$) and a non degenerate ground state this allows to project out the

eigenenergies $H\langle\Psi_T| = E_n\langle\Psi_n|$, such that the above equation reads

$$\frac{\langle\Psi_0|O|\Psi_0\rangle}{\langle\Psi_0|\Psi_0\rangle} = \lim_{\Theta\to\infty} \frac{\sum_{n,m}\langle\Psi_T|\Psi_n\rangle\langle\Psi_m|\Psi_T\rangle\, \mathrm{e}^{-\Theta(E_n-E_m-2E_0)}\langle\Psi_n|O|\Psi_m\rangle}{\sum_n |\langle\Psi_T|\Psi_n\rangle|^2\, \mathrm{e}^{-2\Theta(E_n-E_0)}} \,. \tag{1.24}$$

According to the Suzuki-Trotter decomposition [12, 13, 14] the sum of matrices in an exponent can be written as $\exp(A+B) = \lim_{L\to\infty}(\exp(A/L)\exp(B/L))^L$, such that we can discretize the imaginary-time in the path integral (1.22) into L Trotter-(time-)slices of length $\Delta\tau = \Theta/L$. This allows to separate the single-body Hamiltonian H_t from the two-body interaction

$$\begin{aligned} Z &= \mathrm{Tr}\mathrm{e}^{-\beta H} = \mathrm{Tr}\mathrm{e}^{-\beta\,(H_t+H_U)} = \lim_{L\to\infty} \mathrm{Tr}\left(\mathrm{e}^{-\frac{\beta}{L}H_t}\,\mathrm{e}^{-\frac{\beta}{L}H_U}\right)^L \\ &= \mathrm{Tr}\prod_{i=1}^{L}\left(\mathrm{e}^{-\Delta\tau H_t}\,\mathrm{e}^{-\Delta\tau H_U} + \frac{1}{2}\,\beta\Delta\tau[H_t,H_U] + \beta t U\mathcal{O}(\Delta\tau^2)\right) \,. \end{aligned} \tag{1.25}$$

For a finite L this introduces a systematic error of $\mathcal{O}(\Delta\tau^2)$ (the term linear in $\Delta\tau$ vanishes since a trace over a commutator gives zero), which amounts to an overall systematic error proportional to $\Delta\tau^3$ in the Monte Carlo estimate of observables. The finite $\Delta\tau$ also plays the role of a ultra-violet cut-off where $1/\Delta\tau$ is absorbed in the Hubbard-Stratonovich transformation described in the next section. High frequencies originate from the continuous but not differentiable paths in imaginary time. In the following we will not explicitly state the Trotter error. In general, we employed a finite imaginary time step $\Delta\tau = 0.05/t$ and verified upon extrapolating $\Delta\tau \to 0$, that this value produces no artifacts.

In the Monte Carlo scheme the projection operator $\exp(-\Delta\tau H_t)$ will be applied to the a trial wave function over and over again. Both will be represented by a matrices, such that this is a good spot where one can reduce computation time by optimizing such matrix operations. Where a default matrix product produces costs of $\mathcal{O}(N^3)$, it can be reduced to $\mathcal{O}(N^2)$, by applying the Suzuki-Trotter decomposition to $\exp(-\Delta\tau H_t)$ an additional time. This procedure is called checkerboard decomposition and is described in detail in [10, 11]. Note, using the checkerboard decomposition, a symmetric Suzuki-Trotter decomposition is favorable for small values of U/t, in order to guarantee causal Green's functions (cf. App. A.1).

1.2.2. Hubbard-Stratonovich transformation

At each time step we use the Hubbard-Stratonovich (HS) transformation to bring the Hubbard interaction into bilinear form [15]. The transformation is based on the identity

$$\mathrm{e}^{A^2/2} = \frac{1}{\sqrt{2\pi}}\int d\phi\; \mathrm{e}^{-\phi^2/2-A\phi} \,, \tag{1.26}$$

where the exponential of a square is decomposed by a Gaussian integral. The Hubbard term can be written in squares $n_{i\uparrow}n_{i\downarrow} = \pm[(n_{i\uparrow} \pm n_{i\downarrow})^2 - n]/2$, such that the transformation is given by

$$\mathrm{e}^{\Delta\tau\frac{U}{2}(n_{i\uparrow}\pm n_{i\downarrow})^2} = \left(\frac{\Delta\tau}{2\pi}\right)^{\frac{1}{2}} \int d\phi_i \, \mathrm{e}^{-\frac{\Delta\tau}{2}\phi_i^2 + \Delta\tau\sqrt{U}(n_{i\uparrow}\pm n_{i\downarrow})\,\phi_i} \, . \tag{1.27}$$

This replaces the influence electron-electron interactions by a fictitious field ϕ acting on the electron. Instead of a continuous auxiliary field, it is more convenient to work with discrete variables [16]

$$\mathrm{e}^{-\Delta\tau U\sum_i (n_{i\uparrow}-1/2)(n_{i\downarrow}-1/2)} = C \sum_{s_1,\ldots,s_N=\pm 1} \mathrm{e}^{\alpha\pm\sum_i s_i(n_{i\uparrow}\mp n_{i\downarrow})} \, , \tag{1.28}$$

where on an N site lattice the constant $C = \exp(\Delta\tau U N/4)/2^N$. The transformation reduces the quadratic interaction of the double occupation into a linear interaction coupled to Ising-like variables s_i on each site and imaginary time slice. This rewriting of a many body problem to a manifold of single particle problems will allow us to evaluate the trace in form of a determinant below.

Coupling to spin and charge

In Eq. (1.28) you can see, that the auxiliary fields either couple to the spin, or the charge density. For these two cases the parameter α is given by

$$\cosh(\alpha) = \mathrm{e}^{\pm\frac{1}{2}\Delta\tau U} \, , \qquad \text{or} \qquad \alpha = 2\,\mathrm{arctanh}\left(\sqrt{\pm\tanh\left(\Delta\tau U/4\right)}\right) \, . \tag{1.29}$$

In order to work with real α, most implementations use the coupling to the spin. However, this clearly breaks SU(2) spin rotational invariance for a given configuration of the auxiliary fields, which is only restored after summation over (all) field configurations within the MC process [17]. Unless you study a problem where SU(2) symmetry is broken already, it is favorable to preserve it until broken spontaneously opting for the complex solution for α [18]. The drawback is an increased computational effort.

SU(N) symmetric transformation

For the presented simulations below, we use an SU(2) symmetric HS transformation which allows for a direct generalization to SU(N) symmetric models [19]. The interaction part of the imaginary time evolution operator is expressed as

$$\mathrm{e}^{-\Delta\tau U(n_\uparrow+n_\downarrow-1)^2/2} = \sum_{l=\pm1,\pm2} \gamma(l)\mathrm{e}^{\mathrm{i}\sqrt{\Delta\tau U/2}\,\eta(l)(n_\uparrow+n_\downarrow-1)} + \mathcal{O}(\Delta\tau^4) \, , \tag{1.30}$$

with the two functions γ and η of the four-valued auxiliary field $l = \pm 1, \pm 2$ taking on the values

$$\begin{aligned} \gamma(\pm 1) &= 1 + \sqrt{6}/3 \,, & \eta(\pm 1) &= \pm\sqrt{2\,(3 - \sqrt{6})} \,, \\ \gamma(\pm 2) &= 1 - \sqrt{6}/3 \,, & \eta(\pm 2) &= \pm\sqrt{2\,(3 + \sqrt{6})} \,. \end{aligned} \tag{1.31}$$

The advantage of this representation is the fact, that for each auxiliary field configuration, the SU(N) spin symmetry of the Hubbard model is conserved explicitly. The above HS transformation produces an overall systematic error proportional to $\Delta\tau^3$ in the Monte Carlo estimate of observables which, in comparison to the Trotter error of order $\Delta\tau^2$, is however negligible.

1.2.3. The central quantity: the Green's function

After the HS transformation we are left with non-interacting fermions subject to a time and space dependent field. Since we are dealing with free fermions Wick's theorem is applicable [20, 21, 22]. This enables us to compute arbitrary observables within the PQMC by expressing them in terms of the single particle propagators – the Green's function.

To simplify the further notation we introduce the index $x = (\mathbf{i}, \sigma)$ to define

$$\begin{aligned} H_t &= \sum_{x,y} c_x^\dagger T_{x,y} c_y \equiv \mathbf{c}^\dagger \mathbf{T} \mathbf{c} \,, \\ \alpha \sum_{\mathbf{i}} s_{\mathbf{i}} (n_{\mathbf{i}\uparrow} - n_{\mathbf{i}\downarrow}) &= \sum_{x,y} c_x^\dagger V(\mathbf{s})_{x,y} c_y \equiv \mathbf{c}^\dagger \mathbf{V}(\mathbf{s}_n) \mathbf{c} \,. \end{aligned} \tag{1.32}$$

Furthermore we define the imaginary time propagators

$$\begin{aligned} U_{\mathbf{s}}(\tau_2, \tau_1) &= \prod_{n=n_1+1}^{n_2} \mathrm{e}^{\mathbf{c}^\dagger \mathbf{V}(\mathbf{s}_n)\mathbf{c}} \mathrm{e}^{-\Delta\tau \mathbf{c}^\dagger \mathbf{T} \mathbf{c}} \,, \\ B_{\mathbf{s}}(\tau_2, \tau_1) &= \prod_{n=n_1+1}^{n_2} \mathrm{e}^{\mathbf{V}(\mathbf{s}_n)} \mathrm{e}^{-\Delta\tau \mathbf{T}} \,, \end{aligned} \tag{1.33}$$

where $n_1 \Delta\tau = \tau_1$ and $n_2 \Delta\tau = \tau_2$ and $\mathbf{s}$ denotes the HS-field foreach site and time slice. We can now rewrite the partition function of Eq. (1.25) as (cf. App. A.2)

$$Z = C^m \sum_{\mathbf{s}_1 \ldots \mathbf{s}_m} \mathrm{Tr}[U_{\mathbf{s}}(2\Theta, 0)] = C^m \sum_{\mathbf{s}_1 \ldots \mathbf{s}_m} \det[\mathbf{1} + B_{\mathbf{s}}(2\Theta, 0)] \,. \tag{1.34}$$

For the PQMC algorithm, we will require the trial wave function to be a slater determinant characterized by (the matrix) $\mathbf{P}$ [10]. This can be, e.g., obtained easily for the free

system, or within a mean field approximation. The trial wave function of an N-particle state is expressed in our notation reads

$$|\psi_T\rangle = \prod_{y=1}^{N} \Big(\sum_x c_x^\dagger P_{x,y} \Big) |0\rangle = \prod_{y=1}^{N} \Big(\mathbf{c}_x^\dagger \mathbf{P} \Big)_y |0\rangle \; , \tag{1.35}$$

such that

$$\big\langle \psi_T \big| \mathrm{e}^{2\Theta H} \big| \psi_T \big\rangle = C^m \sum_{\mathbf{s}_1 \ldots \mathbf{s}_m} \det[\mathbf{P}^\dagger B_{\mathbf{s}}(2\Theta, 0) \mathbf{P}] \; , \tag{1.36}$$

with $m\Delta\tau = 2\Theta$. As already stated, the goal is to compute expectation values

$$\frac{\big\langle \Psi_T \big| \mathrm{e}^{-\Theta H} O \mathrm{e}^{-\Theta H} \big| \Psi_T \big\rangle}{\big\langle \Psi_T \big| \mathrm{e}^{-2\Theta} \big| \Psi_T \big\rangle} = \sum_{\mathbf{s}} \mathbf{P}_{\mathbf{s}} \big\langle O \big\rangle_{\mathbf{s}} + \mathcal{O}(\Delta\tau^2) \; , \tag{1.37}$$

and

$$\begin{aligned} \mathbf{P}_{\mathbf{s}} &= \frac{\det[\mathbf{P}^\dagger B_{\mathbf{s}}(2\Theta, 0) \mathbf{P}]}{\sum_{\mathbf{s}} \det[\mathbf{P}^\dagger B_{\mathbf{s}}(2\Theta, 0) \mathbf{P}]} \; , \\ \big\langle O \big\rangle_{\mathbf{s}} &= \frac{\big\langle \psi_T \big| U_{\mathbf{s}}(2\Theta, \Theta)\, O\, U_{\mathbf{s}}(\Theta, 0) \big| \psi_T \big\rangle}{\big\langle \psi_T \big| U_{\mathbf{s}}(2\Theta, 0) \big| \psi_T \big\rangle} \; . \end{aligned} \tag{1.38}$$

The observable we want to compute is the equal-time single-particle Green's function $O = c_x c_y^\dagger = \delta_{x,y} - \mathbf{c}^\dagger \mathbf{A}^{(x,y)} \mathbf{c}$, with $\mathbf{A}^{(x,y)}_{x1,x2} = \delta_{x1,y} \delta_{x2,x}$. Inserting a source term, we know

$$\frac{\partial}{\partial \eta} \ln \big\langle \psi_T \big| U_1 \mathrm{e}^{\eta O} U_2 \big| \psi_T \big\rangle \Big|_{\eta=0} = \frac{\big\langle \psi_T \big| U_1 O U_1 \big| \psi_T \big\rangle}{\big\langle \psi_T \big| U_1 U_2 \big| \psi_T \big\rangle} \; . \tag{1.39}$$

Therefore the Green's function is obtained from

$$\begin{aligned} \big\langle c_x c_y^\dagger \big\rangle &= \delta_{x,y} - \frac{\partial}{\partial \eta} \ln \big\langle \psi_T \big| U_{\mathbf{s}}(2\Theta, \Theta)\, \mathrm{e}^{\eta \mathbf{c}^\dagger \mathbf{A}^{(x,y)} \mathbf{c}}\, U_{\mathbf{s}}(\Theta, 0) \big| \psi_T \big\rangle \Big|_{\eta=0} \\ &= \delta_{x,y} - \frac{\partial}{\partial \eta} \ln \det \Big[\mathbf{P}^\dagger B_{\mathbf{s}}(2\Theta, \Theta)\, \mathrm{e}^{\eta \mathbf{A}^{(x,y)}}\, B_{\mathbf{s}}(\Theta, 0) \mathbf{P} \Big] \Big|_{\eta=0} \\ &= \delta_{x,y} - \frac{\partial}{\partial \eta} \mathrm{Tr} \ln \Big[\mathbf{P}^\dagger B_{\mathbf{s}}(2\Theta, \Theta)\, \mathrm{e}^{\eta \mathbf{A}^{(x,y)}}\, B_{\mathbf{s}}(\Theta, 0) \mathbf{P} \Big] \Big|_{\eta=0} \\ &= \delta_{x,y} - \mathrm{Tr} \Big[\big(\mathbf{P}^\dagger B_{\mathbf{s}}(2\Theta, 0) \mathbf{P} \big)^{-1} \mathbf{P}^\dagger B_{\mathbf{s}}(2\Theta, \Theta) \mathbf{A}^{x,y} B_{\mathbf{s}}(\Theta, 0) \mathbf{P} \Big] \Big|_{\eta=0} \; , \end{aligned} \tag{1.40}$$

where we used the relation $\det A = \exp(\mathrm{Tr} \ln A)$. Cycling the operators within the trace yields

$$G_{\mathbf{s}}(\Theta)_{x,y} = \Big(1 - B_{\mathbf{s}}(\Theta, 0) \mathbf{P} \big(\mathbf{P}^\dagger B_{\mathbf{s}}(2\Theta, 0) \mathbf{P} \big)^{-1} \mathbf{P}^\dagger B_{\mathbf{s}}(2\Theta, \Theta) \Big)_{x,y} \; . \tag{1.41}$$

Using this quantity we can now express arbitrary observables as explained in Sec. 1.2.5.

1.2.4. Sampling procedure

The MC sampling consists now of creating altered auxiliary field configurations $\mathbf{s}'$ based on a single spin-flip algorithm. The acceptance of a proposed spin-flip (and hence a new configuration) is decided stochastically within a Metropolis scheme, given by the Metropolis decision $P_{\text{acc}} = \min[1, R]$. This requires knowledge of the ratio of the configuration weights

$$R = \frac{w[\mathbf{s}']}{w[\mathbf{s}]} = \frac{\mathbf{P}_{\mathbf{s}'}}{\mathbf{P}_{\mathbf{s}}} = \frac{\det[1 + \mathbf{P}^\dagger B_{\mathbf{s}'}(2\Theta, 0)\mathbf{P}]}{\det[1 + \mathbf{P}^\dagger B_{\mathbf{s}}(2\Theta, 0)\mathbf{P}]} \,. \tag{1.42}$$

The change of a single spin in the configuration affects the interaction matrix $\mathbf{V}(\mathbf{s}_n)$

$$\mathrm{e}^{\mathbf{V}(\mathbf{s}'_n)} = \Big[1 + \underbrace{\Big(\mathrm{e}^{\mathbf{V}(\mathbf{s}'_n)}\mathrm{e}^{\mathbf{V}(\mathbf{s}_n)} - 1\Big)}_{\Delta}\Big]\mathrm{e}^{\mathbf{V}(\mathbf{s}_n)} \,. \tag{1.43}$$

Here, the matrix Δ has only one non-vanishing entry $\Delta_{x,y} = \delta_{x,z}\delta_{y,z'}\eta^{(z,z')}$. The propagator changes to $B_{\mathbf{s}'}(2\Theta, 0) = B_{\mathbf{s}}(2\Theta, \tau)(1 + \Delta)B_{\mathbf{s}}(\tau, 0)$, accordingly. Let us introduce the notation $B^{\langle}_{\mathbf{s}} = \mathbf{P}^\dagger B_{\mathbf{s}}(2\Theta, \tau)$, and $B^{\rangle}_{\mathbf{s}} = B_{\mathbf{s}}(\tau, 0)\mathbf{P}$, to compute the ratio

$$\begin{aligned} R = \frac{\det\big[B^{\langle}_{\mathbf{s}}(1 + \Delta^{(i)})B^{\rangle}_{\mathbf{s}}\big]}{\det\big[B^{\langle}_{\mathbf{s}}B^{\rangle}_{\mathbf{s}}\big]} &= \det\Big[B^{\langle}_{\mathbf{s}}\Big(1 + \Delta^{(i)}\Big)B^{\rangle}_{\mathbf{s}}\Big(B^{\langle}_{\mathbf{s}}B^{\rangle}_{\mathbf{s}}\Big)^{-1}\Big] \\ &= \det\Big[1 + B^{\langle}_{\mathbf{s}}\Delta^{(i)}B^{\rangle}_{\mathbf{s}}\Big(B^{\langle}_{\mathbf{s}}B^{\rangle}_{\mathbf{s}}\Big)^{-1}\Big] \\ &= \det\Big[1 + \Delta^{(i)}B^{\rangle}_{\mathbf{s}}\Big(B^{\langle}_{\mathbf{s}}B^{\rangle}_{\mathbf{s}}\Big)^{-1}B^{\langle}_{\mathbf{s}}\Big] \,. \end{aligned} \tag{1.44}$$

In the last equality, we can identify the Green's function (Eq. (1.41)) defined by $1 - G_{\mathbf{s}}(\tau) = B^{\rangle}_{\mathbf{s}}(B^{\langle}_{\mathbf{s}}B^{\rangle}_{\mathbf{s}})^{-1}B^{\langle}_{\mathbf{s}}$. If the proposed spin-flip is accepted, we need to update the Green's function according to the new auxiliary field. Since a single spin-flip only affect one row and one column of the Green's function matrix the Sherman-Morrison formula can be used to implement an efficient updating procedure. Leaving the linear algebra details to the reader (details can be found in [10, 11]), the updated Green's function may be obtained by

$$\begin{aligned} \big[G_{\mathbf{s}'}(\tau)\big]_{x,y} &= \big[1 - (1 + \Delta)B^{\rangle}_{\mathbf{s}}(B^{\langle}_{\mathbf{s}}(1 + \Delta)B^{\rangle}_{\mathbf{s}})^{-1}B^{\langle}_{\mathbf{s}}\big]_{x,y} \\ &= \big[G_{\mathbf{s}}(\tau)\big]_{x,y} - \frac{\big[G_{\mathbf{s}}(\tau)\big]_{x,z}\,\eta^{(z,z')}\,\big[1 - G_{\mathbf{s}}(\tau)\big]_{z',y}}{1 + \eta^{z,z'}\,\big[1 - G_{\mathbf{s}}(\tau)\big]_{z',z}} \,. \end{aligned} \tag{1.45}$$

What is left is to compute the Green's function to an arbitrary and time displaced imaginary times $\tau > 0$,

$$G_{\mathbf{s}}(\tau)\Big(\Theta + \frac{\tau}{2}, \Theta - \frac{\tau}{2}\Big)_{x,y} = \Big[B_{\mathbf{s}}(\tau)\Big(\Theta + \frac{\tau}{2}, \Theta - \frac{\tau}{2}\Big)G_{\mathbf{s}}(\tau)\Big(\Theta - \frac{\tau}{2}\Big)\Big]_{x,y} \tag{1.46}$$

$$G_{\mathbf{s}}(\tau)\Big(\Theta - \frac{\tau}{2}, \Theta + \frac{\tau}{2}\Big)_{x,y} = -\Big[\Big(1 - G_{\mathbf{s}}(\tau)\Big(\Theta - \frac{\tau}{2}\Big)\Big)B^{-1}_{\mathbf{s}}\Big(\Theta + \frac{\tau}{2}, \Theta - \frac{\tau}{2}\Big)\Big]_{x,y} \,.$$

However, the naive propagation above reveals a major technical issue innate to all auxiliary field QMC algorithms: The algorithm demands for repeated matrix-matrix multiplications. However, the propagator matrices are terribly ill-conditioned. Because of the limited machine precision roundoff errors occur, which are blown up exponentially since most contributions are matrix exponentials. As a consequence matrix-matrix multiplications are unstable. Unfortunately, one is interested in small differences encoded in matrices which contain values which span a large range of orders. To overcome this problem, one can employ a stabilization procedure based on a singular value decomposition, which is described in [10, 11].

The efficient implementation to compute unequal times Green's function is based on the crucial observation, that in the PQMC the Green's function is a projector

$$\begin{aligned} G_{\mathbf{s}}(\tau)^2 &= G_{\mathbf{s}}(\tau) \,, \\ (1 - G_{\mathbf{s}}(\tau))^2 &= 1 - G_{\mathbf{s}}(\tau) \,. \end{aligned} \tag{1.47}$$

This property implies that propagators can be broken up into intervals, such that for $\tau_1 > \tau_2 > \tau_3$,

$$\begin{aligned} G_{\mathbf{s}}(\tau_1, \tau_3) &= B_{\mathbf{s}}(\tau_1, \tau_3) G_{\mathbf{s}}^2(\tau_3) = G_{\mathbf{s}}(\tau_1, \tau_3) G_{\mathbf{s}}(\tau_1, \tau_3) \\ &= \underbrace{G_{\mathbf{s}}(\tau_1, \tau_3) B_{\mathbf{s}}^{-1}(\tau_2, \tau_3)}_{G_{\mathbf{s}}(\tau_1, \tau_2)} \underbrace{B_{\mathbf{s}}(\tau_2, \tau_3) G_{\mathbf{s}}(\tau_3)}_{G_{\mathbf{s}}(\tau_2, \tau_3)} \,. \end{aligned} \tag{1.48}$$

Using the property above we can break up a large imaginary time propagation into a set of smaller intervals of length $\tau = N_\tau \tau_1$,

$$G_{\mathbf{s}}(\tau)\Big(\Theta + \frac{\tau}{2}, \Theta - \frac{\tau}{2}\Big) = \prod_{n=0}^{N_\tau - 1} G_{\mathbf{s}}(\tau)\Big(\Theta + \frac{\tau}{2} + (n+1), \Theta - \frac{\tau}{2} + n\tau_1\Big) \,. \tag{1.49}$$

By saving sections of the propagated ground state wave function to memory and clever bookkeeping Feldbacher and Assaad present a highly efficient implementation in Ref. [23, 10].

In principle, the equations presented above give us all the tools necessary to create a Markov chain: Start from a random auxiliary field configuration, compute the Green's function from scratch (Eq. (1.41)), and start sweeping through the auxiliary field (Eq. (1.46)) in order to update the configuration according to Eq. (1.44) and Eq. (1.45).

1.2.5. Observables and Wick's theorem

The fermionic QMC algorithms presented here and in Ch. 2 share the property that they provide access to the single particle Greens function. For a given MC-configuration

Wick's theorem holds and arbitrary observables and correlation functions can be expressed from this central quantity [20, 21, 22]. The general formal rule of the Wick decomposition follows from the definition of the cumulants

$$\langle\langle O_n \dots O_1 \rangle\rangle = \frac{\partial^n}{\partial\eta_n \dots \partial\eta_1} \ln \left\langle \psi_T \middle| U_{\mathbf{s}}(2\Theta,\Theta) \mathrm{e}^{\eta_n O_n} \dots \mathrm{e}^{\eta_1 O_1} U_{\mathbf{s}}(\Theta,0)) \middle| \psi_T \right\rangle \Big|_{\eta_1,\dots,\eta_n=0} , \tag{1.50}$$

with $O_i = \mathbf{c}^\dagger \mathbf{A}^{(i)} \mathbf{c}$. Differentiating the above we obtain

$$\begin{aligned} \langle\langle O_1 \rangle\rangle_{\mathbf{s}} &= \langle O_1 \rangle_{\mathbf{s}} \\ \langle\langle O_2 O_1 \rangle\rangle_{\mathbf{s}} &= \langle O_2 O_1 \rangle_{\mathbf{s}} - \langle O_2 \rangle_{\mathbf{s}} \langle O_1 \rangle_{\mathbf{s}} \\ \langle\langle O_3 O_2 O_1 \rangle\rangle_{\mathbf{s}} &= \langle O_3 O_2 O_1 \rangle_{\mathbf{s}} \\ &\quad - \langle O_3 \rangle_{\mathbf{s}} \langle\langle O_2 O_1 \rangle\rangle_{\mathbf{s}} - \langle O_2 \rangle_{\mathbf{s}} \langle\langle O_3 O_1 \rangle\rangle_{\mathbf{s}} \\ &\quad - \langle O_1 \rangle_{\mathbf{s}} \langle\langle O_3 O_2 \rangle\rangle_{\mathbf{s}} - \langle O_1 \rangle_{\mathbf{s}} \langle O_2 \rangle_{\mathbf{s}} \langle O_3 \rangle_{\mathbf{s}} \\ \dots &= \dots . \end{aligned} \tag{1.51}$$

This leads to the following rule, which may be proven by induction,

$$\begin{aligned} \langle O_n \dots O_1 \rangle_{\mathbf{s}} = \langle\langle O_n \dots O_1 \rangle\rangle_{\mathbf{s}} &+ \sum_{j=1}^{n} \langle\langle O_n \dots \hat{O}_j \dots O_1 \rangle\rangle_{\mathbf{s}} \langle\langle O_j \rangle\rangle_{\mathbf{s}} \\ &+ \sum_{j>i} \langle\langle O_n \dots \hat{O}_j \dots \hat{O}_i \dots O_1 \rangle\rangle_{\mathbf{s}} \\ &\times \langle\langle O_j O_i \rangle\rangle_{\mathbf{s}} + \dots + \langle\langle O_n \rangle\rangle_{\mathbf{s}} \dots \langle\langle O_1 \rangle\rangle_{\mathbf{s}} , \end{aligned} \tag{1.52}$$

where $\hat{O}_j$ means that the operator O_j has bee omitted from the product [24]. The cumulants may now be computed order by order in the same fashion as Eq. (1.40). Although one can exploit some symmetries to reduce the number of distinct terms one has to Wick-decompose, complex observables may consist of a large number of operator sequences. Additionally, the generalization of correlation functions to arbitrary numbers of (spin) flavors presents an especially challenging problem and the task becomes more and more tedious. Fortunately, the Wick decomposition can be implemented in a simple recursive subroutine and the computer can take over most of the work:

We define the observable expressed through fermionic operators in MATHEMATICA. Preserving the ordering of fermionic operators we use a non-commutative expand function to obtain a sequence of terms. Keeping track of the pre-factors, individual terms (operator sequences) are passed to a `Fortran` program to determine all nonzero contractions of the combinations of creator-annihilator pairs, which is a sum of single particle propagators:

```
FUNCTION findPartner(op,list)
  Find an operator in list which matches the quantum numbers
  of op and return its position.
```

`SUBROUTINE decompose(list)`
- Find pairs of operators via `findPartner(op,list)` and pass the remaining part of the operator list to the subroutine recursively.
- Print out each found pair with the leading sign according to the number of commutations necessary to rearrange the operator list.
- Recursively pass the remaining part of the operator list to the subroutine.
- `EXIT` if the number of elements in `list` reaches two.

`PROGRAM wick`
- Create a list of all flavor combinations.
- Foreach combination create a corresponding operator list and decompose it. `CALL decompose(list)`

For, e.g., a six-operator string, the decomposition outlined above is performed like that:

$$\begin{aligned}
\left\langle c^\dagger_{x_3} c_{y_3} c^\dagger_{x_2} c_{y_2} c^\dagger_{x_1} c_{y_1} \right\rangle_{\mathbf{s}} &= \left\langle c^\dagger_{x_3} c_{y_3} \right\rangle_{\mathbf{s}} \left\langle c^\dagger_{x_2} c_{y_2} c^\dagger_{x_1} c_{y_1} \right\rangle_{\mathbf{s}} \\
&\quad + \left\langle c^\dagger_{x_3} c_{y_2} \right\rangle_{\mathbf{s}} \left\langle c_{y_3} c_{y_2} c^\dagger_{x_2} c^\dagger_{x_1} c_{y_1} \right\rangle_{\mathbf{s}} \\
&\quad + \left\langle c^\dagger_{x_3} c_{y_1} \right\rangle_{\mathbf{s}} \left\langle c_{y_3} c_{y_2} c^\dagger_{x_2} c_{y_2} c^\dagger_{x_1} \right\rangle_{\mathbf{s}} \\
&= \left\langle c^\dagger_{x_3} c_{y_3} \right\rangle_{\mathbf{s}} \left(\left\langle c^\dagger_{x_2} c_{y_2} \right\rangle_{\mathbf{s}} \left\langle c^\dagger_{x_1} c_{y_1} \right\rangle_{\mathbf{s}} + \left\langle c^\dagger_{x_2} c_{y_1} \right\rangle_{\mathbf{s}} \left\langle c_{y_2} c^\dagger_{x_1} \right\rangle_{\mathbf{s}} \right) \\
&\quad + \left\langle c^\dagger_{x_3} c_{y_2} \right\rangle_{\mathbf{s}} \left(\left\langle c_{y_3} c^\dagger_{x_2} \right\rangle_{\mathbf{s}} \left\langle c^\dagger_{x_1} c_{y_1} \right\rangle_{\mathbf{s}} - \left\langle c_{y_3} c^\dagger_{x_1} \right\rangle_{\mathbf{s}} \left\langle c^\dagger_{x_2} c_{y_1} \right\rangle_{\mathbf{s}} \right) \\
&\quad + \left\langle c^\dagger_{x_3} c_{y_1} \right\rangle_{\mathbf{s}} \left(\left\langle c_{y_3} c^\dagger_{x_2} \right\rangle_{\mathbf{s}} \left\langle c_{y_2} c^\dagger_{x_1} \right\rangle_{\mathbf{s}} + \left\langle c_{y_3} c^\dagger_{x_1} \right\rangle_{\mathbf{s}} \left\langle c^\dagger_{x_2} c_{y_2} \right\rangle_{\mathbf{s}} \right) .
\end{aligned} \tag{1.53}$$

The results for all terms are collected and simplified by *Mathematica* and you are ready to paste the result to your code. Since the expressions of decomposed observables can take up several pages of code, the simplification significantly enhances the performance of their evaluation.

1.2.6. The sign problem

Away from half filling, or for non-bipartite interactions, particle-hole symmetry is not conserved. This implies that the fermionic determinant defined in Eq. (1.34) is no longer strictly positive. Consequently the weights $w[\mathbf{s}]$ (cf. Eq. (1.42)) can become negative, no longer representing a probability for a specific configuration. In this situation it is necessary to deal with the estimators by taking the absolute value of the weight and include the sign explicitly in the observables

$$\langle A \rangle = \frac{\sum_{\{\mathbf{s}\}} |w[\mathbf{s}]| \ \mathrm{sign}(w[\mathbf{s}])\, A(\mathbf{s})}{\sum_{\{\mathbf{s}\}} |w[\mathbf{s}]| \ \mathrm{sign}(w[\mathbf{s}])} \overset{\mathrm{MC}}{\approx} \frac{\sum_{k=1}^{K} A_k \, sign_k}{\sum_{k=1}^{K} sign_k} \tag{1.54}$$

where

$$\langle sign \rangle = \frac{\mathcal{Z}_w}{\mathcal{Z}_{|w|}} = \frac{\sum_{\{\mathbf{s}\}} w[\mathbf{s}]}{\sum_{\{\mathbf{s}\}} |w[\mathbf{s}]|} = \mathrm{e}^{-\beta N \Delta f} \,. \tag{1.55}$$

Here Δf denotes the difference of the free energy densities. The average sign is strictly positive and real but decreases exponentially with system size and inverse temperature, such that the computational costs will be exponential instead of polynomial. The inverse temperature is interchangeable with the projection parameter 2Θ at $T = 0$ in the PQMC.

Troyer and Wiese [25] argued the sign problem to be generically NP-hard (nondeterministic polynomial), hence not solvable in polynomial growing time effort [26]. Their discussion is based on the mapping of the fermionic quantum system to the classical spin-glass model, which is believed to be NP-hard. Since any NP-hard problem can be mapped onto another with polynomial complexity, a general solution of an NP-hard problem is thus equivalent solving *any* NP-problem. Nevertheless, it is still possible that the sign problem for a *specific* problem may be overcome. For an example in a different model see Chandrasekharan's and Wiese's Meron-Cluster solution [27].

1.2.7. Data analysis

Although several sweeps are skipped between measurements the data are correlated and blue-eyed analysis would severely bias the results. Therefore, the autocorrelation times have to be calculated, uncorrelated means have to be determined and from those the variances can be computed unbiased [28, 11].

Binning and autocorrelation time

Small changes in the configurations of the MC-sampling procedure cause statistical correlations which have to be taken into account in the analysis. To quantify these correlations we define the autocorrelation function for an observable O

$$\begin{aligned} C_O(t) = C_O(O_i, O_{i+t}) &= \big\langle \big(O_i - \langle O_i \rangle\big)\big(O_{i+t} - \langle O_{i+t} \rangle\big) \big\rangle \\ &= \langle O_i O_{i+t} \rangle - \langle O_i \rangle \langle O_{i+t} \rangle \,, \end{aligned} \tag{1.56}$$

where the number index i denotes the number of the measurement and t defines the separation of the measurements in the time-series. In this section we use $\langle \ldots \rangle$ to denote the average over all indices i. In the limit $N \to \infty$ measurements, this becomes the physical expectation value. For $t = 0$ the correlation function equals the variance in case of single uncorrelated measurements σ_O^2. With this definition we introduce the normalized autocorrelation function given by

$$\Gamma(t) = \frac{C_O(t)}{C_O(0)} = \sum_{i=1}^{N-t} \frac{\langle O_i O_{i+t} \rangle - \langle O_i \rangle \langle O_i \rangle}{\langle O_i^2 \rangle - \langle O_i \rangle \langle O_i \rangle} \,, \tag{1.57}$$

with N as the total number of measurements. For increasing separation in the time-series, $\Gamma(t)$ decays exponentially $\Gamma(t) \to a\, \mathrm{e}^{-t/\tau_{O,\mathrm{exp}}}$ for $t \to \infty$, where $\tau_{O,\mathrm{exp}}$ denotes the so-called *exponential* autocorrelation time and a is a constant. The exponential autocorrelation time defines the upper limit of how strongly subsequent measurements are correlated [29]. The variance of correlated measurements is calculated by collecting the diagonal and off-diagonal terms of

$$\begin{aligned}
\sigma^2_{\overline{O}} &= \frac{1}{N^2}\sum_{i,j=1}^{N}\langle O_i O_j\rangle - \frac{1}{N^2}\sum_{i,j=1}^{N}\langle O_i\rangle\langle O_j\rangle = \frac{1}{N^2}\sum_{i,j=1}^{N} C_O\left(|i-j|\right) \\
&= \frac{1}{N^2}\sum_{t=-N+1}^{N-1}\sum_{k=1}^{N-|t|} C_O\left(|t|\right) = \sum_{t=-N}^{N} C_O\left(|t|\right)\frac{N-|t|}{N^2} \\
&= \frac{C_O\left(0\right)}{N}\sum_{t=-N}^{N}\Gamma_O\left(|t|\right)\left(1-\frac{|t|}{N}\right) \\
&= \frac{\sigma^2_O}{N}\,2\left[\frac{1}{2}+\sum_{t=1}^{N}\Gamma_O\left(t\right)\left(1-\frac{t}{N}\right)\right] = \frac{\sigma^2_O}{N}\,2\tau_{O,\mathrm{int}}\ . \qquad (1.58)
\end{aligned}$$

Here, we defined the so-called (proper) *integrated* autocorrelation time

$$\tau_{O,\mathrm{int}} = \frac{1}{2}+\sum_{t=1}^{N}\Gamma_O\left(t\right)\left(1-\frac{t}{N}\right) = \frac{N\sigma^2_{\overline{O}}}{2\,\sigma^2_O}\ , \qquad (1.59)$$

For a large number of data sets the analysis by integration to obtain the integrated autocorrelation time is often too cumbersome for a day by day basis. The binning (or blocking) analysis is much more convenient than full integration of Eq. (1.57). By grouping the incoming data into bins, one forms a new (shorter) time series; large enough bin-sizes result in a series of almost uncorrelated block-values and thus can be analyzed by standard means. For data sets consisting of N correlated measurements O_i, we block them in N_B bins of length k such that $N = N_B\, k$. The block-average of the n-th of N_B bins is $O_{B,n} = (1/k)\sum_{i=1}^{k} O_{(n-1)\,k+i}$. Obviously, the mean value over all bin-averages satisfies $\overline{O}_B = \overline{O}$. If the bins are large enough to form a basically uncorrelated series, their variance can be computed as an unbiased estimator leading to the square of the error of the mean value

$$\epsilon^2_{\overline{O}} \equiv \sigma^2_{\overline{O}} \simeq \frac{\sigma^2_B(N_B)}{N_B} \equiv \frac{1}{N_B\left(N_B-1\right)}\sum_{n=1}^{N_B}\left(O_{B,n}-\overline{O}_B\right)^2\ . \qquad (1.60)$$

The integrated autocorrelation time is now given by

$$\tau_{O,\mathrm{int}}(N_B) = \frac{k\,\sigma^2_B(N_B)}{2\,\sigma^2_{O_i}}\ , \qquad (1.61)$$

which converges, with decreasing binning block-number N_B (and therefore statistical independence), to the integrated autocorrelation time $\tau_{O,\mathrm{int}}$.

Due to these (temporal) correlations of the measurements the statistical error $\epsilon_{\overline{O}} = \sigma_{\overline{O}}$ of the MC-estimator O is increased by a factor $\sqrt{2\,\tau_{O,\mathrm{int}}}$. This leads to the *effective* statistics $N_{\mathrm{eff}} = N/2\tau_{O,\mathrm{int}}$, or respectively $\sigma^2_{\overline{O},\mathrm{eff}} = 2\tau_{O,\mathrm{int}}\,\sigma^2_{\overline{O}}$. This shows that only every $2\,\tau_{O,\mathrm{int}}$-the measurement is approximately uncorrelated. By tuning the number of sweeps skipped between MC-measurements with respect to the integrated autocorrelation time, the computational overhead can be reduced.

Finally, we briefly mention the issue of *critical slowing down*. While the autocorrelation-time depends on the updating algorithm, it is also influenced by the parameters of the lattice system. One can expect the integrated (exponential) autocorrelation time to increase as $\tau_{\mathrm{int}} \sim \xi^z$, where z denotes the dynamical critical exponent and ξ is the leading correlation length in the system *of the MC algorithm* employed. As one approaches a phase transition, the correlation length diverges, or on the finite lattice becomes of the order of the system size $\xi \leq N$ ($\xi \leq L$ for correlations in imaginary time). The computational effort then grows typically like $NL\min[\xi, N, L]^z$. For local updates one expects $z \approx 2$ [30].

Jackknife

With the knowledge of the integrated autocorrelation time, the means of the measured quantities and their error can be computed. Instead of solving the complicated error propagation of non-linear combinations of observables, the Jackknife method allows to obtain a controlled estimate of the variances *automatically*. The method has also the advantage to give reliable results even for a small number of data points.

Similar to the binning analysis, the original data points are blocked into bins of length $k = N/N_B$. To obtain the asymptotic error, k must be significantly larger than the relevant integrated autocorrelation time $\tau_{O,\mathrm{int}}$. With this uncorrelated set of data points the, possibly highly nonlinear, analysis of, e.g., weighted observables will be then repeatedly done with all but one (varying) bins. From all N_B data we calculate the overall average $\overline{O}$. The Jackknife-averages $O_{J,n}$ containing all but one of the block-values is obtained with the n-th-block-average $O_{B,n}$ via

$$O_{J,n} = \frac{N\overline{O} - k\,O_{B,n}}{N-k} \qquad n = 1, \ldots, N_B\ . \tag{1.62}$$

The overall Jackknife-average is $\overline{O}_J = (1/N_B)\sum_{N_B} O_{J,n}$. The N_B Jackknife blocks now containing $N-k$ data are trivially correlated since each of them originates from nearly the same $N_B - 1$ bins. Because of the trivial nature of this correlation, the variance can be corrected by multiplying with a factor $(N_B-1)^2$ leading to the final error

$$\epsilon_O^2 = \sigma_O^2 = \frac{N_B - 1}{N_B} \sum_{n=1}^{N_B} \left(O_{J,n} - \overline{O}_J \right)^2 \ . \tag{1.63}$$

We summarize: from the binning analysis the integrated autocorrelation time can be determined. Blocking the data into bins of a size significantly larger than the integrated autocorrelation time results in approximately statistically independent variables. Finally, we employ the jackknife method to obtain the errors of arbitrary combinations of measured observables.

1.3. Fermions on a lattice: the Hubbard model

The simplest model describing itinerant, interacting fermions is the single band Hubbard model [31, 32, 33]. Named after John Hubbard (1931-1980) it describes the competition between kinetic energy and local Coulomb repulsion, which allows to study metal-insulator transitions. Despite its simple structure the Hubbard model remains unsolved, except for certain limits and one dimension.

1.3.1. The model and its limits

The Hubbard model describes itinerant, interacting electrons by the Hamiltonian

$$H_{\mathrm{H}} = - \sum_{\langle ij \rangle, \sigma} t_{ij} \left(c_{i\sigma}^\dagger c_{j\sigma} + c_{j\sigma}^\dagger c_{i\sigma} \right) + U \sum_i n_{i\uparrow} n_{i\downarrow} \ , \tag{1.64}$$

with the local density $n_{i\sigma} = c_{i\sigma}^\dagger c_{j\sigma}$. The first term describes the kinetic contribution of the electrons which gain the energy t_{ij} (the transfer integrals) via hopping between lattice sites. The symbol $\langle ij \rangle$ represents the nearest neighbor pairs and the fermionic operator $c_{i\sigma}^\dagger$ ($c_{i\sigma}$) creates (annihilates) an electron at site i with spin σ. The second term represents the local Coulomb interaction which contributes the energy U to the Hamiltonian in case two electrons with spins $\sigma, -\sigma$ are located at the same site i. In physical means this, e.g., accounts for the large Coulomb repulsion of two electrons in a single d-orbital.

In one dimension the model is exactly solvable via the Bethe-Ansatz [34, 35, 36, 37] and does not show any quasi-particle excitations near the Fermi-surface. Its low energy physics is defined by collective modes namely spinons and holons (spin- and charge-fluctuations). The two- and higher dimensional Hubbard model is not (yet) exactly solved in the thermodynamic limit. Despite the simplicity of the Hubbard model it is not fully understood [38].

In the *tight-binding* (or *Fermi-gas*) *limit* $U = 0$ the Hamiltonian (1.64) describes free particles and becomes diagonal in k-space. The *atomic limit* ($t = 0$) – where no charge

transfer exists – reduces the Hamiltonian to a single site problem, now diagonal in real space. In the *infinite-U limit* the ground state is a highly degenerate insulator (with log-2 entropy per site) and is described in the Nagaoka-problem, which is only exactly solvable in the cases of one dimension, or a single hole in the half-filled band at arbitrary dimensions. Oddly, the single hole is sufficient to drive the system ferromagnetically [39]! For negative values of the coupling ($U < 0$) one obtains the attractive Hubbard model. Physically, the local attraction can have its origin in the coupling to polarons or local phonons. For values of $U > 0$ the local interaction is repulsive. Then, as a consequence of virtual hopping of two anti-parallel spins the model favors anti-ferromagnetic order. This can be explained nicely in a two-site model whose ground state is spanned by the states $\{0\} = \{|\uparrow,\uparrow\rangle, |\downarrow,\uparrow\rangle, |\uparrow,\downarrow\rangle, |\downarrow,\downarrow\rangle, \}$. First order perturbation theory in the kinetic energy term creates double occupation, which is penalized by the energy U and takes us out of the ground state. However, a second order process leads to a favorable tradeoff between kinetic and potential energy. Second order perturbation theory yields [39]

$$\langle a|H^{(2)}|b\rangle = -\langle a|H_t \frac{1-P_0}{U} H_t|b\rangle = -\sum_{n\notin\{0\}} \langle a|H_t|n\rangle \frac{1}{\langle n|U|n\rangle} \langle n|H_t|b\rangle \,, \tag{1.65}$$

where a, b denotes states in the ground state manifold $\{0\}$ whose projector is P_0, $|n\rangle$ is the doubly occupied state. Each contribution can be expressed by an exchange path illustrated here:

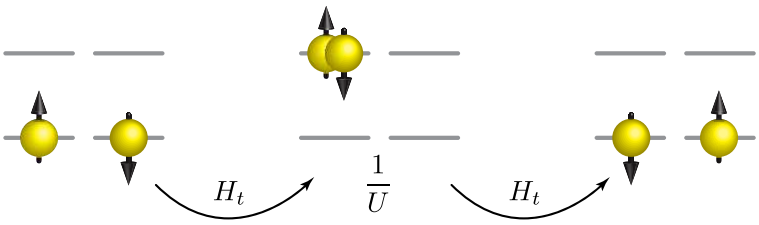

There are four possible paths, depending on the initial spin configuration and the position of the intermediate doubly occupied site. Paths such as $H_t|\uparrow,\uparrow\rangle = 0$ are blocked by the Pauli exclusion principle. In the singly occupied ground state the charge channel does not play a role and states can be expressed by spin operators, such that an effective Hamiltonian in the ground state subspace can be written as an isotropic antiferromagnetic Heisenberg model [39]

$$H^{(2)} = J\mathbf{S}_1 \cdot \mathbf{S}_2 \,, \quad \text{with the superexchange coupling} \quad J = \frac{4t^2}{U} \,. \tag{1.66}$$

This is the perfect example of an emergent energy scale J, for which the physics of the Hubbard model at large, but finite U/t, can be effectively described by the Heisenberg model. A descendant of this low energy effective model is the t-J-model which includes

the effective spin exchange term plus the kinetic energy term. We will encounter the t-J-model again in Ch. 4. A general classification of the phase-transition and phase-boundaries of the two dimensional Hubbard model is discussed by Watanabe and Imada [40].

Hubbard's simple model has lead to genuinely new results. But, unfortunately, it did not provide a solution to its original problem of localized versus itinerant behavior in metallic ferromagnets [31, 32, 33]. Originally designed for the description of ferromagnetism, the Hubbard model does not describe ferromagnetism, except for a few special cases of parameters and lattice types. The Hubbard model is as fundamental to quantum systems as the Ising model to classical statistical physics. It characterizes the essentials of phenomena like filling-, or bandwidth-controlled Mott-Metal-insulator transition, BCS-superconductivity, high temperature superconductivity (who knows?), spin liquids, liquid helium and more (or is assumed to do so) [38].

1.3.2. Hamiltonian symmetries

The discrete symmetries of the Hubbard model can be revealed by particle-hole transformations P, where $P \in Z_2 \to \{1, P\}$ and $P^2 = P$ [38]. The particle-hole transformation in both spin-channels $\sigma = \uparrow, \downarrow$

$$\begin{aligned} P c^\dagger_{i,\sigma} P &= c_{i,\sigma} \\ P c_{i,\sigma} P &= c^\dagger_{i,\sigma} \,, \end{aligned} \tag{1.67}$$

applied to the Hubbard Hamiltonian with a fixed number of electrons in an L-site system allows to deduce

$$H(N_\uparrow, N_\downarrow, U, t) \equiv H(L - N_\uparrow, L - N_\downarrow, U, -t) - U(L - N_\uparrow - N_\downarrow) \,. \tag{1.68}$$

This has the consequence that it is sufficient to study a subspace of the parameters, e.g., less than half-filling and positive S^z, since the remaining subspace can be obtained by particle hole transformation.

On bipartite lattices and for non-frustrated interactions the particle-hole transformation of one spin-channel

$$\begin{aligned} P c^\dagger_{i,\downarrow} P &= (-1)^i c_{i,\downarrow} \\ P c_{i,\uparrow} P &= c_{i,\uparrow} \\ P c^\dagger_{i,\downarrow} c_{j,\downarrow} P &= (-1)^i (-1)^j c^\dagger_{i,\downarrow} c_{j,\downarrow} = c^\dagger_{i,\downarrow} c_{j,\downarrow} \,, \end{aligned} \tag{1.69}$$

shows the equivalency between the repulsive ($U > 0$) and the attractive ($U < 0$) Hubbard model

$$\begin{aligned} H(N_\uparrow, N_\downarrow, U) &\equiv H(L - N_\uparrow, N_\downarrow, -U) + U N_\downarrow \\ &\equiv H(N_\uparrow, L - N_\downarrow, -U) + U N_\uparrow \,. \end{aligned} \tag{1.70}$$

At particle-hole symmetry (half-filling) $L = N_\uparrow = N_\downarrow$, the equivalency of the attractive and the repulsive Hubbard allows for a simple translation of symmetry broken phases from positive to negative U: a spin-density wave becomes a charge density wave (or s-wave pairing), antiferromagnetic spin order becomes charge order and so on.

Also on bipartite lattices the transformation

$$\begin{aligned} Pc^\dagger_{i,\sigma}P &= (-1)^i c^\dagger_{i,\sigma} , \\ Pc_{i,\sigma}P &= (-1)^i c_{i,\sigma} , \end{aligned} \tag{1.71}$$

changes the sign of the creation and annihilation operators on one sublattice. While this implies the change of the sign of the kinetic energy operator, the potential energy operator remains untouched, such that the sign of the hopping t may be chosen at will and

$$H(N_\uparrow, N_\downarrow, U, t) \equiv H(N_\uparrow, N_\downarrow, U, -t) . \tag{1.72}$$

The complexity of the model is mostly contained in its continuous symmetries: While the U(1) gauge freedom of all quantum models and the SU(2) spin rotational symmetry are obvious properties of the constituents of the Hubbard and Heisenberg models, the Hubbard model bears another, more concealed, continuous symmetry: SU(2) charge, or η-pairing symmetry.

We start from the fermionic representation of spin $S^{(a)}_i = \frac{1}{2}\sum_{\alpha,\beta} c^\dagger_{i,\alpha}\boldsymbol{\sigma}^{(a)}_{\alpha,\beta}c_{i,\beta}$ with the Pauli matrices $\boldsymbol{\sigma} = \{\boldsymbol{\sigma}^x, \boldsymbol{\sigma}^y, \boldsymbol{\sigma}^z\}$

$$\begin{aligned} S^x_i &= \frac{1}{2}(c^\dagger_{i,\uparrow}c_{i,\downarrow} + c^\dagger_{i,\downarrow}c_{i,\uparrow}) , \\ S^y_i &= -\frac{\mathrm{i}}{2}(c^\dagger_{i,\uparrow}c_{i,\downarrow} - c^\dagger_{i,\downarrow}c_{i,\uparrow}) , \\ S^z_i &= \frac{1}{2}(n_{i,\uparrow} - n_{i,\downarrow}) . \end{aligned} \tag{1.73}$$

The Hubbard Hamiltonian is invariant against global spin rotations

$$S^{(a)} = \sum_i S^{(a)}_i , \quad \text{where} \quad a \in \{x, y, z\} , \quad \text{and} \quad \mathbf{S} = (S^x, S^y, S^z) , \tag{1.74}$$

which are the generators that form the SU(2) spin algebra, which we will denote as $\mathrm{SU}(2)_\mathrm{s}$. Frequently, the ladder operators $S^+ = S^x + \mathrm{i}S^y$, $S^- = S^x - \mathrm{i}S^y$ and S^z are used as generators, instead. Both definitions of generators are valid since applied to any element out of SU(2) they allow to generate the full group. Once the continuous symmetry is broken, Goldstone modes emerge at zero energy (c.f. Sec. 1.4).

We apply the particle-hole transformation of one spin-channel defined in Eq. (1.69) to the generators of $\mathrm{SU}(2)_\mathrm{s}$, which defines the generators of $\mathrm{SU}(2)_\eta$

$$\eta^{(a)} = PS^{(a)}P , \quad \text{and} \quad \boldsymbol{\eta} = (\eta^x, \eta^y, \eta^z) , \tag{1.75}$$

with the operators $\eta_i^{(a)} = P\frac{1}{2}\sum_{\alpha,\beta} c_{i,\alpha}^\dagger \boldsymbol{\sigma}^{(a)} c_{i,\beta} P$, given by

$$\begin{aligned}
\eta_i^x &= \frac{1}{2}(-1)^i \left(c_{i,\uparrow}^\dagger c_{i,\downarrow}^\dagger + c_{i,\downarrow} c_{i,\uparrow}\right) = \frac{1}{2}(-1)^i \left(\Delta_i^\dagger + \Delta_i\right) \ , \\
\eta_i^y &= \frac{\mathrm{i}}{2}(-1)^i \left(c_{i,\uparrow}^\dagger c_{i,\downarrow}^\dagger - c_{i,\downarrow} c_{i,\uparrow}\right) = \frac{\mathrm{i}}{2}(-1)^i \left(\Delta_i^\dagger - \Delta_i\right) \ , \\
\eta_i^z &= \frac{1}{2}(n_i - 1) \ . \qquad (1.76)
\end{aligned}$$

We take even and odd superpositions to define the common raising and lowering operators

$$\begin{aligned}
\eta_i^+ &= \eta_i^x + \mathrm{i}\eta_i^y = (-1)^i c_{i,\uparrow}^\dagger c_{i,\downarrow}^\dagger = (-1)^i \Delta_i^\dagger \ , \\
\eta_i^- &= \eta_i^x - \mathrm{i}\eta_i^y = (-1)^i c_{i,\downarrow} c_{i,\uparrow} = (-1)^i \Delta_i \ . \qquad (1.77)
\end{aligned}$$

They create (annihilate) double occupancies, carry eigenvalues U and $\big|\Psi\big\rangle = (\eta^\dagger)^n \big|\Psi_0\big\rangle$, hence represent eigenstates of the Hamiltonian [41]. The operators η^+, η^- and η^z represent the generators of $\mathrm{SU}(2)_\eta$. The corresponding primary excitations are referred to as holons and antiholons.

The η-generators commute with the Hamiltonian $[H, \boldsymbol{\eta}] = 0$ and the generators of $\mathrm{SU}(2)_\mathrm{s}$ ($[\mathbf{S}, \boldsymbol{\eta}] = 0$), hence they are independent invariants of the Hubbard Hamiltonian. This implies that the quantities total spin $\mathbf{S}$, S^z, η-pairing and total charge are simultaneously conserved quantities represented by the symmetry groups $\mathrm{SU}(2)_\mathrm{s}$ and $\mathrm{SU}(2)_\eta$: The SU(2) Hubbard Hamiltonian is invariant under symmetry operations out of

$$\mathrm{SU}(2)_\mathrm{s} \times \mathrm{SU}(2)_\mathrm{c}/\mathrm{Z}_2 \ . \qquad (1.78)$$

The U(1) gauge (phase) freedom, which is also contained in SU(2), is a general property of quantum systems and is not explicitly expressed. The reduction by the abelian subgroup (center) Z_2 is because not all representations of both $\mathrm{SU}(N)$ groups are present simultaneously due to their multiplet structure [41]: For example $\mathbf{S}^2$ takes the values $S(S+1)$, where $2S \in \mathbb{N}^0$. The same holds for η such that $S + \eta$ must also be integer. The symmetry (1.78) is often associated with SO(4) symmetry as they both have such commutation relations. However we want to point out that any η-operator applied to a spin state vanishes ($\boldsymbol{\eta}\big|\mathrm{spin}\big\rangle = 0$), hence the product $\eta_i^\alpha S_i^\beta = 0$, which is not a property of SO(4) [42].

The symmetries of the SU(2) Hubbard Heisenberg model can be extended to higher symmetries $\mathrm{SU}(N)$. For $p > 1$, $N - p > 1$ the $\mathrm{SU}(N)$ group contains the subgroups [43]

$$\mathrm{SU}(N) \supset \mathrm{SU}(p) \times \mathrm{SU}(N-p) \times \mathrm{U}(1) \ . \qquad (1.79)$$

We have already shown the spin- and η-pairing symmetry for a single SU(2) group. Hence for $p = 2$ the $\mathrm{SU}(N)$ symmetry for even N is contained in the subgroups

$$\mathrm{SU}(N) \supset \mathrm{SU}(2) \times \mathrm{SU}(2) \times \ldots \mathrm{SU}(2) \times \mathrm{U}(1) \ . \qquad (1.80)$$

This allows to naturally generalize the spin and η-pairing symmetries to $\mathrm{SU}(N)_\mathrm{s}$ and $\mathrm{SU}(N)_\eta$, such that the $\mathrm{SU}(N)$ Hubbard Hamiltonian is invariant under symmetry operations out of $\mathrm{SU}(N)_s \times \mathrm{SU}(N)_c/\mathrm{Z}_N$.

1.4. Quantum phase transitions and order

A quantum phase transition (QPT) is a phase transition strictly defined for $T = 0$ as a consequence of triggering the relative strength (or any non-thermal parameter), which we call g, of two non-commuting operators, or interactions. Neither of them needs to favor a broken symmetry – thus a QPT will not necessarily imply the formation of long range order (LRO) of any kind. Indeed, as will be discussed in Ch. 3 and Ch. 4, deconfined quantum critical points and spin liquid phases represent exceptions to the Landau-Ginzburg-Wilson paradigm of classifying phase transitions in terms of order parameters [44]. Just like a thermal phase transition, a QPT is either of

1st-order associated with a level crossing of energies, the jump of an order parameter or a divergent first derivative of the energy with respect to some ratio of interactions, or

2nd-order (or continuous) where order parameters, the energy and its first derivative change continuously. Higher order derivatives of the energy exhibit divergencies. The special case of the Kosterlitz-Thouless transitions is, in fact, an infinite-order transition.

The quantum critical point g_c is distinguished by diverging correlations (or inverse gaps). A divergent correlation length in space ξ is inextricably linked to a divergent correlation in imaginary time $\xi_\tau^z \sim \xi$. The exponent z is the dynamical critical exponent, which relates space and imaginary time axes, such that the classical dimension d is replaced by $d + z$. However, note that the concept of *local quantum criticality*, e.g., in Kondo-systems, also allows for phase transition local in space, but which are non-local in imaginary time.

At the quantum critical point correlations obey power laws whose exponents are the critical exponents. The critical (scale-invariant) behavior allows to compare with experiments and to merge phase transitions with the same critical exponents into so-called universality classes. While at the quantum critical point a quantum model can be generally mapped onto a classical counterpart, we want to note that *not all* properties of a given quantum system can be obtained from its classical counterpart! Some theories for quantum systems involve long-ranged effective interactions arising from soft modes, real-time dynamics analysis (phase coherence time) or a strong space-time anisotropy, which in general cannot be reproduced by simple mapping. For an instructive review on the topic of QPT we refer the reader to [45].

For interactions with finite range, in general, correlation functions decay with exponentially decreasing amplitude, which reflects the finite correlation length equivalent to short-range order. In the case of long range order, the diverging correlation length indicates a broken symmetry. This can either be a discrete symmetry, e.g., from the point group of the underlying lattice, or a continuous symmetry of the constituent (or collective) degrees of freedom. According to Goldstone's theorem [46, 47, 39], spinless bosonic excitations with zero mass appear when a continuous symmetry is *spontaneously* broken. These Goldstone bosons emerge whenever a continuous symmetry group leaves the Hamiltonian but not the vacuum (ground-state) invariant. Goldstone modes may be seen as additional degree of freedom compensating for the broken symmetry and guaranteeing a theory with equal number of degrees of freedom in the unbroken as well as in the broken phase. Their zero mass reflects the formal definition of the spontaneous symmetry breaking (SSB) where any broken state in the same symmetry group can be obtained with vanishing energy effort. SSB is formally defined in the limit of an external field h of an order parameter

$$\lim_{h\to 0^+} \lim_{N\to\infty} m_{\text{order}} \neq 0 \,. \tag{1.81}$$

We want to emphasize that SSB is not defined for finite systems. Thus to conclude from a finite system to the existence of SSB in the thermodynamical limit by means of finite size extrapolations can be a tricky task. The number of Goldstone bosons is given by the number of broken generators of the system's symmetry group. In solid state theory these gapless excitations are associated with density waves. SSB and hence a diverging correlation function, or a susceptibility χ at some wave vector $\bar{\mathbf{q}}$ results in vanishing energy

$$\lim_{\mathbf{q}\to\bar{\mathbf{q}}} \chi(\bar{\mathbf{q}}) \to \infty \qquad \longrightarrow \qquad \lim_{\mathbf{q}\to\bar{\mathbf{q}}} E(\mathbf{q}) = 0 \,. \tag{1.82}$$

For sufficiently short ranged interactions and finite temperatures the Mermin-Wagner theorem forbids the spontaneous breaking of a continuous symmetry for dimensions $d < 3$ [48, 39]. For the $T = 0$ investigations discussed in this thesis with effective dimensionality $d = 2 + 1$ true LRO and spontaneously broken continuous symmetries are allowed.

One distinguishes between *true* LRO and *quasi* LRO. Where true LRO implies the bijective relation of SSB and long range correlations, quasi LRO does not include the spontaneous breaking of a continuous symmetry. The formal definition of LRO is given by

$$0 \neq m^2_{\text{order}} = \lim_{r\to\infty} \lim_{N\to\infty} \left\langle O(0)O(r)\right\rangle \,, \tag{1.83}$$

where the Os represent arbitrary operators separated in space (or imaginary time) by r.

An overview to rigorous theorems, symmetry breaking and finite size effects in quantum many-body systems (on the lattice) is given by Koma and Tasaki in [49].

Continuous-time QMC: Projective schemes and phonons

2

We extend the weak-coupling diagrammatic determinantal algorithm to projective schemes as well as to the inclusion of phonon degrees of freedom. The projective approach provides a very efficient algorithm to access zero temperature properties. To implement phonons, we integrate them out in favor of a retarded density-density interaction and simulate the resulting purely electronic action with the weak-coupling diagrammatic determinantal algorithm. Both extensions are tested within the dynamical mean field (DMFT) approximation for the Hubbard and Hubbard-Holstein models. This work has been published in [50].

2.1. Introduction

Diagrammatic determinantal quantum Monte Carlo (DDQMC), be it the weak-coupling expansion [51], or hybridization expansion [52] approach, is emerging as the method of choice for impurity solvers [53]. In comparison to the Hirsch-Fye approach [54] they are continuous time methods and thereby free of Trotter errors, more efficient, and more flexible. In this article we concentrate on the weak-coupling algorithm which has been thoroughly reviewed in [55]. After a short review of our implementation of the algorithm, we show how to generalize it to projective schemes as well as to the inclusion of phonon degrees of freedom.

Projective schemes have already been implemented in the framework of the Hirsch-Fye algorithm and used in the context of DMFT [56, 57, 58]. Very similar ideas for the formulation of a projective DDQMC algorithm may be used and are reviewed in Sec. 2.3. With the projective DDQMC, we can reproduce results of [56] at a fraction of the computational cost and access much lower projection parameters.

Phonon degrees of freedom have very recently been implemented in the hybridization formulation of the DDQMC [59]. Since the hybridization approach is based on the expansion in the hybridization, the inclusion of phonons relies on a Lang-Firsov transformation. In the weak coupling approach it is more convenient to integrate out the

phonons in favor of a retarded interaction. The purely electronic model may then be solved efficiently within the weak coupling DDQMC. In Sec. 2.4 we present some details of the algorithm and provide test simulations for the Hubbard-Holstein model in the DMFT approximation.

2.2. The diagrammatic determinantal method for Hubbard interactions

Here we will briefly review the diagrammatic determinantal method for the Hubbard model $H = H_0 + H_U$, with $H_0 = -\sum_{i,j,\sigma} t_{i,j} c^\dagger_{i,\sigma} c_{j,\sigma}$ (cf. Sec. 1.3). The local density $n_{i,\sigma} = c^\dagger_{i,\sigma} c_{i,\sigma}$ and $c^\dagger_{i,\sigma}$ ($c_{i,\sigma}$) creates (annihilates) a fermion in a Wannier state centered around site i (j) and with z-component of spin σ. As will become apparent in the subsequent sections, we write the Hubbard interaction as

$$H_U = \frac{U}{2} \sum_i \sum_{s=\pm 1} \left(n_{i,\uparrow} - 1/2 - s\delta\right) \left(n_{i,\downarrow} - 1/2 + s\delta\right) \ , \tag{2.1}$$

to avoid the negative sign problem at least for impurity and one-dimensional models. After carrying out the sum over the Ising spins, s, one recovers the original Hubbard interaction up to a constant. As will be seen below an adequate choice of δ to avoid the sign problem for a one-dimensional chain reads $\delta = \frac{1}{2} + 0^+$.

A weak coupling perturbation expansion yields for the partition function:

$$\begin{aligned} \frac{Z}{Z_0} \ &= \ \sum_{n=0}^{\infty} \left(\frac{-U}{2}\right)^n \int_0^\beta \mathrm{d}\tau_1 \sum_{i_1,s_1} \cdots \int_0^{\tau_{n-1}} \mathrm{d}\tau_n \\ &\qquad \times \sum_{i_n,s_n} \prod_\sigma \langle [n_{i_1,\sigma}(\tau_1) - \alpha_\sigma(s_1)] \cdots [n_{i_n,\sigma}(\tau_n) - \alpha_\sigma(s_n)] \rangle_0 \ . \end{aligned} \tag{2.2}$$

Here, we have defined $\alpha_\sigma(s) = 1/2 + \sigma s \delta$ and $\langle ... \rangle_0 = \mathrm{Tr}\left[e^{-\beta H_0} ...\right] / Z_0$ with $Z_0 = \mathrm{Tr}\left[e^{-\beta H_0}\right]$. Note that the Ising field s has obtained an additional time index. The thermal expectation value is the sum over all diagrams, connected and disconnected, of a given order n. Using Wick's theorem this sum can be expressed as a determinant where the entries are the Green's functions of the non-interacting system.

$$\langle T\left[n_{\sigma,i_1}(\tau_1)-\alpha_\sigma(s_1)\right]\cdots\left[n_{\sigma,i_n}(\tau_n)-\alpha_\sigma(s_n)\right]\rangle_0 =$$
$$\det\begin{pmatrix} G^0_{i_1,i_1}(\tau_1,\tau_1)-\alpha_\sigma(s_1) & G^0_{i_1,i_2}(\tau_1,\tau_2) & \cdots & G^0_{i_1,i_n}(\tau_1,\tau_n) \\ G^0_{i_2,i_1}(\tau_2,\tau_1) & G^0_{i_2,i_2}(\tau_2,\tau_2)-\alpha_\sigma(s_2) & \cdots & G^0_{i_2,i_n}(\tau_2,\tau_n) \\ \cdot & \cdot & \cdot & \cdot \\ \cdot & \cdot & \cdot & \cdot \\ \cdot & \cdot & \cdot & \cdot \\ G^0_{i_n,i_1}(\tau_n,\tau_1) & G^0_{i_n,i_2}(\tau_n,\tau_2) & \cdots & G^0_{i_n,i_n}(\tau_n,\tau_n)-\alpha_\sigma(s_n) \end{pmatrix} \tag{2.3}$$

with Green's functions

$$G^0_{i,j}(\tau_1,\tau_2) = \langle T c^\dagger_i(\tau_1) c_j(\tau_2)\rangle_0 \,, \tag{2.4}$$

which we have assumed to be spin independent. In the above, T corresponds to the time ordering. Defining a configuration, C_n, by the n Hubbard vertices, as well as the Ising spins introduced in Eq. (2.1) $C_n = \{[i_1,\tau_1,s_1]\cdots[i_n,\tau_n,s_n]\}$, and the *sum* over the configuration space by

$$\sum_{C_n} = \sum_{n=0}^{\infty}\int_0^\beta \mathrm{d}\tau_1 \sum_{i_1,s_1}\cdots\int_0^{\tau_{n-1}}\mathrm{d}\tau_n\sum_{i_n,s_n}\,, \tag{2.5}$$

the partition function can conveniently be written as

$$\frac{Z}{Z_0} = \sum_{C_n}\left(-\frac{U}{2}\right)^n \prod_\sigma \det M_\sigma(C_n)\,. \tag{2.6}$$

Here M_σ is the $n\times n$ matrix of Eq. (2.3). Observables, $O(\tau)$, can now be computed with

$$\langle O(\tau)\rangle = \frac{\sum_{C_n}\left(-\frac{U}{2}\right)^n \prod_\sigma \det M_\sigma(C_n)\langle\!\langle O(\tau)\rangle\!\rangle_{C_n}}{\sum_{C_n}\left(-\frac{U}{2}\right)^n \prod_\sigma \det M_\sigma(C_n)}\,, \tag{2.7}$$

where for $O(\tau)=\prod_\sigma O_\sigma(\tau)$ we have

$$\langle\!\langle O(\tau)\rangle\!\rangle_{C_n} = \frac{\prod_\sigma\langle T\left[n_{i_1,\sigma}(\tau_1)-\alpha_\sigma(s_1)\right]\cdots\left[n_{i_n,\sigma}(\tau_n)-\alpha_\sigma(s_n)\right]O_\sigma(\tau)\rangle_0}{\prod_\sigma\langle T\left[n_{i_1,\sigma}(\tau_1)-\alpha_\sigma(s_1)\right]\cdots\left[n_{i_n,\sigma}(\tau_n)-\alpha_\sigma(s_n)\right]\rangle_0}\,. \tag{2.8}$$

For any given configuration of vertices C_n, Wick's theorem holds. Hence, any observable can be computed from the knowledge of the single particle Green's function

$$\langle\!\langle T c^\dagger_{i,\sigma}(\tau) c_{j,\sigma}(\tau_1)\rangle\!\rangle_{C_n} = G^0_{i,j}(\tau,\tau_1) - \sum_{r,s=1}^{n} G^0_{i,i_r}(\tau,\tau_{i_r})\left(M^{-1}_\sigma\right)_{r,s} G^0_{i_s,j}(\tau_s,\tau_1)\,. \tag{2.9}$$

Here, we have assumed that the non-interacting Green's functions are spin independent. As a consequence of the above equation, it becomes apparent that one can measure directly the Matsubara Green's functions. This aspect facilitates the implementation of the algorithm within the framework of dynamical mean-field theories.

2.2.1. Sign problem

In auxiliary field determinantal methods [10] it is known that the presence of particle-hole symmetry can be used to avoid the negative sign problem. An identical statement holds for the diagrammatic determinantal method. We assume that H_0 is invariant under the particle-hole transformation

$$c^\dagger_{i,\sigma} \to (-1)^i c_{i,\sigma} \; . \tag{2.10}$$

As a consequence,

$$\langle T \prod_{r=1} n\left[n_{i_r,\sigma}(\tau_r) - \alpha_\sigma(s_r)\right]\rangle_0 = (-1)^n \langle T \prod_{r=1} n\left[n_{i_r,\sigma}(\tau_r) - \alpha_{-\sigma}(s_r)\right]\rangle_0 \; , \tag{2.11}$$

such that $\det M_\uparrow = (-1)^n \det M_\downarrow$. A glimpse at Eq. (2.6) will confirm the absence of sign problem for this special case. The above result is independent on the choice of δ introduced in Eq. (2.1). As we will see in Sec. 2.2.3 the algorithm is optimal at $\delta = 0$. In this special case, $\det M_\uparrow = \det M_\downarrow = (-1)^n \det M_\downarrow$ such that only even values of n occur in the sampling. We note that this vanishing of the weight for odd values of n can be avoided by choosing a small value of δ.

In one dimension and in the absence of frustrating interactions, there is no negative sign problem. To be more precise, configurations with negative weights do occur. However, those configurations stem from the real space winding of the fermions and can be eliminated if open boundary conditions are adopted, or a different representation of your degrees of freedom are chosen. The diagrammatic approach also satisfies this property, provided that we choose $\delta = 1/2 + 0^+$. The quantity $\prod_\sigma \det M_\sigma(C_n)$ in Eq. (2.6) is nothing but

$$\mathrm{Tr}\left[e^{-\beta H_0} \prod_\sigma \left[n_{i_1,\sigma}(\tau_1) - \alpha_\sigma(s_1)\right] \left[n_{i_n,\sigma}(\tau_n) - \alpha_\sigma(s_n)\right]\right] \Big/ \mathrm{Tr}\left[e^{-\beta H_0}\right] \; , \tag{2.12}$$

which we can compute within the real-space world-line approach [60, 61]. Here, each world line configuration has a positive weight. Let us consider an arbitrary world-line configuration, and a site (i, τ) in the space-time lattice. Irrespective if this site is empty, singly or doubly occupied the expectation value of the operator $\prod_\sigma \left[n_{i,\sigma}(\tau) - \alpha_\sigma(s)\right]$ will take a negative value. Recall that we have set $\delta = 1/2 + 0^+$. Hence, for each world line configuration the expectation value of the operator $\prod_\sigma \left[(n_{i,\sigma}(\tau) - \alpha_\sigma(s_1)) \cdots (n_{i_n,\sigma}(\tau_n) - \alpha_\sigma(s_n))\right]$ has a sign equal to $(-1)^n$. Summation over all world line configurations yields the expression in Eq. (2.12) which in turn has a sign $(-1)^n$. This cancels the sign of the factor $(-U/2)^n$ in Eq. (2.6), thus yielding an overall positive weight.

In the rewriting of the Hubbard term (see Eq. (2.1)) we have introduced a new dynamical Ising field so as to avoid the negative sign problem at least for the one-dimensional

Hubbard model. Alternatively, one can choose a static Ising field and compensate for it by a redefinition of H_0. Such a static procedure is introduced in [51]. For the class of models considered, we have not noticed substantial differences in performance between static and dynamical choices of Ising fields. We however favor the dynamical version since it allows one to keep the SU(2) spin invariant form of the non-interacting Hamiltonian H_0.

2.2.2. Monte Carlo sampling

In principle two moves, the addition and removal of Hubbard vertices, are sufficient. Note, those move are clearly not sufficient for the particle-hole symmetric case and $\delta = 0$. In this case and as argued in Sec. 2.2.1, the weights vanish for odd values of n, and hence, the algorithm would not be ergodic. One can circumvent this problem by (i) introducing moves which add or remove pairs of vertices or (ii) using a small value of δ. For the simulations presented here we have opted for solution (ii) and chosen in general $\delta = 0.1$ at the expense of a small performance loss. In the Metropolis scheme, the acceptance ratio for a given move reads

$$P_{C\to C'} = \min\left(\frac{T^0_{C'\to C} W(C')}{T^0_{C\to C'} W(C)}, 1\right) . \tag{2.13}$$

where $T^0_{C'\to C}$ corresponds to the probability of proposing a move from configuration C' to configuration C and $W(C)$ corresponds to the weight of the configuration. To add a vertex $T^0_{C_n\to C_{n+1}} = \frac{1}{2N\beta}$ which corresponds to the fact that one has to pick at random an imaginary time in the range $[0,\beta]$, a site i in the range $1\dots N$ (with N the number of sites) as well as an Ising spin. The proposal probability to remove a vertex $T^0_{C_{n+1}\to C_n} = \frac{1}{n+1}$ corresponds to the fact that one will choose at random one of the $n+1$ vertices present in configuration C_{n+1}, hence

$$\begin{aligned} P_{C_n\to C_{n+1}} &= \min\left(-\frac{U\beta N}{(n+1)}\frac{\prod_\sigma \det M_\sigma(C_{n+1})}{\prod_\sigma \det M_\sigma(C_n)}, 1\right) , \\ P_{C_{n+1}\to C_n} &= \min\left(-\frac{(n+1)}{U\beta N}\frac{\prod_\sigma \det M_\sigma(C_n)}{\prod_\sigma \det M_\sigma(C_{n+1})}, 1\right) . \end{aligned} \tag{2.14}$$

Apart from the above addition and removal of vertices, we have implemented moves which flip the Ising spins at constant order n as well as updates which move Hubbard vertices both in space and time.

2.2.3. Tests

The efficiency of the approach relies on the autocorrelation time, which has to be analyzed on a case to case basis, as well as on the average expansion order parameter. For

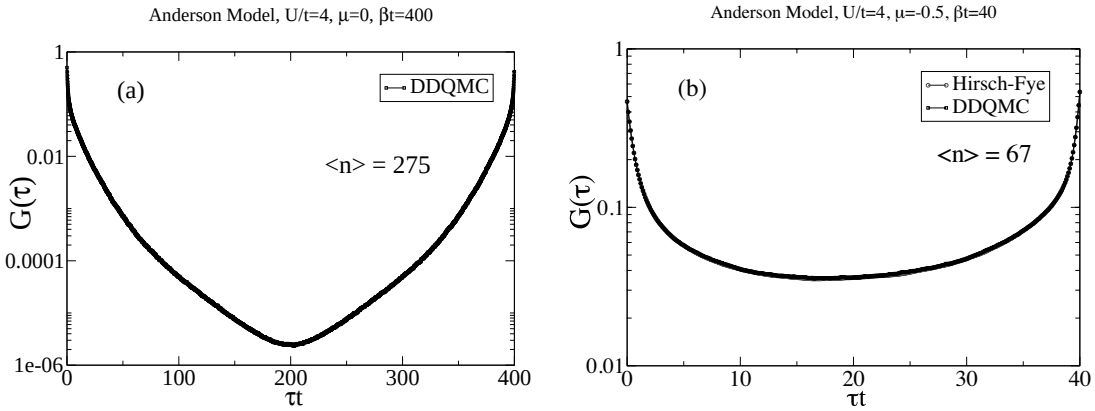

Fig. 2.1.: (Color online) Green's function $G(\tau)$ for the Anderson model of Eq. (2.17). (a) Particle-hole symmetric point, $\mu = 0$. To avoid the vanishing of the weight at odd values of n we have used $\delta = 0.1$ for this simulation. (b) Away from particle-hole symmetry $\mu = -0.5$. For this higher temperature we provide a comparison with the Hirsch-Fye algorithm with Trotter step $\Delta\tau t = 0.1$. Note that in both cases we have used a 32×32 square lattice to generate the non-interacting Green's function $G^0(\tau)$. $\langle n \rangle$ corresponds to the average order expansion parameter.

a general interaction term H_1 the average expansion parameter is given by

$$\begin{aligned}
\langle n \rangle &= \frac{1}{Z} \sum_n \frac{(-1)^n n}{n!} \int_0^\beta \mathrm{d}\tau_1 \cdots \int_0^\beta \mathrm{d}\tau_n \langle T H_1(\tau_1) \cdots H_1(\tau_n) \rangle_0 \\
&= \frac{-1}{Z} \sum_m \frac{(-1)^m}{m!} \int_0^\beta \mathrm{d}\tau_1 \cdots \int_0^\beta \mathrm{d}\tau_m \int_0^\beta \mathrm{d}\tau \langle T H_1(\tau_1) \cdots H_1(\tau_m) H_1(\tau) \rangle_0 \\
&= -\int_0^\beta \mathrm{d}\tau \langle H_1(\tau) \rangle \; . \qquad (2.15)
\end{aligned}$$

For the Hubbard model and replacing H_1 by the form of Eq. (2.1) we obtain

$$\langle n \rangle = -\beta U \sum_i \left[\langle (n_{i,\uparrow} - 1/2)(n_{i,\downarrow} - 1/2) \rangle - \delta^2 \right] \; . \qquad (2.16)$$

Using the same techniques as in auxiliary field QMC methods [10] the CPU costs for the calculation of the acceptance probability and the update for the addition or removal of a vertex scales as n^2. As apparent from Eq. (2.16) a sweep consisting of updating all n vertices results in an effort of n^3. Even though in this method M_σ^{-1} is far better conditioned than in the *classic* determinantal methods [54, 8, 10], it has to be recalculated from scratch after several updates which involves an effort of the order n^3. For the impurity problems presented here, M_σ^{-1} remains very stable, such that recalculation from scratch of M_σ^{-1} is not an issue. In contrast when applying the method to a lattice problem, we find that round-off errors accumulate and a more frequent recalculation of

M_σ^{-1} is required. Hence, because of these two limiting factors the CPU time scales as $(\beta U N)^3$ which is precisely the same scaling as in the Hirsch-Fye approach. Apart from the absence of Trotter errors the advantage of the method lies in a large pre-factor. In the very special case of a single impurity, $N = 1$, and for a particle-hole symmetric Hamiltonian H_0, the speedup is dramatic. Particle-hole symmetry allows one to set $\delta = 0$ such that $\langle n \rangle < \beta U/4$. To obtain this upper bound we have set the double occupancy to zero. Hence a simulation at $U/t = 4$ and $\beta t = 400$ has a maximal average order parameter $\langle n \rangle = 400$. In a Hirsch-Fye approach, one could opt for a Trotter step $\Delta\tau t = 1/8$ and hence 3200 Trotter slices which determines the size of the matrices involved in the simulations. Hence an underestimate of the speedup reads $(3200/400)^3 = 512$. Away from particle-hole symmetry, the speedup is less impressive since we have to set $\delta = 1/2 + 0^+$ to avoid the negative sign problem. We have confirmed the above statements for the Anderson impurity model,

$$H = \sum_{k,\sigma} (\epsilon(k) - \mu) c^\dagger_{k,\sigma} c_{k,\sigma} + \frac{V}{\sqrt{N}} \sum_{k,\sigma} \left(c^\dagger_{k,\sigma} d_\sigma + h.c. \right) + U \left(d^\dagger_\uparrow d_\uparrow - 1/2 \right) \left(d^\dagger_\downarrow d_\downarrow - 1/2 \right),$$

with Hubbard interaction U and hybridization V. Here $c^\dagger_{k,\sigma}$ ($c_{k,\sigma}$) creates (annihilates) a fermion in the conduction band at momentum k with spin σ and the dispersion relation $\epsilon(k) = -2t(\cos(k_x) + \cos(k_y))$. The operators $d^\dagger_\sigma$ (d_σ) create (annihilate) an impurity electron, respectively. Our results, including a comparison with the Hirsch-Fye algorithm, are presented in Fig. 2.1.

Finally let us note that applying the method to a one-dimensional Hubbard model of length N, yields a very poor performance in comparison to standard finite temperature BSS auxiliary field algorithms [8] since those methods scale as $\beta U N^3$ [10].

2.3. Generalization to projective approaches

Projective approaches rely on the filtering out of the ground state, $|\Psi_0\rangle$ from a trial wave function $|\Psi_T\rangle$, which is required to be non-orthogonal to $|\Psi_0\rangle$

$$\frac{\langle \Psi_0 | O | \Psi_0 \rangle}{\langle \Psi_0 | \Psi_0 \rangle} = \lim_{\Theta \to \infty} \frac{\langle \Psi_T | e^{-\frac{\Theta}{2} H} O e^{-\frac{\Theta}{2} H} | \Psi_T \rangle}{\langle \Psi_T | e^{-\Theta H} | \Psi_T \rangle} \,. \tag{2.17}$$

For convenience and simplicity, we will assume that $|\Psi_T\rangle$ is the ground state of H_0, such that for a given value of Θ the right hand side of the above equation can be written as

$$\frac{\langle \Psi_T | e^{-\frac{\Theta}{2} H} O e^{-\frac{\Theta}{2} H} | \Psi_T \rangle}{\langle \Psi_T | e^{-\Theta H} | \Psi_T \rangle} = \lim_{\beta_0 \to \infty} \frac{\mathrm{Tr}\, e^{-\beta_0 H_0} e^{-\frac{\Theta}{2} H} O e^{-\frac{\Theta}{2} H}}{\mathrm{Tr}\, e^{-\beta_0 H_0} e^{-\Theta H}} \,. \tag{2.18}$$

With the definition $Z_p = \mathrm{Tr}\left[e^{-\beta_0 H_0} e^{-\Theta H}\right]$ and $Z_{p,0} = \mathrm{Tr}\left[e^{-(\beta_0+\Theta)H_0}\right]$ a weak coupling expansion yields

$$\begin{aligned}\frac{Z_p}{Z_{p,0}} &= \sum_{n=0}^{\infty}\left(\frac{-U}{2}\right)^n \int_0^{\Theta} \mathrm{d}\tau_1 \sum_{i_1,s_1} \cdots \int_0^{\tau_{n-1}} \mathrm{d}\tau_n \\ &\quad \times \sum_{i_n,s_n}\prod_{\sigma} \langle [n_{i_1,\sigma}(\tau_1) - \alpha_\sigma(s_1)] \cdots [n_{i_n,\sigma}(\tau_n) - \alpha_\sigma(s_n)]\rangle_{p,0} \ , \quad (2.19)\end{aligned}$$

where $\langle ... \rangle_{p,0} = \mathrm{Tr}\left[e^{-(\beta_0+\Theta)H_0} ...\right]/Z_{p,0}$. The similarity to the finite temperature algorithm is now apparent. We use Wick's theorem to express the expectation value on the right hand side of Eq. (2.19) in terms of the product of two determinants. Taking the limit $\beta_0 \to \infty$ we obtain

$$\langle \Psi_T | e^{-\Theta H} | \Psi_T \rangle \equiv \lim_{\beta_0 \to \infty} \frac{Z_p}{Z_{p,0}} = \sum_{C_n} \left(-\frac{U}{2}\right)^n \prod_{\sigma} \det M_{\sigma,p}(C_n) \ . \quad (2.20)$$

Here, the sum runs over all configurations C_n and Eq. (2.5). Note that β in Eq. (2.5) has to be replaced by Θ. The matrices $M_{\sigma,p}$ have precisely the same form as the matrices M_σ, but since we have taken the limit $\beta_0 \to \infty$, the thermal non-interacting Green's functions have to be replaced by the zero temperature ones:

$$G^0_{p,i,j}(\tau_1,\tau_2) = \langle \Psi_T | T c_i^\dagger(\tau_1) c_j(\tau_2) | \Psi_T \rangle \ . \quad (2.21)$$

Hence, as in the Hirsch-Fye approach, the step from a finite temperature to zero-temperature code is very easy and essentially amounts in replacing the finite temperature non-interacting Green's functions by the zero temperature ones. However, there is an important difference concerning measurements: measurements of observables which do not commute with the Hamiltonian have to be carried out in the middle of the imaginary time interval $[0,\Theta]$ to avoid boundary effects [10]. We have tested this approach by reproducing Fig. 1 of the article [56] where the projective Hirsch-Fye algorithm was incorporated in the DMFT self-consistency cycle. Fig. 2.2 shows the results for the half-filled Hubbard model at $U/t = 4.8$, density of states $N(\omega) = \frac{8}{\pi W^2}\sqrt{W^2/4 - \omega^2}$ and band-width $W = 4t$. Excellent agreement with the former Hirsch-Fye based results [56] both at finite temperatures and in the limit $\Theta \to \infty$ were obtained. However, the diagrammatic approach allows to access much larger projection parameters and/or lower temperatures. We refer the reader to Ref. [56] for the implementation of the projective formalism in the self-consistency cycle.

2.4. Application to the Hubbard-Holstein Model

Weak coupling DDQMC allows a very simple inclusion of phonon degrees of freedom. The path we follow here is to integrate out the phonons in favor of a retarded interaction,

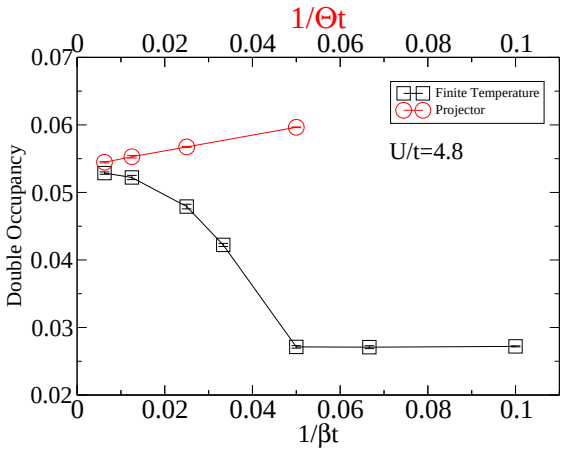

Fig. 2.2.: (Color online) DMFT calculation of the double occupancy for the half-filled Hubbard model as a function of i) temperature $1/\beta$ and ii) projection parameter $1/\Theta$. In the projective approach, observables are computed in the imaginary time range $[\Theta/4, 3\Theta/4]$. This rather large measurement interval explains the slight discrepancy with the data of Ref. [56] for the projective code and at finite values of Θ. However, extrapolation to $\Theta \to \infty$ where the measurement range becomes irrelevant yields results consistent with Ref. [56].

and then solve the purely electronic model with the DDQMC approach. Starting from the Hubbard-Holstein model with Einstein phonons we show how to integrate out the phonons, describe some details of the algorithm and then present results within the DMFT approximation.

2.4.1. Integrating out the phonons

The Hubbard-Holstein Hamiltonian we consider reads

$$\begin{aligned} H &= -\sum_{i,j,\sigma} t_{i,j} c^{\dagger}_{i,\sigma} c_{j,\sigma} + U \sum_{i} \left(n_{i,\uparrow} - 1/2\right)\left(n_{i,\downarrow} - 1/2\right) \\ &\quad + g \sum_{i} Q_i \left(n_i - 1\right) + \sum_{i} \frac{P_i^2}{2M} + \frac{k}{2} Q_i^2 \, . \end{aligned} \tag{2.22}$$

Here, $n_i = \sum_{\sigma} n_{i,\sigma}$ and the last two terms correspond respectively to the electron-phonon coupling, g, and the phonon-energy. The Hamiltonian is written such that for a particle-hole symmetric band, half-filling corresponds to chemical potential $\mu = 0$. Opting for fermion coherent states

$$c_{i,\sigma}|c\rangle = c_{i,\sigma}|c\rangle \, , \tag{2.23}$$

$c_{i,\sigma}$ being a Grassmann variable, and a real space representation for the phonon coordinates

$$Q_i|q\rangle = q_i|q\rangle \, , \tag{2.24}$$

the path integral formulation of the partition function reads

$$Z = \int [\mathrm{d}q] \left[dc^\dagger dc \right] e^{-(S_U + S_{\mathrm{ep}})} , \tag{2.25}$$

with

$$\begin{aligned} S_U &= \int_0^\beta \mathrm{d}\tau \sum_{i,j,\sigma} c^\dagger_{i,\sigma}(\tau) \left(\delta_{i,j} \frac{\partial}{\partial \tau} - t_{i,j} \right) c_{j,\sigma}(\tau) \\ &\quad + U \sum_i (n_{i,\uparrow}(\tau) - 1/2)(n_{i,\downarrow}(\tau) - 1/2) , \end{aligned} \tag{2.26}$$

$$S_{\mathrm{ep}} = \int_0^\beta \mathrm{d}\tau \sum_i \frac{M \dot{q_i}^2(\tau)}{2} + \frac{k}{2} q_i^2(\tau) + g\, q_i(\tau)(n_i(\tau) - 1) . \tag{2.27}$$

In Fourier space,

$$q_j(\tau) = \frac{1}{\sqrt{\beta N}} \sum_{k,\Omega_m} e^{-i(\Omega_m \tau - kj)} q_{k,m} , \tag{2.28}$$

where Ω_m is a bosonic Matsubara frequency, the electron phonon part of the action reads

$$S_{\mathrm{ep}} = \sum_{\Omega_m, k} \frac{M}{2} \left(\Omega_m^2 + \omega_0^2 \right) q^\dagger_{k,m} q_{k,m} + g q_{k,m} \rho^\dagger_{k,m} , \tag{2.29}$$

$$\rho^\dagger_{k,m} = \frac{1}{\sqrt{\beta N}} \int \mathrm{d}\tau \sum_j e^{-i(\Omega_m \tau - kj)} (n_j(\tau) - 1) . \tag{2.30}$$

Gaussian integration over the phonon degrees of freedom leads to a retarded density-density interaction

$$\int [\mathrm{d}q]\, e^{-S_{\mathrm{ep}}} = e^{\int_0^\beta \mathrm{d}\tau \int_0^\beta \mathrm{d}\tau' \sum_{i,j} [n_i(\tau) - 1] D^0(i-j, \tau - \tau') [n_j(\tau') - 1]} . \tag{2.31}$$

For Einstein phonons the phonon propagator is diagonal in real space,

$$\begin{aligned} &D^0(i-j, \tau - \tau') = \delta_{i,j} \frac{g^2}{2k} P(\tau - \tau') \ \text{ with} \\ &P(\tau) = \frac{\omega_0}{2\left(1 - e^{-\beta\omega_0}\right)} \left(e^{-|\tau|\omega_0} + e^{-(\beta - |\tau|)\omega_0} \right) . \end{aligned} \tag{2.32}$$

Hence the partition function of the Hubbard-Holstein model takes the form.

$$Z = \int dc^\dagger dc e^{-(S_U - \int_0^\beta \mathrm{d}\tau \int_0^\beta \mathrm{d}\tau' \sum_{i,j} [n_i(\tau) - 1] D^0(i-j, \tau - \tau') [n_j(\tau') - 1])} . \tag{2.33}$$

In the anti-adiabatic limit, $\lim_{\omega_0 \to \infty} P(\tau) = \delta(\tau)$ such that the phonon interaction maps onto an attractive Hubbard interaction of magnitude g^2/k. We are now in a position to apply the DDQMC algorithm by expanding in both the retarded and Hubbard interactions.

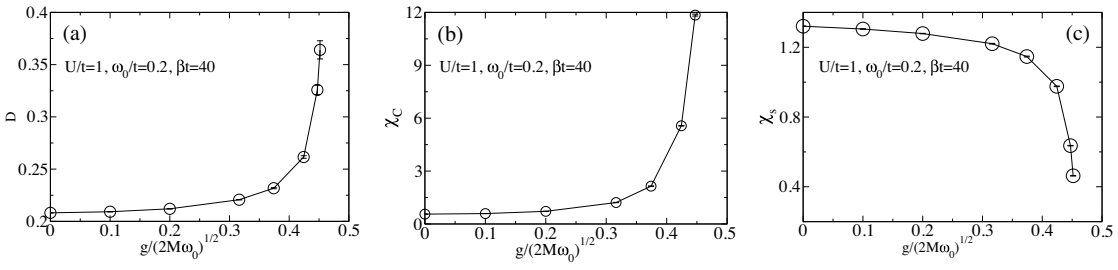

Fig. 2.3.: (a) Double occupancy, (b) local charge susceptibility and (c) local spin susceptibility for the Hubbard-Holstein model in the DMFT approximation.

.

2.4.2. Formulation of DDQMC for the Hubbard-Holstein model

To avoid the minus-sign problem at least for the one-dimensional chains we rewrite the phonon retarded interaction as:

$$H_P(\tau) = -\frac{g^2}{4k}\int_0^\beta \mathrm{d}\tau' \sum_{i,\sigma,\sigma'}\sum_{s=\pm 1} P(\tau-\tau')\left[n_{i,\sigma}(\tau)-\alpha_+(s)\right]\left[n_{i,\sigma'}(\tau')-\alpha_+(s)\right] \ . \quad (2.34)$$

For each phonon vertex, we have introduced an Ising variable: s. Summation over this Ising field reproduces, up to a constant, the original interaction. Since the phonon term is attractive the adequate choice of signs is $\alpha_+(s) \equiv 1/2 + s\delta$, irrespective of the spin σ and σ'. A similar argument as presented in Sec. 2.2.1 then guarantees the absence of a sign problem for chains. Following Eq. (2.1) we rewrite the Hubbard term as

$$H_U(\tau) = \frac{U}{2}\sum_{i,s}\prod_{\sigma}(n_{i,\sigma}(\tau)-\alpha_\sigma(s)) \ . \quad (2.35)$$

To proceed with a description of the implementation of the algorithm it is useful to define a general vertex

$$V(\tau) = \left\{i,\tau,\sigma,\tau',\sigma',s,b\right\} \ , \quad (2.36)$$

where b defines the type of vertex at hand, Hubbard ($b=0$) or phonon ($b=1$). For this vertex we define a sum over the available phase phase

$$\sum_{V(\tau)} = \sum_{i,\sigma,\sigma',s,b}\int_0^\beta \mathrm{d}\tau' \ , \quad (2.37)$$

a *weight*

$$w\left[V(\tau)\right] = \delta_{b,0}\frac{U}{2} - \delta_{b,1}P(\tau-\tau')\frac{g^2}{4k} \ , \quad (2.38)$$

as well as

$$\begin{aligned} H\left[V(\tau)\right] &= \delta_{b,0}\delta_{\sigma,\uparrow}\delta_{\sigma',\downarrow}\delta(\tau-\tau')\left[n_{i,\uparrow}(\tau)-\alpha_+(s)\right]\left[n_{i,\downarrow}(\tau)-\alpha_-(s)\right] \\ &\quad +\delta_{b,1}\left[n_{i,\sigma}(\tau)-\alpha_+(s)\right]\left[n_{i,\sigma'}(\tau')-\alpha_+(s)\right] . \end{aligned} \tag{2.39}$$

With the above definitions, the partition function can now be written as

$$\begin{aligned} \frac{Z}{Z_0} = \sum_{n=0}^{\infty}(-1)^n \int_0^\beta \mathrm{d}\tau_1 \sum_{V_1(\tau_1)} w[V_1(\tau_1)] \cdots \int_0^{\tau_{n-1}} \mathrm{d}\tau_n \\ \times \sum_{V_n(\tau_n)} w\left[V_n(\tau_n)\right] \langle T H\left[V_1(\tau_1)\right] \cdots H\left[V_n(\tau_n)\right]\rangle_0 . \end{aligned} \tag{2.40}$$

As for the Hubbard model, a configuration consists of a set vertices $C_n = \{V_1(\tau_1), \ldots, V_n(\tau_n)\}$. For a given configuration the thermal expectation value maps onto the product of two determinants in the spin up and spin down sectors. The Monte Carlo sampling follows precisely the scheme presented in Sec. 2.2.2, namely the addition and removal of vertices.

2.4.3. Application to the Hubbard-Holstein model using DMFT

We have applied the above algorithm to the Hubbard-Holstein model within the DMFT approximation. We use a semicircular density of states, $N(\omega) = \frac{8}{\pi W^2}\sqrt{W^2/4-\omega^2}$ with band-width $W = 4t$. Throughout this section, we set $U/t = 1$, $\omega_0 = 0.2t$, $\mu = 0$, and use the finite temperature implementation of the algorithm at $\beta t = 40$. The choice $\mu = 0$ corresponds to half-filling. Fig. 2.3a plots the double occupancy, $D = \langle n_{i,\uparrow} n_{i,\downarrow}\rangle$ as a function of the electron-phonon coupling. To compare at best with the results of Ref. [62] we write the phonon coordinates in terms of bosonic operators, $Q = \frac{1}{\sqrt{2M\omega_0}}\left(a + a^\dagger\right)$, and plot our results as a function of

$$\tilde{g} = g/\sqrt{2M\omega_0} . \tag{2.41}$$

Comparison of the results of Fig. 2.3a with those of Ref. [62], show excellent agreement and a critical electron-phonon coupling for the transition to the bipolaronic insulator at $\tilde{g}_c \simeq 0.45t$.

We have equally computed the local spin and charge susceptibilities:

$$\chi_{\substack{C\\S}} = \int_0^\beta \mathrm{d}\tau \left\langle \left[n_{i,\uparrow}(\tau) \pm n_{i,\downarrow}(\tau)\right]\left[n_{i,\uparrow} \pm n_{i,\downarrow}\right]\right\rangle . \tag{2.42}$$

As can be seen in Fig. 2.3b in the vicinity of the transition local charge fluctuations grow substantially and local spin fluctuations (see Fig. 2.3c) are suppressed. The suppression

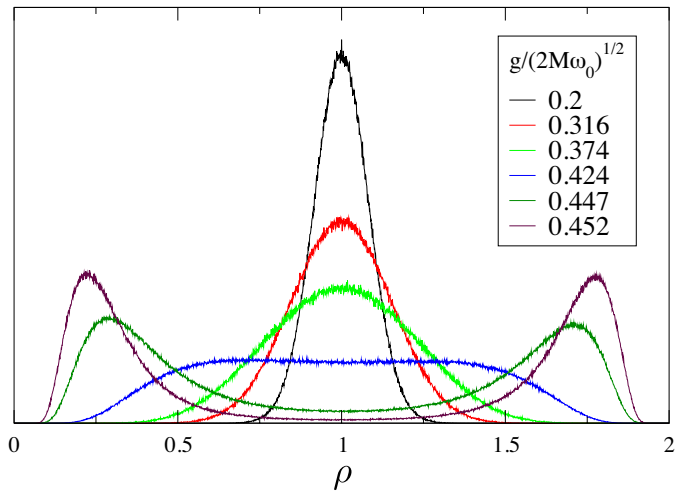

Fig. 2.4.: (Color online) The normalized histogram of the local density ρ of the Hubbard-Holstein model at half-filling with $U/t = 1$, $\omega_0 = 0.2t$ and $\beta t = 40$, for several values of the electron-phonon coupling g.

of χ_S signals singlet pairing of polarons. The chemical potential $\mu = 0$ sets the average particle number $\rho = 1$ but the particle number itself oscillates strongly between an empty or doubly occupied site. This can be seen by taking histograms as shown in Fig. 2.4. In the vicinity of the transition a two peak structure corresponding to a doubly occupied or empty site emerges. Close to the transition it becomes increasingly hard to guarantee a symmetric histogram – corresponding to the particle-hole symmetry of the model – and the simulation ultimately freezes in the doubly occupied or empty state.

2.5. Conclusions

We have presented two extensions of the diagrammatic determinantal method: projective schemes as well as the inclusion of phonons. In both cases we have tested successfully the approach for the Hubbard as well as for the Hubbard-Holstein models in the DMFT approximation. The inclusion of phonons is not limited to Einstein modes and in principle any dispersion relation can be easily implemented. One of the strong points of the weak-coupling DDQMC can be extended very easily to larger clusters and used as a solver for cluster extensions of dynamical mean-field theories [63]. The crucial issue here is the severity of the sign problem as the cluster size increases. This is an issue which would need to be answered on a case to case basis.

Since the publication of the study presented in this chapter, continuous-time QMC (CTQMC) methods have become *the* standard for impurity solvers. CTQMC in the weak-coupling approach and in the hybridization expansion [52] have been joined by CT-AUX, a CTQMC method for quantum impurity models, which combines the weak-

coupling expansion with an auxiliary-field decomposition [64]. CT-AUX has been shown to be equivalent to the weak-coupling CTQMC for Hubbard-type interactions and the relation between these CTQMC methods and the Hirsch-Fye QMC method has been established, identifying the latter as an approximation within CTQMC [65].

Also in cluster simulations CTQMC has been proven to be a powerful tool. Assaad used the advances of the weak-coupling DDQMC described in this chapter to investigate the spin, charge, and single-particle spectral functions of the one-dimensional quarter filled Holstein model [66]. Additionally, the extension of the weak-coupling CTQMC to the perturbation theory in imaginary and real time allows to study the time dependent evolution of a thermal initial state [67, 68], e.g., in the context of quantum quenches [69].

Valence bond solid on honeycomb layers

3

In this chapter we investigate the scenario of the breakdown of a valence bond solid (VBS) in an $S = 1/2$ quantum antiferromagnet with non-frustrating four-spin interaction on the single and bilayer hexagonal lattice. We introduce basic facts about the valence bond basis and the valence bond projector quantum Monte Carlo and highlight some of their unique features. Employing this $T = 0$ quantum Monte Carlo method we find a first-order VBS-Néel phase transition in the single layer system. In the bilayer the Néel regime separates the VBS and a disordered (zero tilted) phase by a continuous quantum phase transition. A quantum critical point marking a direct VBS-VBS or VBS-disorder transition is absent. This behavior is attributed to the Z_3 ground state degeneracy imposed by the lattice and allows rigid valence bond configurations to survive while spin fluctuations are enhanced.

3.1. The valence bond basis

The valence bond (VB) basis consists of states in which the spins are paired up into singlets

$$|V\rangle = |[i_1, j_1][i_2, j_2] \cdots [i_{N/2}, j_{N/2}]\rangle \ . \tag{3.1}$$

Here $[i, j]$ denotes a singlet formed by the spins at sites i and j

$$[i, j] = \frac{1}{\sqrt{2}}(|\uparrow_i\downarrow_j\rangle - |\downarrow_i\uparrow_j\rangle) \ , \tag{3.2}$$

and the total number of sites N is assumed to be even. While in principle one can include all possible pairings of the spins, it is convenient to only consider a smaller basis in which the sites are first divided into two groups, A and B, of $N/2$ spins each, and to take the subset of singlets $[i, j]$ which connect elements of A with B [70, 71, 72] (see Fig. 3.1). This is naturally fulfilled in bipartite lattices, yet the VB basis can also be applied to non-bipartite lattices. This restricted VB basis has $(N/2)!$ states, which is still massively overcomplete: the singlet space has $N!/[(N/2)!^2(N/2 + 1)]$ dimensions [70].

N	Singlets	AB tilings
1	1	1
2	2	2
3	5	6
4	13	24
5	42	120
6	132	720

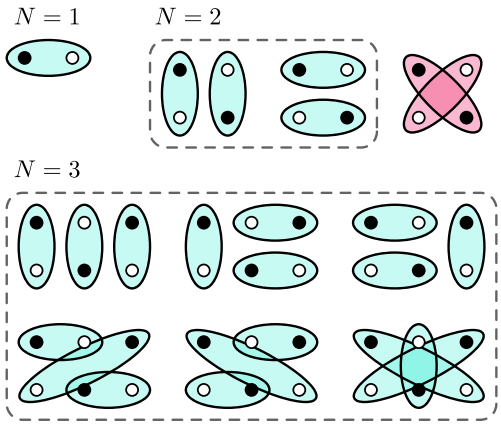

Fig. 3.1.: Dimensionality of the singlet space and the massively overcomplete VB basis restricted to AB tilings. The right hand side shows all possible arrangements for $N = 3$ singlets. AB tilings are colored light-blue, non-AB-tilings in pink.

The VB basis states are all non-orthogonal – in two dimensions two VB states $|P\rangle$, $|Q\rangle$ overlap such that they form loops. The overlap is given by $\langle P|V\rangle = 2^{N_\ell - N/2}$, where N_ℓ is the number of loops formed. The number of loops and their length can be associated with observables like the magnetizations, correlations and entanglement measures.

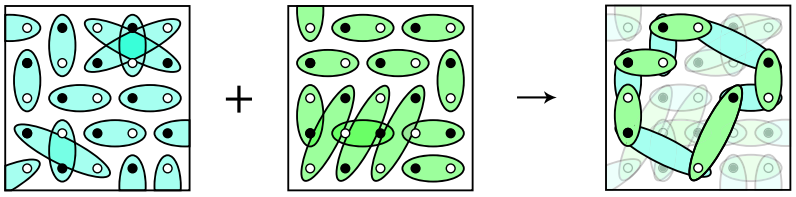

$|P\rangle$ $\quad$ $|Q\rangle$ $\quad$ $\langle Q|P\rangle = 2^{N_\ell - N/2} \neq \delta_{P,Q}$

The VB basis was introduced already in the early 1930s [70, 73, 74] and has played an important role in exactly solvable models [70, 75, 76, 77]. Later, it became a tool for describing spin liquids (cf. Sec. 4.1) – the resonating valence bond (RVB) mechanism introduced by Fazekas and Anderson [78, 79], in which the ground state is dominated by short valence bonds. In exact diagonalization studies the VB basis is useful in cases where the restriction to short bonds (as can be found in, e.g., spin liquids) is justified. Variational calculations in the VB basis have been carried out for the 2D Heisenberg model [72]. Furthermore, Liang realized that a variational VB state could be considerably improved by stochastically projecting it with an operator $(-H)^m$ for large m [80, 81]. Later, Santoro et al. devised a Green's function method for calculating energies in the VB basis [82]. Some formal results for the VB basis, have been discussed recently in the references [83, 84].

3.2. Valence bond projector QMC

Quantum Monte Carlo (QMC) simulations of spin systems have traditionally been carried out in the basis of eigenstates of the spin-z operators S^z. In the case of $S = 1/2$ considered here, this basis is build by up and down-spins. For the prototypical model of interacting quantum spins, the antiferromagnetic ($J > 0$) Heisenberg Hamiltonian given in Eq. (3.3), this basis is clearly natural and convenient. Off-diagonal operators acting on a basis state just flip two spins or destroy the state. There exists a variety of efficient finite temperature simulation methods realized as discretized [85, 86, 30], continuous imaginary-time [87, 88] path integrals and stochastic series expansion [89, 90]. Although these methods can be generalized and adapted to work in other bases, e.g., that of singlet states of spin pairs, the implementation of this basis in QMC simulations is rather cumbersome. Except to overcome fundamental problems like the infamous sign problem the necessary effort for development and computation is not economical. Ground state investigations are usually done via finite-temperature simulations extrapolated to the low temperature limit, or zero-temperature simulations usually based on the repeated application of the Hamiltonian to a trial state to obtain the ground state wave function. Both approaches are typically realized in the spin-z basis.

Recently, Sandvik introduced a new $T = 0$ QMC projector method formulated in the VB basis [91, 92, 93]. In this approximation free scheme, the ground state is obtained by applying a high power of the Hamiltonian to an arbitrary VB trial state [80, 81]. Consider the projection operator $H_{i,j}$ derived from the Heisenberg Hamiltonian

$$-H/J = \sum_{\langle ij \rangle} \left(\mathbf{S}_i \mathbf{S}_j - \frac{1}{4} \right) = \sum_{\langle ij \rangle} H_{ij} = \sum_b H_b \,, \tag{3.3}$$

where b labels all nearest neighbor bonds on a given lattice. The singlet projection operator H_{ij} reconfigures valence bonds $[i, j]$ such that

$$H_{ij}[i,j] = [i,j] \quad \text{and} \quad H_{ij}[i,l][k,j] = \frac{1}{2}[i,j][k,l] \,. \tag{3.4}$$

The illustrations below shows what happens when a singlet projector H_{ij} acts on a VB basis state:

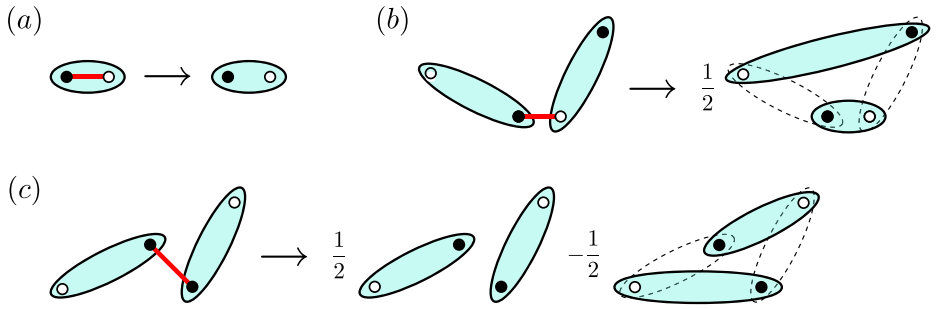

(a) i, j belong to the same bond the state is unchanged with a matrix element 1; (b) i, j belong to different bonds, then the bonds are reconfigured with a matrix element $1/2$; (c) i, j belong to different bonds, but the same sublattice, then the state branches into two terms where bonds remain unchanged with a matrix elements $1/2$ and $-1/2$. The positive-definitness of Eq. (3.4) depends on the sites i, j being in different sublattices. In the following we only consider cases (a) and (b), as case (c) will lead to the infamous sign-problem. Consecutive application of H_b allows to implement more complex interactions of the form

$$H_Q = -Q \sum_{\langle ijkl\ldots\rangle} \left(\mathbf{S}_i \cdot \mathbf{S}_j - \frac{1}{4}\right)\left(\mathbf{S}_k \cdot \mathbf{S}_l - \frac{1}{4}\right) \ldots \ . \tag{3.5}$$

In Eq. (3.5) the indices $\langle ijkl\ldots\rangle$ refer to, e.g., the four corners of an elementary plaquette in a square lattice, such that ij and kl form two parallel adjacent links. For $Q > 0$ and bipartite links ($\langle ij\rangle$, $\langle kl\rangle$, ...) these interactions are non-frustrated and SU(2) invariant. For parallel adjacent links of a plaquette these interactions correspond to (incomplete) ring exchange terms which permute spins around a plaquette. They destabilize Néel-order and favor singlet ground states with short-range magnetic correlations. These interactions can, of course, also be realized in other methods like, e.g., stochastic series expansion [94], but require a tremendous development effort and are not the methods of choice to investigate the ground state of models with multiple spin(dimer)-interactions.

The non-orthogonality of the VB basis enables a simple importance sampling and no specific variational state or extrapolations are needed. The ground state is achieved in the infinite-evolution limit of a singlet trial state. Consider a trial wave function (TWF) $\big|\psi\big\rangle$ and its expansion in terms of eigenstates $\big|\psi\big\rangle = \sum_n c_n \big|n\big\rangle$. Choosing the constant C such that the lowest eigenvalue $E_0 - C$ is the largest in magnitude, the m-fold application of $(C - H)$ onto the TWF will project out the ground state

$$(C-H)^m\big|\psi\big\rangle \to c_0(C-E_0)^m\left[\big|0\big\rangle + \frac{c_1}{c_0}\left(\frac{(C-E_1)}{(C-E_0)}\right)^m \big|1\big\rangle + \ldots\right] , \tag{3.6}$$

provided a finite overlap $\big\langle\psi\big|0\big\rangle \neq 0$ exists, which is the case for arbitrary $\big|\psi\big\rangle$ due to the non-orthogonality of the basis. Note that due to the over-completeness of the basis this expansion is not unique, but it nevertheless yields the correct ground state. In order to obtain ground state properties on finite lattices, a finite expansion length is sufficient. We define a sequence of projection operators

$$(C-H)^m = \left(\sum_{b=1}^{N_b} H_b\right)^m = \sum_r P_r \ , \qquad P_r = H_{b^r_{N/2}} \ldots H_{b^r_2} H_{b^r_1} \ . \tag{3.7}$$

When a projector string P_r acts on a VB state $\big|V\big\rangle$, the result is again a VB state $\big|V(r)\big\rangle$, however reconfigured and carrying the weight w_r determined by the number of off-diagonal operations in the evolution from $\big|V\big\rangle$ to $\big|V(r)\big\rangle$:

$$P_r\big|V\big\rangle = w_r\big|V(r)\big\rangle \ , \quad \text{with} \quad w_r = 2^{-n_o} \ . \tag{3.8}$$

Ground state properties for any operator expectation value $\langle A \rangle$ can be estimated by calculating the matrix elements between two propagated states

$$\langle A \rangle = \frac{\sum_{r,l} \langle V | P_l^* A P_r | V \rangle}{\sum_{r,l} \langle V | P_l^* P_r | V \rangle} = \frac{\sum_{r,l} w_l w_r \langle V(l) | A | V(r) \rangle}{\sum_{r,l} w_l w_r \langle V(l) | V(r) \rangle} = \left\langle \frac{\langle V(l) | A | V(r) \rangle}{\langle V(l) | V(r) \rangle} \right\rangle . \quad (3.9)$$

For spin and dimer correlations the matrix elements are related to the loop structure of the overlap graph. For the example of the spin correlation function $\langle \mathbf{S}_i \cdot \mathbf{S}_j \rangle$ the matrix elements are

$$\frac{\langle V(l) | \mathbf{S}_i \cdot \mathbf{S}_j | V(r) \rangle}{\langle V(l) | V(r) \rangle} = \begin{cases} +3/4, & \text{if } i,j \in \text{same loop, same sublattice,} \\ -3/4, & \text{if } i,j \in \text{same loop, different sublattices,} \\ 0, & \text{if } i,j \in \text{different loops.} \end{cases} \quad (3.10)$$

Monte Carlo updates consist of altering existing, or proposing new operator sequences P_r and P_l. The random change of a given number of operators in the operator string allows for an simple update scheme, requires the full propagation of the trial wave-function, though. The number of update attempts can be optimized [92]. The Metropolis acceptance probability is simply expressed in the numbers of changed off-diagonal operations and the ratio of overlaps $v = 2^{N_\ell - N_b}$,

$$P_{\text{acc}} = \min \left[\frac{w_r^{\text{new}}}{w_l^{\text{old}}} \frac{v^{\text{new}}}{v^{\text{old}}}, 1 \right] = \min[2^{(n_o^{\text{old}} - n_o^{\text{new}}) + (N_\ell^{\text{new}} - N_\ell^{\text{old}})}, 1] . \quad (3.11)$$

Sandvik and Evertz have recently proposed a variation of the VB projector QMC in which they extend the well known loop-updates of the spin-z basis to the VB projector algorithm [95, 30]. The significant disadvantage in their approach is that VB configurations must still be mapped onto the spin-z basis. Beach recently formulated a more *natural* version of cluster-updates, based on a series expansion of the evolution operator where no mapping is necessary [93].

Obviously, estimators converge faster, the larger the overlap of the TWF with the ground state is, hence a smaller projection length m is necessary. A key observation in Liang's original motivation for introducing a projector technique in the VB basis was to improve on a variational calculation by improving the bond-length distribution h of the valence bonds [80, 81]. Liang and others had studied a variational amplitude-product state for the 2D Heisenberg model of the form [72]

$$|\Psi\rangle = \sum_k f_k |V_k\rangle , \qquad f_k = \prod_{b=1}^{N/2} h(x_{bk}, y_{bk}) , \quad (3.12)$$

where x_{bk} and y_{bk} are the x- and y-lengths of bond b in VB state k. There are three basic approaches to improve the TWF in this respect:

(*i*) Make an educated guess, e.g., construct a TWF with the appropriate length distribution $h(l)$ of the valence bonds. This of course requires you to know some things about the ground state beforehand. For a d-dimensional cubic Heisenberg model the lengths l can be estimated within a mean field approach to be $h \sim l^{-d+1}$ [84].

(*ii*) Update the TWF during the Monte Carlo process [83]. With the state (Eq. (3.12)) an expectation value is given by

$$\langle A \rangle = \frac{\sum_{kp} f_k f_p \langle V_p | V_k \rangle \frac{\langle V_p | A | V_k \rangle}{\langle V_p | V_k \rangle}}{\sum_{rl} f_k f_p \langle V_p | V_k \rangle} , \tag{3.13}$$

which can be evaluated using importance sampling of the VB configurations with weight $f_k f_p \langle V_p | V_k \rangle$. Liang and coworkers introduced a very simple updating scheme for the VB configurations [72]: Choose two next-nearest-neighbor sites we label sites 1 and 2, e.g., ones on a diagonal of a 4-site plaquette (in principle any two arbitrary sites work as well) and reconfigure the bonds such as if the projection operator would have been applied to a bond connecting these two sites. The two bonds connected to them are reconfigured in the only possible way which maintains only bonds between the A and B sublattices (cf. Eq. (3.4) and the accompanying figure thereafter). Labeling the bonds connected to the sites 1 and 2 by $b = 1, 2$, the Metropolis acceptance probability is, assuming that the bond update was made in $|V_k\rangle$, resulting in $|V_{k'}\rangle$,

$$P_{\text{accept}} = \min \left[\frac{h(x_{1k'}, y_{1k'}) h(x_{2k'}, y_{2k'})}{h(x_{1k}, y_{1k}) h(x_{2k}, y_{2k})} \frac{\langle V_p | V_{k'} \rangle}{\langle V_p | V_k \rangle}, 1 \right] . \tag{3.14}$$

This allows to update and optimize the TWF during the QMC process. After each update of the TWF the weights and overlaps have to be computed from scratch.

(*iii*) Implement a self-consistent adaptation of the TWF during the warmup phase [83]. Consider the probability distribution $P(x, y)$ of valence bonds. In an amplitude-product state (3.12) it is clear that probabilities and amplitudes are related in some monotonic way $P(x, y) \sim h(x, y)$, hence increasing $h(x, y)$ for some given (x, y) will lead to a larger $P(x, y)$. In order to optimize the probability distribution $P_0(x, y)$ of the TWF we propagate the state, measure the propagated probability distribution $P_m(x, y)$ and adjust $P_0(x, y)$ accordingly, such that $P_0(x, y) \to P_m(x, y)$. If this is done for m sufficiently large, then the trial state has a bond distribution identical to that of the exact ground state. An illustration of the improvement using methods (*ii*) and (*iii*) is shown for the 32×32-site AF Heisenberg model in Fig. 3.2.

A unique advantage of the VBPQMC is that an non-magnetic triplet state can be projected and measured simultaneously with the singlet, at essentially no additional overhead. Consider a triplet bond $(|\uparrow\downarrow\rangle + |\downarrow\uparrow\rangle)/\sqrt{2}$ represented by $[\![a, b]\!]$. Formally, a triplet state can be created by acting on a singlet with $S_i^z - S_j^z$:

$$(S_i^z - S_j^z)[i, j] = [\![i, j]\!] . \tag{3.15}$$

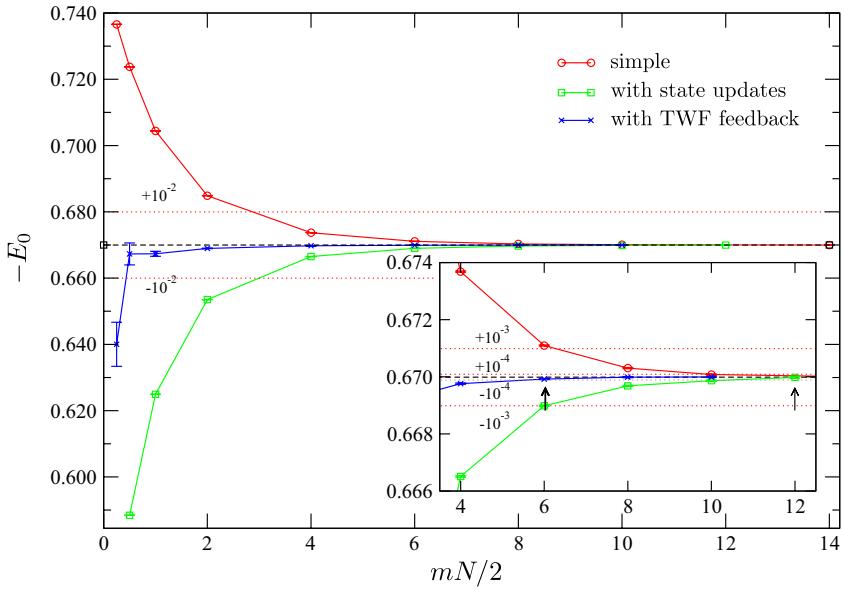

Fig. 3.2.: Comparison of the convergence of the energy density performing the projection scheme on an unchanging TWF (red circles); adapting the TWF via MC-updates (green boxes); optimizing the bond-length distribution in the TWF during the equilibration in a feedback algorithm (blue crosses). The inset shows a blown-up range of the energy axis, where arrows indicate the individual convergence within errorbars. Dashed lines show the deviation from the converged value in powers of 10.

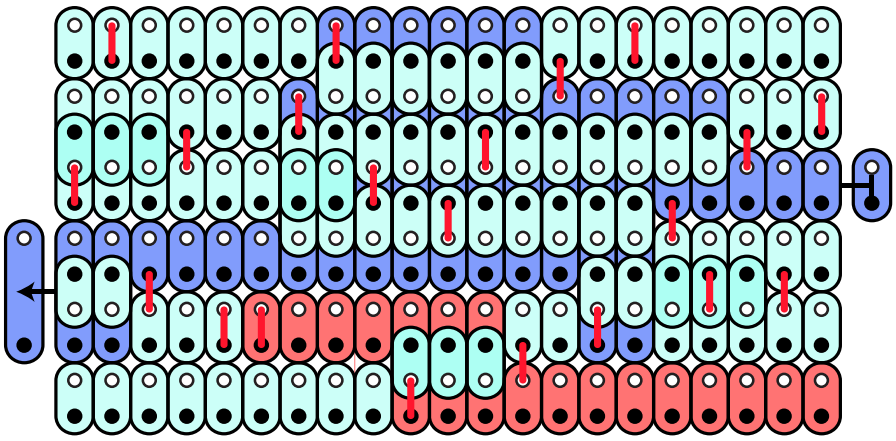

Fig. 3.3.: Propagation of a state (from right to left), with a surviving triplet marked in blue, and a triplet destroyed during propagation in light-red. Thick red lines denote the positions where the projection operators are applied. Adapted from Ref. [93].

The eigenvalue of H_{ab} operating on $[\![a,b]\!]$ is 0, hence the projection operator acting on the sites spanned by a triplet will *destroy* the triplet. If H_{bc} is applied to $[a,b][\![c,d]\!]$, bonds are reconfigured exactly as in the case when they were singlets and the new state is $[\![a,d]\!][c,b]/2$. This enables an improved estimator for the singlet-triplet gap following a simple scheme [96]: Carrying out the simulation with only singlets, one of the bonds can be flagged as a triplet at the measurement stage. The state is then propagated the usual way (cf. Fig. 3.2). During the propagation, a diagonal operation on the triplet will destroy it. The estimator for the first excited energy level E_1 can now be averaged over all $N/2$ initial choices for a triplet, with contributions coming only from surviving configurations. Obviously, the survival ratio depends on the propagation length m. An infinite long propagation $m \to \infty$ will eventually rid the state of all triplets, but typically there are enough survivors left at large enough m to compute converged triplet properties. The triplet energy E_1 can be estimated using (Eq. (3.9)), taking into account that the number of diagonal operators $n_d \to n_d - n_t$, where, for surviving triplet configurations, n_t is the number of triplet bonds of length 1. This can vastly improve the estimate of the gap compared to taking the difference $E_1 - E_0$, where the energies are obtained from two independent simulations. The improvement can be up to orders of magnitude and is largely due to partial cancellation of correlated statistical errors in E_0 and E_1. This idea can be extended to determine the spin gap at arbitrary momenta, but proves practical only in the vicinity of the nodal points of the spin dispersion [92]. Other triplet properties have been discussed in Ref. [83].

Since its introduction [96], the VB projector QMC has been improved by more efficient updates [95, 30] and extended by constraints on the bond-lengths to investigate the crossover from the valence bond models to quantum dimer models [97]; it has been extended to the magnetized sector and odd numbers of sites [98], as well as to treat SU(N) models [99]. Furthermore, besides improved estimators like for the spin gap, the simulation in the VB basis allows to access entropy measures like the Valence Bond Entanglement Entropy [100], von Neumann Entanglement Entropy [101] and Renyi Entanglement Entropy [102], and permits the measurement of the fidelity of states (the differential overlap between different ground states) [103, 104].

3.3. The JQ-model on honeycomb layers

There is an ongoing interest in continuous quantum phase transitions between phases which feature different spontaneously broken symmetries. The prominent example is the transition from a Néel state to a valence bond solid (VBS) state in an $S = 1/2$ antiferromagnet on the square lattice [105, 106, 107, 108]. While the Néel state breaks the SU(2) spin-invariance of the Hamiltonian, the VBS state breaks translational symmetry of the lattice and SU(2) symmetry remains conserved. This phase transition is continuous and stands in contradiction to Landau-Ginzburg-Wilson (LGW) theory which predicts phase

coexistence, an intermediate phase, or a first-order transition, instead. The nature of the critical theory remained unclear until recently [107, 108]. At the *deconfined* quantum critical point the elementary excitations are gapless, spatially deconfined spinons which carry fractionalized spin, accompanied by an emergent U(1) gauge field. The basic conception is that topological defects in the Néel order condensate into the manifold degenerate paramagnetic ground state breaking translational symmetry. Excitations on either side of the critical point are confined, gapped magnons with $S = 1$, which are weakly coupled via the mediating U(1) gauge field.

A different class of transitions which provide instances of deconfined criticality in quantum magnets is given by continuous order-order transitions between two VBS phases. Several effective field theories and quantum dimer models have been suggested to show such a transition [109, 110, 111]. Quantum dimer models introduced by Rokhsar and Kivelson [112] are based on the RVB theory introduced by Fazekas and Anderson [79, 113]. They have been successful in reproducing basic features of quantum (para)-magnets where short-range spin-correlations dominate. Here again effective field theories (although with different operator identities) are a powerful tool to describe the systems at the critical point [114]. Quantum dimer models can also be mapped onto effective classical models and tackled numerically [109]. However, these approaches can only give suggestions for a concrete $S = 1/2$ Hamiltonian which is supposed to correspond to their model. Several recent numerical studies [91, 94, 115, 116] have been able to provide first evidence for such an exotic phase transition in an actual $S = 1/2$ Hamiltonian without approximation and without the restriction to short range valence bonds only. The nature of the quantum phase transition (QPT) is still controversial, though [117, 118, 119].

A more profound understanding of generic features of quantum fluctuation driven phase transitions in spin-models is also of relevance in strongly correlated systems [120]. This includes cuprates like La_2CuO_4 whose effective magnetic behavior can be described by Heisenberg models with cyclic ring exchange [121, 122]. It is known that ring exchange in SU(2) invariant models can destroy magnetic order and drive the system into a VBS phase [123]. While quantum antiferromagnets on the square lattice have been intensively studied, spin models on the hexagonal (honeycomb) lattice deserve attention due to their special lattice properties. Although the lattice is bipartite, like the square lattice, quantum fluctuations can be expected to be larger due to the reduced number of nearest neighbors (see Sec. 1.1).

It is clearly of interest to find tangible $S = 1/2$ models where a direct (second order) phase transition between two paramagnetic (or paramagnetic-Néel) phases can be studied by the exact means of quantum Monte Carlo (QMC) on large lattices. Stimulated by [110] we investigate the JQ-model on the bilayer honeycomb lattice as a candidate for a continuous transition between two VBS-states which posses different symmetries. Both phases are paramagnetic ground states with gapped $S = 1$ excitations. If the scenario of a direct QPT holds, two different VBS order parameters acquire finite values on either side of the transition while antiferromagnetic (AF) order is suppressed. Right at the

critical point neither VBS nor AF order should exist. A good candidate for a model where a paramagnetic ground state can be realized and which can be studied by QMC is the JQ-Hamiltonian recently introduced by Sandvik [91]

$$H = J \sum_{\langle ij \rangle} \mathbf{S}_i \cdot \mathbf{S}_j - Q \sum_{\langle ijkl \rangle} \Big(\mathbf{S}_i \cdot \mathbf{S}_j - \frac{1}{4} \Big) \Big(\mathbf{S}_k \cdot \mathbf{S}_l - \frac{1}{4} \Big) \, , \tag{3.16}$$

where $\langle ij \rangle$ denotes in-plane nearest neighbor sites in the single layer and inter-plane nearest neighbors in the bilayer system. $\langle ijkl \rangle$ refers to four of the six corners of an elementary plaquette in a layer, such that ij and kl form two parallel adjacent links. For $Q > 0$ this model is non-frustrated on any bipartite lattice. The SU(2) invariant four-spin interaction corresponds to an (incomplete) ring exchange term which permutes spins around a plaquette. It favors a singlet ground state with short-range magnetic correlations.

We employ the ground state projector QMC in the VB basis which is ideally suited for multi-spin interactions formed out of singlet projection operators $(\mathbf{S}_i \cdot \mathbf{S}_j - 1/4)$. In this scheme, the ground state is obtained by repeated application of the Hamiltonian to a self-optimized singlet trial state. The method incorporates valence bonds of arbitrary range. This allows to capture the complete physics of valence bond fluctuations. In this paper lattices of size $N = 2L^2$ ($N = 4L^2$) up to $L = 32$ ($L = 24$) are considered for the single layer (bilayer). Symmetric lattices were constructed such that dimerization patterns are prevented to order alongside a preferred lattice dimension.

Our central result is that spin fluctuations destroy staggered dimerization in favor of AF order on both, the single and the bilayer system. Signs of phase separation precede the strong first order phase transition to a Néel phase, which is an artifact of the Monte Carlo sampling procedure. Note the extremely small energy scale of the plot. In the bilayer this magnetic phase separates the staggered dimer order from the magnetically disordered (paramagnetic) phase with dimers on the rungs. The latter transition is presumably a continuous transition similar to the magnetic disorder-order transition in the Heisenberg bilayer system.

In a Néel state a spin gains energy from all its anti-aligned neighbors. Opposed to that a maximum entangled pair, spin-singlet or dimer can only be formed with a single other spin. Hence Néel order is the dominant ground state in most two, or higher dimensional antiferromagnets. Bipartite lattices favor AF order, especially. The spin-spin correlation function and the squared magnetization

$$C_s(\mathbf{r}) = \langle \mathbf{S}(0) \cdot \mathbf{S}(\mathbf{r}) \rangle \, , \tag{3.17}$$

$$M^2 = \frac{1}{N} \sum_{\mathbf{r}} C_s(\mathbf{r}) (-1)^{r_{a_1} + r_{a_2}} \, , \tag{3.18}$$

are used to measure SU(2) symmetry breaking. In a lattice with a low coordination number as the honeycomb lattice ($Z = 3$), AF order can be assumed to be less pronounced

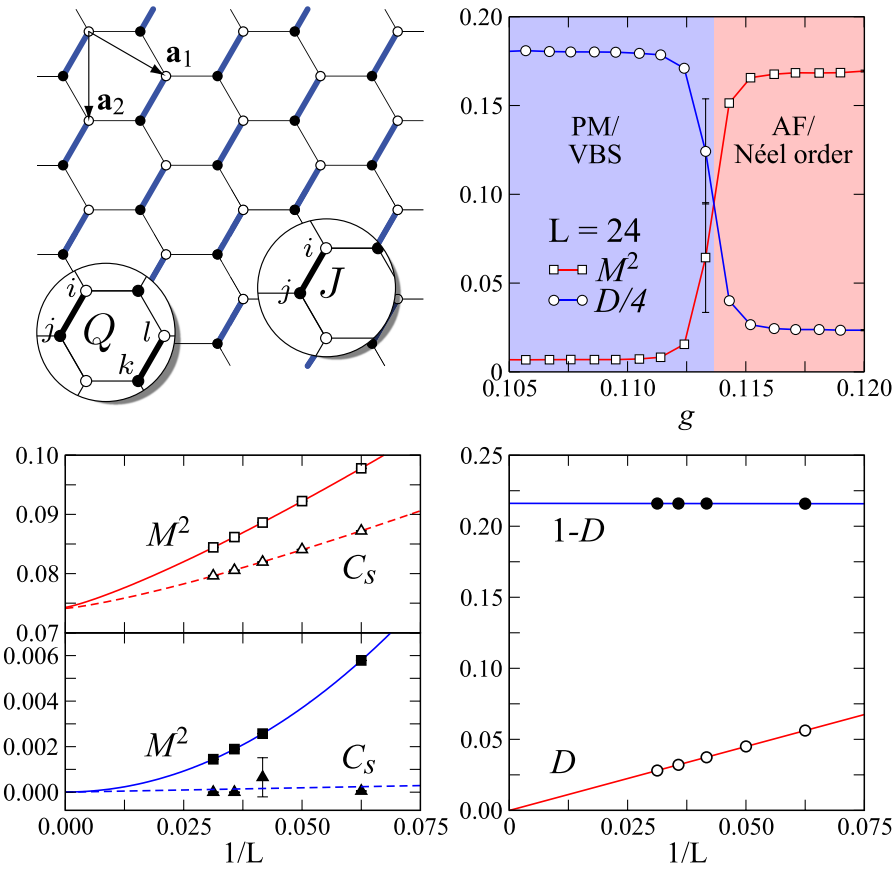

Fig. 3.4.: Top left: The honeycomb lattice where the unit cell consists of two sites with open and filled circles. The basis vectors $\mathbf{a}_1$ and $\mathbf{a}_2$ define the three symmetry directions of the lattice: $\mathbf{a}_1$, $\mathbf{a}_2$ and $\mathbf{a}_1 - \mathbf{a}_2$. Strong (blue) bonds represent singlets $(|\uparrow\downarrow\rangle - |\downarrow\uparrow\rangle)/\sqrt{2}$ and show one of the threefold degenerate staggered VBS pattern. Top right: Phase diagram for the ($L = 24$) honeycomb lattice which shows a first order transition at $g \approx 0.11$ from a VBS to a Néel state. Lines are guides to the eye only. Bottom: Finite size extrapolation of the squared magnetization, spin-spin correlations (left panel) and the dimer order parameter (right panel) in the extreme limits $g = 0$ (filled symbols) and $g \to \infty$ (open symbols). The two order parameters measuring different broken symmetries acquire finite values on complimentary sides of the transition only.

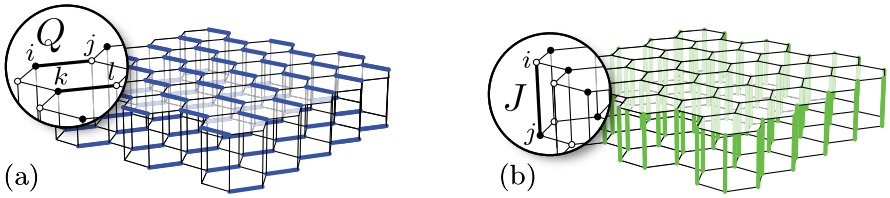

Fig. 3.5.: Cartoon picture of VBS states on the bilayer honeycomb lattice in the (a) small $g = J/Q$ limit: one of the threefold degenerate maximal tilted (staggered ordered) states. (b) large g limit: zero tilt (magnetically disordered) state where no lattice symmetry is broken. Colored (gray) lines represent singlet bonds.

and the disadvantage of each spin forming a VB with another is less severe. Already Read and Sachdev obtained a possible ground state of alternating plaquettes with three dimers and *empty* plaquettes (the star-shape or Kekule pattern) by means of a large-N expansion [106]. This kind of VB crystal breaks rotational and translational lattice symmetry. Analogous to the order parameter Read and Sachdev used to characterize VBS order on the square lattice we define the dimerization order parameter

$$D = \frac{1}{N_c}\sum_{\mathbf{r}} \mathrm{e}^{-\frac{4\mathrm{i}\pi}{3}\mathbf{r}\cdot\mathbf{a}_1}\Big(\mathbf{S}_1(\mathbf{r})\cdot\mathbf{S}_2(\mathbf{r}) + \mathrm{e}^{-\frac{4\mathrm{i}\pi}{3}}\,\mathbf{S}_1(\mathbf{r})\cdot\mathbf{S}_2(\mathbf{r}+\mathbf{a_1}-\mathbf{a_2}) + \mathrm{e}^{-\frac{2\mathrm{i}\pi}{3}}\,\mathbf{S}_1(\mathbf{r})\cdot\mathbf{S}_2(\mathbf{r}-\mathbf{a_2})\Big)\,, \quad (3.19)$$

to identify the breaking of the D_{6h} lattice symmetry. Here $\mathbf{a}_1$, $\mathbf{a}_2$, and $\mathbf{a}_3 = \mathbf{a}_1 - \mathbf{a}_2$ are the vectors along the symmetry axes of the lattice and $\mathbf{r}$ runs over all unit cells $N_c = L^2$. The preceding phase factor set to $-4\mathrm{i}\pi/3$ allows to test for staggered dimerization.

3.3.1. Single layer

For small $g = J/Q$ (setting $Q = 1.0$), staggered order in the hexagonal lattice is strong. At $g = 0$ the squared order parameter for the infinite system extrapolates to $D^2 = 0.7839(2)$ (see Fig. 3.4 (bottom-right)). The system essentially locks in a threefold degenerate ground state spontaneously breaking the Z_3 lattice symmetry as depicted in Fig. 3.4 (top-left). This fully staggered dimerized pattern with energy $E_{\mathrm{col}} = -(3/4)^2 = -0.5625$ is one of threefold degenerate classical realizations close to the true ground state. The extrapolation of the ground state energy per site of $E = -0.5923(1)$ indicates that quantum fluctuations of the Q-term are relevant though. Excitations are gapped consisting of breaking a singlet into a triplet.

In the extreme limit $g \to \infty$ the Hamiltonian on the single layer equals the AF quantum Heisenberg model. Extrapolating to infinite lattice size we find a long range Néel

order where ground state is indefinitely degenerate. We give an improved estimate for the magnetization of $m_{\mathrm{hc}} = 0.2720(9)$. Compared to the square lattice ($m_{\mathrm{sq}} = 0.3070(3)$, [124]) the magnetization is reduced due to enhanced quantum fluctuations. Previous investigations by series expansions around the Ising limit [125], world line QMC [126], stochastic series expansion QMC [127] and exact diagonalization [128] are consistent with this estimate.

The competition between the dimerizing Q-term and the AF ordering J-term leads to a first order transition at $g = J/Q \approx 0.11$. Fig. 3.4(top-right) shows the phase diagram for increasing AF coupling coupling for a $L = 24$ system. Already at moderate lattice size the order parameters show characteristic behavior for a first order phase transition. At the transition point the staggered order has a steep drop-off, while the magnetization jumps to finite values. The finite size extrapolations of the order parameter in the extreme limits of the two phases are shown in Fig. 3.4(bottom). Also the evolution of the energy and histograms of the staggered order parameter support the first order type as we will show exemplary for the bilayer case.

3.3.2. Bilayer

Motivated by Vishwanath et al. [110] we now turn to the nature of the transition between two different VBS states as depicted in Fig. 3.5. In the bilayer setup the four spin interaction acts in the planes only and the layers are coupled antiferromagnetically. For $g \to 0$ the two layers are decoupled and staggered order is strong as we have already seen in the single layer. In the limit $g \to \infty$, spins in the two layers form singlets on the rungs as shown in Fig. 3.5b. The Hamiltonian reduces to an effective two-site problem, which we denote as the disordered, or zero tilt phase according to [109]. The system then is in a paramagnetic (magnetically disordered) phase. Although no lattice symmetry is broken this resembles a second kind of VBS [110].

Figure 3.6 (top-left) shows the phase diagram for increasing interlayer coupling ratio $g = J/Q$ for an $L = 16$ system. For non-frustrating ring exchange and AF coupling J the infamous sign problem restricts reasonable QMC simulations to $g \geq 0$. The two order parameters characterizing the phases are plotted in Fig. 3.6 (top left). For small g staggered order in the almost decoupled layers remains strong. The dimer order only slightly decreases with increasing g before collapsing abruptly, giving way to AF order at $g \approx 0.036(2)$. The finite size extrapolation of the squared magnetization and spin-spin correlations and the squared dimer order parameter close to the transition at $g = 0.025$ and $g = 0.0492$ are shown in Fig. 3.6 (bottom). In the phase $g < g_c$ the VBS order parameter is finite and the magnetization scales to zero (blue curves). For $g > g_c$ the complementary scaling behavior is seen (red curves).

As in the single layer the sudden change of the order parameters suggests a strong first order phase transition. To support this claim Fig. 3.6 (top-right) shows the behavior of the energy close to the phase transition for different system sizes. The kink in the

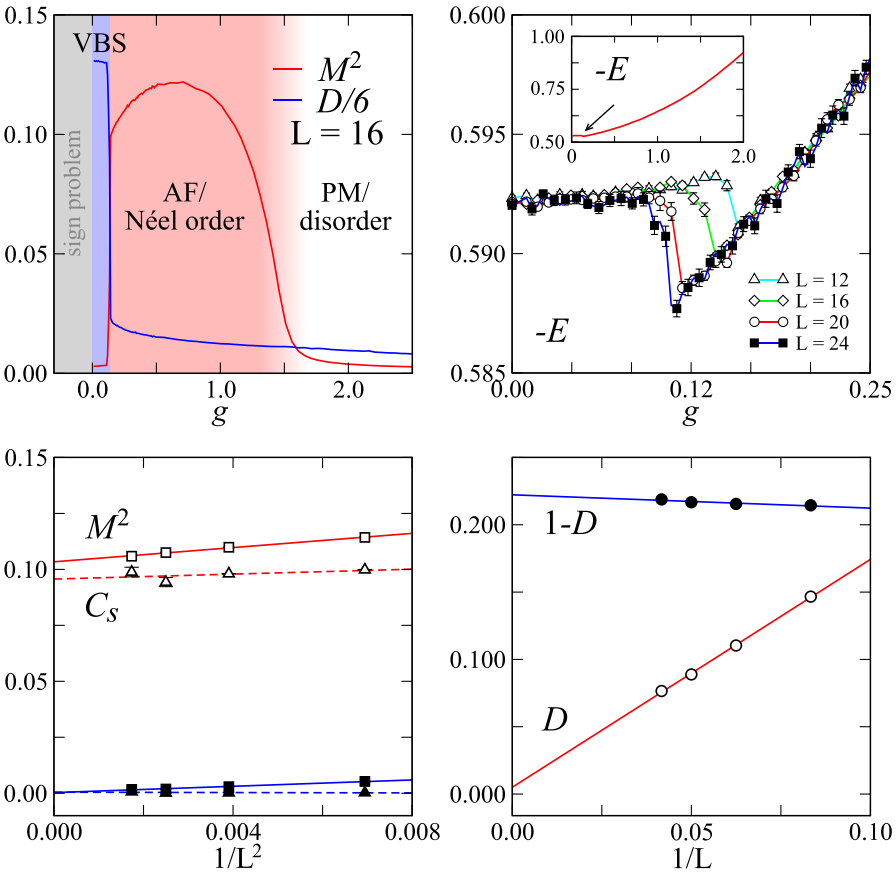

Fig. 3.6.: Top left: Phase diagram for the ($L = 20$) bilayer system which shows a first order transition at $g \approx 0.036$ from a VBS to a Néel state and the continuous Néel order to disorder transition at $g_c \approx 0.5$. Top right: The closeup of the energy per site at the first order transition shows signs of phase separation, which is an artifact of the sampling procedure – note the small energy scale. Lines are guides to the eye only. The arrow in the inset indicates the position of the kink in the developing energy. Bottom: Finite size extrapolation of the squared magnetization and spin-spin correlations (left panel) and the dimer order parameter (right panel) close to the transition at $g = 0.025$ (filled symbols) and $g = 0.0492$ (open symbols).

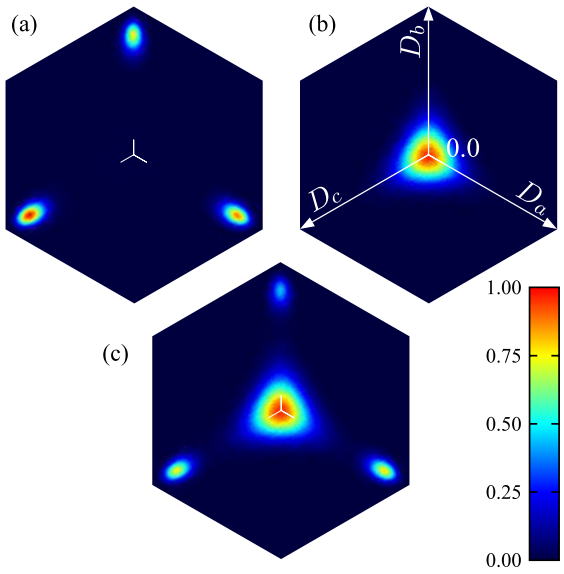

Fig. 3.7.: (Color online) Histograms of the staggered order parameter of the $L = 12$ system. (a) In the VBS phase three distinct maxima indicate staggered order along the three symmetry axes of the lattice. (b) At the proximity of the level crossing where tunneling between the extremal configurations via the zero order interface is visible due to the finite lattice size. (c) The magnetic phase with vanishing staggered order.

energy remains strong for all investigated system sizes and indicates phase separation. Thus a mixture of regions of magnetic order and dimer order is energetically favorable before the ground state collapses into to a system spanning wave function of Néel order. The tunneling time between energetically equivalent configurations grows exponentially with the system size and the Monte Carlo sampling is increasingly dominated by rare tunneling events between configurations with dimer-ordered, short range valence bonds and those with resonating, long range bonds. To overcome large autocorrelation times we employed quantum parallel tempering in the coupling J.

In the intermediate magnetic phase the magnetization increases with g beyond the first order phase boundary. Spin-spin correlations C_s exhibit long range order indicating that SU(2) symmetry is spontaneously broken and the system is in a Néel state. We attributed the large magnetization to the fact that the four spin term induces strong correlations between the parallel adjacent spins in the combs. Thus, although one might expect spin fluctuations to increase with interlayer coupling, the spin degrees of freedom become more rigid. The elementary excitations are the gapless broken generators of the SU(2) symmetry group. With increasing inter-layer coupling g the AF order is continuously destroyed and spins dimerize on the rungs of the bilayer. This behavior is well known from the O(3)-type transition in the Heisenberg square lattice and honeycomb lattice bilayer system. The critical behavior is presumably consistent with the 3D

classical Heisenberg universality class [129].

The nature of the first order transition can be seen best in the histograms of the staggered dimer order parameter along one symmetry axis

$$D_e = \frac{1}{N_c} \sum_{\mathbf{r}} \langle \mathbf{S}(\mathbf{r}) \cdot \mathbf{S}(\mathbf{r}+\mathbf{e}) \rangle \ . \tag{3.20}$$

A staggered dimerized state along the lattice $\mathbf{a}_1$ axis would give a sharp maximum at $D_{a_1} = 1$, while $D_{a_2} = D_{a_3} = 0$ and vice versa for dimerization along the other axes. A plaquette state would give rise to peaks at $-D_{a_1} = -D_{a_2} = -D_{a_3}$). Fig. 3.7 shows the color-coded histogram of the probability distribution $P(D_{a_1}, D_{a_2}, D_{a_3})$ close to the level crossing for an $L = 12$ system. In the VBS phase three maxima at the far end of the axes correspond to strong staggered order. Tunneling between these extremal configurations of order is possible due to the finite lattice size and takes place only via crossing the Néel ordered interface, which can be seen as the central maximum in Fig. 3.7b. A direct transition between staggered ordered states is not observable. In the magnetic phase with the central maximum (Fig. 3.7c), distortions in the probability distribution along the order axes stem from the influence of the four-spin term. This can be seen in Fig. 3.6 in the nonzero dimerization order parameter in the AF and disordered phase as well.

3.4. Realizations

The JQ-model studied here is a thinkable approximation for the low energy physics in real compound, as long as the ratio of J/Q is large. The admixture of a (incomplete) ring exchange term mimics next nearest neighbor and plaquette interactions. However, for the coupling ratios relevant for this investigation no realistic compound exists to our knowledge and this study focussed on model properties only.

Nevertheless let us give some real world examples for honeycomb spin systems. While honeycomb layers can be found in materials quite often, it is hard to find effective spin-1/2 nearest-neighbor antiferromagnets among them. Usually, longer-range interactions are important like in $Bi_3Mn_4O_12(NO_3)$, which is best modeled by a spin-1/2 honeycomb structure with nearest and next-nearest neighbor AF spin interactions [130]. Antiferromagnetic spin-1/2 systems, which are well described by a nearest-neighbor AF Heisenberg model, have been reported to be realized in the $C_4H_{10}NO$-salt [131] and Na_2IrO_3 [132]. Also β-$Cu_2V_2O_7$ [133] is an, albeit slightly anisotropic, AF spin-1/2 honeycomb lattice system.

Honeycomb layers are also found in transition-metal thiophosphates MPS_3, where M is a first row transition metal. Their effective spin degrees of freedom are typically larger than $S = 1/2$, though. Neutron diffraction and magnetic susceptibility studies on $MnPS_3$, $FePS_3$, and $NiPS_3$ antiferromagnets [134, 135, 136] ($S = 5/2$, $S = 2$, and $S = 1$, respectively) showed the existence of quite different types of ordering and hence

magnetic exchange couplings among the different compounds. Whereas for $FePS_3$ and $NiPS_3$ the metal ions are coupled ferromagnetically to two of the nearest neighbors and antiferromagnetically to the third, for $MnPS_3$ all nearest neighbors interactions within a layer are AF [127].

3.5. Discussion and outlook

We discussed Monte Carlo simulations of the JQ-model on the honeycomb single layer and bilayer and present the phase diagram in the unfrustrated regime ($Q > 1$). In the bilayer system at increasing coupling between the layers we find a strong first order quantum phase transition to an intermediate Néel phase followed by a continuous order-disorder transition similar to the Heisenberg bilayer system. A direct (continuous) transition from Néel-VBS or VBS-VBS phases is not found for the JQ-model on hexagonal lattices.

We argue that, as one moves along the transition in an extended parameter space (corresponding to some additional, possibly frustrated, interaction), one may access a regime where both the magnetic and VBS order fluctuations are critical. Comparing the honeycomb lattice with the square lattice we conclude that the route from a Z_3 degenerate ground state to an emergent U(1) symmetry at criticality is far longer than from Z_4 to U(1). A competing interaction which creates a higher-degenerate ground state might enable a continuous transition from a Néel state to a VBS. The bilayer setup leads to a pronounced Néel regime.

Another interesting aspect would be to extend the interaction to a six-spin exchange of the form $H_Q = \sum_{\langle ijklmn\rangle}(\mathbf{S}_i \cdot \mathbf{S}_j - \frac{1}{4})(\mathbf{S}_k \cdot \mathbf{S}_l - \frac{1}{4})(\mathbf{S}_m \cdot \mathbf{S}_n - \frac{1}{4})$, where $\langle ijklmn\rangle$ denotes the sites around a hexagonal plaquette. This interaction mimics Hamiltonian found in hexagonal quantum dimer models and may lead to, either another VBS (e.g., Kekule dimerization) or even a magnetically disordered ground state as in a spin liquid.

Spin liquid emerging in two-dimensional correlated Dirac fermions

4

At sufficiently low temperatures, condensed-matter systems tend to develop order. An exception are quantum spin-liquids, where fluctuations prevent a transition to an ordered state down to the lowest temperatures. While such states are possibly realized in two-dimensional organic compounds, they have remained elusive in experimentally relevant microscopic two-dimensional models. Here, we show by means of large-scale quantum Monte Carlo simulations of correlated fermions on the honeycomb lattice, a structure realized in graphene, that a quantum spin-liquid emerges between the state described by massless Dirac fermions and an antiferromagnetically ordered Mott insulator. This unexpected quantum-disordered state is found to be a short-range resonating valence bond liquid, akin to the one proposed for high temperature superconductors.

In this chapter we give an introduction to the notion of quantum spin liquids (QSL), the theoretical approaches to effective models, and present our investigation of the SU(2) Hubbard model on the honeycomb in detail. In the end we discuss examples of compounds and other realizations which potentially show spin liquid ground states. Parts of this chapter have been published in [137].

4.1. Spin liquids

4.1.1. Origins & definition

The original concept of a QSL is tied to the phenomenon of antiferromagnetic (AF) order. It was believed for a long time that ferromagnetic order is the dominant type of magnetic order in nature. Nowadays we know that due to the fermionic properties of electrons and the resulting superexchange AF order is more often to be found at low temperatures and ferromagnetism is the exception, indeed. In 1970 Louis Néel was rewarded the Nobel prize for his pioneering studies of the magnetic properties of solids, including his proposal of AF order about 1930, which was based purely on theoretical arguments. Lev Landau (Nobel Prize in Physics 1962) was known to have his difficulties with antiferromagnetism and suggested quantum fluctuations to mix Néels classical solution $\downarrow\uparrow\downarrow\uparrow\downarrow\uparrow$ with that

obtained by reversal of moments $\left|\downarrow\uparrow\right\rangle \rightarrow \left|\uparrow\downarrow\right\rangle$. This notion was supported by the fact that Hans Bethe (Nobel prize in Physics 1967) in 1931 found the exact eigenvalues and eigenvectors of the one-dimensional AF Heisenberg model ruling out a magnetically ordered ground state. Only much later in 1950 Clifford G. Shull (Nobel Prize in Physics 1994) was able to use neutron diffraction to confirm Néels suggestion of AF order as the natural ground state in some compounds.

In fact, although the classical picture of AF order provides an efficient trial wave function, quantum fluctuations really do play a significant role in antiferromagnetically ordered states at low temperatures, especially at low dimensionality and for $S = 1/2$ moments. For the simple example of the one dimensional AF Heisenberg chain we see that the Néel state is not exact eigenstate. The Hamiltonian converts pairs of up- and down-spins into singlets (see illustration below) – zero point fluctuation generate states which deviate from the Néel state. The true ground state of the AF Heisenberg chain shows critical AF correlations and hence appears to be ordered but lacks true long range order due to its one-dimensionality (see Sec. 1.4). In two dimensions the ground state of the AF Heisenberg model is truly AF ordered, but the local moment is far from the saturation value of 1/2 per site because of strong quantum fluctuations.

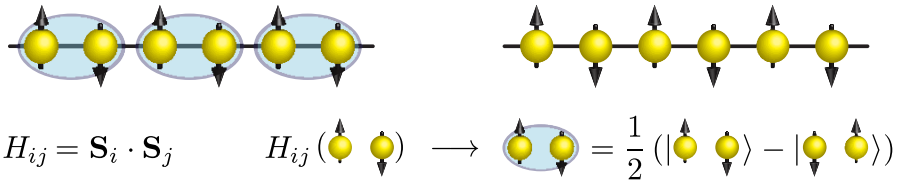

Consider the spin chain above – the energy per bond of a singlet trial wave function (illustrated on the left) is $-(1/2)S(S+1)J = (3/8)J$ versus $-(1/4)J$ for AF order (right). Since (3/8) is larger than (1/4) (at least last time I checked), energy can be minimized by forming spin singlets instead of AF order and Néel order can be destroyed in favor of quantum fluctuations. This led Phil Anderson (Nobel Prize in Physics 1977) to introduce the idea of using spin-singlets to describe the ground state of the frustrated AF Heisenberg model on the triangular lattice in 1973 [78, 79]. Indeed, the equal superposition of short range singlets (or valence bonds) is a good trial wave function for the true ground state. The important point however is that the singlets must not order in a regular pattern such as to form a valence bond solid (VBS). Instead, fluctuations lead to a ground state best described by the equal superpositions of singlet pairs (of arbitrary range) covering the lattice. Since this can be effectively approximated by a trial wave function of flippable valence bond configurations on the basic building blocks (plaquettes) of the lattice, the state is dubbed resonating valence bond (RVB) state [78, 79, 39].

Most ground states found in nature are conventional, either being metallic or insulating. In the latter case they usually exhibit some type of order and thus confinement.

One dimensional systems pose an exception for their particular properties, which we will explain further here. For higher dimensions some insulating states, like the RVB state, however do not break any symmetry at all, which lead to the notion of spin liquids. The definition of a QSL is not unambiguous, but among all the definitions to be found in literature the following idea is shared.

> *A spin liquid is a Mott insulator quantum ground state in which there is no long range (magnetic) order and neither symmetries of the constituent degrees of freedom nor the spatial symmetries of the lattice are broken.*

In one dimensional systems so-called *trivial* spin liquids can be found – the most simple example is the rung-dimerized two leg ladder, where no symmetry is broken, but which could also be classified as a valence bond solid (VBS). In higher than one dimension no dimer covering can be found which would not break a lattice symmetry, such they can be truly called *non-trivial* spin liquids. There, excitations are expected to consist of breaking a singlet pair into two spin-1/2 particles (spinons), which are (weakly) coupled to an emergent SU(2), U(1), or Z_2 gauge field. These spinons may even form a Fermi sea – consider the implication: this is the prime example of fermionic statistics emerging from a purely bosonic starting point [138]. Additionally, QSLs provide the starting ground for superconductivity: the fluctuating spin singlet pairs produced by the exchange interaction become charged superconducting (Cooper) pairs when the insulating state is destroyed upon doping, by frustration, or reduced correlations [113, 139, 112].

4.1.2. Effective models, ground state properties & classification

The spin liquid picture has been extended to a full body of theoretical models, mostly in terms of field theories [138, 140, 141]. The basic idea of these is to start from the Heisenberg interaction

$$H = \sum_{\langle ij \rangle} \mathbf{S}_i \cdot \mathbf{S}_j \ , \tag{4.1}$$

and to introduce Schwinger fermions which carry spin $\mathbf{S} = \frac{1}{2} f^\dagger_\alpha \boldsymbol{\sigma}_{\alpha\beta} f^\dagger_\beta$. Instead of introducing Schwinger fermions also Schwinger bosons can be employed. Generally, boson representation is better for describing Néel order, or gapped spin liquids, whereas fermionic representation is favorable for describing gapless spin liquids (in some cases also Schwinger fermions can lead to gapped ground states). Which mean field theory is closer to the truth remains an open question [142]. The interaction is then written as

$$\mathbf{S}_i \cdot \mathbf{S}_j = -\frac{1}{4} f^\dagger_{i\alpha} f_{j\alpha} f^\dagger_{j\beta} f_{i\beta} - \frac{1}{4} \left(f^\dagger_{i\uparrow} f^\dagger_{j\downarrow} - f^\dagger_{i\downarrow} f^\dagger_{j\uparrow} \right) \left(f^\dagger_{j\uparrow} f^\dagger_{i\downarrow} - f^\dagger_{j\downarrow} f^\dagger_{i\uparrow} \right) + \frac{1}{4} f^\dagger_{i\alpha} f_{i\alpha} \ . \tag{4.2}$$

Note, that to implement the spin algebra correctly the constraint of single occupation $\sum_\alpha f^\dagger_\alpha f_\alpha = 1$ is necessary, such that no charge fluctuations are allowed. The constraint

can be enforced by use of a Lagrange multiplier λ in the action. The interaction can be approximated by

$$\mathbf{S}_i \cdot \mathbf{S}_j = -\frac{1}{4} f^\dagger_{i\alpha} f_{j\alpha} \chi_{ij} - \frac{1}{4} \left(f^\dagger_{i\uparrow} f^\dagger_{j\downarrow} - f^\dagger_{i\downarrow} f^\dagger_{j\uparrow} \right) \Delta_{ij} + \frac{1}{4} f^\dagger_{i\alpha} f_{i\alpha} \, . \tag{4.3}$$

Here, $\chi_{ij} = \left\langle f^\dagger_{j\beta} f_{i\beta} \right\rangle$ and $\Delta_{ij} = \left\langle f^\dagger_{j\uparrow} f^\dagger_{i\downarrow} - f^\dagger_{j\downarrow} f^\dagger_{i\uparrow} \right\rangle$ are the mean field values of the hopping and pairing channels. The partition function is given by $Z = \int d\chi d\lambda df df^\dagger \mathrm{e}^{-S}$, with the action

$$S = \int d\tau \sum_i \left[f^\dagger_{i\alpha} \partial_\tau f_{i\alpha} + \mathrm{i}\lambda_i (f^\dagger_{i\alpha} f_{i\alpha} - 1) \right] + \sum_{ij} \left[2J |\chi_{ij}|^2_+ J (\chi_{ij} f^\dagger_{j\alpha} f_{i\alpha} + \mathrm{h.c.}) \right] \, . \tag{4.4}$$

Solving the saddle point equations obtained by minimizing the free energy with respect to the mean field parameters $\frac{\partial F}{\partial \chi_{ij}} \stackrel{!}{=} 0$ and $\frac{\partial F}{\partial \Delta_{ij}} \stackrel{!}{=} 0$, one finds two possible solutions: (i) For χ_{ij} real and constant: a fermi sea (ii) for χ_{ij} complex: flux phases and a Dirac (point-like) sea. For the latter in the deconfined phase, fermions and gauge fields emerge as new particles at low energy. The spinons are not free particles, but minimally coupled to the gauge field, which leads to a new critical state: the spin liquid. The complex phase of χ_{ij} becomes a compact (quantized) gauge field on the links, while the $\mathrm{i}\lambda$ becomes a time component. The amplitude of χ_{ij} is gapped and may be dropped since only the low energy degrees of freedom are expected to play a significant role. The symmetry of the emergent field denotes under which transformations the system remains invariant. The physical meaning of the emergent U(1) gauge field (which also could be of Z_2 symmetry for gapped spin liquids, or even of SU(2) symmetry) manifests itself in the fact that fermions pick up a Berry phase as they hop around a plaquette. This can be represented by a gauge flux through the plaquette and is related to spin chirality, which can be measured by $\left\langle \mathbf{S}_i \cdot (\mathbf{S}_j \times \mathbf{S}_k) \right\rangle$ [143].

The general mean field approach outlined above for gapless spin liquid states and explained detailed in [138, 142] describes a compact gauge field coupled to fermions, but lacks a tangible microscopic model. In general Eq. (4.1) alone leads to AF order on bipartite lattices and 120° AF order on the triangular lattice; the ground state of the Hamiltonian in 4.1 on the Kagome lattice is actually a good candidate for a QSL. However, additional (higher order spin interaction) terms

$$H = \sum_{\langle ij \rangle} \mathbf{S}_i \cdot \mathbf{S}_j + \dots \, , \tag{4.5}$$

might create enough frustration to prevent magnetic order. In fact, frustration is believed to play a crucial role to allow for QSLs [144]. It enhances the number of low lying excitations, which increases the entropy at low temperatures; quantum fluctuations are enhanced due to the large density of states at low energies which prevents magnetic order and frustrated hopping reduces the nesting of the Fermi surface.

As mentioned above, spin-liquids can also be classified according to their gauge field symmetry. Gapless (algebraic) spin-liquids, or long-range RVB states are characterized by critical spin-spin correlations [145, 140, 19, 146, 147] and can be effectively described by U(1) field theories. A spin-liquid with a finite spin-gap can be modeled in terms of a short-range RVB characterized by short-ranged dimer-dimer correlations [78, 79, 139, 112, 148]. Short-range RVB states are modeled in general by quantum dimer models [112, 148, 149], which capture the fluctuations of singlets in a RVB state, with dimers being a strong-coupling representation of nearest-neighbor singlets [112]. These quantum dimer models represent the low energy effective models for many QSLs. Depending on the lattice geometry, quantum dimer models can exhibit a fully gapped short-range RVB phase, as e.g., on the triangular lattice [150]. For bipartite lattices at the Rokhsar-Kivelson point [112] and within the U(1) spin-liquid phase stabilized for spatial dimensions $d > 2$ [151] they can, in turn, also exhibit spin liquid states with gapless excitations. Fully gapped phases of quantum dimer models, i.e. Z_2 spin-liquids are characterized by a non-trivial topological order as described below. Let us also mention here the concept of *projective symmetry groups* (PSG), which has become a practical tool to investigate QSL phases of spin models [152, 153].

Another possibility is to classify the QSL based on the statistics of their gaps and excitations. In the following Δ_{singlet} denotes the gap to singlet excitations, and Δ_s is the (spin-)gap to triplet excitations. Wen divided spin liquids into the classes [152, 138, 154, 153]

Rigid spin liquid: All excitations are gapped and may have either bosonic, fermionic or fractional statistics. $\Delta_s \neq 0$ and $\Delta_{\text{singlet}} \neq 0$.

Topological spin liquid: All excitations are gapped but for singlet excitations, such that the ground state has topologically degenerate sectors. $\Delta_s \neq 0$ and $\Delta_{\text{singlet}} = 0$ [155, 149].

Fermi spin liquid: Spinons are gapless and described by Fermi liquid theory (spinons are effectively free particle close to the spinon-Fermi-surface). $\Delta_s = 0$ and $\Delta_{\text{singlet}} = 0$.

Algebraic spin liquid: Spinons are gapless but cannot be described by free fermionic, or bosonic particles. Spin and dimer correlations are interlocked and algebraically decaying (critical) [156, 141, 157]. $\Delta_s = 0$ and $\Delta_{\text{singlet}} = 0$.

Bose spin liquid: The excitations are gapless and described by a free-boson theory. $\Delta_s = 0$ and $\Delta_{\text{singlet}} = 0$.

The case $\Delta_s = 0$ and $\Delta_{\text{singlet}} \neq 0$ can be excluded by Goldstone's theorem since the gapless spin-excitations demand a singlet ground state. In this list we added the second item to the original list for completeness. Here we distinguished between the rigid- and the topological QSL, although they are assumed to be equivalent. However, it cannot

be excluded that these are actually separate kinds of QSLs. The topological property describes the existence of degenerate ground state sectors with vanishing overlap. This implies that in phase space these ground state sectors cannot be connected by local transformations. For topological insulators consisting of itinerant electrons the further implications are a quantized Hall conductivity σ_{xy} and the occurrence of (protected) edge states at the boundaries of the systems [158, 159]. Note that all the different QSLs can have different elementary excitations beyond spinons, like visons, non-abelian quasi-particles, or even no quasiparticles at all [146].

In the context of this classification the following conjecture on the possible ground states of short-range spin models can be frequently found in the literature: For the family spin-1/2 Heisenberg models with short-range interactions on two dimensional lattices with non-integer spin in the repeat unit, the ground state breaks at least one of the two symmetries SU(2) and lattice-point-group over all continuous range of the coupling ratio g. This statement would allow a QSL to only exist at a singular coupling g, e.g., g_c. So far there has been no definite counter example. The requirement of non-integer spin in the repeat unit is chosen such that Hastings generalization of the Lieb-Schulz-Mattis theorem does not apply. The Lieb-Schultz-Mattis theorem [160] states that spin chains must exhibit either a unique ground state with gapless excitations or a multiply degenerate ground state (which may or may not have a gap). It has been generalized to antisymmetric, self-conjugate representations of SU($2N$) [161] and higher dimensions [162, 163, 164], including topological ground state degeneracies [165]. Important for this chapter is the fact that because of the two orbital structure of the hexagonal lattice, each carrying a spin-1/2, the generalization of the Lieb-Schultz-Mattis theorem does not apply to the half-filled Hubbard model on the honeycomb. Nevertheless, also for half-integer spins per unit cell such as the triangular lattice there exist candidate counter examples, like the Heisenberg model with ring exchange on the triangular lattice [166].

How do you decide if a given Hamiltonian has a QSL ground state? If you have access to the full ground state wave function, e.g., in integrable systems, density matrix renormalization group simulations, or exact diagonalization, then one can scrutinize the wave function using reduced density matrices to look for possible orderings (or better the absence thereof) [167]. Gapped QSLs are characterized by short-range correlations but long-range entanglement, termed *topological entanglement entropy* – a counterintuitive prediction made by the authors in references [168, 169]. The (von Neumann) entropy follows an area (L) law $S(L) \approx \alpha L + \gamma$. The corrections γ are specific to the model and are related to the nature of the elementary excitations of the QSL. For the example of a Z_2 QSL (short-range RVB) $\gamma = -\ln(2)$ [170]. If you don't have the ground state wavefunction, like in QMC, you are left with the burden to proof a negative: the absence of order. This is obviously a very hard problem!

While there exists a large number of effective models for QSLs, it seems extremely difficult to find physically realistic Hamiltonians in two and higher dimensions which exhibits a spin liquid ground state. Starting from the more general and non-frustrated

Hubbard model on the honeycomb lattice, we will show in this chapter that more than 30 years after their original proposal we may finally have a realistic example of a QSL in higher than one dimension.

4.2. SU(2) Hubbard model on the honeycomb

The quantum mechanical description of the relativistic electron was attained by Dirac, who revealed both its intrinsic angular momentum (the spin), with a half-integer quantum number $S = 1/2$, and the existence of its antiparticle, the positron [171]. Both obey the Fermi-Dirac statistics, which implies that two identical particles cannot occupy the same quantum mechanical state. Such particles are generically called fermions. In case of a vanishing rest mass, the energy of Dirac fermions is a linear function of momentum. Such massless Dirac fermions were recently observed in two-dimensional solid-state systems like graphene [172, 173] and surfaces of bismuth based compounds [174, 175]. For graphene, a single layer of carbon atoms with honeycomb structure, unusual electronic behavior is anticipated, and partly verified experimentally, due to the two-dimensional Dirac-like dispersion of the electrons at low energies [1]. The interplay of a relativistic dispersion with interactions at half-filling is expected to lead to a quantum phase transition between the semimetal (SM) at low and a Mott insulator (MI) at high interaction strengths [157, 176]. Here, a Mott insulator is an insulating state that results not from the band structure alone, but is due to the effects of interactions. Such correlation effects can be displayed by the Hubbard model in its most basic form, as exemplified in high temperature superconductivity [146], or with ultra-cold fermionic atoms loaded in optical lattices [177, 178]. Studies of Hubbard-like models on the honeycomb lattice suggested the emergence of exotic phases such as gapless QSL [141, 157], charge density waves [179], quantum spin Hall states [180, 179], or superconductivity [181] at or near a density of one fermion per site (half-filling for the two-species case).

Given the various phases proposed for fermions on a honeycomb lattice based on Hubbard-like models, it is important to explore the ground state properties in the intermediate coupling regime of the original lattice model with an unbiased method. Due to the absence of a sign-problem in determinantal quantum Monte Carlo (QMC) simulations (see Sec. 1.2) in the half-filled case, it is the method of choice for extrapolations to the thermodynamic limit (TDL), leading to essentially exact results limited only by the statistical noise. Employing large-scale QMC simulations of the spin-$\frac{1}{2}$ Hubbard model at half-filling on the honeycomb lattice, we show that for intermediate interactions a gapped non-magnetic phase destroys the semimetal before the transition to an antiferromagnetically ordered Mott insulator at strong interactions sets in. This quantum spin-liquid phase is characterized by local correlations that correspond to a resonating valence-bond (RVB) state [78, 79] as proposed in the context of high temperature superconductivity [113, 139, 146].

Following their original proposals [78, 79, 113, 139], spin-liquid states were established in effective models of singlet-dynamics such as quantum dimer models [112, 148, 149]. Our results show that RVB states are realized in a microscopic model of correlated electrons, bringing closer their observation in experiments. Honeycomb lattices of group IV elements [182] and ultra-cold fermionic atoms loaded in optical lattices [183, 177, 178] appear as promising candidate systems to realize the RVB state out of Dirac fermions.

4.2.1. Phase diagram from quantum Monte Carlo

Previous numerical studies of the Hubbard model on the honeycomb lattice [184, 185] suggested that a single quantum phase transition separates the paramagnetic weak-coupling SM phase from a strong-coupling AF MI. At strong enough repulsion, antiferromagnetism is certainly possible since the honeycomb lattice is bipartite, so that AF order is not geometrically frustrated. However, the honeycomb lattice has the smallest coordination number in two dimensions, such that the effect of quantum fluctuations is the strongest. Hence, the competition between the tendency to order and quantum fluctuations requires a detailed analysis of correlations and a careful extrapolation to the TDL in order to characterize the possible phases. Here, we present results based on projective (temperature $T = 0$) determinantal QMC simulations in the canonical ensemble at half-filling. In order to assess the above scenarios, we focus in particular on the region near the Mott transition.

The Hamiltonian of the spin-$\frac{1}{2}$ Hubbard model on the honeycomb lattice (cf. Sec. 1.1 and Sec. 1.3) equals

$$H = -t \sum_{\langle i,j\rangle,\alpha} (c^\dagger_{i\alpha} c_{j\alpha} + c^\dagger_{j\alpha} c_{i\alpha}) + U \sum_i n_{i\uparrow} n_{i\downarrow} \,, \tag{4.6}$$

where $c^\dagger_{i\alpha}$ ($c_{i\alpha}$) denotes the creation (annihilation) operator for fermions of spin $\alpha = \uparrow, \downarrow$ on lattice site i, and $n_{i\alpha} = c^\dagger_{i\alpha} c_{i\alpha}$. Here, t denotes the nearest-neighbor hopping amplitude, and $U \geq 0$ the strength of the onsite repulsion. At $U = 0$, the tight-binding Hamiltonian has a linear dispersion near the Dirac points (K, K' – cf. Sec. 1.1), where the conduction and valence bands touch at half-filling, corresponding to a density $\sum_\alpha \langle n_{i\alpha}\rangle = 1$. At half-filling, the finite-U region can be studied using projective QMC to obtain ground state expectation values of any physical observable (cf. Sec. 1.2). The phases described in the following correspond to extrapolations to the TDL. For that purpose we study lattices of $N = 2L^2$ sites with periodic boundary conditions, and linear sizes up to $L = 18$. To monitor the electronic properties of the system upon increasing U, we extracted the single-particle excitation gap $\Delta_{sp}(\mathbf{k})$ from the imaginary-time displaced Green's function.

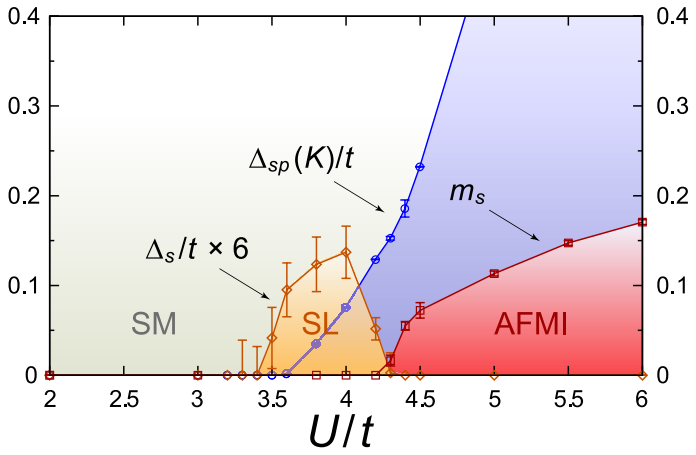

Fig. 4.1.: Phase diagram for the Hubbard model on the honeycomb lattice at half-filling. The semimetal (SM) and the AF Mott insulator (AFMI) are separated by a gapped spin liquid (SL) phase in an intermediate coupling regime. $\Delta_{sp}(K)$ denotes the single-particle gap and Δ_s the spin gap. m_s denotes the staggered magnetization whose saturation value is 1/2.

Green's function and single-particle gap

To probe the single-particle properties, we measured the imaginary-time displaced Green's function

$$G(\mathbf{k},\tau) = \frac{1}{2}\sum_a \langle c^\dagger_{\mathbf{k}a\uparrow}(\tau) c_{\mathbf{k}a\uparrow}(0)\rangle = \frac{1}{2}\sum_a \langle c^\dagger_{\mathbf{k}a\downarrow}(\tau) c_{\mathbf{k}a\downarrow}(0)\rangle \ , \tag{4.7}$$

where $c^{(\dagger)}_{\mathbf{k}a\alpha}(\tau) = \mathrm{e}^{\tau H} c^{(\dagger)}_{\mathbf{k}a\alpha} \mathrm{e}^{-\tau H}$. The single-particle gap $\Delta_{sp}(\mathbf{k})$ is obtained from $G(\mathbf{k},\tau) \propto \exp(-\tau\Delta_{sp}(\mathbf{k}))$ at large imaginary time τ, and corresponds to the particle (or hole) excitation energy with respect to the chemical potential $\mu = 0$ at half-filling, in this particle-hole symmetric system. At $U = 0$, the single-particle gap vanishes at the Dirac points K and K', and we thus considered $\Delta_{sp}(K)$ in detail. The quality of the data (cf. Fig. 4.2a) allows us to safely determine the quasi-particle gap from the unequal time one-particle Green's function without the need to invoke maximum entropy. Details on the extraction procedure can be found in Sec. 5.6.1 and Fig. 5.4.

$\Delta_{sp}(\mathbf{k})$ gives the minimal energy necessary to extract one fermion from the system, and corresponds to the gap that can be observed in photoemission experiments. As shown in Fig. 4.1, $\Delta_{sp}(K) = 0$ for U/t below about 3.5, as expected for a SM. For larger U/t, the system enters into an insulating phase due to interactions. The values of the gap are obtained via an extrapolation of the QMC data to the TDL as shown in Fig. 4.2a. From previous analysis of the model, one expects long-range AF correlations when the MI appears. We therefore measured the AF spin structure factor S_{AF} that reveals long-range AF order if $m_s^2 = \lim_{N\to\infty} S_{AF}/N > 0$.

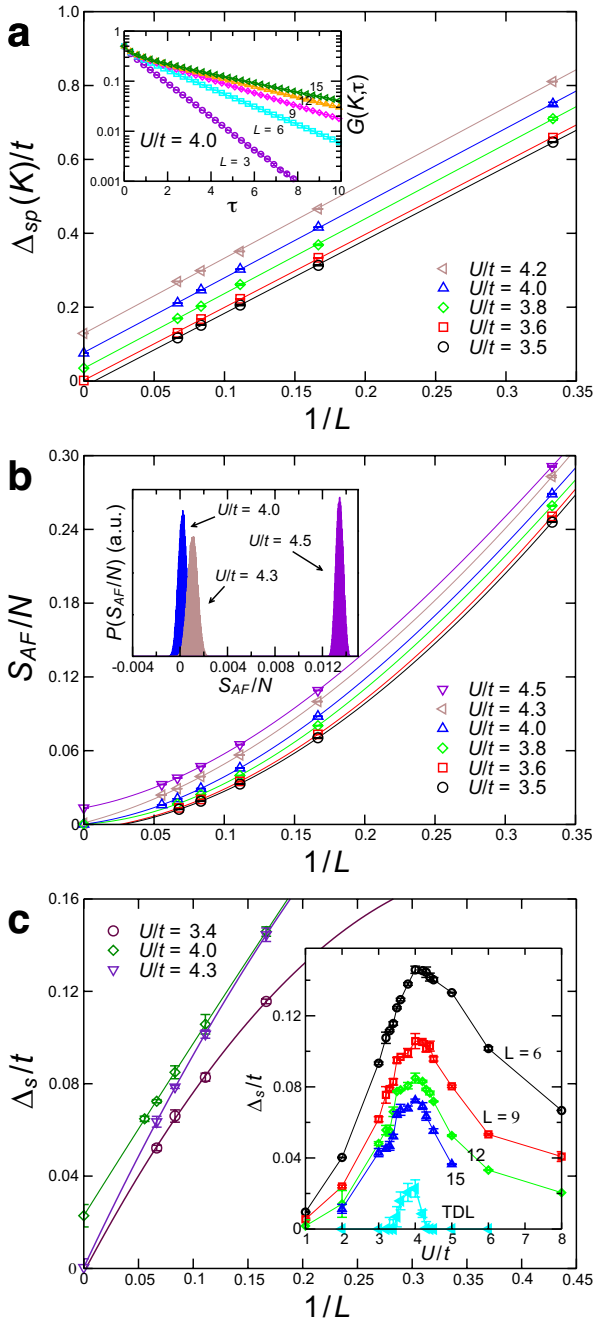

Fig. 4.2.: Finite size extrapolations of the excitation gaps and the antiferromagnetic structure factor. **a**, Single-particle gap at the Dirac point $\Delta_{sp}(K)$ for different values of U/t, linear in $1/L$. $\Delta_{sp}(K)$ is obtained by fitting the tail of the Green's function (inset) to the form $e^{-\tau\Delta_{sp}(K)}$. **b**, Antiferromagnetic structure factor S_{AF} for various values of U/t using 3rd order polynomials in $1/L$. AF order appears beyond $U/t = 4.3$, as seen in the histograms from a Monte Carlo bootstrapping analysis (inset). **c**, Spin gap Δ_s at different values of U/t, using 2nd order polynomials in $1/L$.

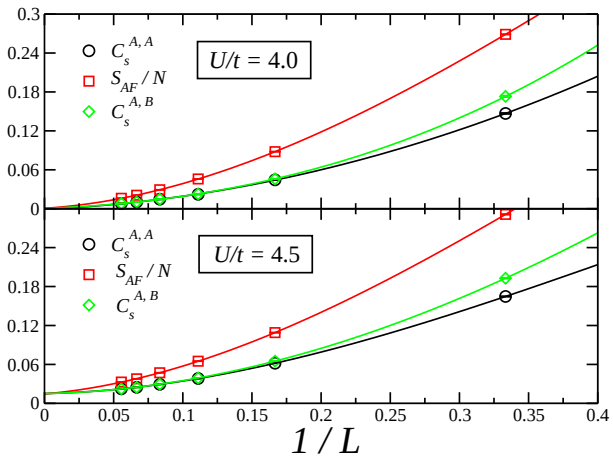

Fig. 4.3.: Comparison of the finite size scaling between the spin correlations $C_s^{A,A}$ and $C_s^{A,B}$ at the largest available distance and the staggered structure factor S_{AF} at $U/t = 4$ (upper panel) and $U/t = 4.5$ (lower panel), using 3rd order polynomials in $1/L$.

Spin correlations

The AF order at large values of U/t resides within the unit cell of the honeycomb lattice. Hence, the spin structure factor for AF order relates to the staggered spin correlations at the Γ point (cf. Sec. 1.1 for the notation in momentum space),

$$S_{AF} = \frac{1}{N}\Big\langle \Big[\sum_{\mathbf{r}} (\mathbf{S}_{\mathbf{r}A} - \mathbf{S}_{\mathbf{r}B})\Big]^2 \Big\rangle \,. \tag{4.8}$$

In addition to the above structure factor, we also probed directly the spin-spin correlation functions. In the following, for the correlation between two local operators O_1 and O_2, we employ a short notation for the cumulant,

$$\langle\langle O_1 O_2 \rangle\rangle := \langle O_1 O_2 \rangle - \langle O_1 \rangle \langle O_2 \rangle \,. \tag{4.9}$$

The spin-spin correlations

$$C_s^{a,b}(\mathbf{r}, \mathbf{r}') = \langle\langle \mathbf{S}_{\mathbf{r}a} \cdot \mathbf{S}_{\mathbf{r}'b} \rangle\rangle \,, \tag{4.10}$$

are measured at the largest available distance $\mathbf{d}_L = ([L/2+1]-1)\,\mathbf{a}_1 + ([L/2+1]-1)\,\mathbf{a}_2$ for different system sizes, and performed a finite size scaling of both $C_s^{A,A} = C_s^{A,A}(0, \mathbf{d}_L)$ and $C_s^{A,B} = -C_s^{A,B}(0, \mathbf{d}_L)$. A comparison of the scaling of these quantities to S_{AF} is shown for both $U/t = 4$ and $U/t = 4.5$ in Fig. 4.3, exhibiting the consistency between these different approaches to quantify the spin correlations in the ground state.

Figure 4.3 shows the QMC results together with a finite size extrapolation. The results of the latter are also presented in the phase diagram of Fig. 4.1 together with Fig. 4.2b. AF order appears beyond $U/t = 4.3$, a value that is consistent with previous

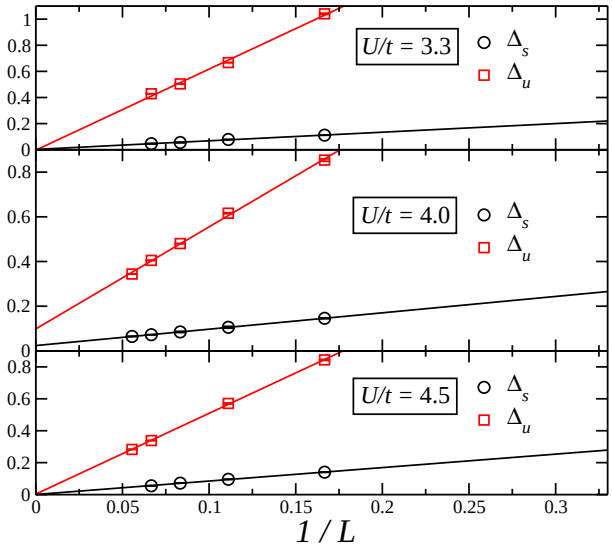

Fig. 4.4.: Comparison of the finite size scaling between the staggered spin gap Δ_s and the uniform spin gap Δ_u at $U/t = 3.3, 4$ and 4.5 (top to bottom). The extrapolated values in the thermodynamic limit for $U/t = 4$ are $\Delta_s = 0.023 \pm 0.007$ and $\Delta_u = 0.099 \pm 0.001$.

estimates for the onset of long-ranged AF order [184, 186, 185, 187]. This leaves an extended window $3.5 < U/t < 4.3$, within which the system is neither a SM, nor an AF MI.

Further details on the nature of this intermediate region are obtained by examining the spin excitation gap, extracted from the long-time behavior of the imaginary-time displaced spin-spin correlation function.

Spin excitation gaps

The gaps for spin excitations at momentum vector $\mathbf{k}$ are obtained from the imaginary-time displaced spin-spin correlation functions for both the staggered sector,

$$S_s(\mathbf{k}, \tau) = \langle\langle (\mathbf{S}_{\mathbf{k}A}(\tau) - \mathbf{S}_{\mathbf{k}B}(\tau)) \cdot (\mathbf{S}_{\mathbf{k}A}(0) - \mathbf{S}_{\mathbf{k}B}(0)) \rangle\rangle \ , \tag{4.11}$$

as well as the uniform sector,

$$S_u(\mathbf{k}, \tau) = \langle\langle (\mathbf{S}_{\mathbf{k}A}(\tau) + \mathbf{S}_{\mathbf{k}B}(\tau)) \cdot (\mathbf{S}_{\mathbf{k}A}(0) + \mathbf{S}_{\mathbf{k}B}(0)) \rangle\rangle \ , \tag{4.12}$$

where $\mathbf{S}_{\mathbf{k},a}(\tau) = \mathrm{e}^{\tau H} \mathbf{S}_{\mathbf{k},a} \mathrm{e}^{-\tau H}$. Similarly as for the single-particle gap, the spin excitation gaps are obtained from $S_s(\mathbf{k}, \tau) \propto \exp(-\tau \Delta_s(\mathbf{k}))$, and $S_u(\mathbf{k}, \tau) \propto \exp(-\tau \Delta_u(\mathbf{k}))$ at large imaginary time τ. The staggered spin gap $\Delta_s = \Delta_s(\Gamma)$ can be calculated directly via the staggered spin-spin correlations at the Γ point. However, since the total magnetization

$\mathbf{S}_{tot} = \mathbf{S}_{\Gamma A} + \mathbf{S}_{\Gamma B}$ commutes with the Hamiltonian of the system, $[\mathbf{S}_{tot}, H] = 0$, the uniform spin gap Δ_u cannot be extracted from the uniform spin-spin correlations at the Γ point in a canonical QMC simulation. Instead, one obtains $\Delta_u = \lim_{\mathbf{k}\to\Gamma} \Delta_u(\mathbf{k})$ from measurements performed at the finite momenta closest to the Γ point for each finite system.

We consider first the spin gap Δ_s, which vanishes inside the AF phase due to the emergence of two Goldstone modes, as well as in the gapless SM phase. Figure 4.2c shows finite size estimates of Δ_s for different values of U/t, along with an extrapolation to the TDL. A finite value of Δ_s persists within an intermediate parameter regime $3.5 < U/t < 4.3$, while it vanishes both within the SM and the AF phase. This dome in the spin gap is also seen in the inset of Fig. 4.2c, that displays both the finite-size data and the extrapolated values of Δ_s as a function of U/t.

The uniform gap Δ_u is found to be even larger than Δ_s inside the intermediate region (e.g., $\Delta_u = 0.099 \pm 0.001$ at $U/t = 4$), and vanishes in the SM and the AF phase. Hence, this intermediate insulating region corresponds to a spin-gap phase. Figure 4.4 shows the finite size data for these gaps at $U/t = 3.3, 4$ and 4.5. For $U/t = 4$, both gaps scale to finite values in the thermodynamic limit, with Δ_u being about four times as large as Δ_s. For the other two values of U/t, both gaps clearly vanish in the thermodynamic limit.

Kinetic energy density & double occupations

From analyzing the U-dependence of the kinetic energy density,

$$E_{\text{kin}} = \frac{1}{N}\langle -t \sum_{\langle i,j\rangle,\alpha} (c^\dagger_{i\alpha} c_{j\alpha} + c^\dagger_{j\alpha} c_{i\alpha})\rangle \,, \tag{4.13}$$

we obtain further insight into these different regimes and the emergence of local moments. As shown in Fig. 4.5, the curvature d^2E_{kin}/dU^2 changes sign near $U/t = 4.3$. This marks a characteristic change from the weak-coupling region of positive curvature with delocalized electrons to the strong-coupling AF region with negative curvature. In the latter region, localized spins form and order in an AF state. In the intermediate spin-gap region, fluctuations are large enough to still prevent the formation of well-localized magnetic moments. Note, that around $U/t = 3.5$, a change in the curvature can be observed, that adds to the already presented evidence for an intermediate phase. For completeness we also how the evolution of the double occupation with U/t in Fig. 4.6. The same discussion carried out on the kinetic energy above could also be performed by looking the first derivative of the double occupations $d(n_\uparrow n_\downarrow)/dU$.

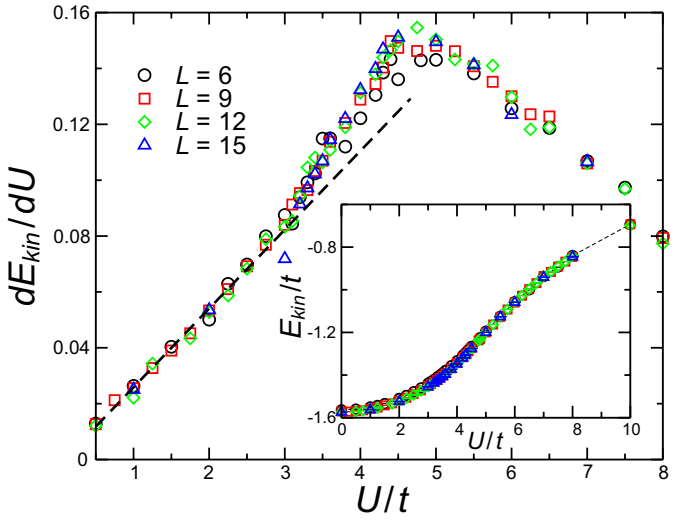

Fig. 4.5.: Derivative dE_{kin}/dU of the kinetic energy density as a function of U/t for systems of different sizes. The dashed line is a fit to the low-U behavior. The inset shows the QMC data for the kinetic energy density E_{kin} from which the derivative is obtained by numerical differentiation. Statistical errors are smaller than the symbol size.

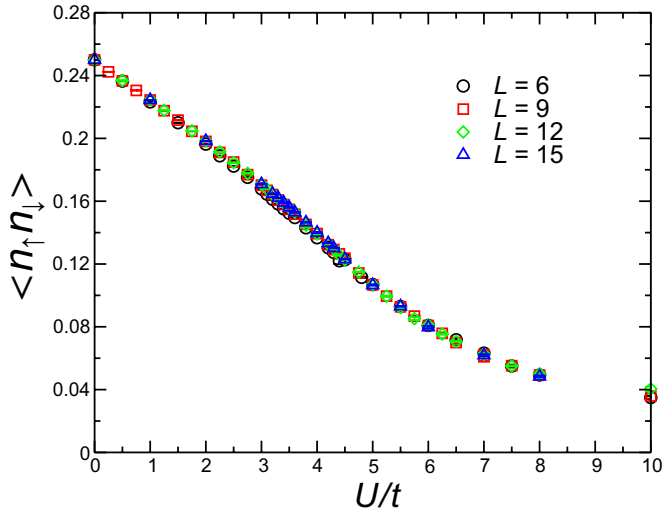

Fig. 4.6.: Derivative of the double occupation as a function of U/t for systems of different sizes.

4.2.2. Characterization of the spin-gap phase

The observation of a finite spin gap rules out a gapless spin-liquid [141, 157], quantum spin Hall states [179], as well as triplet superconductivity [181]. The remaining possibilities can be enumerated by considering the coupling to order parameters that lead to the opening of a mass gap in Dirac fermions [188], and hence account for the single-particle gap observed in the QMC data: (i) singlet superconductivity, (ii) a quantum Hall state (QHS) [189], (iii) charge density wave (CDW) order [179] and (iv) a valence bond crystal (VBC).

Flux quantization and measurements to test for superconductivity

In order to assess if superconductivity arises in the vicinity of the Mott transition, we used the method of flux quantization which probes the superfluid density and is hence independent of the specific symmetry of the pair wave function [190, 191, 192] – details are given in App. A.4.

In the flux quantization measurement, we thread a magnetic flux Φ, in units of the flux quantum Φ_0, through the center of a torus on which the electronic system lies. From the functional form of the ground state energy with respect to the threaded flux, $E_0(\Phi/\Phi_0)$, we can distinguish between normal and superconducting ground states. The signature of the latter requires that the macroscopic energy difference $E_0(\Phi/\Phi_0) - E_0(\Phi/\Phi_0 = 1/2)$ scales in the thermodynamic limit to a periodic function of period $1/2$, and the occurrence of an energy barrier between $\Phi/\Phi_0 = 0$ and $\Phi/\Phi_0 = 1/2$. In contrast, a metallic phase is characterized by $E_0(\Phi/\Phi_0) - E_0(\Phi/\Phi_0 = 1/2)$ vanishing as a power law as a function of system size, while in an insulating phase, it would vanish exponentially.

Let us use an analogy (or better an argument from topology) to put the rather complex idea of phase dependance into a simple example, which demonstrates the phase structure in the case of a superconducting current [142]: Imagine your (closed) belt to be a room-temperature superconducting ring. Each point in the ring can be associated associated with a phase or an angle. Now, since super-currents can only run if there is a phase-twist, open the belt, twist one of the endings (doesn't matter how often) and close the belt again. In whichever way you bend and twine your superconducting ring – uhm, belt – you will never get rid of the twist. That is in simple words why a superconducting current never stops.

The superconducting state corresponds to a system spanning, macroscopic wave function. In contrast, insulators are gapped with short range correlations and a localized wave function (An exception to that statement are topological insulator which are believed to have long-range entangled ground states). The superconducting state would hence *feel* the energy barrier – super-currents are trapped and cannot dribble away.

Figure 4.7 compares the QMC results of the macroscopic energy difference at $U = 0$

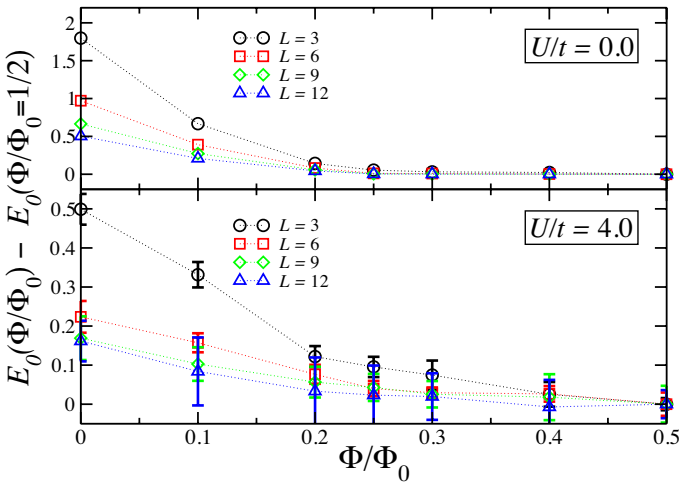

Fig. 4.7.: The energy difference of $E_0(\Phi/\Phi_0) - E(\Phi/\Phi_0 = 1/2)$ for different system sizes at $U/t = 0$ and $U/t = 4$. Note that the scale for $U/t = 4$ is four times smaller than for $U/t = 0$. The flattening of the energy differences exclude the superconducting ground state at both $U/t = 0$ and $U/t = 4$.

with that at $U/t = 4$. In both cases one clearly observes the vanishing of this quantity in the thermodynamic limit. Hence, no signal for superconductivity is obtained from these flux quantization measurements.

In addition, we measured pair correlations, ruling out superconductivity in (extended) s-, p-, d-, and f-wave channels. Order parameters for superconductivity are in principle obtained from considering the irreducible representations of the D_6 point group of the honeycomb lattice, which can be described as a triangular lattice with a basis of two atoms in the sublattices A and B, respectively. For the following, it is convenient to repeat the three lattice vectors related to the three nearest neighbor bonds $\boldsymbol{\delta} = \{\mathbf{0}, -\mathbf{a}_2, \mathbf{a}_1 - \mathbf{a}_2\}$, (cf. Sec. 1.1) and introduce the vectors

$$\boldsymbol{\delta}'_1 = \mathbf{a}_2, \quad \boldsymbol{\delta}'_2 = \mathbf{a}_2 - \mathbf{a}_1, \quad \boldsymbol{\delta}'_3 = -\mathbf{a}_1, \quad \boldsymbol{\delta}'_4 = -\boldsymbol{\delta}'_1, \quad \boldsymbol{\delta}'_5 = -\boldsymbol{\delta}'_2, \quad \boldsymbol{\delta}'_6 = -\boldsymbol{\delta}'_3,$$

connecting a given lattice site to its six next-nearest neighboring lattice sites.

The Cooper pair wave function of a superconducting state is a product of a spin, orbital and a sublattice component. Since Pauli's principle requires the wave function to be antisymmetric under particle exchange, we obtain the following possibilities for spin-singlet pairing: for an even (odd) orbital part, the wave function must be symmetric (antisymmetric) under sublattice exchange. It is convenient to introduce pair creation operators in the singlet channel

$$\Delta^\dagger(\mathbf{r}, a; \mathbf{r}', b) = c^\dagger_{\mathbf{r}a\uparrow} c^\dagger_{\mathbf{r}'b\downarrow} - c^\dagger_{\mathbf{r}a\downarrow} c^\dagger_{\mathbf{r}'b\uparrow} \,, \tag{4.14}$$

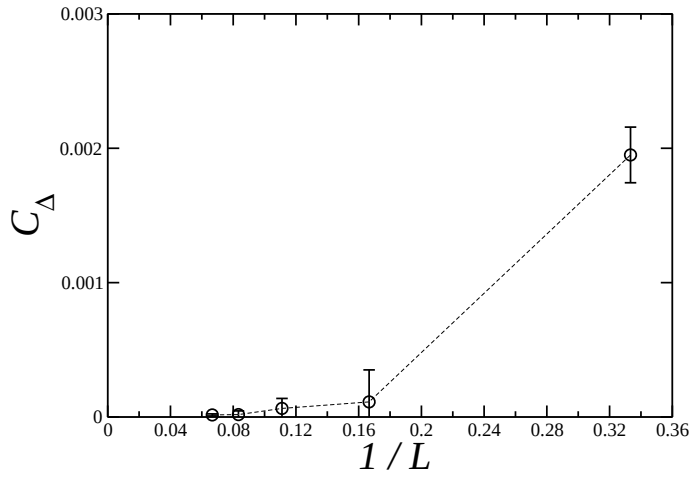

Fig. 4.8.: Finite size scaling of on-site s-wave pairing correlation C_Δ at $U/t = 4$.

where $a, b \in \{A, B\}$. The operator

$$\Delta_s^\dagger(\mathbf{r}) = \frac{1}{2}(\Delta^\dagger(\mathbf{r}, A; \mathbf{r}, A) + \Delta^\dagger(\mathbf{r}, B; \mathbf{r}, B)) \; , \tag{4.15}$$

describes on-site s-wave pairing, which is symmetric under sublattice exchange. In Fig. 4.8, we show the s-wave pair-pair correlation function $C_\Delta = |\langle \Delta_s(0)\Delta_s^\dagger(\mathbf{d}_L)\rangle|$ at the largest distance at $U/t = 4$. No long-ranged pairing correlation sustains to the thermodynamic limit; instead, the on-site pair-pair correlation function decreases rapidly.

Extended pair creation operators based on nearest neighbor pairing can be expressed in terms of phase factors f_1^a, f_2^a, f_3^a, $a \in \{A, B\}$,

$$\Delta^\dagger(\mathbf{x}, f_1^A, f_2^A, f_3^A, f_1^B, f_2^B, f_3^B) = \sum_{i=1}^{3} [f_i^A \Delta^\dagger(\mathbf{r}, A; \mathbf{r} + \boldsymbol{\delta}_i, B) + f_i^B \Delta^\dagger(\mathbf{r}, B; \mathbf{r} - \boldsymbol{\delta}_i, A)] \; . \tag{4.16}$$

For an extended s-wave,

$$\Delta_{\text{ext-}s}^\dagger(\mathbf{r}) = \Delta^\dagger(\mathbf{r}, 1, 1, 1, 1, 1, 1) \; . \tag{4.17}$$

Nearest neighbor p-wave states relate to

$$\Delta_{p_x}^\dagger(\mathbf{r}) = \Delta^\dagger(\mathbf{r}, 0, +1, -1, 0, -1, +1) \; , \tag{4.18}$$

$$\Delta_{p_y}^\dagger(\mathbf{r}) = \Delta^\dagger(\mathbf{r}, 0, +1, +1, 0, -1, -1) \; , \tag{4.19}$$

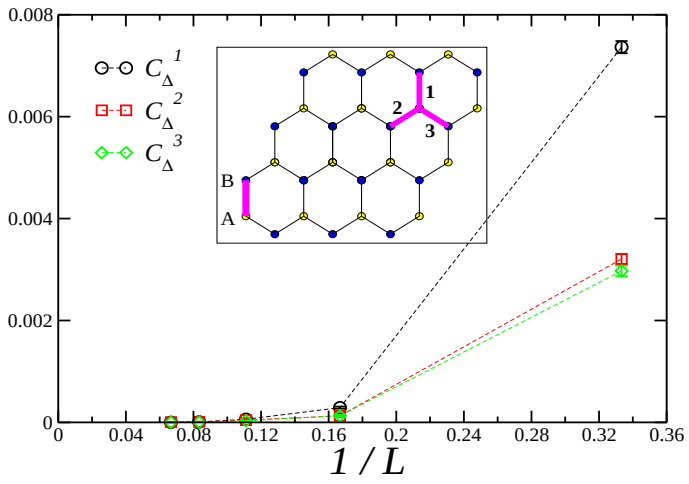

Fig. 4.9.: Finite size scaling of nearest neighbor pair correlation C^i_Δ at $U/t = 4$. The inset illustrates the three inequivalent directions with respect to the reference bond marked by AB.

and nearest neighbor d-wave states to

$$\Delta^\dagger_{d_{xy}}(\mathbf{r}) = \Delta^\dagger(\mathbf{r}, 0, +1, -1, 0, +1, -1) , \tag{4.20}$$

$$\Delta^\dagger_{d_{x^2-y^2}}(\mathbf{r}) = \Delta^\dagger(\mathbf{r}, -2, +1, +1, -2, +1, +1) . \tag{4.21}$$

In terms of next-nearest neighbors, one furthermore obtains the singlet f-wave state

$$\Delta^\dagger_f(\mathbf{r}) = \sum_{j=i}^{6} (-1)^i [\Delta^\dagger(\mathbf{r}, A; \mathbf{r} + \mathbf{r}_i, A) - \Delta^\dagger(\mathbf{r}, B; \mathbf{r} + \mathbf{r}_i, B)] . \tag{4.22}$$

In order to probe for superconductivity based on nearest neighbor or next-nearest neighbor pairing in the above symmetry sectors, we directly measured in real-space the various inequivalent pair-pair correlation functions at the largest distances on the finite lattices,

$$C^i_\Delta = |\langle\langle \Delta(0, A; 0, B) \Delta^\dagger(\mathbf{d}_L, A; \mathbf{d}_L + \boldsymbol{\delta}_i, B) \rangle\rangle| , \quad i = 1, 2, 3, \tag{4.23}$$

for the nearest neighbor pairing states, and

$$C^{AA,i}_\Delta = |\langle\langle \Delta(0, A; \boldsymbol{\delta}_1, A) \Delta^\dagger(\mathbf{d}_L, A; \mathbf{d}_L + \boldsymbol{\delta}_i, A) \rangle\rangle| \tag{4.24}$$

$$C^{AB,i}_\Delta = |\langle\langle \Delta(0, A; \boldsymbol{\delta}_1, A) \Delta^\dagger(\mathbf{d}_L, B; \mathbf{d}_L + \boldsymbol{\delta}_i, B) \rangle\rangle| , \quad i = 1, ..., 6, \tag{4.25}$$

for next-nearest neighbor pairing states both within the same sublattice and between the two sublattices. As shown in Fig. 4.9 and Fig. 4.10, both nearest neighbor and next-nearest neighbor pair-pair correlation functions are very weak, even reaching zero within

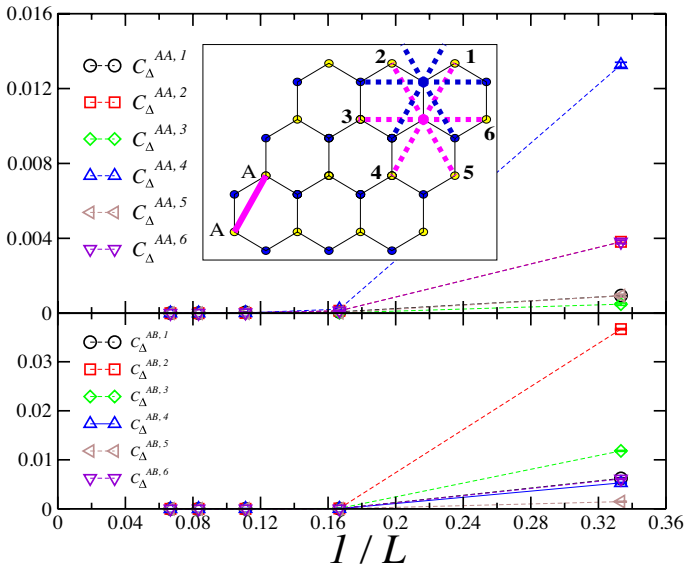

Fig. 4.10.: Finite size scaling of the next-nearest neighbor pair correlations $C_\Delta^{AA,j}$ and $C_\Delta^{AB,j}$ at $U/t = 4$. The inset illustrates the inequivalent directions with respect to the reference bond marked by AA, with the lower (upper) star corresponding to equal (different) sublattices.

statistical errors for $L \geq 9$. From this, we exclude pairing in all the above symmetry sectors, since the full Cooper pair correlations $\langle \Delta_{ext.-s}(0)\Delta^\dagger_{ext.-s}(\mathbf{d}_L)\rangle$, $\langle \Delta_{p_x}(0)\Delta^\dagger_{p_x}(\mathbf{d}_L)\rangle$, $\langle \Delta_{p_y}(0)\Delta^\dagger_{p_y}(\mathbf{d}_L)\rangle$, $\langle \Delta_{d_{xy}}(0)\Delta^\dagger_{d_{xy}}(\mathbf{d}_L)\rangle$, $\langle \Delta_{d_{x^2-y^2}}(0)\Delta^\dagger_{d_{x^2-y^2}}(\mathbf{d}_L)\rangle$, and $\langle \Delta_f(0)\Delta^\dagger_f(\mathbf{d}_L)\rangle$ are linear superpositions of the above pair-pair correlation functions, and hence vanish in the thermodynamic limit.

Both, flux quantization as well as a direct measurement of pair correlations lead to no sign of superconductivity. We can thus exclude superconductivity in the half-filled Hubbard model on the honeycomb lattice in the intermediate phase.

Currents, bond and density correlations in the charge sector

Charge density wave (CDW) order and quantum Hall states (QHS), or charge currents, trigger a breaking of the sub-lattice symmetry and thereby open a mass gap at the mean-field level. To exclude these effects as the cause for the spin-gapped phase we first measure the density-density correlation function, which is given by

$$C_d^{a,b}(\mathbf{r},\mathbf{r}') = \langle\langle n_{\mathbf{r}a} n_{\mathbf{r}'b}\rangle\rangle \,, \tag{4.26}$$

where $a, b \in \{A, B\}$. At half-filling, $\langle n_{\mathbf{r}a}\rangle = \langle n_{\mathbf{r}b}\rangle = 1$. Figure 4.11 shows the finite size scaling of the density correlations at the largest distance, $C_d^{A,A} = |C_d^{A,A}(0,\mathbf{d}_L)|$ and $C_d^{A,B} = |C_d^{A,B}(0,\mathbf{d}_L)|$ at $U/t = 4$. Both scale to zero in the thermodynamic limit, and

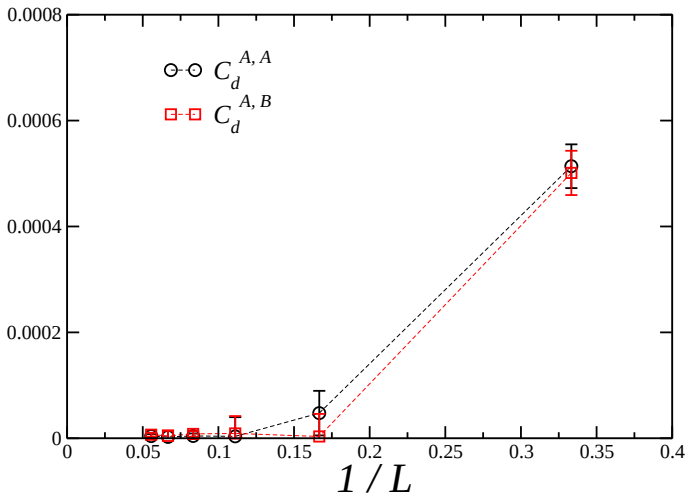

Fig. 4.11.: Finite size scaling of the density correlation functions $C_d^{A,A}$ and $C_d^{A,B}$ at $U/t = 4$.

no long-range density correlations persist. Furthermore, in comparison with the spin correlations, the density correlations are seen to be significantly weaker and essentially zero within the statistical error for system sizes $L \geq 9$. Consistently, we also find no long-range density ordering when analyzing the density structure factor (not shown).

Next, we present our results on the dimer-dimer correlations in the charge sector. We measured both the correlations between the kinetic energy bond operators and the current operators. Correlations between the kinetic energy bond operators

$$k(\mathbf{r}, a; \mathbf{r}', b) = \sum_{\alpha} (c^{\dagger}_{\mathbf{r}a\alpha} c_{\mathbf{r}'b\alpha} + c^{\dagger}_{\mathbf{r}'b\alpha} c_{\mathbf{r}a\alpha}) \,, \tag{4.27}$$

and the current operators

$$j(\mathbf{r}, a; \mathbf{r}', b) = -i \sum_{\alpha} (c^{\dagger}_{\mathbf{r}a\alpha} c_{\mathbf{r}'b\alpha} - c^{\dagger}_{\mathbf{r}'b\alpha} c_{\mathbf{r}a\alpha}) \,, \tag{4.28}$$

can be defined between both nearest-neighbor and next-nearest neighbor sites on the honeycomb lattice.

To probe for VBC-like order in the kinetic energy sector, we measured the three inequivalent dimer-dimer correlation functions

$$C^i_k = |\langle\langle k(0, A; 0, B) k(\mathbf{d}_L, A; \mathbf{d}_L + \boldsymbol{\delta}_i, B) \rangle\rangle| \,, \quad i = 1, 2, 3, \tag{4.29}$$

at the largest distance $\mathbf{d}_L$ on the finite lattices. For an illustration of the different relative bond orientations, see the inset of Fig. 4.12. The upper panel of Fig. 4.12 shows the finite size scaling of the C^i_k at $U/t = 4$. These correlations scale to zero in the

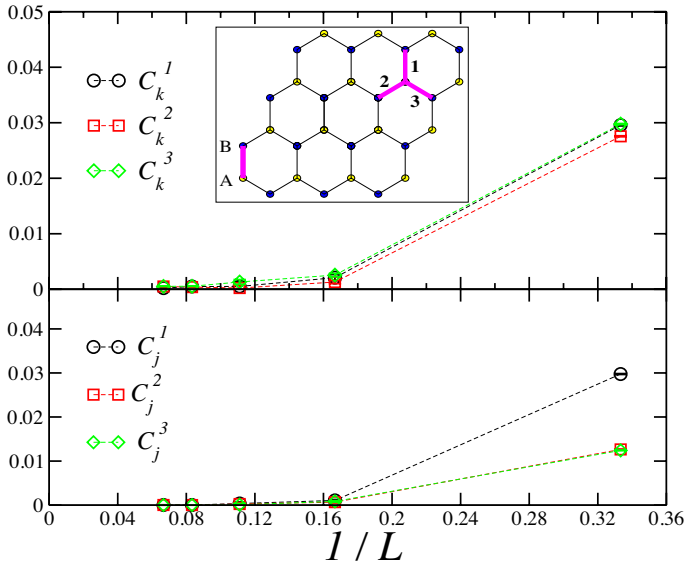

Fig. 4.12.: Finite size scaling of the nearest-neighbor correlations C_k^i and C_j^i at $U/t = 4$. The inset illustrates the three inequivalent directions with respect to the reference bond marked by AB.

thermodynamic limit, hence no long-ranged bond order in the kinetic energy persists. Furthermore, in comparison with the spin correlations, these correlations are also seen to be significantly weaker.

To probe for the persistence of nearest-neighbor currents in the ground state, we measured the current-current correlation functions between the bonds of the honeycomb lattice

$$C_j^i = |\langle\langle j(0,A;0,B) j(\mathbf{d}_L,A;\mathbf{d}_L+\boldsymbol{\delta}_i,B)\rangle\rangle| \,, \quad i=1,2,3, \tag{4.30}$$

at the largest distance $\mathbf{d}_L$ on the finite lattices. The corresponding finite size scalings are shown in the lower panel of Fig. 4.12. Again, long range correlations in the thermodynamic limit can be clearly excluded, indicating the absence of currents between nearest neighbor sites in the ground state.

To probe for bond order and currents between next-nearest neighbor sites, we measured all inequivalent next-nearest neighbor bond-bond and current-current correlation functions at the largest distances both within the same sublattice and between the two sublattices,

$$C_k^{AA,i} = |\langle\langle k(0,A;\boldsymbol{\delta}_1',A) k(\mathbf{d}_L,A;\mathbf{d}_L+\boldsymbol{\delta}_i',A)\rangle\rangle| \,, \tag{4.31}$$

$$C_j^{AA,i} = |\langle\langle j(0,A;\boldsymbol{\delta}_1',A) j(\mathbf{d}_L,A;\mathbf{d}_L+\boldsymbol{\delta}_i',A)\rangle\rangle| \,, \tag{4.32}$$

$$C_k^{AB,i} = |\langle\langle k(0,A;\boldsymbol{\delta}_1',A) k(\mathbf{d}_L,B;\mathbf{d}_L+\boldsymbol{\delta}_i',B)\rangle\rangle| \,, \tag{4.33}$$

$$C_j^{AB,i} = |\langle\langle j(0,A;\boldsymbol{\delta}_1',A) j(\mathbf{d}_L,B;\mathbf{d}_L+\boldsymbol{\delta}_i',B)\rangle\rangle| \,, \quad i=1,...,6. \tag{4.34}$$

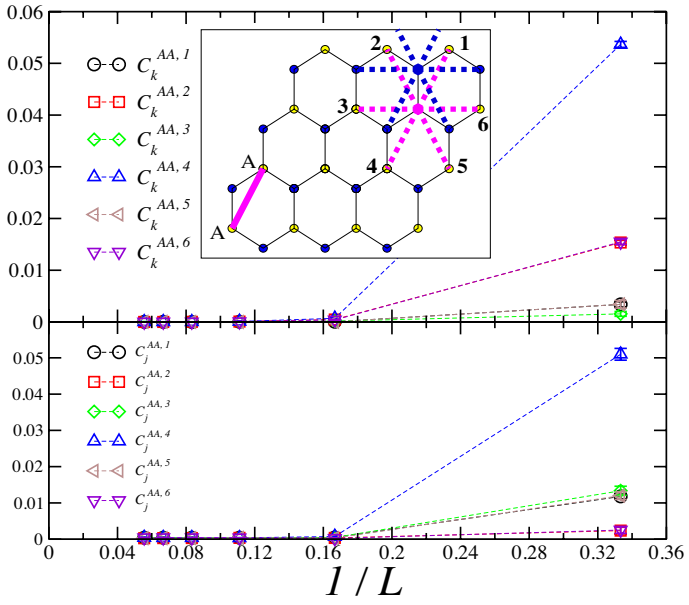

Fig. 4.13.: Finite size scaling of the next-nearest neighbor correlations $C_k^{AA,i}$ and $C_j^{AA,i}$ at the largest distance at $U/t = 4$. The inset illustrates the inequivalent directions with respect to the reference bond marked by AA, with the lower (upper) star corresponding to equal (different) sublattices.

The QMC data for the correlations within the same sublattice at $U/t = 4$ are shown in Fig. 4.13. Both $C_k^{AA,i}$ and $C_j^{AA,i}$ all scale to zero in the thermodynamic limit. The corresponding correlations between the two sublattices similarly decay to zero in the thermodynamic limit (not shown). Thus neither bond ordering nor currents persist between next-nearest neighbor sites in the ground state at $U/t = 4$.

The lack of order in the charge sector rules out the breaking of sublattice and time reversal symmetries, as required for the QHS, in the pristine Hubbard model. Possibly, extensions of the form of next-nearest neighbor Coulomb interactions, or spin-orbit coupling are necessary to reach such a state [179, 189].

Dimer-dimer, spin-currents and spin-bond correlations

To examine the occurrence of a VBC, we probed for dimer-dimer correlations between separated dimers formed by nearest neighbor bonds $\langle ij \rangle$ and $\langle kl \rangle$. We measured the dimer-dimer correlation functions

$$D_{ij,kl} = \langle\langle (\mathbf{S}_i \cdot \mathbf{S}_j - \frac{1}{4})(\mathbf{S}_k \cdot \mathbf{S}_l - \frac{1}{4}) \rangle\rangle \, , \tag{4.35}$$

Figure 4.14 shows the results of the correlation between singlet dimers at $U/t = 4.0$. The striped bond is the one with respect to which correlations were determined. Positively

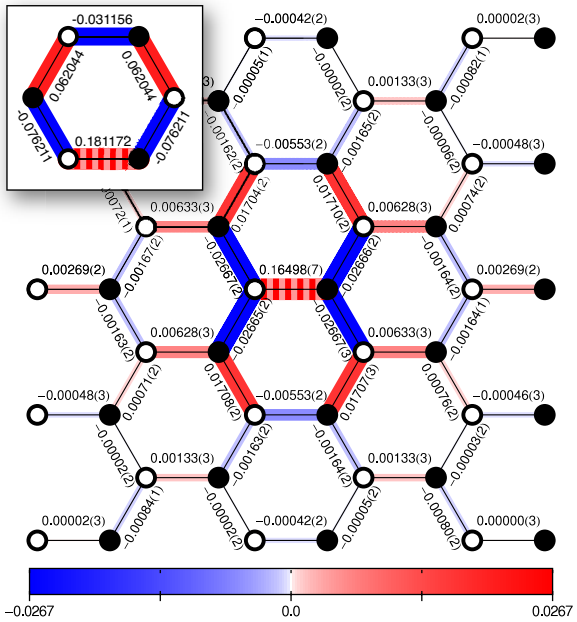

Fig. 4.14.: Real space plot of the spin dimer-dimer correlations. The correlation function $D_{ij,kl}$ (cf. SI) for a $L = 6$ system at $U/t = 4$, together with the same correlation for the isolated Hubbard hexagon also at $U/t = 4$ (inset). The reference bonds are dressed with stripes. Numbers in parenthesis indicate the standard error of the last digit.

correlated bonds will be present at the same time with the reference bond and negative correlations correspond to bonds which are unlikely to exist when there is a bond at the reference location. The correlations are found to be short-ranged, and consistent with the dominance of a RVB state within the hexagons of the honeycomb lattice [128]. This can be seen by comparing the singlet-correlations with those of an isolated hexagon (inset Fig. 4.14), the classical example of the resonance phenomenon in conjugated π-electrons [193]. Accordingly, we find no long-ranged order from the dimer-dimer structure factors in Fourier space. Our results thus reveal a genuinely exotic state of matter, where no spontaneous symmetry breaking is observed, while a spin-gap is present. It corresponds to a spin-liquid RVB state in the intermediate coupling regime in the vicinity of the Mott transition.

We furthermore measured correlations between the spin-current operators

$$j_s(\mathbf{r}, a; \mathbf{r}', b) = -i \sum_{\alpha} (-1)^{\alpha} (c^{\dagger}_{\mathbf{r}a\alpha} c_{\mathbf{r}'b\alpha} - c^{\dagger}_{\mathbf{r}'b\alpha} c_{\mathbf{r}a\alpha}) \,, \tag{4.36}$$

as well as the spin-bond operators

$$k_s(\mathbf{r}, a; \mathbf{r}', b) = \sum_{\alpha} (-1)^{\alpha} (c^{\dagger}_{\mathbf{r}a\alpha} c_{\mathbf{r}'b\alpha} + c^{\dagger}_{\mathbf{r}'b\alpha} c_{\mathbf{r}a\alpha}) \,, \tag{4.37}$$

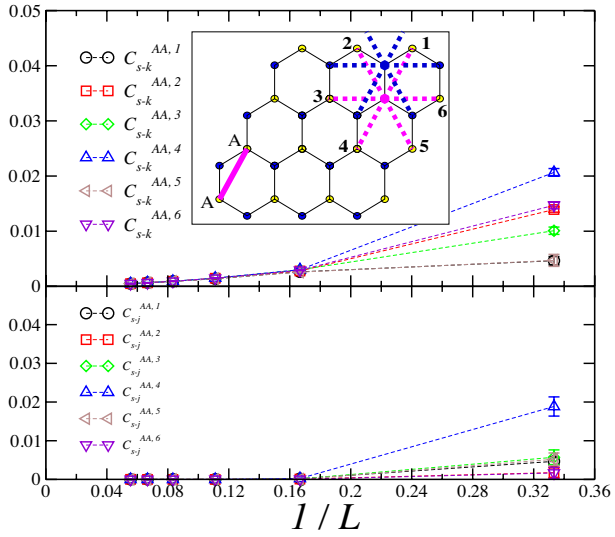

Fig. 4.15.: Finite size scaling of the next-nearest neighbor correlations $C_{s-k}^{AA,i}$ and $C_{s-j}^{AA,i}$ at the largest distance at $U/t = 4$. The inset illustrates the inequivalent directions with respect to the reference bond marked by AA, with the lower (upper) star corresponding to equal (different) sublattices.

for next-nearest neighbor sites. We measured these correlations between all inequivalent pairs of next-nearest neighbor sites both within the same sublattice and between the two sublattices at the largest distance on the finite lattices,

$$C_{s-k}^{AA,i} = |\langle\langle k_s(0,A;\boldsymbol{\delta}_1',A)k_s(\mathbf{d}_L,A;\mathbf{d}_L+\boldsymbol{\delta}_i',A)\rangle\rangle| \,, \tag{4.38}$$

$$C_{s-j}^{AA,i} = |\langle\langle j_s(0,A;\boldsymbol{\delta}_1',A)j_s(\mathbf{d}_L,A;\mathbf{d}_L+\boldsymbol{\delta}_i',A)\rangle\rangle| \,, \tag{4.39}$$

$$C_{s-k}^{AB,i} = |\langle\langle k_s(0,A;\boldsymbol{\delta}_1',A)k_s(\mathbf{d}_L,B;\mathbf{d}_L+\boldsymbol{\delta}_i',B)\rangle\rangle| \,, \tag{4.40}$$

$$C_{s-j}^{AB,i} = |\langle\langle j_s(0,A;\boldsymbol{\delta}_1',A)j_s(\mathbf{d}_L,B;\mathbf{d}_L+\boldsymbol{\delta}_i',B)\rangle\rangle| \,, \quad i=1,..,6. \tag{4.41}$$

Figure 4.15 shows the finite size scaling of the correlations within the same sublattice at $U/t = 4$. They all decay to zero in the thermodynamic limit. The corresponding correlations between different sublattices show a similar behavior (not shown). Thus neither spin-bond order nor spin-currents persist between next-nearest neighbor sites in the ground state at $U/t = 4$.

Order parameters for spin-nematicity

The Néel state is a uniaxial magnet in which SU(2) is partially broken down to U(1), resulting in Goldstone modes. More complete SU(2) breaking schemes exist in non-collinear magnets with more than two ferromagnetic sublattices or more generally in helicoidal antiferromagnets. In these systems SU(2) symmetry is completely broken

with three Goldstone modes and the order parameter can be described as biaxial (or as a gyro) [123]. Spin-nematic phases introduced by Andreev and Grishchuk [194] with no net magnetic moment break SU(2) symmetry as spins are correlated in a plane but individual spins remain disordered. The signature of nematicity (quadrupolar-order, octupolar-order, ...) is the breaking of rotational (point group) symmetry without breaking the translational symmetry of the lattice.

Neither the spin correlations, nor the AF structure factor yielded signatures of SU(2) symmetry breaking. However, these measurements test for AF order with the unit cell only, which still allows for non-collinear order with a point group symmetry other than the one tested in the spin correlations. To probe for nematic order, we measured the correlations of the operators

$$Q^{xy}(\mathbf{r}, a; \mathbf{r}', b) = \frac{1}{2}(S^x_{\mathbf{r}a} S^y_{\mathbf{r}b} + S^y_{\mathbf{r}'a} S^x_{\mathbf{r}'b}) \ , \tag{4.42}$$

for the **n**-type nematics and

$$V(\mathbf{r}, a; \mathbf{r}', b) = \mathbf{S}_{\mathbf{r},a} \times \mathbf{S}_{\mathbf{r}',b} \ , \tag{4.43}$$

for the **p**-type nematics [194] in real-space at the largest distances on the finite lattices,

$$\begin{aligned} C^i_Q &= |\langle\langle Q^{xy}(0, A; 0, B) Q^{xy}(\mathbf{d_L}, A; \mathbf{d_L} + \boldsymbol{\delta}_i, B)\rangle\rangle| \ , \\ C^i_V &= |\langle V(0, A; 0, B) V(\mathbf{d_L}, A; \mathbf{d_L} + \boldsymbol{\delta}_i, B)\rangle| \\ &= |\langle (\mathbf{S}_{0,A} \cdot \mathbf{S}_{\mathbf{d_L},A})(\mathbf{S}_{0,B} \cdot \mathbf{S}_{\mathbf{d_L}+\boldsymbol{\delta}_i,B}) - (\mathbf{S}_{0,A} \cdot \mathbf{S}_{\mathbf{d_L}+\boldsymbol{\delta}_i,B})(\mathbf{S}_{0,B} \cdot \mathbf{S}_{\mathbf{d_L},A})\rangle| \ , \end{aligned} \tag{4.44}$$

$i = 1, 2, 3$.The upper panel of Fig. 4.16 displays the behavior of C^i_Q and the lower panel displays that of C^i_V, for system size $L = 3, 6, 9, 12$ at $U/t = 4$. These correlations are very weak, reaching zero within statistical errors for $L \geq 12$. Thus, we exclude the possibility of spin-nematic states inside the intermediate coupling regime.

4.2.3. Further insight into the RVB state

The QMC results presented above uncover the realization of a quantum spin-liquid state with short-range RVB correlations in correlated fermions on a non-frustrated, bipartite lattice. In principle, such quantum-disordered states can occur in different flavors as described in Sec. 4.1.2. The observation of a finite spin-gap is consistent with the characterization of the observed spin-liquid in terms of short-range RVB states [78, 79, 139, 112, 148], also in accordance with the observed short-ranged dimer-dimer correlations. Short-range RVB states are modeled in general by quantum dimer models [112, 148, 149], which fall into the class of Z_2 spin liquids. Fully gapped phases of quantum dimer models are furthermore characterized by a non-trivial topological order, implying e.g., an emerging ground state degeneracy of two-dimensional systems with periodic boundary conditions in the TDL [155, 149].

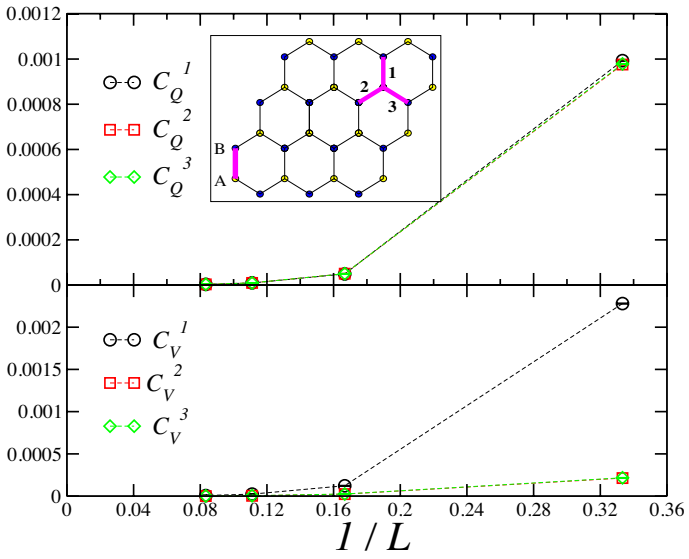

Fig. 4.16.: Finite size scaling of the nearest neighbor correlations C_Q^i and C_V^i at the largest distance at $U/t = 4$. The inset illustrates the inequivalent directions with respect to the reference bond marked by AB.

In order to assess, whether topological order can characterize the short-range RVB in our case, we examine the low-energy singlet excitations. As proven in an exact theorem by Lieb [195], the finite systems used in our numerical simulations have a non-degenerate singlet ground state for any finite value of $U > 0$. Hence, degeneracy can only appear in the TDL. If so, low-energy singlet states should be present, with decreasing excitation energy as the system size increases. Since our QMC method projects out the finite system's ground state from a singlet trial wavefunction, we can monitor the expectation value of the internal energy $E(\Theta)$, where Θ is the projection parameter (cf. Sec. 1.2). Here all contributions from singlet states with the same quantum numbers as the ground state are included, that have a finite overlap with the trial wave function.

We consider the internal energy as a function of the projection parameter Θ,

$$E(\Theta) = \frac{\langle \Psi_T | \mathrm{e}^{-\Theta H/2} H \mathrm{e}^{-\Theta H/2} | \Psi_T \rangle}{\langle \Psi_T | \mathrm{e}^{-\Theta H} | \Psi_T \rangle} \,, \tag{4.45}$$

where $|\Psi_T\rangle$ is the trial wave function (cf. Sec. 1.2). Let $\{|n\rangle\}$ be the set of eigenstates of H. Then, we have

$$E(\Theta) - E_0 = \frac{1}{1 + R(\Theta)} \sum_{n>0} \mathrm{e}^{-(E_n - E_0)\Theta} (E_n - E_0) \frac{|\langle n | \Psi_T \rangle|^2}{|\langle 0 | \Psi_T \rangle|^2} \,, \tag{4.46}$$

where E_0 is the ground state energy, $|0\rangle$ the ground state, and define

$$R(\Theta) = \sum_{n>0} \mathrm{e}^{-(E_n - E_0)\Theta} \frac{|\langle n|\Psi_T\rangle|^2}{|\langle 0|\Psi_T\rangle|^2} \,. \tag{4.47}$$

Next, we consider an energy scale

$$\epsilon \ll (E_1 - E_0)/N \,, \tag{4.48}$$

where E_1 is the energy of the first excited singlet and the singlet gap $\Delta_{\mathrm{singlet}} = (E_1 - E_0)$, with the same quantum numbers as the ground state, and define Θ^*, such that for $\Theta > \Theta^*$, $(E(\Theta) - E_0)/N < \epsilon$. Typically, ϵ can be taken of the order of the statistical error in the energy, such that the condition on ϵ is clearly fulfilled. However, ϵ is not defined in terms of the statistical errors; the only defining condition on ϵ is (4.48). With such a definition we have

$$\epsilon = \frac{1}{N} \sum_{n>0} \frac{\mathrm{e}^{-(E_n - E_0)\Theta^*}}{1 + R(\Theta^*)} (E_n - E_0) \frac{|\langle n|\Psi_T\rangle|^2}{|\langle 0|\Psi_T\rangle|^2} \ll \Delta_{\mathrm{singlet}}/N \,, \tag{4.49}$$

such that

$$\frac{R(\Theta^*)}{1 + R(\Theta^*)} < \sum_{n>0} \frac{\mathrm{e}^{-(E_n - E_0)\Theta^*}}{1 + R(\Theta^*)} \frac{(E_n - E_0)}{\Delta_{\mathrm{singlet}}} \frac{|\langle n|\psi_T\rangle|^2}{|\langle 0|\psi_T\rangle|^2} \ll 1 \,, \tag{4.50}$$

so that it also holds that $R(\Theta^*) \ll 1$. The last inequality also implies that

$$\mathrm{e}^{-\Delta_{\mathrm{singlet}}\Theta^*} \frac{|\langle 1|\Psi_T\rangle|^2}{|\langle 0|\Psi_T\rangle|^2} \ll 1 \,, \tag{4.51}$$

since the sum in $R(\Theta)$ consists of positive definite terms.In case the overlaps in the last inequality are finite,

$$\Delta_{\mathrm{singlet}}\Theta^* \gg 1 \,, \tag{4.52}$$

such that $1/\Theta^*$ provides a lower bound for the singlet gap. In case $|\langle 1|\Psi_T\rangle|^2/|\langle 0|\Psi_T\rangle|^2 \ll 1$ such that the inequality (4.51) is fulfilled due to a vanishing overlap, we miss the lowest excited singlet state, and $1/\Theta^*$ provides a lower bound for the next lowest singlet with a finite overlap with the trial wave function.

For the determination of the lower bound for singlet states we concentrated on the value $U/t = 4$, centered in the RVB phase. We verified that in the case $L = 2$, where the system can be fully diagonalized, setting $\epsilon = 10^{-3}t$, $1/\Theta^* = (0.74 \pm 0.04)t$ is a lower bound. Namely, for this system size, $\Delta_{\mathrm{singlet}} = 1.84t$ for the first excited singlet state of momentum $\mathbf{k} = 0$. We also verified that this state has an overlap of 0.22 with the trial wave function. The above value of ϵ corresponds to the maximal error for all system sizes. The uncertainty in the determination of Θ^* is taken as the maximum between (i)

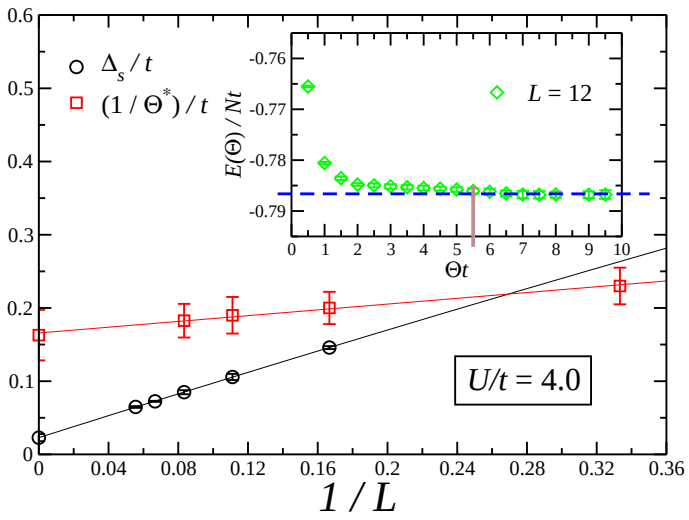

Fig. 4.17.: Lower bound $1/\Theta^* \sim \Delta_{\text{singlet}}$ for $L = 3$, 6, 9, and 12 at $U/t = 4$. For comparison, the values of the spin-gap are reproduced. The inset shows the internal energy $E(\Theta)$ as a function of the projection parameter Θ for the $L = 12$ system. The vertical bar gives the position of Θ^*. Error bars in Δ_s and $E(\Theta)$ denote standard errors. For the determination of the error bars in $1/\Theta^*$, see the text.

the distance from Θ^* to the value of Θ for $E(\Theta)/N = E(\Theta^*)/N - \epsilon$ and (ii) the distance between two consecutive values of Θ around Θ^*. By means of error propagation, we then estimate the error in $1/\Theta^*$.

In Fig. 4.17 we display $1/\Theta^*$ for $L = 3$, 6, 9, and 12, and an extrapolation to the TDL. In all these cases, the lower bound is above the spin-gap, as well as the extrapolation to the TDL. Hence, we find no evidence for singlet states with the same quantum numbers as the ground state, that may become degenerate with it in the thermodynamic limit. However, we cannot definitely exclude topological order, if the relevant singlet states happen to have a vanishing overlap with our trial wave function. For the future, it will be interesting to explore the low-energy singlets beyond the projective scheme, and probe for soft modes similarly as does, e.g., the construction of finite momentum trial states in quantum dimer models [112, 149].

4.3. Realizations

4.3.1. Organic charge-transfer salts

There is a series of candidate compounds for QSLs which are best described by models of local moments like $ZnCu_3(OH)_6Cl_2$ also known as Herbertsmithite[1] [196], Vesignietite $BaCu_3V_2O_8(OH)_2$ [197], or $Na_4Ir_3O_8$ [198], for which no spin order could be found

[1] A mineral discovered in Chile in 1972 and named after Herbert Smith.

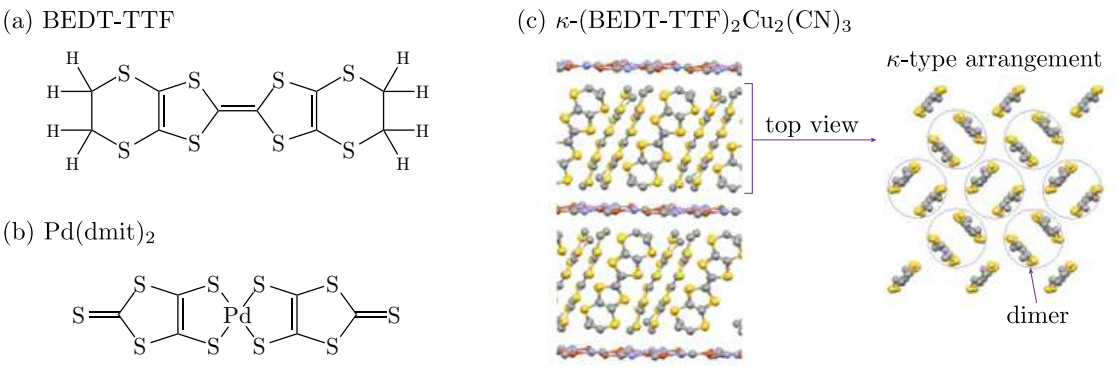

Fig. 4.18.: The molecules bis-(ethylene-dithio)-tetra-thia-fulvalene (BEDT-TTF) (a) and Palladium-1,3-dithiole-2-thione-4,5-dithiolate (Pd[dmit]$_2$) (b) on which the frustrated organic charge transfer salts are based on. The quasi-two-dimensional layers of organic molecules are separated by the anion-layer, here formed by $Cu_2(CN)_3$ (c). In the crystallographic κ-phase the organic molecules arrange themselves in dimers which form slightly distorted triangular lattice.

down to the mK range by means of μ-spin relaxation. Their structures are the highly frustrated Kagome- (2D), Pyrochlor- (3D), or Hyper-Kagome-lattices (3D). If not by geometry they can have frustrating interactions such as $Bi_3Mn_4O_12(NO_3)$, which is best modeled by a spin-1/2 honeycomb structure with nearest and next-nearest neighbor AF spin interactions [130]. Also, in He^3 films, which form triangular lattices, ring exchange is suspected to frustrate the system further. Due to the extremely small exchange coupling of $J \sim$ mK experiments are very difficult, though [199].

However, here we will focus on materials where electrons retain some of their itinerant properties. This can be found in the organic charge-transfer salts where one can observe rich physics in experimentally accessible magnetic fields and pressure ranges. The organic charge-transfer salts can be synthesized in ultra-pure single crystals and hydrostatic pressure of the order of kbars and chemical pressure by substitution of elements provide means of manipulating the materials enough to induce phase transitions between different ground states. A recent review of spin liquids in the organic Mott insulators has been published by Powell and McKenzie [154]. The two most prominent QSL candidates are the organic charge-transfer salts κ-(BEDT-TTF)$_2$X and β'-Z[Pd(dmit)]$_2$.

κ-(BEDT-TTF)$_2$X

is an organic charge transfer salt based on the molecule bis-(ethylene-dithio)-tetra-thia-fulvalene (BEDT-TTF) or often simply referred to as ET. The κ denotes crystallographic phase, which by far is the most widely studied and where frustration is known to play a dominant role (see Fig. 4.18). The organic molecules form in pairs (dimers) of quasi-two-

dimensional layers which are separated by the anion-layer. Charge is transferred from the organic layer to the anions X. Band structure calculations predict the organic molecules to have π orbitals with nodes in the plane of the molecules with strong overlap due to their proximity. The amplitude for hopping between the dimers is significantly smaller than between the molecules within a dimer. This suggests to treat the dimers as single units forming a distorted triangular lattice and carrying a free electron. The absolute energies are still under debate, but angle-dependent magnetoresistance (AMRO) measurements, which allow to map out the Fermi surface, suggest the in-layer hopping t to be of the order of tens of eV, where interlayer hopping $t_\perp$ is negligible in the μeV range. Also controversial is the amount of anisotropy (or distortion of the lattice) within the layer. The ratio t/t' is believed to be in the range $[0.75, 1.1]$ which yields frustration effect must be significant. The local Coulomb repulsion U is estimated to be of the order of the hopping such that the system can be understood in terms of a half-filled Hubbard model on the (anisotropic) triangular lattice [200, 141, 201, 154].

The strength of the electronic correlations and the degree of frustration is determined by the anion X and the applied hydrostatic pressure, e.g., for $Cu(NCS)_2$ and $Cu[N(CS)_2]Br$ the compound becomes superconducting below $\sim$10 K at ambient pressure, for $Cu[N(CS)_2]Cl$ the ground state is an AF Mott insulator at ambient pressure, and for $Cu_2(CN)_3$ and $Cu[N(CS)_2]Cl$ the systems undergo a Mott transition to a superconducting states under modest pressure of a few 100 bar. Frustration is the greatest in κ-(BEDT-TTF)$_2$Cu$_2$(CN)$_3$ which probably has a spin liquid ground state (Fig. 4.19a). Shiziumi and coworkers [202] measured the spin susceptibilities: in the Mott insulating phase the spin degrees of freedom are described by a Heisenberg model with an AF exchange coupling of $J \sim 250$ K close to the Mott transition. While $Cu[N(CS)_2]Cl$ shows a clear magnetic phase transition at $\sim$27 K, the compound with the $Cu_2(CN)_3$ anion lacks signatures of such a phase transition in the susceptibility down to 32 mK. This temperature is four orders of magnitude smaller than the exchange coupling which led Shiziumi *et al.* to propose κ-(BEDT-TTF)$_2$Cu$_2$(CN)$_3$ as a QSL. The absence of evidence for long-range magnetic order is supported by NMR spectra at temperatures as low as 20 mK!

Two recent experiments have attempted to identify the low lying excitations and the existence of a gap. S. Yamashita and coworkers measured the specific heat [205], M. Yamashita and others measured the thermal conductivity [204]. However, the two groups came to contradictory conclusions. Figures Fig. 4.19b,c show the temperature dependence of the in-plane thermal conductivity κ(T) in zero field for two different single crystals of deuterated κ-(BEDT-TTF)$_2$Cu$_2$(CN)$_3$. As the temperature is lowered, the thermal conductivity decreases and exhibits a broad hump around $T^* \sim 6\ K$. This characteristic anomaly, which can also be seen in the specific heat (cf. Fig. 4.20c) and the NMR relaxation rate, is subject to controversy and requires further investigations. Figure 4.19c shows the thermal conductivity at low temperatures, measured in two samples and under different magnetic fields. For a metal one expects the thermal conductivity

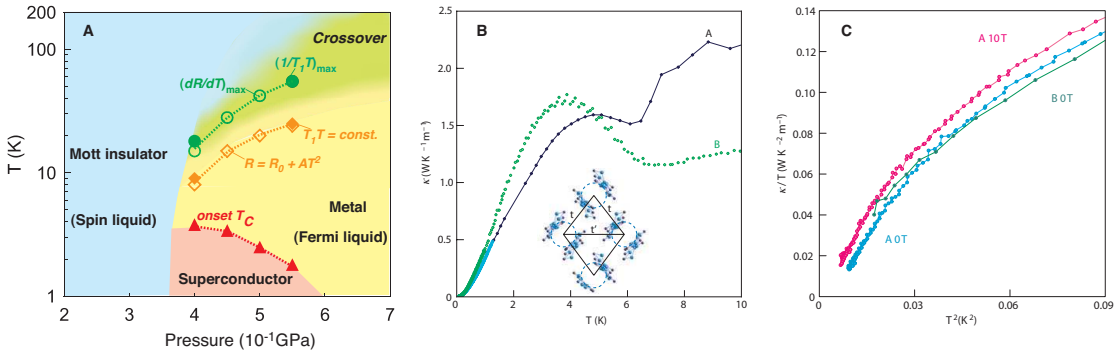

Fig. 4.19.: **A** Pressure-temperature phase diagram of κ-(BEDT-TTF)$_2$Cu$_2$(CN)$_3$ taken from [203] which is believed to be a spin liquid at ambient and low pressure, since in the Mott insulating phase no magnetic long range order can be found down to 20 mK. **B** Temperature dependence of the in-plane thermal conductivity κ(T) in zero field for two different single crystals of deuterated κ-(BEDT-TTF)$_2$Cu$_2$(CN)$_3$. As the temperature is lowered, κ(T) decreases and exhibits a broad hump starting to increase at around $T^* \sim 6\ K$. **C** Thermal conductivity of κ-(BEDT-TTF)$_2$Cu$_2$(CN)$_3$ at low temperature measured in two samples and under different magnetic fields. Plotted over T^2 the curvatures hint contributions come mostly from fermions with a magnetic field dependance. Panels **B** and **C** were adapted from Ref. [204]

to behave like $\kappa(T) = \alpha T + \beta T^3 + \ldots$, where fermions give rise to the linear term, since phonons contribute to the cubic term [206]. Since the graph is plotted against T^2 and the data does not lie on a straight line phonons do not seem contribute significantly. Also, the field dependence hints towards contributions from magnetic excitations, since phonons would not couple the magnetic field. These arguments and the fact that the thermal conductivity extrapolates to zero led M. Yamashita and coworkers to conclude that the spin liquid state of κ-(BEDT-TTF)$_2$Cu$_2$(CN)$_3$ is *gapped*.

S. Yamashita and coworkers measured the specific heat [205]. Figures 4.20a,b show results for two different samples under different magnetic fields. Note the deviation between the two samples in the low temperature region, which is attributed to magnetic impurities. Figures 4.20b also contains the data of the antiferromagnetic insulators κ-(BEDT-TTF)$_2$Cu[N(CN)$_2$]Cl, deuterated κ-(d_8:BEDT-TTF)$_2$Cu[N(CN)$_2$]Br and β'-(BEDT-TTF)$_2$ICl$_2$ for comparison. The existence of a linear contribution in T, even in the insulating state of κ-(BEDT-TTF)$_2$Cu$_2$(CN)$_3$, is clearly observed. In contrast to the insulators, the low temperature extrapolation of κ-(BEDT-TTF)$_2$Cu$_2$(CN)$_3$ is finite, which demonstrates a large residual entropy. The plots of $C_p(T)/T$ against T^2 suggests a large linear term in $C_p(T) = \gamma T + \beta T^3$, hence *gapless* fermionic excitations, which is also backed by bulk magnetic susceptibility measurements. In Fig. 4.20c the specific heat is shown over a larger temperature range along with its derivative to emphasize the 6 K anomaly already encountered in the thermal conductivity measurements.

Clearly, it is an important question why these two experiments measuring the specific heat and the thermal conductivity lead to such different conclusions, which demands

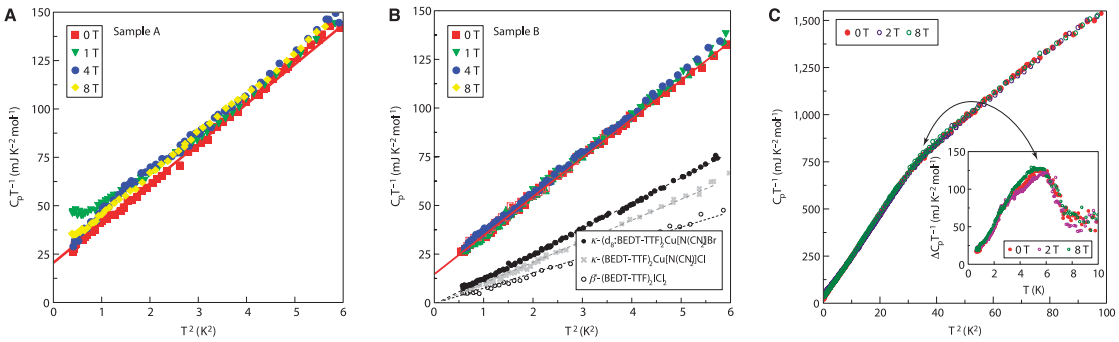

Fig. 4.20.: Low-temperature heat capacities of κ-(BEDT-TTF)$_2$Cu$_2$(CN)$_3$ for two different samples shown in **A** and **B** under different magnetic fields, respectively. **B** also contains the data of the typical antiferromagnetic insulators κ-(BEDT-TTF)$_2$Cu[N(CN)$_2$]Cl, deuterated κ-(d_8:BEDT-TTF)$_2$Cu[N(CN)$_2$]Br and β'-(BEDT-TTF)$_2$ICl$_2$ for comparison. The existence of a linear contribution in T, even in the insulating state of κ-(BEDT-TTF)$_2$Cu$_2$(CN)$_3$, is clearly observed. A low-temperature deviation of κ-(BEDT-TTF)$_2$Cu$_2$(CN)$_3$ is notable, which demonstrates that large entropy exists in the low-temperature region. **C** Temperature dependence of the heat capacity around the anomalous temperature of 6 K under different magnetic fields. The inset shows the difference of the heat capacities of κ-(BEDT-TTF)$_2$Cu$_2$(CN)$_3$ and κ-(BEDT-TTF)$_2$Cu(NCS)$_2$, which highlights the hump structure around 6 K. The arrow indicates the anomaly on the different axes. Panels have been adapted from [205].

further investigations.

β'-Z[Pd(dmit)$_2$]$_2$

is the second exampled of an organic charge transfer salt with a potentially QSL ground state and shares many properties with the κ-(BEDT-TTF), but is less well studied [207, 208]. It is based on Pd(dmit)$_2$ molecules, where dmit stands for 1,3-dithiole-2-thione-4,5-dithiolate. The compound is usually simply referred to as dmit. The Z denotes the anions which form layers separating the quasi two dimensional organic molecules. Of particular interest is the QSL candidate compound EtMe$_3$Sb[Pd(dmit)$_2$]$_2$ (or Sb-1). In the β' crystal phase again molecules for dimers which arrange themselves in an anisotropic half-filled triangular lattice. The electronic structure resembles the κ-salt, albeit more anisotropic. The AF exchange coupling is similar large $J \sim 240$ K and again no magnetic order could be found down to temperature of 1.37 K – two orders of magnitude smaller than J [207]. Also in Sb-1 a low temperature anomaly has been observed in NMR spectra. Whether or not this is related to the κ-salt is an open question. Figure 4.21 show the thermal conductivity measured by M. Yamashita and coworkers [209] for two samples, the dmit-131 spin-liquid compound known as Sb-1 and the non-magnetic dmit-221. A clear peak in κ_{xx}/T is observed in dmit-131 around 1 K, which is also seen as a hump in κ_{xx}. The lower temperature behavior of κ_{xx}/T plotted against T^2 reveals a residual $\kappa_{xx}(T)/T$, which cannot be seen for dmit-221, nor the κ-salt

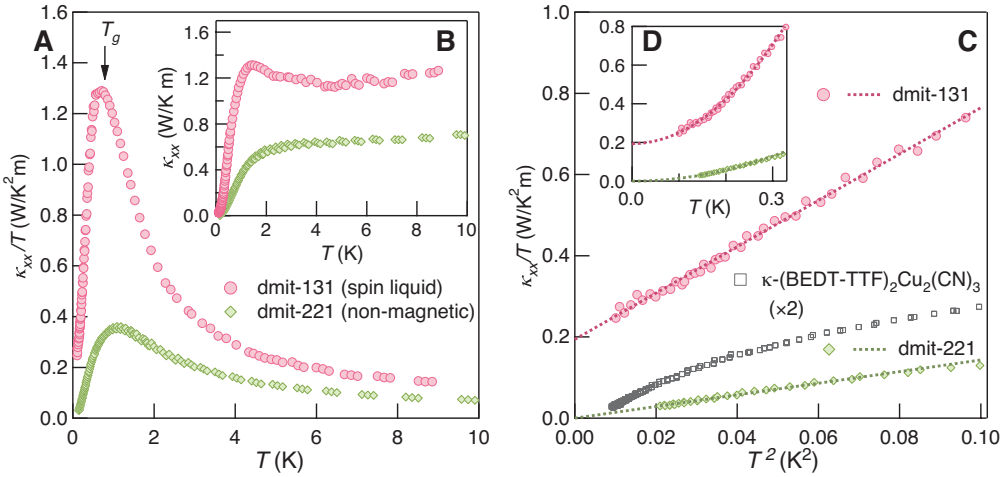

Fig. 4.21.: The temperature dependence of $\kappa_{xx}(T)/T$ for two samples, the dmit-131 spin-liquid compound known as Sb-1 and the non-magnetic dmit-221. **A** A clear peak in κ_{xx}/T is observed in dmit-131 around 1 K, which is also seen as a hump in κ_{xx} (**B**). Lower temperature plot of κ_{xx}/T as a function of T^2 (**C**) and T (**D**) of dmit-131, dmit-221 along with κ-(BEDT-TTF)$_2$Cu$_2$(CN)$_3$. A clear residual of $\kappa_{xx}(T)/T$ is resolved in dmit-131 in the zero-temperature limit. Panels have been adapted from [209].

(data taken from Ref. [204]), which is a clear signature for gapless excitations. Another important finding reported in this paper is that a spin gap is observed in the magnetic field dependence of the thermal conductivity. This seems puzzling since the thermal conductivity clearly shows that there are gapless excitations. However, excitations with any spin state can be excited thermally, but the field does not couple to (the non-magnetic) singlet excitations. Therefore, these results suggest that Sb-1 is a QSL with a finite singlet-triplet gap.

Another interesting fact is, that in a kinetic approximation (ballistic energy propagation), the thermal conductivity can be written as $\kappa_{xx} = C_s v_s l_s/3$, with the specific heat C_s, the velocity v_s and the mean free path l_s of the quasi-particles responsible for the elementary excitations. Estimates of the mean free path l_s from the thermal conductivity suggest l_s reaches up to 1000 inter-spin spacings! This implies low scattering rates and almost free spins.

4.3.2. Atomic monolayers & heterostructures

Deposited on the surface on a substrate, or suspended, bridging a gap, it is still controversial whether graphene is a correlated material or not [176, 210, 211, 1]. Although there are arguments for significant correlations (some of them can be found in [212, 176, 210, 211]), the (community) trend leads away from correlations physics in graphene. A major argument against local Coulomb correlations is the lack of states at the Fermi level which

excludes an effective screening process. While graphene is unlikely to bear the necessary correlations, in expanded graphene – a carbon monolayer deposited or grown on a substrate which interatomic distance does not match the natural spacing of graphene, or uniaxially stretched suspended graphene – the ratio U/t might be enhanced.

Since the publication of the Scotch tape technique to *manufacture* graphene [213] the research in the synthesization of monolayer honeycomb lattices based on group IV and nearby elements has prospered [214]. Another possible candidate is monolayer Silicon, where the nearest neighbor distance is expected to be approximately 50% larger than in graphene, such that correlations effects are enhanced [182]. In fact, first attempts succeeded in synthesizing single-crystal silicon monolayers [215].

Recently, an intriguing setup using a heterostructure was reported [216]. The (quasi) two-dimensional electron gas in a modulation-doped AlGaAs/GaAs semiconductor is subjected to a lateral potential with honeycomb geometry. The structure consists of an array of pillars with honeycomb geometry, formed on the surface by an etching process. The pillars induce a lateral potential modulation. They were able to show a transition from a conducting to an insulating regime can be induced by changing the voltage of a metallic gate deposited on top of the array. The possibility to control the localized/delocalized nature of the electronic states suggests to use of this system as a *quantum simulator* (similar to cold atoms in optical lattices) in a regime dominated by electron correlations.

4.3.3. Optical lattices

Ultra-cold atoms loaded into optical lattices are the most promising approach to realize SU(N) symmetric models. The experimental setup and methods are hence introduced in the chapter on the SU(N) Hubbard Heisenberg model (cf. Sec. 5.7). Let us note that the experimental detection of a QSL in realized in optical lattices is inherently different from the experimental means available in condensed matter system (crystals). At the moment, the experimental setup delimits the spectrum of accessible measurements and observations, which excludes the suggested methods of detection outlined in the next section, unfortunately.

4.3.4. Experimental detection

An important question is how to identify a QSL states experimentally. Besides thermal transport and to prove the absence of order down to the lowest as seen above (cf. Sec. 4.3.1), let us make some general remarks and mention some recent ideas.

The susceptibility measures the spin excitations. In the spectral representation it is given by

$$\chi^{+-}(\mathbf{q}, \mathrm{i}\omega_n) = \int_0^\beta d\tau \mathrm{e}^{\mathrm{i}\omega_n \tau} \left\langle T_\tau S^-(\mathbf{q}, \tau) S^+(-\mathbf{q}, 0) \right\rangle , \tag{4.53}$$

where $\beta = 1/k_{\mathrm{B}}T$ is the inverse temperature, τ is the imaginary time, ω_n are the Matsubara frequencies, and $S^{\pm}$ are the spin raising/lowering operators. From its form it is obvious that for a singlet ground state at zero temperature singlet excited states do not contribute to the dynamical spin susceptibility. Because of the spin-flip operators the matrix elements of the spin operators between the singlet ground state and any singlet excited state must be zero. Hence at low temperatures, only triplet excitations can contribute to the uniform magnetic susceptibility. This includes NMR relaxation rates, Knight shift, and the inelastic neutron scattering cross section [154]. Furthermore, the singlet spectrum will neither shift, nor split in a magnetic field. In contrast, triplets will split and the corresponding spectral weight be redistributed. The specific heat capacity and the thermal conductivity at low temperatures reflect contributions from all sectors, including triplet and singlet excitations. Comparing the temperature dependence of the measurements of the spin susceptibility and the specific heat capacity should allow to distinguish between elementary singlet-, or and triplet-excitaions in order to gain information about the low energy spectrum.

In Ref. [217] it is suggested that the dynamical spin correlations are dominated by highly dispersive excitation continua at medium to high energies, a characteristic signature once the $S = 1$ waves fractionalize into pairs of deconfined S=1/2 spinons. Also, the almost free excitations follow incommensurate dispersion relations. In spin liquids with deconfined excitations, these will contribute to the thermal Hall response due to Lorentz force, hence under application of an external magnetic field. The predictions in Ref. [218] promise a clear experimental method to prove the existence of the deconfined spinons via a thermal transport phenomenon.

In Sec. 4.1.2 we noted the different spinon Fermi surfaces emerging in a QSL ground state. Although the bulk may be gapped in the one-particle and charge spectrum, spinon excitation can be gapless. To measure a spinon Fermi surface remains a nontrivial task, though. Norman and Micklitz proposed an experiment to identify the potential existence of a spinon Fermi surface by looking for oscillatory coupling between two ferromagnets via a spin liquid spacer [219]. They investigate three candidate spin liquids and predict that in all cases long period oscillations should be present, the period of which would identify the Fermi wave vector of the spinon surface. The requirements on the specimen appear very challenging, though.

In App. A.5 we show the spectra of the one-particle Green's function and the dynamical spin susceptibility. The spin susceptibility shows well defined quasiparticles (singlet-triplet excitations) and no clear sign of a continuum of excitations. However, note that we have very limited momentum resolution and must use of the stochastic analytic continuation [220, 221] to obtain spectra at real frequencies. These problems and the enormous amount of computations time necessary in order to obtain high precision results for a clean analytic continuation, limit the quality, reliability and interpretation of the spectra.

Although not a direct measure of the *liquidity*, it can be helpful to to quantify the

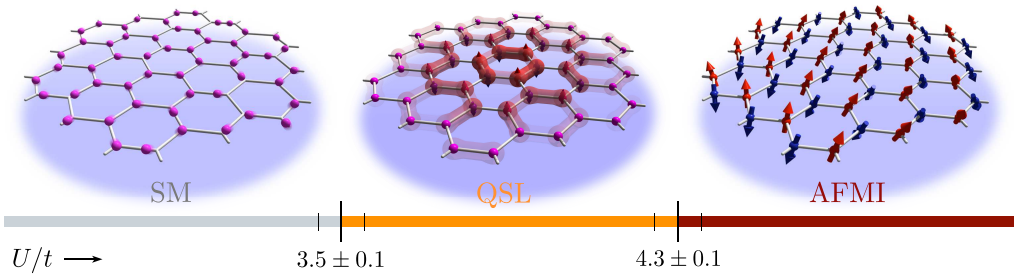

amount of frustration in a system in to support the suggestion of an QSL in a compound. Ramirez introduced the measure of the ratio of the Curie-Weiss temperature over the Néel temperature $f = T_{CW}/T_N$ [222]. Balents discussed this measure in his review on frustrated magnetism [144]. This measure has the limitation that it does not separate the effects of fluctuations, dimensionality and frustration. Especially the dimensionality plays an important role since T_N is exactly zero in two dimensional systems but is determined by the interlayer coupling in quasi two dimensional systems.

Unfortunately, it seems as difficult in experiment as in theoretical approaches to pin down the existence of a QSL ground state.

4.4. Discussion and outlook

The presence of a spin-liquid in the Hubbard model on the bipartite honeycomb lattice close to an AF Mott insulator resembles the situation in the organic antiferromagnet κ-(BEDT-TTF)$_2$Cu$_2$(CN)$_3$, which has been argued to display a spin-liquid state [202, 204], albeit the latter system is on a triangular lattice and hence frustrated. This difference can be reconciled starting from the strong-coupling limit of the Hubbard model, i.e. a nearest-neighbor Heisenberg model, that close to the Mott transition acquires corrections that induce efficient frustrations to the spin degrees of freedom. In fact, a Klein Hamiltonian for a spin-liquid state on the honeycomb lattice was constructed, including extended exchange interactions [223]. In the strong coupling regime it is reasonable to describe the low energy physics by an effective $S = 1/2$ Heisenberg Hamiltonian, which can be derived from the Hubbard model in the large-U limit (cf. [224, 225] and Sec. 1.3). For up to fourth order perturbation theory the Hamiltonian reads

$$H = \sum_{\langle ij \rangle} \left(\frac{4t^2}{U} - \frac{16t^4}{U^3} \right) \mathbf{S}_i \cdot \mathbf{S}_j + \sum_{\langle\langle ij \rangle\rangle} \frac{4t^4}{U^3} \mathbf{S}_i \cdot \mathbf{S}_j + \dots \tag{4.54}$$

Hence the J_1-J_2 Heisenberg model, where both couplings are antiferromagnetic would be the first guess for an effective model.

A more pronounced difference is the appearance of superconductivity in the organic systems upon pressure, that is equivalent to a reduction of the ratio U/t in the Hubbard

model [226]. The absence of superconductivity in our system could be due to the vanishing density of states at the Fermi energy. In this case, a finite coupling strength is needed, at least in the BCS-frame [227]. However, having an unexpected realization of a short-range RVB state, it would be highly interesting to explore the consequences of doping, in a spirit rather close to the original scenario proposed by Anderson [113] and Kivelson *et al.* [139] for the cuprates. In particular, for the fully gapped short-range RVB state, the finite spin-gap sets the energy scale of pairing in the superconducting state [139]. In this respect, the value obtained for the spin-gap is rather promising. The largest value attained is $\Delta_s \sim 0.025t$ (Fig. 1), that for t in the range of 1.5 to 2.5 eV (in graphene is $t = 2.8$ eV [1]) corresponds to a temperature scale ranging from 400 to 700 K. The question of doping the system is unfortunately beyond the means of QMC due to the notorious sign problem.

As already mentioned there have been several studies before investigating the semimetal to AF order transition by the means of QMC [184, 186, 185, 187]. But why haven't these investigation detected and unraveled the intermediate phase before? One reason might be the extremely small energy scale of the spin gap of $0.025t$. In finite temperature investigations, one needs at least a temperature of the order of the spin gap to discern it from thermal fluctuations. The finite temperature investigation [185] studied systems up to $L = 15$ at temperatures of typically $0.125t$, and the investigation in Ref. [187] studied systems up to $L = 12$ and temperature $0.0625t$. Both investigations were performed at too high temperatures to be able to identify the intermediate phase. The latter study even looked at excitation gaps, albeit only *after* the use of Maximum Entropy to continue the dynamical correlation function to the real axes. Maximum Entropy has the unfortunate effect to broaden and slightly shift excitations, such that gaps cannot be reliably extracted. The oldest $T = 0$ study [184] was obviously handicapped by the lack of computer power, the largest lattices were of linear dimension $L \leq 10$. The investigation in Ref. [186] also employed projector QMC and studied lattices of linear dimension up to $L \leq 16$ (in even steps of L). However they seem to have only focused on the antiferromagnetic structure factor and spin correlations without looking at excitations gaps.

Our findings, based on a controlled numerical framework, open a new facet of quantum spin-liquids, where an appreciable amount of doubly-occupied sites are present, extending well beyond the regime of localized spin physics. They also enable us and others to study a QSL in a non-frustrated, realistic model under controlled approximations. And there are many open questions to follow up: How sensitive is the intermediate phase to the introduction of new interactions terms? Does superconductivity arise upon doping? Is the QSL unstable upon creating an anisotropy in the hopping – will it crystalize into a VBS? Using finite temperature algorithms, can we go to low enough temperatures and large enough lattices to study the dynamics? Does the specific heat at finite temperature support the evidence of the lack of excitations below the spin gap? Can we increase our precision such that we are able to obtain clear spectrum of the spin

excitations?

In response to the publication of our results presented here, already a number of papers has been published which aim to shed further light on the intermediate phase. We are looking forward to future investigations of the half-filled Hubbard model on the honeycomb lattice.

SU(N) Hubbard-Heisenberg model on the honeycomb

5

Symmetry is central to physics not merely as a mathematical aid but constitutes a conceptual tool. Generalizing SU(2) symmetric models to higher symmetry SU(N) enables us to obtain an analytically solvable model in the limit $N \to \infty$, and for finite N it provides the setup in which one can explore strong correlation physics that arises from quantum fluctuations. Correlations can be large enough to melt any form of classical order, leading to various exotic states. Such SU(N) models can accommodate several types of symmetry broken and disordered states and allow naturally for quantum states of matter. This enables us to study the melting of phases as correlations change by varying the degree of symmetry N.

5.1. Introduction

As N decreases from large values down to the physical limit of $N = 2$ fluctuations increase. Starting from $N \to \infty$ this requires the inclusion of fluctuations about the mean-field state. In principle, this problem can be recast in the form of a $1/N$ perturbative analysis of gauge fields strongly coupled to fermionic matter. Unfortunately, the lack of control makes it hard to quantify the reliability of such an expansion in the physically most important SU(2) case. This makes it essential to explore the ground state properties with unbiased methods to determine how far perturbative approaches at large-N including $1/N$ corrections can be trusted. Non-frustrated two dimensional systems prove to be most efficiently tackled by means of quantum Monte Carlo (QMC): Recently, Beach *et al.* presented the ground state phase diagram of the SU(N) Heisenberg model on the square lattice as a function of continuous N using a conjugate representation. They found a continuous quantum phase transition from a valence bond crystal to the antiferromagnet – a transition beyond the Landau Ginzburg Wilson paradigm as it directly connects two phases of different broken symmetries [99]. Another intriguing phase diagram obtained by QMC simulations has been presented by Assaad [19]; in the half-filled SU(N) Hubbard Heisenberg model on the square lattice quantum fluctuation at $N = 4$

were found to be large enough to prevent any form of order, leading to a gapless quantum spin liquid amidst Néel, π-flux and valence bond crystal phases.

Inspired by the rich phase diagrams of SU(N) models, we study the Hubbard Heisenberg quantum antiferromagnet on the honeycomb lattice. Two dimensional honeycomb structures are of particular interest, owing to their unique properties (see Sec. 1.1) and the accelerating advances in their synthesis with constituent atoms of the group IV, and binary compounds of the groups III-V and groups II-VI [213, 215, 1]. The low coordination number $z = 3$ puts the dimensionality of the hexagonal lattice in between the linear chain and the square lattice, thus fluctuations can be expected to play an important role. A specific feature is the Dirac-like dispersion of the tight-binding band structure with its point-like Fermi surface at the Brillouin zone boundary: the nodal- or K-points. The linearly vanishing density of states at the Fermi level is the cause for the robustness of the system against superconducting and magnetic instabilities. Weak local Coulomb repulsion only renormalizes the Fermi velocity and the system remains in a paramagnetic state. However, a sufficiently large interaction causes the semimetal ground state to become unstable, and turns the system into an insulator. Once a dynamical gap is generated, the low energy properties of the system fundamentally change. The authors have shown recently the unexpected emergence of a quantum spin liquid in the half-filled SU(2) Hubbard on the honeycomb lattice [137] – a state which could not have been foreseen starting from the large-N limit.

In this chapter we present basic properties of the special unitary group and we investigate the reliability of $1/N$ corrections to large-N results by means of numerically exact QMC simulations. We study the melting of phases as correlations increase with decreasing N in the SU(N) Hubbard Heisenberg model on the honeycomb lattice and determine wether the quantum spin liquid found in the SU(2) Hubbard model at intermediate coupling is a specific feature, or exists also in the t-J model.

5.2. The special unitary group

Groups, their properties, their representations and their implications are a vast topic on their own and are covered in detail in countless books, some of them being [228, 229, 230, 231, 232]. In the following we will give some basic facts on the special unitary group, its representations and the useful Fierz identity, all which are important for the investigation covered in this chapter.

5.2.1. Basic properties

The special unitary group of degree N, denoted SU(N), is the group of unitary matrices (of size $N \times N$ in the fundamental representation) with determinant 1 and matrix multiplication as the group operation. This group is an inherent part of the standard model in particle physics and also finds wide application in condensed matter since the

symmetry of the electron's spin degree of freedom is effectively represented by elements of SU(2). Here are some basic fact about the group:

Any unitary matrix U satisfies $U^\dagger U = \mathbf{1}$ and can be written as

$$U = \mathrm{e}^{\mathrm{i}H} \,, \tag{5.1}$$

where H is hermitian ($H^\dagger = H$) and $H = -\mathrm{i}\ln U$. The unitarity of the group implies $\det U = 1$ and hence the tracelessness of H:

$$\det U = \mathrm{e}^{\mathrm{Tr}[\ln U]} = \mathrm{e}^{\mathrm{Tr}[\mathrm{i}H]} = 1 \quad \rightarrow \quad \mathrm{Tr}\, U = 0 \,. \tag{5.2}$$

The considerations above imply that any $N \times N$ unitary matrix with unit determinant can be generated by an $N \times N$ traceless hermitian matrix.

The SU(N) algebra is generated by N^2 operators, which satisfy the commutator relationship

$$[S_{ij}, S_{kl}] = \delta_{jk} S_{il} - \delta_{il} S_{kj} \,, \tag{5.3}$$

where $i, j, k, l = 1, 2, \ldots, N$. However, one of these operators $S_0 = \sum_{i=1}^{N} \hat{O}_{ii}$ satisfies $[S_0, S_{ij}] = 0$ which implies that the number of *independent* generators of SU(N) is $(N^2 - 1)$. Another approach to determine the number of generators, or independent group parameters, is to consider the generator matrix $U = \mathrm{e}^{\mathrm{i}H}$. Since the diagonal elements of H must be real ($H_{ii} = H_{ii}^*$), the tracelessness condition allows for $(N - 1)$ independent parameters. Additionally there are the $(N^2 - N)$ complex off-diagonal elements, each corresponding to two real parameters. Yet this factor of two is cancelled by the hermitian condition ($H_{ij} = H_{ji}^*$). In total $N \times N$ unitary matrices have $(N - 1) + (N^2 - N) = (N^2 - 1)$ independent parameters.

As already pointed out in Sec. 1.3.2, SU(N) contains the subgroups [43]

$$\mathrm{SU}(N) \supset \mathrm{SU}(p) \times \mathrm{SU}(N - p) \times \mathrm{U}(1) \,, \quad \text{for} \quad p > 1 \,, N - p > 1 \,. \tag{5.4}$$

While the special unitary groups themselves are non-abelian (its elements do not commute, c.f. Eq. (5.3)) they contain an abelian center which is isomorphic to the cyclic group Z_N. For SU(2) the center is Z_2 and consists of the matrices $\mathbf{1}$ and $-\mathbf{1}$.

5.2.2. Group representations

The choice of the representation of the symmetry group defines the physical interpretation. Different representations result in different eigenvalues of the Casimir invariants. Hence different spin degrees of freedom and multiplet-structures allow for different ground states. Additionally, translational symmetries of the lattice might not be preserved [233, 234, 105, 235].

A practical way to illustrate different representations of the special unitary group SU(N) is to use Young tableaux. These diagrams consist of N boxes in a particular

arrangement: each box may be interpreted as a basis vector, where their horizontal (vertical) arrangement corresponds to the symmetric (anti-symmetric) combination. Taking the familiar example of the SU(2)-singlet and the non-magnetic SU(2)-triplet in the S^z basis the Young tableaux are

$$\begin{array}{|c|}\hline 1 \\ \hline 2 \\ \hline \end{array} \equiv \frac{1}{\sqrt{2}}[|\uparrow\downarrow\rangle - |\downarrow\uparrow\rangle] \,, \qquad \begin{array}{|c|c|}\hline 1 & 2 \\ \hline \end{array} \equiv \frac{1}{\sqrt{2}}[|\uparrow\downarrow\rangle + |\downarrow\uparrow\rangle] \quad . \tag{5.5}$$

The enumeration follows the simple rule, that boxes to the right and the leftmost in next column must carry an equal or larger number. For $N = 2$ and two boxes one can have the arrangements

$$\begin{array}{|c|}\hline 1 \\ \hline 2 \\ \hline \end{array} \,, \quad \begin{array}{|c|c|}\hline 1 & 1 \\ \hline \end{array} \,, \quad \begin{array}{|c|c|}\hline 2 & 2 \\ \hline \end{array} \,, \quad \begin{array}{|c|c|}\hline 1 & 2 \\ \hline \end{array} \,. \tag{5.6}$$

The boxes above correspond to the singlet and the three triplets. All possible arrangements of the N boxes for the group SU(N), according to this rule, correspond to the dimensionality of the matrix representation. While some representations can be split into smaller arrangements the representation of smallest dimensionality is the irreducible, or fundamental representation. For SU(N) groups this is represented by a single Young tableau as shown in panel 5.7a, below. As there are N different boxes, group elements can be represented by N-rank matrices at the smallest.

$$\begin{array}{lll} (a) & (b) & (c) \\ \begin{array}{|c|}\hline 1 \\ \hline \end{array} & \begin{array}{cc} i & j \\ \begin{array}{|c|}\hline 1 \\ \hline 3 \\ \hline \end{array} & \begin{array}{|c|}\hline 2 \\ \hline 4 \\ \hline \end{array} \end{array} & \begin{array}{cc} i & j \\ \begin{array}{|c|}\hline 1 \\ \hline 2 \\ \hline 4 \\ \hline \end{array} & \begin{array}{|c|}\hline 3 \\ \hline \end{array} \end{array} \end{array} \tag{5.7}$$

For electronic systems each box can be identified with a fermion of a different flavor, hence the filling of a lattice is given by the number of boxes (fermions) distributed on the lattice. The antisymmetric, self-conjugate representation representation considered throughout this chapter is represented by Young tableaux with one column of $N/2$ boxes per site as shown in panel (b) for the example of SU(4). Here i and j denote site indices on different sublattices. The vertical arrangement denotes the antisymmetry of the flavor indices (and hence the state) with respect to permutations. The product of two

self-conjugate representations on different sites leads to the multiplet structure given by

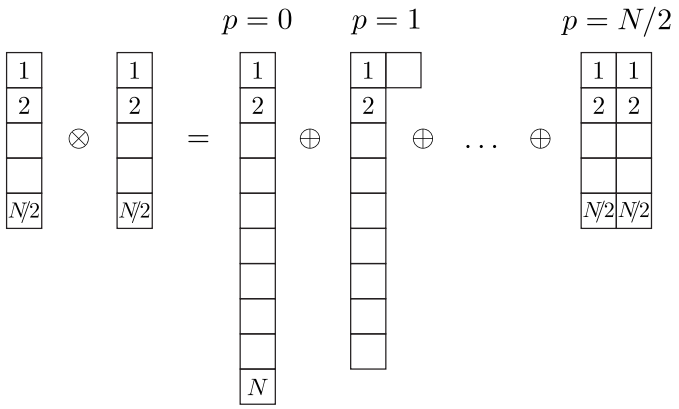

(5.8)

where the state $p = 0$ is the only totally antisymmetric combination of tableaux representing the SU(N)-singlet. The local Hilbert space has dimension 2^N and is spanned by the states

$$\prod_{\alpha=1}^{N} (c^\dagger_{i,\alpha})^{u_\alpha} \big|0\big\rangle \ , \qquad \text{with} \qquad u_\alpha = \{0,1\} \ . \tag{5.9}$$

For localized spin systems the most commonly used representation is the conjugate representation with $(N-1)$ boxes on one sublattice and a single box on the other shown in panel (c). These are the fundamental and the anti-fundamental representations on different sublattices, respectively. This representation allows to easily describe the ground state in terms of valence bonds (singlets) connecting odd and even sites. Yet the conjugate representation clearly distinguishes between the sublattices and hence breaks translation symmetry of the lattice – a property which is crucial to maintain in itinerant electron systems. In contrast, the totally anti-symmetric representation (b) preserves translational symmetry and is the representation of choice in our investigation here.

The representation not only afflicts lattice symmetries, but also sets the magnitude of the spin. Thanks to Perelemov and Popov [236] we know the quadratic Casimir invariant for the different representations (as a function of p, c.f. 5.8) takes the values

$$S_{\alpha\beta}S_{\beta\alpha} = c^\dagger_\alpha c_\beta c^\dagger_\beta c_\alpha = (N^2 + N - p(2N+1-p))/8 \ . \tag{5.10}$$

Here α, β denote the flavors which run from one to N. Hence for $N > 2$ and any representation other than the fundamental the spin increases and yields values other than $S = \frac{1}{2}$ or $\mathbf{S}^2 = \frac{3}{4}$. Note that the limit $N \to \infty$ is nevertheless different from the classical limit $S \to \infty$. Where the large-S limit kills quantization, the large-N limit is a mean-field limit, still allowing for operators and commutation relations.

5.2.3. A concrete example: SU(4)

In order to answer the question what an SU(N) ground state actually looks like we choose $N = 4$ as an example to illustrate the ground state and the definition of so called flavor-singlets.

For a half-filled, bipartite lattice in the large-U limit of no double occupation and $N/2$ boxes per site, such that no flavor has a majority, one can put one of the six flavor combinations $\{(1,2),(1,3),(1,4),(2,3),(2,4),(3,4)\}$ on each sublattice. Here we use the shortcut (i,j) to denote the antisymmetric combination of the boxes $\boxed{i}$ and $\boxed{j}$. The remaining flavor combination on the other sublattice follows naturally. In the large-U limit of no double occupation, the Hilbert space for a single site is

$$\mathrm{span}\{c^\dagger_{i,1}c^\dagger_{i,2}|0\rangle, c^\dagger_{i,1}c^\dagger_{i,3}|0\rangle,\ c^\dagger_{i,1}c^\dagger_{i,4}|0\rangle,\ c^\dagger_{i,2}c^\dagger_{i,3}|0\rangle,\ c^\dagger_{i,2}c^\dagger_{i,4}|0\rangle,\ c^\dagger_{i,3}c^\dagger_{i,4}|0\rangle\}\,. \tag{5.11}$$

For two sites, the possible states and their multiplicities are

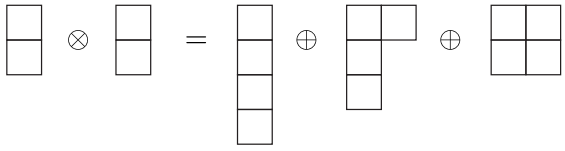

$$6 \otimes 6 = 1 \oplus 15 \oplus 20 \tag{5.12}$$

An exact theorem by Lieb [195] states that for finite systems the ground state must be a non-degenerate singlet for any finite value of $U > 0$. Indeed, contracting two sites there is only one non-degenerate, singlet-state given by the totally antisymmetric combination of Young tableaux for $p = 0$. Using exact diagonalization for large values of U we were able to determine the ground state of the SU(4) large-U Hubbard model, which yields

$$\begin{aligned}|0\rangle \;=\; \frac{1}{\sqrt{6}}\Big(&\underbrace{|(1,2),(3,4)\rangle}_{①} - \underbrace{|(1,3),(2,4)\rangle}_{②} + \underbrace{|(1,4),(2,3)\rangle}_{③} \\ &+ \underbrace{|(2,3),(1,4)\rangle}_{④} - \underbrace{|(2,4),(1,3)\rangle}_{⑤} + \underbrace{|(3,4),(1,2)\rangle}_{⑥}\Big)\,.\end{aligned} \tag{5.13}$$

The ground state must comprise an SU(4)-singlet, which is no longer of the simple structure known from SU(2). According to [233, 234] there should also be $N/2$ singlets emanating from each site. Indeed, one can form two singlets as antisymmetric contractions of indices similar to the well known SU(2) structure, e.g., $(①-⑤)/\sqrt{2}$ and $(④-②)/\sqrt{2}$, or other combinations. We identify these singlets as *flavor*-singlets.

5.2.4. The SU(N) generators

Increasing the number of flavors puts us out of our comfort zone. As we have seen, the ground state for $N > 2$ is a non-trivial superposition of different flavor-combinations on

the sublattices other than we are used to describe in terms up-, and down-spins. There is a simple way out in understanding these states – just stick to the (broken) symmetries. Instead of developing a complicated physical picture of states of higher symmetry N, one can solely focus on the familiar correlation functions and order parameters which measure certain symmetries. Their algebraic structure hardly changes and allows to rely on SU(2) analogs like magnetization (spin-symmetry breaking), dimerization (translational- and rotational-symmetry breaking) and coherence (phase breaking).

The spin generators can be easily generalized to more flavors [39]

$$\tilde{S}_{i,\alpha,\beta} = c^\dagger_{i,\alpha} c_{i,\beta} \ , \tag{5.14}$$

where α, β denote the flavors running from $1, \ldots, N$. The generators obey the SU(N) algebra under the (local) constraint for the fermions

$$\sum_\alpha c^\dagger_{i,\alpha} c_{i,\alpha} = N/2 \ , \tag{5.15}$$

which ensures spin-only algebra at the filling of one particle per site. While this constraint is fulfilled in spin-systems by their very definition, in itinerant electron systems charge fluctuations are present and the constraint is included into the generators to guarantee the tracelessness $\mathrm{Tr}\, S^{(a)}_N = 0$:

$$S_{i,\alpha,\beta} = c^\dagger_{i,\alpha} c_{i,\beta} - \delta_{\alpha,\beta} \frac{1}{N} \sum_\gamma c^\dagger_{i,\gamma} c_{i,\gamma} \ . \tag{5.16}$$

The Kronecker-Delta takes care of the diagonal contributions (the equivalents to S^z) and imposes the constraint from Eq. (5.15). For example at SU(2) the sum runs over the flavors $\alpha, \beta \in \{\uparrow, \downarrow\}$ and

$$\begin{aligned}
\mathbf{S}_i \cdot \mathbf{S}_j &= \sum_{\alpha,\beta} S_{i,\alpha,\beta} S_{j,\beta,\alpha} \\
&= \sum_{\alpha,\beta} \left(c^\dagger_{i,\alpha} c_{i,\beta} - \delta_{\alpha,\beta} \frac{1}{N} \sum_\gamma c^\dagger_{i,\gamma} c_{i,\gamma} \right) \left(c^\dagger_{j,\beta} c_{j,\alpha} - \delta_{\alpha,\beta} \frac{1}{N} \sum_\gamma c^\dagger_{j,\gamma} c_{j,\gamma} \right) \\
&\overset{N=2}{=} (c^\dagger_{i\uparrow} c_{i\uparrow} - \frac{1}{2} n_i)(c^\dagger_{j\uparrow} c_{j\uparrow} - \frac{1}{2} n_j) + (c^\dagger_{i\uparrow} c_{i\downarrow})(c^\dagger_{j\downarrow} c_{j\uparrow}) \\
&\quad + (c^\dagger_{i\downarrow} c_{i\uparrow})(c^\dagger_{j\uparrow} c_{j\downarrow}) + (c^\dagger_{i\downarrow} c_{i\downarrow} - \frac{1}{2} n_i)(c^\dagger_{j\downarrow} c_{j\downarrow} - \frac{1}{2} n_j) \\
&= S^+_i S^-_j + S^-_i S^+_j + 2 S^z_i S^z_j \ .
\end{aligned} \tag{5.17}$$

The sum over two flavors will generate N^2 spin operators. From these one can construct the (N^2-1) generators in the irreducible representation since there are only (N^2-1) *independent* operators. However, as long as the operators applied to any element of SU(N) can create all other elements, independently whether they are a linear combination of the original (N^2-1), or the original (N^2-1) themselves, we call them generators.

5.2.5. Generators and the Fierz identity

The generators of the symmetry groups inherent in a system are the direct correspondents to order parameters of a system. When investigating a specific state, one wants to test wether or not certain a generator is broken. This is done by measuring correlation functions which capture the symmetry breaking. In general they can be constructed out of products of generators. The Fierz identity is very useful to easily compute the product of generators in order to later Wick-decompose them. Here we derive the Fierz identity for the fundamental matrix representation and the more general operator expressions of spin-spin products:

We normalize the generators T_N^a of the SU(N) spin algebra such that for $N = 2$ the common definition of the total spin $\mathbf{S}^2 = \frac{3}{4}$ holds, also known as the (first) quadratic Casimir invariant. Assuming that we are in the fundamental representation of SU(N), the first two Casimir invariants read [229]

$$C_1(N) = \frac{1}{2}\,, \qquad C_2(N) = \frac{N^2-1}{2N}\,. \tag{5.18}$$

This implies the definition

$$\mathrm{Tr}[T_N^a T_N^b] = \frac{1}{2}\delta^{ab}\,, \qquad T_N^a T_N^a = C_2(N)\cdot\mathbf{1}\,. \tag{5.19}$$

Note, that we sum over repeated indices according to the Einstein convention. Following [237] these definitions allow to generalize the SU(2) Fierz identity to arbitrary N which is used in the Wick decomposition of several observables: Any regular complex $N \times N$ matrix can be expanded in the basis of diagonal and off-diagonal contributions given by the set $\{\mathbf{1}, \mathbf{T}^a\}$, where the $\mathbf{T}$s are $N \times N$ matrices for the generators in fundamental representation

$$\mathbf{A} = c_0\mathbf{1} + c_a\mathbf{T}^a\,, \tag{5.20}$$

where

$$c_0 = \frac{1}{N}\mathrm{Tr}[\mathbf{A}]\,, \qquad c_a = 2\mathrm{Tr}[\mathbf{A}\cdot\mathbf{T}^a]\,. \tag{5.21}$$

Substituting Eq. (5.21) into Eq. (5.20), the matrix is defined by the elements

$$(\mathbf{A})_{ij} = \frac{1}{N}\delta_{ij}(\mathbf{A})_{kk} + 2\,(\mathbf{A})_{lk}(\mathbf{T}^a)_{kl}(\mathbf{T}^a)_{ij}\,. \tag{5.22}$$

For any regular matrices the relation $\mathbf{A}\mathbf{A}^{-1} = \mathbf{1}$ holds, and we can multiply with A_{lk}^{-1} to rewrite the above

$$\begin{aligned}(\mathbf{A})_{ij}(\mathbf{A})_{lk}^{-1} &= \frac{1}{N}\delta_{ij}(\mathbf{A})_{kk}(\mathbf{A})_{lk}^{-1} + 2\,(\mathbf{A})_{lk}(\mathbf{A})_{lk}^{-1}(\mathbf{T}^a)_{kl}(\mathbf{T}^a)_{ij}\\ \delta_{il}\delta_{kj} &= \frac{1}{N}\delta_{ij}\delta_{kl} + 2\,(\mathbf{T}^a)_{ij}(\mathbf{T}^a)_{kl}\,,\end{aligned} \tag{5.23}$$

such that we get the generalized Fierz identity for the fundamental representation of two generators of SU(N)

$$(\mathbf{T}^a)_{kl}(\mathbf{T}^a)_{ij} = \frac{1}{2}\delta_{il}\delta_{kj} - \frac{1}{2N}\delta_{ij}\delta_{kl} \; . \tag{5.24}$$

To double check, we can re-obtain the first of the $(N-1)$ quadratic Casimir invariants, if we choose the indices of the l.h.s. to correspond to the matrix product of the generators. The contraction of double indices yields

$$(C_2(N)\cdot\mathbf{1})_{ik} = (\mathbf{T}^a)_{ij}(\mathbf{T}^a)_{jk} = \frac{1}{2}\delta_{ik}\delta_{jj} - \frac{1}{2N}\delta_{ij}\delta_{jk} = \delta_{ik}\frac{N^2-1}{2N} \; . \tag{5.25}$$

Another way to derive the generalized Fierz identity is to start from the operator definition of the SU(N) generators, here with site index i,j and flavors α,β

$$S_{\mathbf{r},\alpha,\beta} = \frac{1}{\sqrt{2}}\Big(c^\dagger_{i,\alpha}c_{i,\beta} - \delta_{\alpha\beta}\frac{1}{N}\sum_\gamma c^\dagger_{i,\gamma}c_{i,\gamma}\Big) \; . \tag{5.26}$$

The product of the generators then yields

$$\begin{aligned}
S_{i,\alpha,\beta}S_{j,\beta,\alpha} &= \frac{1}{2}\Big(c^\dagger_{i,\alpha}c_{i,\beta} - \delta_{\alpha\beta}\frac{1}{N}\sum_\gamma c^\dagger_{i,\gamma}c_{i,\gamma}\Big)\Big(c^\dagger_{j,\beta}c_{j,\alpha} - \delta_{\alpha\beta}\frac{1}{N}\sum_{\gamma'} c^\dagger_{j,\gamma'}c_{j,\gamma'}\Big) \\
&= \frac{1}{2}\sum_{\alpha,\beta} c^\dagger_{i,\alpha}c_{i,\beta}c^\dagger_{j,\beta}c_{j,\alpha} \\
&\quad -\frac{1}{2N}\sum_{\alpha,\beta}\delta_{\alpha\beta}\Big(\sum_\gamma c^\dagger_{i,\gamma}c_{i,\gamma}\Big)c^\dagger_{j,\beta}c_{j,\alpha} \\
&\quad -\frac{1}{2N}\sum_{\alpha,\beta}\delta_{\alpha\beta}c^\dagger_{i,\alpha}c_{i,\beta}\Big(\sum_{\gamma'} c^\dagger_{j,\gamma'}c_{j,\gamma'}\Big) \\
&\quad +\frac{1}{2N^2}\sum_{\alpha,\beta}\delta_{\alpha\beta}\delta_{\alpha\beta}\Big(\sum_\gamma c^\dagger_{i,\gamma}c_{i,\gamma}\Big)\Big(\sum_{\gamma'} c^\dagger_{j,\gamma'}c_{j,\gamma'}\Big) \; .
\end{aligned}$$

The last two terms cancel each other and we obtain the operator version of the Fierz identity (cf. Eq. (5.24))

$$S_{i,\alpha,\beta}S_{j,\beta,\alpha} = \frac{1}{2}\sum_{\alpha,\beta} c^\dagger_{i,\alpha}c_{i,\beta}c^\dagger_{j,\beta}c_{j,\alpha} - \frac{1}{2N}\sum_{\alpha,\beta} c^\dagger_{i,\alpha}c_{i,\alpha}c^\dagger_{j,\beta}c_{j,\beta} \; . \tag{5.27}$$

Let us note here that the generalization of the Fierz identity given above is derived from the matrices in the fundamental representation. While the matrix representation defines the total spin (cf. Eq. (5.24)), the operator expression Eq. (5.27) is independent of the representation.

5.3. SU(N) Hubbard Heisenberg model

The SU(N) Hubbard Heisenberg model at half-filling reads $H = H_t + H_U + H_J$, where

$$\begin{aligned} H_t &= -t \sum_{\mathbf{r},\mathbf{r}'} \sum_{\alpha} \left(a^\dagger_{\mathbf{r},\alpha} b_{\mathbf{r}',\alpha} + b^\dagger_{\mathbf{r}',\alpha} a_{\mathbf{r},\alpha} \right) , \\ H_U &= \frac{U}{N} \sum_{\mathbf{r}} \left[\left(\sum_{\alpha} a^\dagger_{\mathbf{r},\alpha} a_{\mathbf{r},\alpha} - \frac{N}{2} \right)^2 + \left(\sum_{\alpha} b^\dagger_{\mathbf{r},\alpha} b_{\mathbf{r},\alpha} - \frac{N}{2} \right)^2 \right] , \\ H_J &= -\frac{J}{N} \sum_{\mathbf{r},\mathbf{r}'} \left(D^\dagger_{\mathbf{r},\mathbf{r}'} D_{\mathbf{r},\mathbf{r}'} + D_{\mathbf{r},\mathbf{r}'} D^\dagger_{\mathbf{r},\mathbf{r}'} \right) . \end{aligned} \tag{5.28}$$

Here $a^\dagger_{\mathbf{r},\alpha}$ creates a fermion of flavor α on sublattice A in unit cell $\mathbf{r}$. The associated density operator on sublattice A is $n_{\mathbf{r}} = \sum_\alpha a^\dagger_{\mathbf{r},\alpha} a_{\mathbf{r},\alpha}$. Operators for sublattice B are defined accordingly. Owing to the bipartite nature of the lattice, hopping with matrix element t occurs only between nearest neighbor orbitals A and B of unit cells related by the set of vectors $\mathbf{r} - \mathbf{r}' = \{\mathbf{0}, \mathbf{a}_1 - \mathbf{a}_2, -\mathbf{a}_2\}$.

The operators in the Heisenberg term H_J are defined as $D_{\mathbf{r},\mathbf{r}'} = \sum_\alpha a^\dagger_{\mathbf{r},\alpha} b_{\mathbf{r}',\alpha}$. At $N = 2$ the spin exchange term can be also expressed as

$$H_J = \frac{J}{N} \sum_{\mathbf{r},\mathbf{r}'} \mathbf{S}_{\mathbf{r}} \cdot \mathbf{S}_{\mathbf{r}'} + [(n_{\mathbf{r}} - 1)(n_{\mathbf{r}'} - 1) - 1] \ . \tag{5.29}$$

Here we use the fermionic representation of the spin 1/2 operators on a sublattice $\mathbf{S} = \frac{1}{2} \sum_{\alpha,\beta} a^\dagger_\alpha \boldsymbol{\sigma}_{\alpha,\beta} a_\beta$, where $\boldsymbol{\sigma}$ is the vector of Pauli matrices. In the strong coupling limit $U/t \to \infty$ charge fluctuations are suppressed and one obtains the Heisenberg interaction which can be generalized to SU(N)

$$\mathbf{S}_{\mathbf{r}} \cdot \mathbf{S}_{\mathbf{r}'} = \sum_{\mathbf{r},\mathbf{r}'} \sum_{\alpha,\beta} S_{\mathbf{r},\alpha,\beta} S_{\mathbf{r}',\beta,\alpha} \ , \tag{5.30}$$

which creates flavor-singlets on the bonds connecting $\mathbf{r}$ and $\mathbf{r}'$. These bonds are commonly referred to as valence bonds. The operators

$$S_{\mathbf{r},\alpha,\beta} = \frac{1}{\sqrt{2}} \left(a^\dagger_{\mathbf{r},\alpha} a_{\mathbf{r},\beta} - \delta_{\alpha,\beta} \frac{1}{N} \sum_{\gamma} a^\dagger_{\mathbf{r},\gamma} a_{\mathbf{r},\gamma} \right) , \tag{5.31}$$

($S_{\mathbf{r}',\alpha,\beta}$ for sublattice B, accordingly) correspond to the generators of the SU$(N)_s$ spin symmetry group of the Hamiltonian in Eq. 5.28. They satisfy the commutation relations $[S_{\alpha,\beta,\mathbf{r}}, S_{\gamma,\delta,\mathbf{r}'}] = \delta_{\mathbf{r}\mathbf{r}'} (\delta_{\gamma,\beta} S_{\alpha,\delta,\mathbf{r}} - \delta_{\alpha,\delta} S_{\gamma,\beta,\mathbf{r}})$.

Equivalent to the SU(2) Hubbard model at half-filling ($\rho = 1$) the particle hole transformation in one flavor channel: $a^\dagger_{\mathbf{r},\alpha} \to a_{\mathbf{r},\alpha}$, $b^\dagger_{\mathbf{r},\alpha} \to -b_{\mathbf{r},\alpha}$ leads to the doublon creator

$\eta^\dagger = \sum_{\mathbf{r},\mathbf{r}'} \sum_{\alpha,\beta} (a^\dagger_{\mathbf{r},\alpha} a^\dagger_{\mathbf{r},\beta} - b^\dagger_{\mathbf{r}',\alpha} b^\dagger_{\mathbf{r}',\beta})$. It has been shown for $N = 2$ that $\big|\Psi\big\rangle = (\eta^\dagger)^n \big|\Psi_0\big\rangle$ represent eigenstates of the Hamiltonian [41]. For a pair of flavors the generators η form an SU(2) algebra and are associated with charge (double occupancy). The symmetries can be naturally generalized from the SU(2) case to SU(N), such that the Hamiltonian in Eq. 5.28 is invariant under symmetry operations out of $\mathrm{SU}(N)_s \times \mathrm{SU}(N)_c / \mathrm{Z}_N$ (see Sec. 1.3.2).

The choice of the representation of the symmetry group defines the physical interpretation. Following [105, 233, 234, 19] in this work we use the antisymmetric, self-conjugate representation defined by the local constraint

$$\sum_\alpha a^\dagger_{\mathbf{r},\alpha} a_{\mathbf{r},\alpha} = \sum_\alpha b^\dagger_{\mathbf{r},\alpha} b_{\mathbf{r},\alpha} = \rho \frac{N}{2} \,, \tag{5.32}$$

such that at half-filling ($\rho = 1$) we have $N/2$ electrons per site. As we allow for charge fluctuations this representation is sustained by the constraint (5.32) on average. This representation preserves translational symmetry and allows to capture the crucial competition between quantum mechanical instabilities.

In the following the Hubbard Heisenberg model considered in this paper is obtained by setting $U = 0$ in Eq. (5.28). It is well known that the Hubbard term in the large-N approximation is insufficient to break a continuous symmetry spontaneously, allowing for paramagnetic states only. Hence, the large-N results are not affected by a finite value of U. For finite N we expect the local Coulomb repulsion to only shift the phase boundaries and the model to become more and more Heisenberg-like. Furthermore, choosing $U = 0$ allows to significantly reduce the computational costs. We want to point out that this definition of a t-J-type model does not restrict phase space to singly occupied sites. Charge fluctuations and doubly occupied sites (although they are suppressed) can occur. We will refer to it as the *unconstrained* t-J model. The influence of charge fluctuations will be discussed.

5.4. Large-N Limit

The large-N limit and the mean field (MF) approximation lead to the same saddle point equations, which means they represent the very same limit starting from two different approaches. Either starting from a path integral formulation [234, 19], or the Hamiltonian [39], MF theory gives the *most likely* quadratic Lagrangian, or single-particle Hamiltonian that approximates the energy and correlations of the model in question.

The MF approximation is in close relation to Fermi-liquid theory. Developed by Landau, it is a one to one correspondence between interacting fermions and non-interacting quasi-particles [238]. The interacting ground state is assumed to have a sharp Fermi surface, which results in well defined quasi-particles close to the Fermi level. This is due

to Pauli's principle which blocks the scattering inside the Fermi sea (the only allowed scattering mechanism is by creating electron-hole pairs), resulting in a quasi-particle lifetime which is much longer than the inverse of the excitation energy. The quasi-particles behave like electrons in a noninteracting system, and as a consequence, the Fermi-liquid properties are described by the same expressions as the corresponding Fermi-gas ones. Thus it is possible to account for the effect of interactions by renormalizing model parameters, such as the effective mass.

This fundamental idea is also realized in the MF approximation. In general, the infinite number of degrees of freedom are divided into two sets. While a small set of degrees of freedom is treated exactly, the effects of the remaining degrees of freedom are summarized as a MF acting on the first set. Within this approach one approximates the full Hamiltonian by neglecting the influence of quantum fluctuations. Minimizing the free energy with respect to a control parameter leads to an Ansatz for a solution which is then determined self-consistently. This local approximation becomes exact in the limit of infinite coordination number, or equivalently, infinite dimensions.

For some operators A, B we define the deviations from their thermodynamical mean

$$\begin{aligned} A &= \langle A\rangle + (A - \langle A\rangle) \\ B &= \langle B\rangle + (B - \langle B\rangle)\,, \end{aligned} \tag{5.33}$$

and consider the fluctuations of their correlations to be small, such that

$$\begin{aligned} 0 &\simeq \big(A - \langle A\rangle\big)\,\big(B - \langle B\rangle\big) \\ AB &\simeq \langle A\rangle\langle B\rangle + A(B - \langle B\rangle) + B(A - \langle A\rangle)\,. \end{aligned} \tag{5.34}$$

Let us note here again, that (in general) the unbiased MF-decoupling of local interactions, like the Hubbard local Coulomb repulsion, leads to a trivial MF Hamiltonian which is only shifted by an energy proportional to the MF control (order) parameter. This can be overcome by *explixit* breaking of symmetries, like the spin-rotational-, or sublattice symmetry. Of course, this choice biases towards this certain type of symmetry breaking. In this investigation we want to start out from an unbiased approach in order to enhance correlations with decreasing N, which will eventually break SU(N) spin rotational symmetry spontaneously. The Hubbard term in our Hubbard Heisenberg model would only contribute a constant energy shift to the MF decoupling and we will set $U/t = 0$.

Starting from the operators for the Heisenberg term in Eq. (5.28) ($D_{\mathbf{r},\mathbf{r}'} = \sum_\alpha a^\dagger_{\mathbf{r},\alpha} b_{\mathbf{r}',\alpha}$), we define the deviation operators

$$D_{\mathbf{r},\mathbf{r}'} = \langle D_{\mathbf{r},\mathbf{r}'}\rangle + \big(D_{\mathbf{r},\mathbf{r}'} - \langle D_{\mathbf{r},\mathbf{r}'}\rangle\big)\,, \tag{5.35}$$

such that

$$\begin{aligned} D^\dagger_{\mathbf{r},\mathbf{r}'} D_{\mathbf{r},\mathbf{r}'} &= \left[\overline{\langle D_{\mathbf{r},\mathbf{r}'}\rangle} + \left(D^\dagger_{\mathbf{r},\mathbf{r}'} - \overline{\langle D_{\mathbf{r},\mathbf{r}'}\rangle}\right)\right]\left[\langle D_{\mathbf{r},\mathbf{r}'}\rangle + \left(D_{\mathbf{r},\mathbf{r}'} - \langle D_{\mathbf{r},\mathbf{r}'}\rangle\right)\right] \\ &= \overline{\langle D_{\mathbf{r},\mathbf{r}'}\rangle}\langle D_{\mathbf{r},\mathbf{r}'}\rangle + \overline{\langle D_{\mathbf{r},\mathbf{r}'}\rangle}\left(D_{\mathbf{r},\mathbf{r}'} - \langle D_{\mathbf{r},\mathbf{r}'}\rangle\right) + \left(D^\dagger_{\mathbf{r},\mathbf{r}'} - \overline{\langle D_{\mathbf{r},\mathbf{r}'}\rangle}\right)\langle D_{\mathbf{r},\mathbf{r}'}\rangle \\ &\quad + \underbrace{\left(D^\dagger_{\mathbf{r},\mathbf{r}'} - \overline{\langle D_{\mathbf{r},\mathbf{r}'}\rangle}\right)\left(D_{\mathbf{r},\mathbf{r}'} - \langle D_{\mathbf{r},\mathbf{r}'}\rangle\right)}_{=0} \\ &= D_{\mathbf{r},\mathbf{r}'}\overline{\langle D_{\mathbf{r},\mathbf{r}'}\rangle} + D^\dagger_{\mathbf{r},\mathbf{r}'}\langle D_{\mathbf{r},\mathbf{r}'}\rangle - \left|\langle D_{\mathbf{r},\mathbf{r}'}\rangle\right|^2 . \end{aligned} \tag{5.36}$$

We define the mean-field values $\langle D_{\mathbf{r},\mathbf{r}'}\rangle$ by the complex parameters $Z_{\mathbf{r},\mathbf{r}'}$. This allows to restate the SU(2) Heisenberg Hamiltonian $H_J = -\frac{J}{4}\sum_{\mathbf{r},\mathbf{r}'}\left(D^\dagger_{\mathbf{r},\mathbf{r}'}D_{\mathbf{r},\mathbf{r}'} + D_{\mathbf{r},\mathbf{r}'}D^\dagger_{\mathbf{r},\mathbf{r}'}\right)$ as

$$\begin{aligned} H^{\mathrm{MF}} &= H_t + H_J^{\mathrm{MF}} \\ &= -t\sum_{\mathbf{r},\mathbf{r}'}\left(D^\dagger_{\mathbf{r},\mathbf{r}'}D_{\mathbf{r},\mathbf{r}'} + \mathrm{h.c.}\right) - \frac{J}{2}\sum_{\mathbf{r},\mathbf{r}'}\left(D^\dagger_{\mathbf{r},\mathbf{r}'}\overline{\langle D_{\mathbf{r},\mathbf{r}'}\rangle} + D^\dagger_{\mathbf{r},\mathbf{r}'}\langle D_{\mathbf{r},\mathbf{r}'}\rangle - \left|\langle D_{\mathbf{r},\mathbf{r}'}\rangle\right|^2\right) \\ &= -t\sum_{\mathbf{r},\mathbf{r}'}\left(D^\dagger_{\mathbf{r},\mathbf{r}'}D_{\mathbf{r},\mathbf{r}'} + \mathrm{h.c.}\right) - \frac{J}{2}\sum_{\mathbf{r},\mathbf{r}'}\left(D^\dagger_{\mathbf{r},\mathbf{r}'}Z^*_{\mathbf{r},\mathbf{r}'} + D^\dagger_{\mathbf{r},\mathbf{r}'}Z_{\mathbf{r},\mathbf{r}'} - Z_{\mathbf{r},\mathbf{r}'}Z^*_{\mathbf{r},\mathbf{r}'}\right) \\ &= \sum_{\mathbf{r},\mathbf{r}'}\left(t' D_{\mathbf{r},\mathbf{r}'} + t'^* D^\dagger_{\mathbf{r},\mathbf{r}'} + \frac{J}{2}Z_{\mathbf{r},\mathbf{r}'}Z^*_{\mathbf{r},\mathbf{r}'}\right) . \end{aligned} \tag{5.37}$$

Here we introduced the renormalized hopping $t' = -t - \frac{J}{2}Z_{\mathbf{r},\mathbf{r}'}$ to emphasize the fact that the MF model is a one-particle Hamiltonian. Minimizing the free energy yields the saddle point equations

$$\begin{aligned} F(Z_{\mathbf{r},\mathbf{r}'}) &= -\frac{1}{\beta}\ln \mathrm{Tr}\, \mathrm{e}^{-\beta H^{\mathrm{MF}}(Z_{\mathbf{r},\mathbf{r}'})} , \\ \frac{\partial F}{\partial Z_{\mathbf{r},\mathbf{r}'}} &\stackrel{!}{=} 0 \quad \rightarrow \quad \langle D_{\mathbf{r},\mathbf{r}'}\rangle \stackrel{!}{=} Z_{\mathbf{r},\mathbf{r}'} , \end{aligned} \tag{5.38}$$

which become exact in the large-N limit. Notice that the creation and annihilation operators used in the operators above (Eq. (5.35) etc.), are not N-flavored spinors, but correspond to spinless fermion operators.

As has been shown for the square lattice this mean-field Hamiltonian is unstable towards a staggered flux pattern and dimerization due to the Fermi surface instability caused by the perfect nesting of the tight binding model. Although the limit $N \to \infty$ allows to obtain simplified Hamiltonians, their solution still remains not completely trivial. This situation especially becomes difficult as one allows for a large number of degrees of freedom. Here, we solve the mean-field equations for a 256×256 lattice of six site (nine bonds) unit cells which retain the $\mathrm{C}_{6,v}$ symmetry of the lattice. This

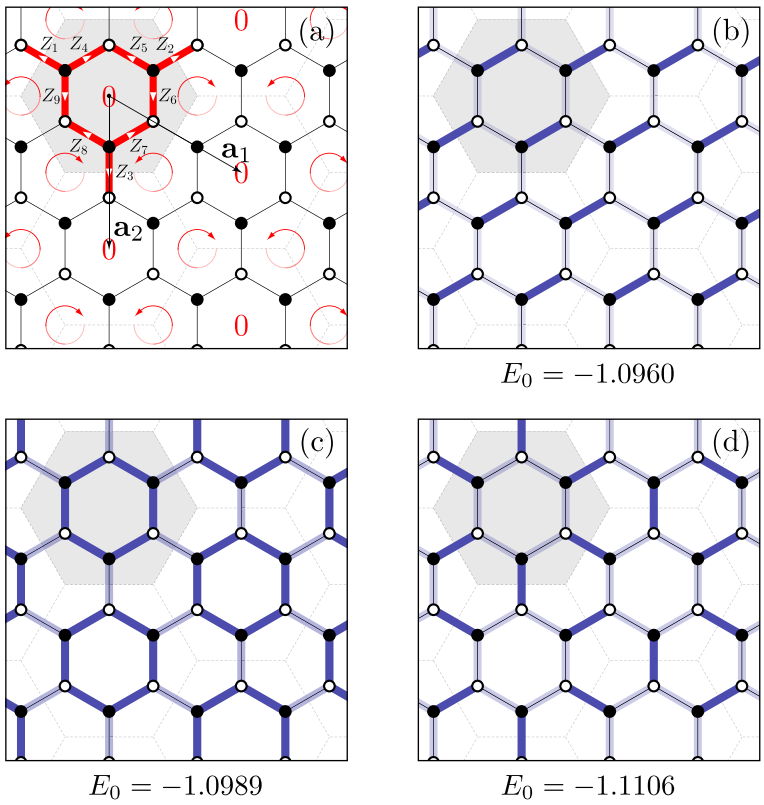

Fig. 5.1.: Definition of the six site unit cell used to solve the saddle point equations self-consistently (a). The corresponding nine bonds of the chosen unit cell are shown in red. Red arrows on the centers of the plaquettes depict a possible flux-pattern arising on the honeycomb lattice which could be realized with this large unit cell. Indeed, no (staggered) flux phase emerges in the large-N limit. Staggered order (b) and plaquette order (c) are metastable dimerized states. For small values of $t/J < 0.21$ a star-shaped dimerization pattern (d) forms, spontaneously breaking translational symmetry of the lattice. The dimer patterns and the corresponding energies are obtained for $t/J = 0.1$, $N = 6 \times L^2 = 6 \times 256^2$.

setup allows to obtain a large number of possible states. In Fig. 5.1a the definition of the six site unit cell with the corresponding nine bonds is shown. Their orientation is indicated by white arrows. Red arrows on the centers of the plaquettes depict a possible flux-pattern which could arise on the honeycomb lattice and could be realized with this choice of unit cell.

To solve the saddle point equations (5.38) self-consistently we define the operators for the six-site unit cell in the spinor $\mathbf{\Psi}_\mathbf{k}^\dagger = (a_\mathbf{k}^\dagger, b_\mathbf{k}^\dagger, \ldots, f_\mathbf{k}^\dagger)$. The Hamiltonian $H = \sum_\mathbf{k} \mathbf{\Psi}_\mathbf{k}^\dagger \mathbf{H}_\mathbf{k}^{\mathrm{MF}} \mathbf{\Psi}_\mathbf{k}$ can be brought to diagonal form with a unitary transformation

$$\begin{aligned} H &= \sum_{\mathbf{k}} \boldsymbol{\Psi}_{\mathbf{k}}^{\dagger} \overbrace{\mathbf{U}_{\mathbf{k}}^{\dagger}\mathbf{U}_{\mathbf{k}}}^{\mathbf{1}} \mathbf{H}_{\mathbf{k}}^{\mathrm{MF}} \overbrace{\mathbf{U}_{\mathbf{k}}^{\dagger}\mathbf{U}_{\mathbf{k}}}^{\mathbf{1}} \boldsymbol{\Psi}_{\mathbf{k}} \\ &= \sum_{\mathbf{k}} \underbrace{\boldsymbol{\Psi}_{\mathbf{k}}^{\dagger}\mathbf{U}_{\mathbf{k}}^{\dagger}}_{\boldsymbol{\gamma}_{\mathbf{k}}^{\dagger}} \underbrace{\mathbf{U}_{\mathbf{k}}\mathbf{H}_{\mathbf{k}}^{\mathrm{MF}}\mathbf{U}_{\mathbf{k}}^{\dagger}}_{(E_1,\ldots,E_6)_{\mathbf{k}}\cdot\mathbf{1}} \underbrace{\mathbf{U}_{\mathbf{k}}\boldsymbol{\Psi}_{\mathbf{k}}}_{\boldsymbol{\gamma}_{\mathbf{k}}} \\ &= \sum_{n,\mathbf{k}} E_{n,\mathbf{k}} \boldsymbol{\gamma}_{n,\mathbf{k}}^{\dagger} \boldsymbol{\gamma}_{n,\mathbf{k}} \,. \end{aligned} \tag{5.39}$$

Here we defined the quasi-particle operators $\boldsymbol{\gamma}$ related to the original particle operators via

$$\boldsymbol{\gamma}^{\dagger} = \boldsymbol{\Psi}^{\dagger}\mathbf{U}^{\dagger}\,, \quad \boldsymbol{\gamma} = \mathbf{U}\boldsymbol{\Psi} \quad \longleftrightarrow \quad \boldsymbol{\Psi}^{\dagger} = \boldsymbol{\gamma}^{\dagger}\mathbf{U}\,, \quad \boldsymbol{\Psi} = \mathbf{U}^{\dagger}\boldsymbol{\gamma}\,, \tag{5.40}$$

and $E_{n,\mathbf{k}}$ is the n-th eigenvalue at momentum $\mathbf{k}$. The diagonalization of the Hamiltonian allows to measure expectation values for the parameters $Z = \langle \Psi^{\dagger}\Psi \rangle = \langle \boldsymbol{\gamma}^{\dagger}\mathbf{U}\mathbf{U}^{\dagger}\boldsymbol{\gamma} \rangle$ on the bonds spanned by $\mathbf{r}, \mathbf{r}'$. Feeding the expectation values back into the Hamiltonian the procedure is repeated until self-consistency is achieved and the saddle point equations (5.38) are fulfilled. This way we are able to obtain solutions for the parameters $Z_{\mathbf{r},\mathbf{r}'}$ which are proportional to the bond strength and carry a flux ϕ,

$$\begin{aligned} Z_{\mathbf{r},\mathbf{r}'} &= r_{\mathbf{r},\mathbf{r}'} \mathrm{e}^{\mathrm{i}\phi_{\mathbf{r},\mathbf{r}'}} \,, \\ r_{\mathbf{r},\mathbf{r}'} &= Z_{\mathbf{r},\mathbf{r}'}^{*} Z_{\mathbf{r},\mathbf{r}'} \propto \mathbf{S}_{\mathbf{r}} \cdot \mathbf{S}_{\mathbf{r}'} + \mathrm{const} \,. \end{aligned} \tag{5.41}$$

For a large ratio t/J hopping dominates and all parameters $Z_{\mathbf{r},\mathbf{r}'}$ are equal and real, thus the system is semimetallic. Below a critical value of $t/J = 0.21$ we find the parameters of minimal energy can be expressed by the two bond strengths r_{A} and r_{B}

$$\begin{aligned} r_1 = r_2 = r_3 = r_{\mathrm{A}} \,, \\ r_4 = r_5 = r_6 = r_7 = r_8 = r_9 = r_{\mathrm{B}} \,, \\ \phi_i = 0 \,. \end{aligned} \tag{5.42}$$

For $r_{\mathrm{A}} \neq r_{\mathrm{B}}$ (or equivalent degenerate solutions) this corresponds to the star-shape pattern shown in Fig. 5.1d, also known as Kekule texture. This three-fold degenerate groundstate spontaneously breaks lattice rotational and translational symmetry. Figures 5.1b and 5.1c are metastable solutions close to the true ground state. The dimerization pattern is consistent with the approximative solution found in Ref [239]. The energy per unit cell for homogeneous bond strength at $t/J = 0.1$ is $E_0 = -1.0921$).

The evolution of the dimerization order parameter and the flux is pictured in Fig. 5.2. In contrast to the large-N t-J model on the square lattice, where the dimerization is

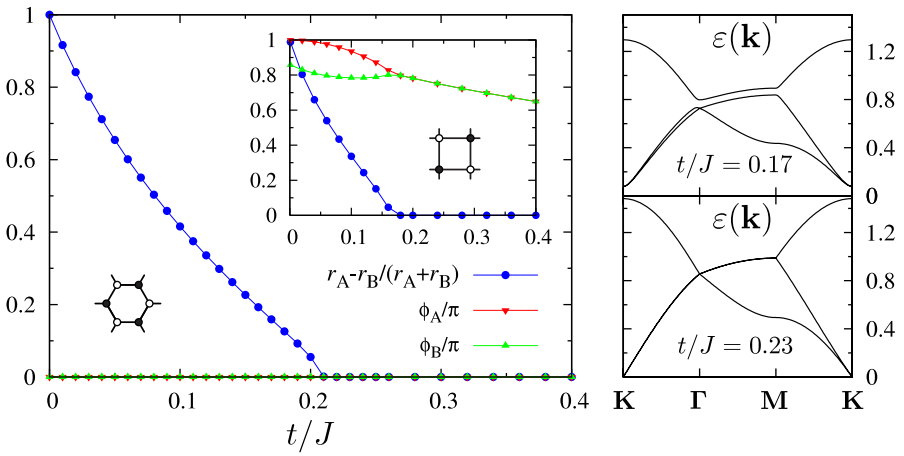

Fig. 5.2.: Dimerization (circles) and flux order parameters (triangles) as a function of hopping over spin exchange. There exists no persistent flux. The inset shows the results for the square lattice for comparison, the panels on the right show the one particle spectral function close to the phase transition from a band insulator to a semimetal.

accompanied by the emergence of a staggered flux pattern [19], on the honeycomb lattice the flux ϕ remains zero over the whole parameter space. For comparison, the inset shows the same quantities for the square lattice. There a d-density wave ground state, which is a semimetal with a homogeneous phase on all bonds, is unstable towards box dimerization below $t/J \approx 0.17$ [19]. The two plots on the right hand side show the energy spectrum along the high symmetry path of the hexagonal Brillouin zone and close to the phase transition. Here, the nodal point is shifted to the Γ-point because of the structure of the six site unit cell. In the semimetal phase the low energy spectrum is linear in $\mathbf{k}$ and gapless. As one enters the dimerized phase the unit cell triples and the first Brillouin zone is cut in thirds. At the boundaries of the new Brillouin zone the band degeneracy is lifted by the $\mathbf{K}$-periodic potential of the dimer-pattern and an excitation gap opens.

The stability of the large-N results can be tested and improved by means of random phase approximation, where essentially, Gaussian fluctuations of order $1/N$ around the saddle point solution are taken into account. However, the SU(N) generalized formulation of the projector QMC allows to tackle arbitrary values of N exactly, such that we will use QMC at a large value of N to test the stability of the dimerization against correlations.

5.5. Projector quantum Monte Carlo for SU(N)

To capture the complex interplay of a multitude of degrees of freedom at finite N we employ ground state ($T = 0$) projector QMC (PQMC), which has been introduced in

Sec. 1.2 and which has been proven to be an unbiased and controlled method to solve the SU(N) Hubbard Heisenberg model exactly at arbitrary (even) values of N. Due to the absence of a sign-problem in determinantal QMC simulations in the half-filled case, it is the method of choice for extrapolations to the thermodynamic limit (TDL), leading to essentially exact results limited only by the statistical noise. A detailed description of the algorithm is given in [19, 10]. We will now explain technical details required to carry out efficient simulations at SU(N) symmetry.

The Monte-Carlo approach relies on the path integral formulation of the partition function. The imaginary time axis can be Trotter decomposed into m imaginary time slices where $m\Delta\tau = \beta$. This introduces a systematic error of order $(\Delta\tau t)^2$. We found a finite imaginary time-step $\Delta\tau t = 0.05$ to be sufficiently small and verified by extrapolating $\Delta\tau \to 0$ that this finite imaginary time step produces no artifacts. Using the Hubbard Stratonovich (HS) transformation two-body terms can be decoupled at the cost of bosonic fields represented by a complex variable z_b per bond b. The partition function in the limit $\Delta\tau \to 0$ is given by a functional integral over the space and imaginary time dependent HS fields $\{z\}, \{\bar{z}\}$ as

$$Z \propto \int \prod_b \mathrm{D}\mathrm{Re} z_b(\tau)\, \mathrm{D}\mathrm{Im} z_b(\tau)\, \mathrm{e}^{-NS(\{z\},\{\bar{z}\})}. \tag{5.43}$$

The action reads

$$S(\{z\},\{\bar{z}\}) = \underbrace{\int \mathrm{d}\tau\, J \sum_b |z_b(\tau)|^2}_{S_0} \; \underbrace{- \ln \mathrm{Tr}\left[T \mathrm{e}^{-\int_0^\beta \mathrm{d}\tau h(\tau)}\right]}_{S'},$$

with $h(\tau)$ being the interacting part of the Lagrangian (Hamiltonian) which is mapped onto the noninteracting field of auxiliary spins by the HS transformation (c.f. Sec. 1.2). In general, $\mathrm{e}^{-NS(z,\bar{z})}$ is not a positive quantity which leads to the notorious sign problem in Monte Carlo simulations. However, at half-band filling and even values of N particle-hole symmetry leads to the absence of a minus-sign problem. At this filling, and under the canonical transformation

$$a^\dagger_{\mathbf{r}} \to -a_{\mathbf{r}}\,, \qquad b^\dagger_{\mathbf{r}} \to b_{\mathbf{r}}\,, \tag{5.44}$$

the Hamiltonian $h(\tau)$ transforms as $h(\tau) \to \overline{h(\tau)}$. This implies that $S' = \overline{S'}$, hence S' is real and

$$\mathrm{e}^{-NS} = \mathrm{e}^{-NS_0} \left[\mathrm{Tr}\left[T \mathrm{e}^{-\int_0^\beta \mathrm{d}\tau h(\tau)}\right]\right]^N\,, \tag{5.45}$$

is positive. The equation above also reflects the realization in the Monte Carlo simulation, where S' is represented by a determinant which is the same for all N flavors.

Interested in the ground state properties, we choose a projective method. We choose a trial wave function of the form

$$\left|\Psi_T\right\rangle = \left|\Psi_T\right\rangle_1 \otimes \left|\Psi_T\right\rangle_2 \otimes \cdots \otimes \left|\Psi_T\right\rangle_N , \tag{5.46}$$

which is assumed to have a finite overlap $\left\langle\Psi_T\middle|\Psi_0\right\rangle$ (which is generally fulfilled for finite systems). Here $\left|\Psi_T\right\rangle_\alpha$ is the ground state of the single particle Hamiltonian in the flavor α Hilbert subspace

$$H^0_\alpha = -t \sum_{\mathbf{r},\mathbf{r}'} a^\dagger_{\mathbf{r},\alpha} b_{\mathbf{r}',\alpha} \exp\left(\frac{2\pi \mathrm{i}}{\Phi_0} \int_{\mathbf{r}}^{\mathbf{r}'} \mathrm{d}\boldsymbol{\ell} \cdot \mathbf{A}\right) + \text{h.c.} . \tag{5.47}$$

Here, $\Phi_0 = he/c$ is the flux quantum. We choose a thrusted flux Φ/Φ_0 sufficiently small such that it is negligible within the achieved numerical accuracy to guarantee the non-degeneracy of the trial wave function such that the simulation can converge to a distinct ground state (c.f. Sec. 1.2). The projection parameter Θ used to obtain the ground state wave function $\left|\Psi_0\right\rangle = -\Theta H \left|\Psi_T\right\rangle$ is typically $\Theta t = 30$ (plus the imaginary time used for the propagations of unequal time correlations functions).

Simulations are performed for systems of linear size $L = 3$, 6, 9, 12, 15 and 18 with $2L^2$ sites to capture the nodal points. Compared to the square lattice, on the honeycomb lattice, finite size effects are much more pronounced due to large fluctuations and the reduced coordination number. A rough estimate using linear spin wave theory predicts that the asymptotic scaling of the staggered magnetization with system size is reached for linear dimension $L \geq 36$, only. Therefore we will include higher orders of $1/L$ in our finite size extrapolations.

5.6. Finite N

Our results are summarized in the phase diagram shown in Fig. 5.3. Here, we consider the half-filled unconstrained t-J model as a function of N and t/J. The $t = 0$ line corresponds to the Heisenberg model where charge fluctuations are completely suppressed. In the large-N limit, the data stems from the mean-field calculation given in Sec. 5.4. All our simulations are carried out with the projective QMC algorithm discussed in Sec. 1.2.

From large-N down to $N = 4$ we essentially reproduce the saddle point result with a somewhat larger value of t/J, reflecting the instability of the semimetal in favor of the star-shape spin-dimerized phase or valence bond solid (VBS). The phase diagram provides a pedagogical example for the failure of an unbiased large-N approach to describe the SU(2) ground state. Even if one takes corrections to the large-N limit into account, only the explicit breaking of symmetries allows to obtain a rough guess of the true ground state. Indeed, two of the authors have recently shown the validity of a symmetry breaking mean-field treatment of the Hubbard model on the honeycomb lattice in

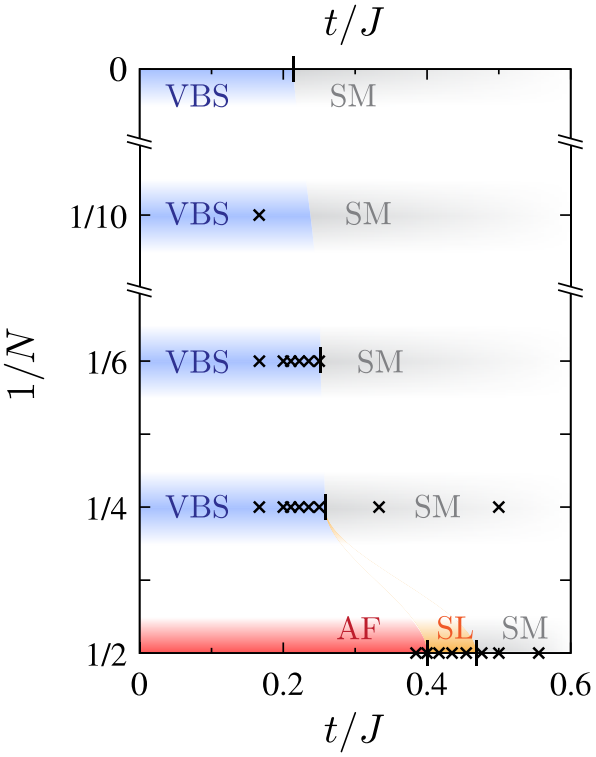

Fig. 5.3.: Phase diagram in the parameter space t/J and $1/N$ for even N. Crosses denote the parameter ratio t/J for which QMC simulations have been carried out. For all N the system undergoes a quantum phase transition (QPT) from a semimetal (SM) to a an insulator. While for $N \geq 4$ the insulating state is a star-shape VBS (Kekule texture), at $N = 2$ the semimetal and an antiferromagnetic (AF) insulator are separated by an intermediate phase which we identify as a potential spin liquid (SL) [137].

the presence of a in-plane magnetic field in the weak and strong coupling regime [240]. However, in the intermediate coupling regime Hartree Fock mean field utterly fails to reproduce the true ground state properties.

The most interesting feature of the phase diagram occurs at $N = 2$ where for increasing t/J the spin-symmetry is spontaneously broken and the ground state is Néel ordered. However, the opening of a single-particle gap and the onset of magnetization in the antiferromagnetic (AF) phase do not coincide. Instead a supposedly disordered, gapped spin-liquid phase precedes the transition separating semimetal and antiferromagnet. This scenario is in accordance with the SU(2) Hubbard model which has been reported in [137].

We will now discuss ground state properties of the t-J model as a function of J/t and for increasing correlations with decreasing N. In Sec. 5.6.1 we introduce the observables considered to characterize the different phases for the exemplary case of $N = 10$. Sections

5.6.2 and 5.6.3 discuss the influence of enhanced correlations on the dimerized ground state at large J/t and Sec. 5.6.4 treats the emergence of new phases at the SU(2) level.

5.6.1. SU(10) and observables

In order to test the stability of the star-shape dimerization obtained in the large-N limit for large J (cf. Fig. 5.1d) we perform a PQMC simulation at the large value of $N = 10$ and $J/t = 6.0$. To detect whether the dimerization is persistent against the introduction of correlations and to capture other types of symmetry breaking we measure observables and correlation functions according to Eq. 1.23. For the correlation between two local operators O_1 and O_2, we employ the short notation for the cumulant

$$\langle\langle O_1 O_2 \rangle\rangle := \langle O_1 O_2 \rangle - \langle O_1 \rangle \langle O_2 \rangle \, . \tag{5.48}$$

The structure factor S_{AF} on one sublattice is associated with the antiferromagnetic breaking of flavor-symmetry

$$S_{\mathrm{AF}}(\mathbf{q}) = \sum_{\mathbf{r}} \sum_{\alpha,\beta} \mathrm{e}^{\mathbf{iqr}} \langle\langle \mathbf{S}_{\mathbf{0},\alpha,\beta} \cdot \mathbf{S}_{\mathbf{r},\beta,\alpha} \rangle\rangle \, . \tag{5.49}$$

On the basis of the SU(2) case of spin-symmetry breaking we will refer to it as (staggered) magnetization. Nearest neighbor AF order is established within the unit cell, where, e.g., the z-component of the magnetic moment points up on orbital A and down on orbital B. The corresponding momentum at which the system orders is then $\mathbf{q} = \mathbf{\Gamma}$.

Our code allows for the efficient measurement of unequal-time correlation functions [23]. For an observable $O(\mathbf{q})$ we can compute

$$S_O(\mathbf{q}, \tau) = \langle O(\mathbf{q}, \tau) O(-\mathbf{q}, 0) \rangle - \delta_{\mathbf{q},\mathbf{0}} \langle O(\mathbf{0}, 0) \rangle^2 \, . \tag{5.50}$$

The long imaginary time behavior allows us to extract the corresponding gaps without the need to invoke Maximum Entropy. We can derive the primary low energy excitation from a fit to the decay behavior of the unequal time correlations which gives us a lower bound to the excitation spectrum and defines the excitation gap. As an example, Fig. 5.4 shows the imaginary time, one-particle Green's function $G(\mathbf{q}, \tau) = \langle c^\dagger_{\mathbf{q}}(\tau) c_{-\mathbf{q}} \rangle$ at one of the nodal points $\mathbf{K}$, located at the corner of the Brillouin zone. Since the data points are correlated in imaginary time τ we consider the proper covariance matrix in our least squares fits to the asymptotic slope of the Green's function which take the form $y(\tau) = a_0 \exp(-\Delta\, x)$. The inset shows the fitted slope, which corresponds to the single-particle gap Δ_{sp}, as a function of the fitting range which runs from τ_{start} to the maximally projected timescale. As can be seen the slope is constant over a large range of τ_{start}. The actual τ_{start} for which the data is extracted is chosen with respect to the onset on asymptotic scaling behavior of the Green's function. Dotted lines in the inset show the magnitude of the errorbars for a typically $\tau_{\mathrm{start}} \approx 4$.

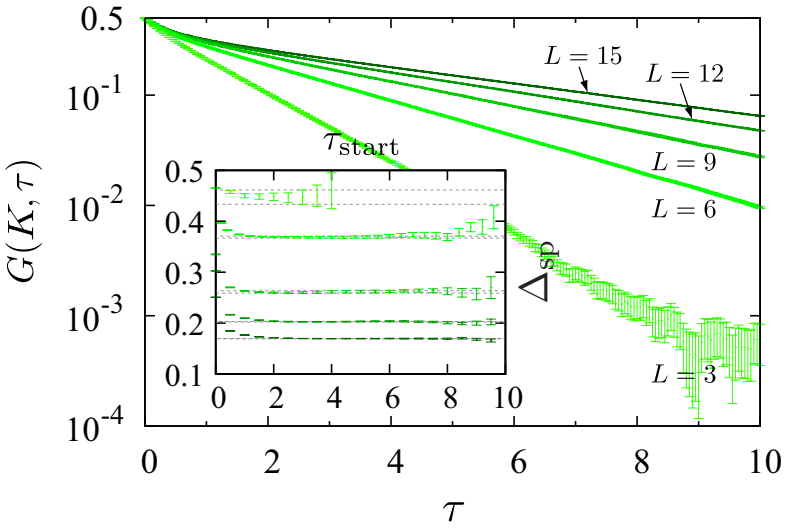

Fig. 5.4.: Exemplary unequal time Green's functions $G(\mathbf{q},\tau) = \langle c^\dagger_{\mathbf{q}}(\tau) c_{-\mathbf{q}} \rangle$ at the nodal point for different system sizes. The inset shows the fitted slope, which corresponds to the single-particle gap Δ_{sp}, as a function of the fitting range [τ_{start}:10]. Since data points are correlated in imaginary time τ we consider the proper covariance matrix in our fits. Dotted lines show the errorbars for the τ_{start}, which has been actually taken to extract the gap.

The quality of the data allows us to safely determine the single-particle gap from the unequal time one-particle Green's function and the singlet-triplet gap (or spin gap) from the unequal time spin-spin correlation. Unfortunately, for most of our parameters, the unequal time density-density correlation decays rapidly to the order of numerical accuracy, such that is not possible to reliably extract a charge gap.

Figure 5.5 shows the spin structure factor, the spin gap and the single-particle gap at $J/t = 6.0$ as a function of $1/L$. The fits performed are of the form $y(L) = \sum_{i=0}^{N_i} a_i L^{-i}$, where the order N_i depends on the number of available system sizes and is chosen according to the least value of the sum of squared residuals, such that $\chi^2/N_i \approx 1$. In the particular case shown in Fig. 5.5 a fit of second order in $1/L$ gives the best result.

In accordance with the singlet formation predicted by the mean-field approach we find a large spin and single-particle gap. The primary excitations in the flavor (spin) sector out of the ground state correspond to the transformation of a singlet on a bond (i,j) into a triplet at the energy cost of the singlet-triplet gap. Each flavor-singlet (triplet) is an odd (even) superpositions of a pair of flavors α, β on the sites at $\mathbf{r},\mathbf{r}'$ forming a bond $(a^\dagger_{\mathbf{r},\alpha} b^\dagger_{\mathbf{r}',\beta} \mp a^\dagger_{\mathbf{r},\beta} b^\dagger_{\mathbf{r}',\alpha})$, which is the contraction of arbitrary pairs of particle and hole indices. Hence SU(N) flavor symmetry is conserved, as long as $\alpha \neq \beta$. This is correctly reflected in the absence of long range magnetic order as S_{AF} scales to zero. It follows that singlet states have $N/2$ valence bonds emanating from each site. The

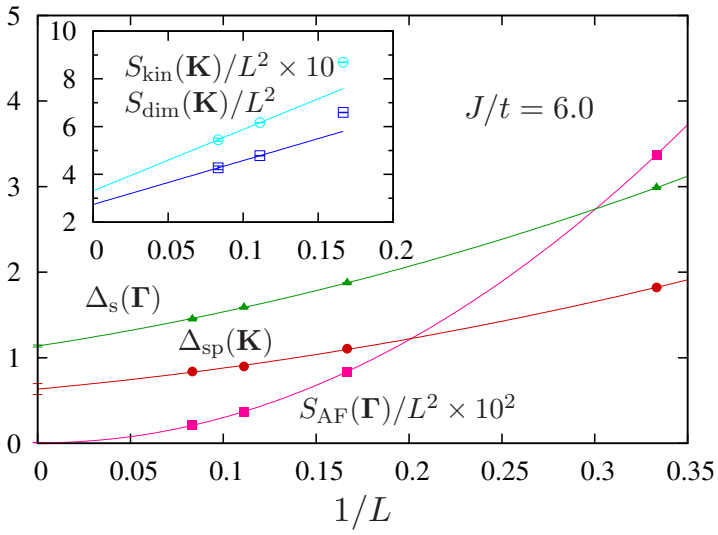

Fig. 5.5.: $N = 10$ — Finite size extrapolation of the staggered susceptibility $S_{\rm AF}$, spin gap $\Delta_{\rm s}$ and single-particle gap $\Delta_{\rm sp}$ in the star-shape valence bond crystal close to the large-N limit for $J/t = 6.0$. The inset shows that both dimer-dimer correlations and bond-energy correlations extrapolate to a finite value.

injection of an additional electron (e.g., via inverse photoemission spectroscopy (IPES)) on top of a dimerized ground state is a higher excitation since the single-particle gap is significantly larger than the spin gap. The dimerized phase or VBS consists of flavor-singlets (triplets) in an ordered pattern. A VBS is thus present when at least one flavor pair orders along a geometric pattern of bonds.

To capture the formation of a valence bond solid we measure the dimer-dimer structure factor

$$S_{\rm dim}(\mathbf{q}) = \sum_{\mathbf{r},\mathbf{r}',\mathbf{s},\mathbf{s}'} \sum_{\alpha,\beta,\gamma,\delta} \mathrm{e}^{\mathrm{i}\mathbf{q}\mathbf{r}} \langle\!\langle (\mathbf{S}_{\mathbf{0},\alpha,\beta} \cdot \mathbf{S}_{\mathbf{r}',\beta,\alpha} - 1/4)(\mathbf{S}_{\mathbf{s},\gamma,\delta} \cdot \mathbf{S}_{\mathbf{s}',\delta,\gamma} - 1/4) \rangle\!\rangle \,, \qquad (5.51)$$

where $\mathbf{r}, \mathbf{r}', \mathbf{s}, \mathbf{s}'$ denote two pairs of nearest neighbor sites corresponding to two bonds. The offset of $-1/4$ we will be omitted in finite size extrapolations and is used only in real-space plots to emphasize the correlation patterns. A finite value in the thermodynamic limit (TDL) corresponds to long range order of valence bonds which breaks the translational and/or rotational symmetry of the lattice. From the ordering vector $\mathbf{q}$ the geometry of the pattern can be deduced, which can be also and more easily distinguished in the real-space correlation pattern of $S_{\rm dim}$. In the definition in Eq. 5.51 we neglect the influence of charge fluctuations (compare Eq. 5.29). Although charge fluctuations are present, they are suppressed with increasing J/t and the observable clearly determines the breaking of a lattice symmetry. The dimer-dimer structure factor is sensitive to

singlet and triplet correlations. The inset of Fig. 5.5 shows the extrapolation to a finite value of the dimer structure factor at $\mathbf{K}$, which corresponds to the ordering vector of the star-shape pattern.

In addition to the magnetic bond-bond correlations we measure the correlation of the kinetic energy between bonds which is usually known as bond energy correlation

$$S_{\mathrm{kin}}(\mathbf{q}) = \sum_{\mathbf{r},\mathbf{r}',\mathbf{s},\mathbf{s}'} \sum_{\alpha} \mathrm{e}^{\mathrm{i}\mathbf{q}(\mathbf{r}-\mathbf{s})} \langle\langle (a^{\dagger}_{\mathbf{r},\alpha} b_{\mathbf{r}',\alpha} + b^{\dagger}_{\mathbf{r}',\alpha} a_{\mathbf{r},\alpha})(a^{\dagger}_{\mathbf{s},\alpha} b_{\mathbf{s}',\alpha} + b^{\dagger}_{\mathbf{s}',\alpha} a_{\mathbf{s},\alpha}) \rangle\rangle \; .$$

The bond energy correlation measures correlation of the mobility of charges along nearest neighbor bonds and hence captures lattice symmetry breaking in the charge channel. The bond energy correlations can be assumed to lock in with the dimer-dimer correlations producing a strong signal on bonds where a spin-singlet (triplet) exists. However, they not necessarily have to coincide.

In the VBS phase electrons are essentially frozen (confined to the singlet-bonds) and can be reduced to quasi localized magnetic moments. This can be seen in the inset of Fig. 5.5 and the small magnitude of the bond energy correlations. Nevertheless, we find the bond energy correlations qualitatively follow the dimer-dimer correlations as expected for a state where spin and charge degrees of freedom are confined.

Figure 5.6 shows the real-space dimer-dimer correlations. The pattern of the six jagged star radiating from the empty plaquettes can be clearly identified. The bond strength is indicated by color and thickness and reflects the existence of a singlet, or triplet relative to the striped reference bond. Hence, the VBS obtained as solution in the $N \to \infty$ limit is robust against correlations at finite N.

5.6.2. SU(6)

At $N = 6$ the picture essentially remains the same: Figure 5.7 shows the opening of the gaps and the magnetization for different values of J/t. Single-particle and spin gap open simultaneously indicating the spontaneous dimerization into a VBS. The dimer-dimer and bond energy correlations in Fig. 5.8 complement this statement. Thus, the SU(6) t-J model also exhibits a QPT from a semimetal to a star-shape VBS.

5.6.3. SU(4)

At the SU(4) level, correlations start to be strong enough to significantly affect the stability of the VBS. Figure 5.9 show the evolution of the spin and single-particle gap over a large range of J/t. Both gaps open simultaneously and the magnetization remains zero. However, the dimer-dimer correlations exhibit an unusual finite size scaling, totally different from the usual algebraic, or exponential decay with system size.

Compared to the TDL, correlations are usually overestimated on small lattices. However, Fig. 5.10 shows that the signal is actually stronger on large lattices, thus the order

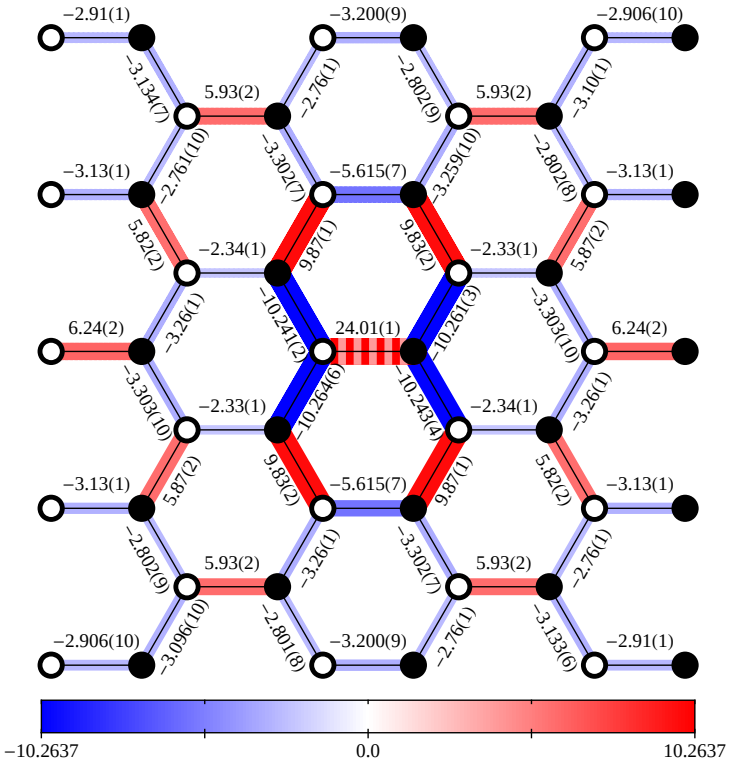

Fig. 5.6.: $N = 10$ — Real-space dimer-dimer correlations S_{dim} on a sections of an $L = 6$ lattice for $J/t = 6.0$. The bond strength is indicated by color and thickness and stands for the probability to find a singlet (triplet) relative to the striped reference bond.

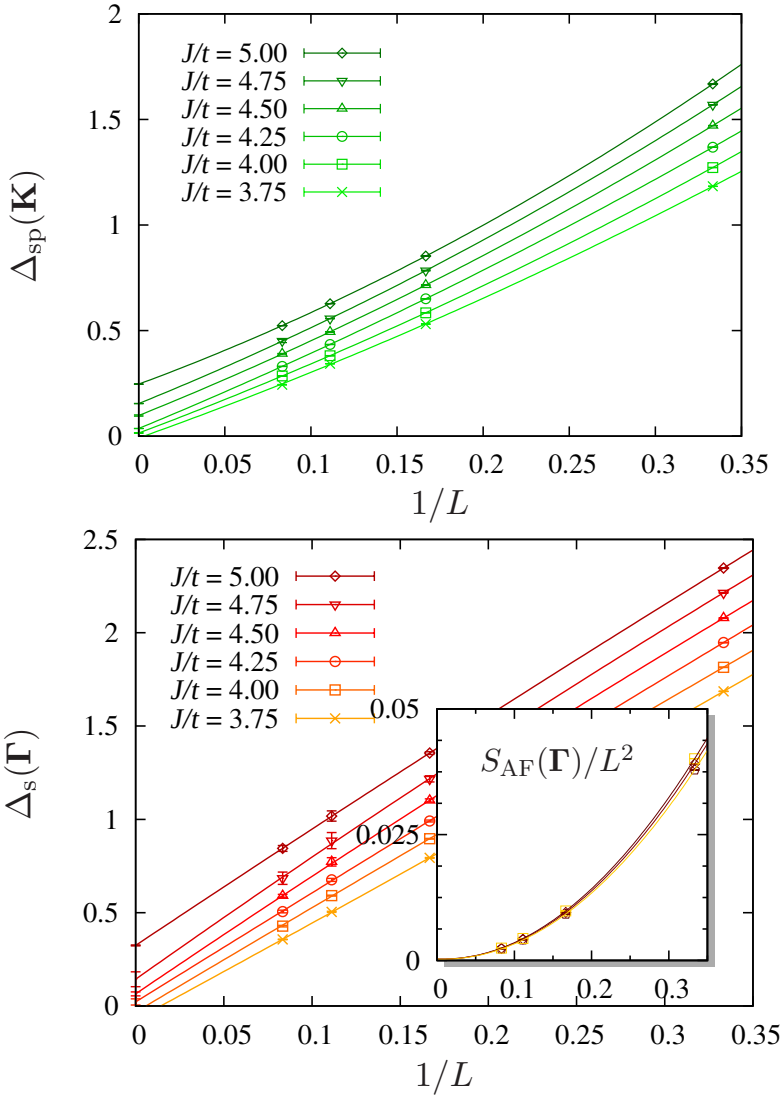

Fig. 5.7.: $N = 6$ — The scaling of the spin and charge excitation gaps show the onset of an insulating phase for $J/t \approx 4.25$, in the absence of long range magnetic correlations (inset).

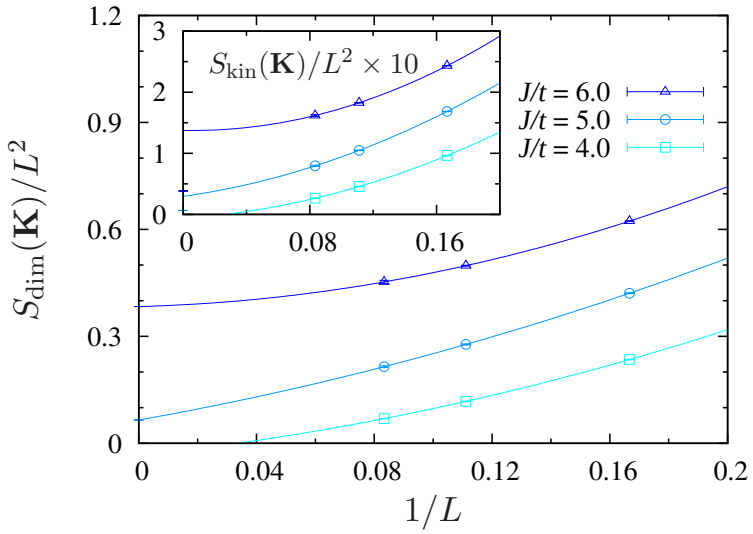

Fig. 5.8.: $N = 6$ — Dimer-dimer correlations S_{dim} and bond energy correlations S_{kin} extrapolated to the TDL. Note the small scale of the bond energy correlations compared to the dimer-dimer correlations. The onset of long range dimerization at $J/t > 4$ coincides with the opening of excitation gaps in Fig. 5.7.

is underestimated on small lattices. The reason for such a behavior can have different origins. One example is that the lattice is so small that it prevents the system to establish a certain dimerization pattern. Another reason would be that the lattice dimensions are incommensurate with a certain pattern. The influence of this misfit then vanishes for large lattice sizes. A direct comparison of the real-space dimer-dimer correlations on an $L = 6$ lattice in Fig. 5.6 and Fig. 5.11 shows that one can still identify the star-shape pattern, although the dimerization is much less pronounced. We can infer that this VBS type also survives for $N = 4$, but fluctuations, which play a more significant role on small lattices, diminish the order.

Apart from the deviating behavior for small lattices the dimer-dimer structure factor extrapolates to finite values for $J/t > 4.0$. Concluding from the opening of the gaps shown in Fig. 5.10 we attribute the vanishing dimer-dimer structure factor at $J/t = 4.0$ to the strong finite size effects and expect it to scale to a finite value as one takes sufficiently large lattices into account. Although the scaling behavior changes significantly, the gain in magnetic energy still surpasses the loss of electronic (kinetic) energy and the VBS prevails. The strong fluctuations found suggest, that the system is close to a phase transition. Indeed, the insulating phase we find below for SU(2) is an antiferromagnet, so there must be at least one QPT as a function of N, which is driven by correlations. Unfortunately, at the moment the vicious sign problem prevents reasonable QMC simulations with fermions for odd N.

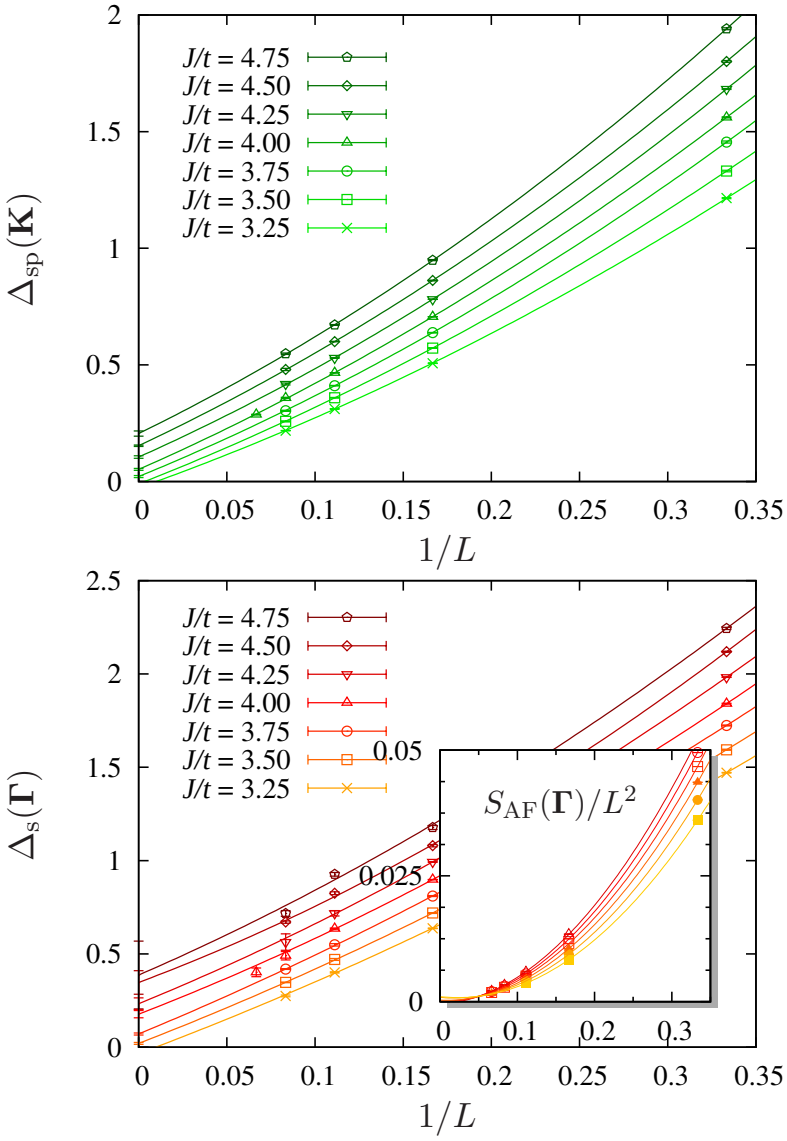

Fig. 5.9.: $N = 4$ — Finite size extrapolation of the single particle and spin gap across the transition from a semimetal to an insulating state located at $J/t \approx 3.75$. The inset shows the finite size extrapolation of the spin structure factor on sublattice A which remains zero for all values of J/t which is consistent with the absence of magnetism in the semimetal as well as with the spin gapped phase.

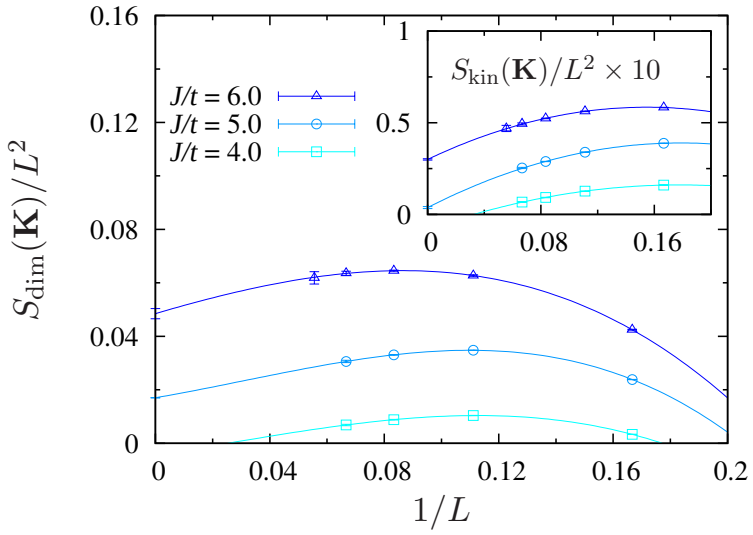

Fig. 5.10.: $N = 4$ — The plot shows the drastic change in the scaling behavior in the finite size scaling of the dimer-dimer correlations at momentum $\mathbf{K}$ (compare with Fig. 5.8).

5.6.4. SU(2)

The proximity of the unconstrained t-J model to the Hubbard model allows to directly compare the two models. The authors have shown recently that, contrary to prior knowledge, the SU(2) Hubbard model on the honeycomb lattice does not undergo a direct QPT from a semimetal to an antiferromagnetic insulator, but rather exhibits an intermediate phase [137]. Starting from the semimetal and increasing the interaction the following happens: The spin exchange (electron-electron) interaction causes particle-hole excitations to condense into (relative) local moments and spin scattering becomes substantial. The system undergoes a Mott-Hubbard QPT induced by charge and spin correlations without breaking any symmetry. The moments form loose bonds of all length scales, although predominately short ranged. Excitations acquire mass as they need to either break a bond, or require to overcome energy to excite a singlet into a triplet. Eventually, as a consequence of the increasing magnetic exchange (super-exchange in the Hubbard model), the pre-formed moments separate and are pushed onto different sublattices according to their spin flavor. Once they form long-range order, rotational spin symmetry is broken, excitations turn massless again and the system becomes a Mott-Heisenberg insulator.

Owing to the possibility of charge fluctuations, this potential spin liquid phase can also be found in the unconstrained t-J model. In the same manner as in the SU(2) Hubbard model, in Fig. 5.12 we can identify the opening of a single-particle gap at $J/t \approx 2.15$ prior to the onset of magnetization at $J/t \approx 2.6$. However, charge fluctuations

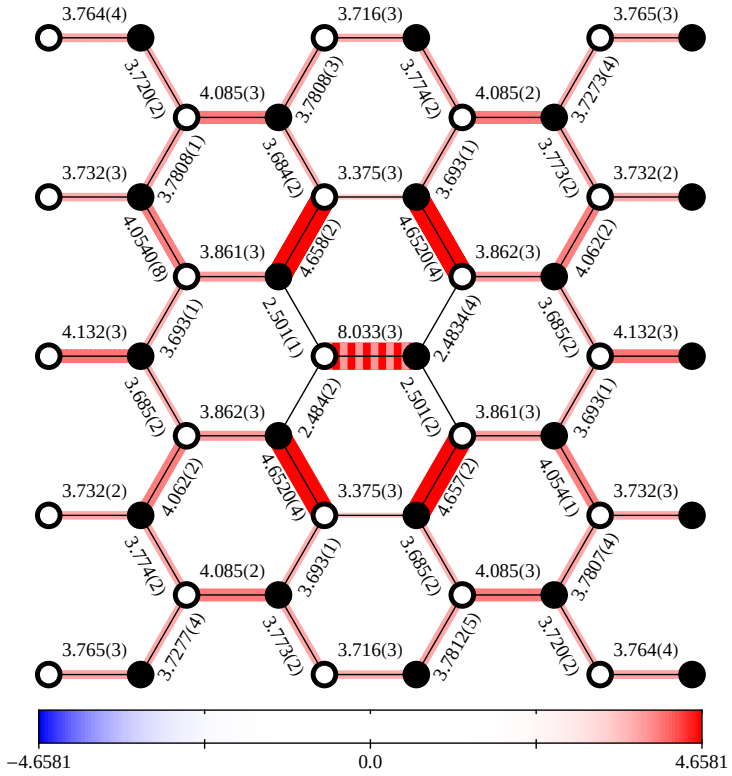

Fig. 5.11.: $N = 4$ — Real-space dimer-dimer correlations S_{dim} on a section of an $L = 6$ lattice for $J/t = 6.0$. Although, compared to Fig. 5.6, fluctuations are much more pronounced, the star-shape dimerization prevails. A color scale has been chosen such that the persistent dimerization pattern is easily to identify.

are suppressed in the t-J model and the intermediate phase subsists over a much more narrow region of J/t. Dimer-dimer, singlet and triplet pairing of s-, d-, p- and f-wave symmetry, nearest neighbor and next-nearest neighbor bond-energy, as well as current-current correlations all vanish in the scaling limit $L \to \infty$. We therefore reproduce the intermediate spin-liquid phase already obtained for the SU(2) Hubbard model (for a detailed discussion see [137]).

Unfortunately, to extract a reliable estimate for the spin gap in the intermediate phase and the TDL is not feasible in the t-J model. We know the spin excitations must be gapless in the semimetal phase for $J/t \leq 2.15$ and from the spontaneous breaking of the SU(2) spin symmetry in the magnetic phase we can conclude that the spin gap vanishes for $J/t \geq 2.6$ due to the emergence of the two Goldstone modes. Following the results obtained for the SU(2) Hubbard model on the honeycomb lattice we expect the spin gap to be finite in the intermediate region. However, considering the error bars, the scaling (Fig. 5.13) does not allow to infer the existence of a finite spin gap. The inset shows the histograms of the errors obtained from a bootstrapping procedure of a $\mathcal{O}(1/L^2)$ fit. Although the trend seems right for the opening and closing of the spin gap, the large variances exclude a definite statement.

Although the potential spin-liquid phase is characterized by the absence of order (and the spin gap) one can probe wether the liquid phase is featureless on short length scales or not. Indeed, the real-space dimer-dimer correlations reveal a resonating valence bond (RVB) pattern which regains the cost of AF exchange by the resonance between many different configurations. This is also equivalent to short range spin correlations (cf. Fig. 5.14). The inset shows the same correlation for the isolated Hubbard hexagon also at $U/t = 4$.

We want to point out that the intermediate phase is purely a product of charge fluctuations. This is why, compared to the Hubbard model, the intermediate phase is less pronounced in the t-J model. The regular t-J model on the honeycomb lattice at half-filling, where double vacancies are projected out and phase space is restricted to singly occupied sites is per definition an insulator equivalent to the Heisenberg model and this phase will not be observable.

In Fig. 5.15 the evolution of the double occupancy, kinetic and magnetic (potential) energy are shown as a function of spin exchange. Double occupation is suppressed with increasing J/t (Fig. 5.15). In the limit $J/t \to \infty$ charge fluctuations and kinetic energy vanish and the Hamiltonian (Eq. 5.28) reduces to the pure Heisenberg model. While the kinetic energy decreases, the magnetic energy increases with J/t. The plot of the double occupancy also shows its first derivate with respect to J/t. One can approximate that the maximum of the slope, which marks the emergence of a new phase dominated by potential energy rather than kinetic energy, coincides with the onset of magnetism at J_{c_2} and not with the opening of the single-particle gap. As has been argued for the SU(2) Hubbard model, this suggests that the intermediate phase is in closer relation to the weak coupling than the strong coupling fix-point. It also agrees with the picture of moments

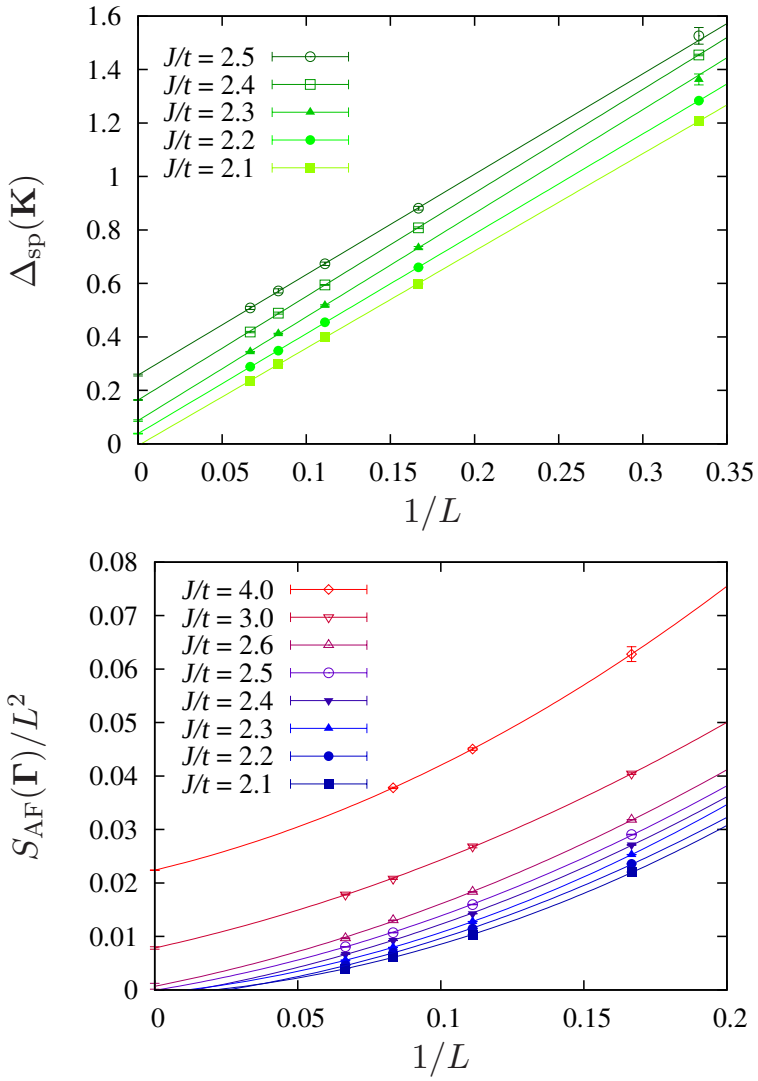

Fig. 5.12.: $N = 2$ — Single-particle gap and the antiferromagnetic structure factor as a function of system size. One can see the opening of the single-particle gap at $J/t \approx 2.2$ while the magnetization remains zero before antiferromagnetic order sets in at $J/t \approx 2.6$.

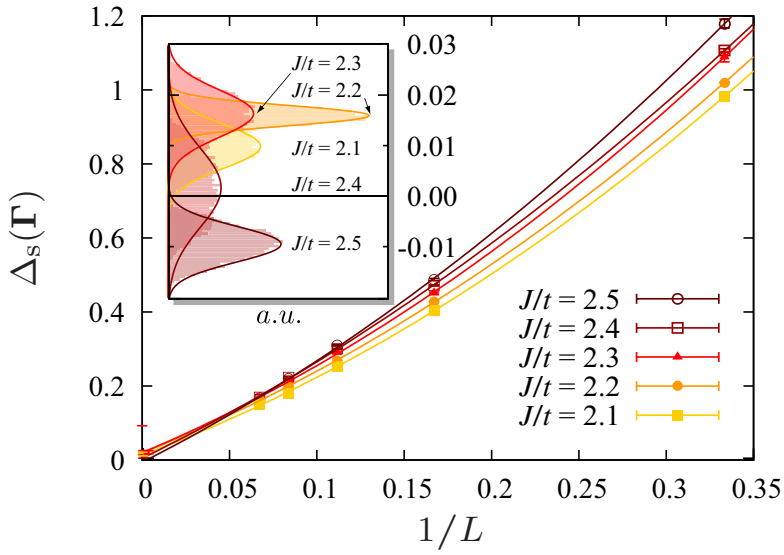

Fig. 5.13.: $N = 2$ — The scaling of the lowest lying spin excitation yields zero within error bars for all values of J/t. The inset shows the distribution of the extrapolated spin gap from a bootstrapping analysis.

localizing at the Mott-Heisenberg transition rather the precedent Mott-Hubbard QPT.

5.7. Realizations

SU(N) quantum models are not purely theoretical exercises – their abstract framework may be realized with ultracold atoms in optical lattices [241, 242, 243] which provide a versatile toolkit to realize and study correlated models. Recently, it has been argued that fermionic alkaline earth atoms in optical lattices can realize a variety of models with enlarged spin rotation symmetry SU(N) [244, 245, 246, 247, 248, 249]. Multi-flavor models can also be realized in quantum dot arrays [250] and represent effective models in electronic systems with multiple orbital degrees of freedom, e.g., the Kugel-Khomskii model [251, 252, 253, 254, 255].

In this section we will introduce a few general properties of ultracold atomic gases in optical lattices and of alkaline-earth atoms in optical lattices, the latter proving to be the most versatile implementation of SU(N) symmetric models. Here we roughly follow [244, 256].

5.7.1. Ultracold atomic gases

Ultracold atoms in optical lattices provide defect-free systems, in which the relevant parameters can be independently controlled, thus allowing quantitative comparisons of

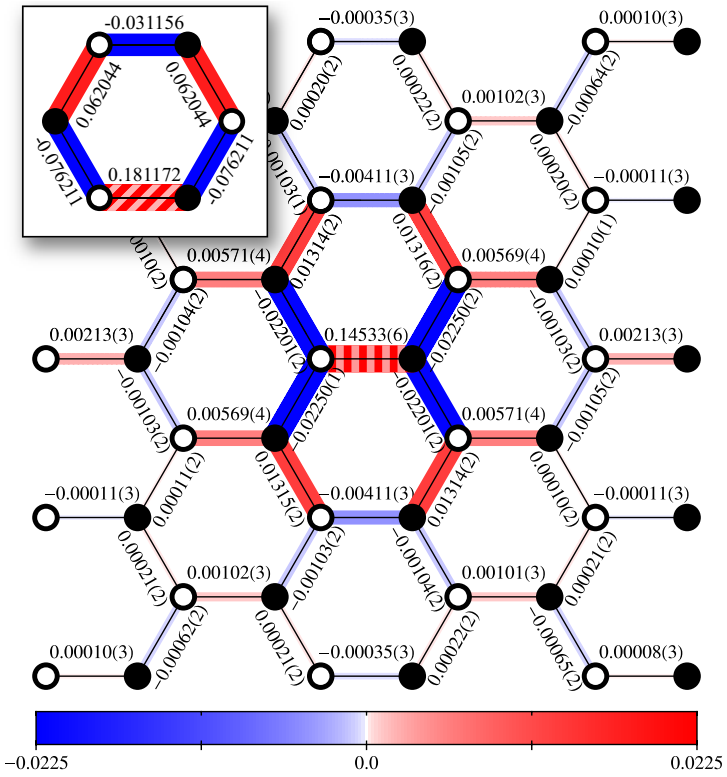

Fig. 5.14.: $N = 2$ — Real-space dimer-dimer correlations S_{dim} on a section of an $L = 6$ lattice for $J/t = 2.3$ showing short range RVB (spin) correlations. The striped bond is the reference.

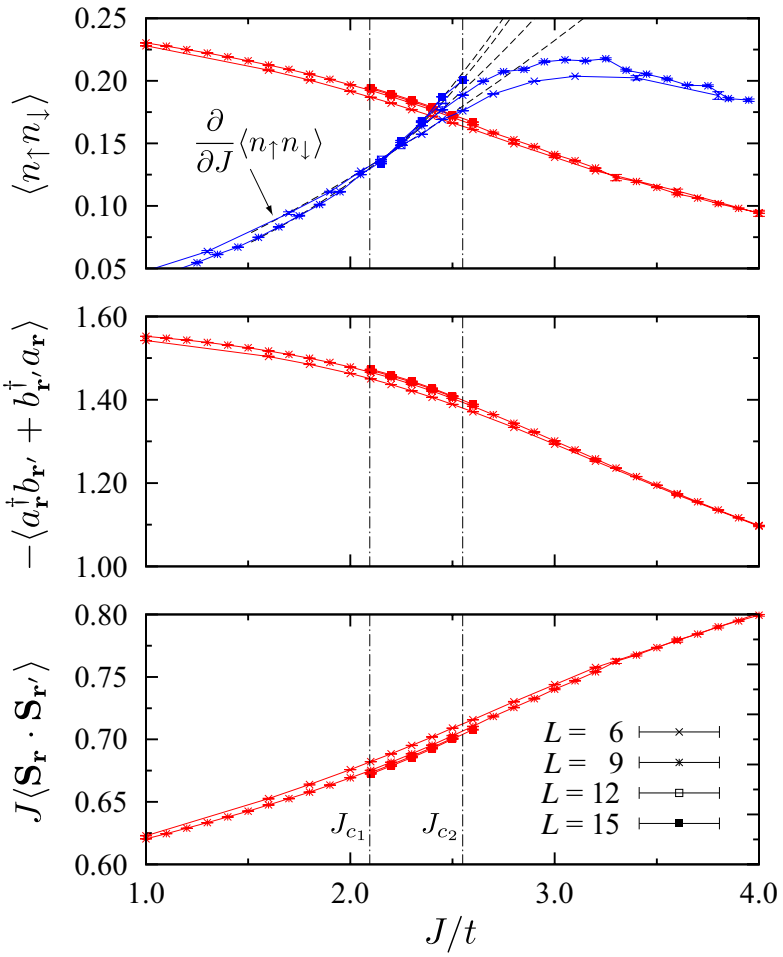

Fig. 5.15.: $N = 2$ — Double occupancy (its derivative), negative kinetic energy and the spin exchange per site in units of t. The critical points are indicated by the dashed-dotted lines.

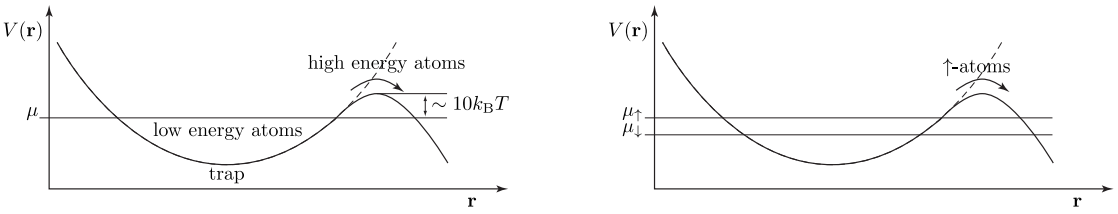

Fig. 5.16.: Evaporative cooling (left) and depolarization (right) can be used to cool cold atomic (Fermi) gases at their final stage. The skewed optical and magnetic potential allows high energy atoms to dribble off, leaving behind low energy atoms only.

the experiment with modern quantum many-body theories. While people also cool molecules and ions we will focus on atomic gases as their application is most closely related to the lattice models discussed in this work. In general neutral atoms are cooled which act as either bosons or fermions depending on their internal structure. This way fermionic atoms can be used to imitate single electrons, albeit on energy and time scales way larger than those found in condensed matter systems.

In the atomic, molecular and optical physics (AMO) community people mostly use alkali metals (lithium (Li), sodium (Na), potassium (K), rubidium (Rb), caesium (Cs), francium (Fr)) in the mass range of ^{6}Li–^{133}Cs. They are easy to work with in the sense that their elemental properties are well understood. Their internal degrees of freedom are basically given by their *spin*-states, which are hyperfine states of the nuclear spin and the electrons in the incomplete shells. Clouds with densities of 10^{11}–10^{15} atoms/cm^3 can be prepared. Note that this appears to be a rather dilute gas (air: $\sim 10^{16}$ molecules/cm^3 at normal conditions). However the thermal de Broglie wavelengths are usually of the order or larger than the interatomic spacing of a few micrometers which make the gas not dilute on their own terms. These large length scales are within the range of visible light and hence allow for direct optical imaging.

Cold atomic gases can be cooled down to temperatures of 10^{-6}–10^{-9} K, but note that thermometry is tricky in these systems: One cannot simply put a thermoelectric element into the cloud in order to measure the temperature without destroying it. Temperature can be estimated by measuring the population of exited atoms and then fitting it to the expected (Bose/Fermi-Dirac) distribution. Next to various versions of laser cooling [257, 258], the techniques applied at the final stage of cooling are evaporative cooling and depolarization.

In evaporative cooling the optical and magnetic potential is skewed which allows high energy atoms to dribble off one of the potential barriers, leaving behind low energy atoms only. These leakage barriers are typically $\approx 10k_\mathrm{B}T$, hence the Temperature can be decreased by 1/10. Since this cooling method relies on the fact that there exist excited atoms, it needs atom-atom interactions to continuously produce high-energy atoms via scattering and does not work for one-component Fermi-gases. Depolarization exploits

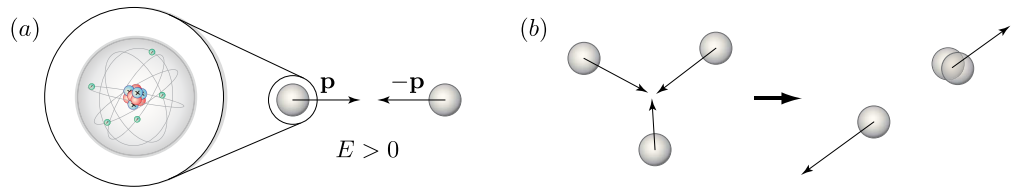

Fig. 5.17.: Two-atom (a) and three-atom (b) collisions in ultracold atomic gases. While molecule formation is forbidden in the former case, molecules can form in (b) where a third atom takes up the released binding energy.

the imbalance of species in a multi-component (Fermi) gas. Is the chemical potential of one species higher than the one of the other, a skewed potential allows the *hot* species to leave the trap, thus depolarizing towards a balanced population ($\mu_\uparrow \to \mu_\downarrow$ in Fig. 5.7.1).

Maintaining the temperature throughout an experiment is another difficulty. The evaporative cooling process is usually uphold throughout experiments (without optical lattices) such that the temperature will drift. Switching on an optical lattice freezes the evaporative cooling but the system will heat up due to one- and three-body losses, which are described in the following.

These gases are in general metastable against the formation of molecular ground states. Indeed, at the given temperatures and sufficiently dense clouds their *ground-state* should be metallic. However, the tradeoff between (controlled) scattering length and density prevents the condensates to solidify. For sufficient cooling the formation of molecules via two-body collisions is forbidden by the conservation of energy and momentum illustrated in Fig. 5.7.1. Nevertheless, three-body recombination processes can still form molecules as one of the three atoms takes up the energy released by binding two atoms – an unfortunate fact that is one of the major limitations on the density and the life time of cold atomic gases [259].

Another factor which limits the density of the atomic gas are one-body losses caused by collisions with particles from the environment (the *vacuum*-chamber). One- and three-body losses create holes in the distribution of atoms. Where holes in weakly interacting Bose gases holes do not influence the condensates much (as there are no states below the chemical potential), in fermionic gases they produce heating and increase entropy significantly. This is the reason why cooling fermions to very low temperatures has been less successful than for bosons. The prime example, Mott insulating states, has been created with bosons [260] and six years later with fermions [177, 178]. For both bosonic and fermionic systems, the Mott insulating state can be probed for a vanishing compressibility by testing the response of the system to a change in external confinement. Magnetically ordered phases which require much lower temperature regimes (of the order of the magnetic exchange coupling) have been elusive, yet. While these influences limit the stability of the atomic clouds, experiments can last up to a few seconds, but survive often less than a second. Nonetheless, the microscopic time scale, set by two-atom

scattering, is of the order of microseconds and hence allows to study out-of-equilibrium as well as equilibrium properties within the given timeframe.

Hitting the atoms with lasers they can be subjected to a species (α) dependent single-atom external potential $V_\alpha(\mathbf{r}) = \sum_\omega P_\alpha(\omega) I(\mathbf{r}, \omega)$. Here, P_α stands for the real part of the polarizability (the imaginary part defines the absorption) and I is the intensity of the laser of frequency ω at position $\mathbf{r}$. This allows to form attractive or repulsive regions in space with respect to ω. In general, a set of focussed beams is used to create a smooth confining potential and beams of standing waves, speckles, or holograms may be used to create optical lattices that vary rapidly with $\mathbf{r}$ on a scale larger than the wavelength of visible light. In principle this allows for arbitrary (periodic) structures including hexagonal topologies [261, 262]. To avoid absorption, scattering and heating it is essential to keep the frequencies ω away from the absorption lines of the trapped gas.

The interactions between the neutral atoms are short ranged and much smaller than the de Broglie wavelength. This includes identical fermions (consisting of complex atoms) where the antisymmetry of the wave function excludes interactions of the same kind at the same location (Pauli's principle). However, Feshbach resonance can be exploited to greatly enhance interactions if the atoms are on the verge of forming a weakly bound state [263, 264, 265, 266]. By changing the magnetic field, bound states close to the continuum may be shifted into the same, such that the scattering length a_s diverges. While for bosons this enhancement of interactions also enhances three-body losses, which eventually destroys the atomic gas, for (two- and multi-species) fermionic gases Pauli blocking prevents the formation of molecules and allows to tune to strong interactions.

A limitation of most current experiments is that the ultracold quantum gas has to be trapped in a magnetic or optical trap using a (usually) harmonic confinement potential. This creates thus an inhomogeneous chemical potential such that the atom density distribution is more or less defined by the confining potential, e.g., in a Mott insulating state this leads to characteristic ring-shaped Mott-regions [267]. In *time-of-flight* images one essentially records the momentum distribution of the gas after its release from the trap to probe the whole system, with the disadvantage that one averages over regions with different density and potentially different phases. Recently, there has been progress in *in-situ* imaging of bosonic atoms in a two-dimensional optical lattice with single atom resolution [268, 269, 270]. Here, the optical lattice is projected and observed through the same microscope and allows to directly record real-space images of the locations of the atoms to locally probe the system in a specific phase.

Although these so-called *quantum simulators* (ultracold atoms loaded into optical lattices) are confronted with a large number of difficulties they represent a fast advancing toolkit to study equilibrium and (more easily) out-of-equilibrium physics of microscopic models even beyond the crystalline condensed matter systems [271]. This includes the possibility to tackle multi-component fermion systems as discussed in the next section.

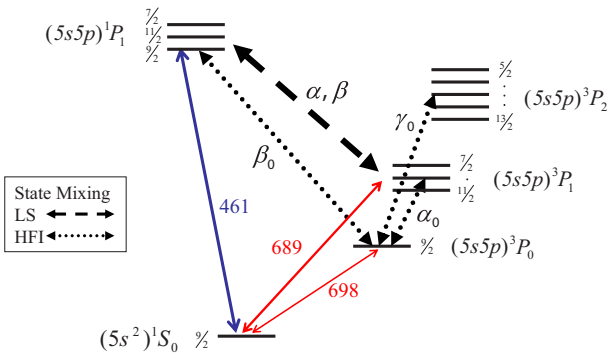

$$|^3P_0\rangle = |^3P_0^0\rangle$$
$$|^3P_1\rangle = \alpha|^3P_1^0\rangle + \beta|^1P_1^0\rangle$$
$$|^3P_2\rangle = |^3P_2^0\rangle$$
$$|^1P_1\rangle = -\beta|^3P_1^0\rangle + \alpha|^1P_1^0\rangle$$

$$|^3P_0\rangle_{\text{HFI}} = |^3P_0^0\rangle + \alpha_0|^3P_1\rangle + \beta_0|^1P_1\rangle + \gamma_0|^3P_2^0\rangle$$

$$\alpha_0 = 2 \times 10^{-4}$$
$$\alpha = 0.9996 \qquad \beta_0 = -4 \times 10^{-6}$$
$$\beta = -0.028 \qquad \gamma_0 = -1 \times 10^{-6}$$

Fig. 5.18.: Simplified ^{87}Sr energy level diagram (not to scale) adapted from [272]. Relevant optical transitions are shown as solid arrows, with corresponding wavelengths given in nanometers. Hyperfine structure sublevels are labeled by total angular momentum I. State mixing of the $^1S_0$ and $^3P_0$ states due to the spin-orbit (LS) interaction is shown as a dashed arrow, dotted arrows represent the hyperfine interaction (HFI) induced state mixing of the $^3P_0$ state with the other $I = 9/2$ states in the $5s5p$ manifold. State mixing due to LS and HF interaction are given alongside the coupling coefficients for an impression of the coupling strengths.

5.7.2. Alkaline-earth atoms in an optical lattice

Compared to the alkali metals mentioned above, the alkaline-earth metals, a series of elements comprising group two of the periodic table (beryllium (Be), magnesium (Mg), calcium (Ca), strontium (Sr), barium (Ba) and radium (Ra)), bear a crucial difference: The existence of a long-lived metastable excited state $^3P_0$ (with lifetime $\sim$ 150s for ^{87}Sr) which is coupled to the ground state $^1S_0$ through an ultranarrow, doubly forbidden transition [248, 272]. Since these two states both carry electronic angular momentum $J = 0$ they show almost perfect decoupling of J from the nuclear spin I. This implies that, aside from constraints by the fermionic antisymmetry, the (spatially isotropic) s-wave scattering lengths are nearly independent from the nuclear spin. This feature allows to model SU(N) symmetric models with $N = 2I + 1$ as large as $N = 10$ (e.g., $I = 9/2$ for ^{87}Sr) [248, 249].

Figure 5.7.2 shows a simplified energy level diagram for ^{87}Sr [272]. The ^{87}Sr structure allows to prepare nuclear spin states in both the $^1S_0$ and the $^3P_0$ state, decoupled from the electronic state. These states can be manipulated independently by lasers, allowing for the construction of nuclear spin states of different magnetic quantum number $m_I = -I, \ldots, I$. They are insensitive to magnetic field fluctuations, because they belong to different transition families and are separated by optical frequencies [249].

Interactions between two ^{87}Sr atoms are characterized by the four s-wave scattering lengths for two atoms $^1S_0$ (S) and $^3P_0$ (P): a_X, $X = SS$, PP, SP^+, SP^-, in the electronic states $|SS\rangle$, $|PP\rangle$ and $(|SP\rangle \pm |PS\rangle)/\sqrt{2}$. For a collision of any combinations of S and P states with $J = 0$ the decoupling of nuclear and electronic degrees of freedom

can be assumed such that the four scattering lengths are independent of the nuclear spin. While this assumption is well justified for S-S and S-P collisions because of the lack of inelastic scattering channels, the P-P collisions are likely to lead to losses (cf. Fig. 5.7.2). Therefore, unless a more suitable element can be identified, realizations are limited to situations where two atoms in a P-state never occupy the same state.

These features allow to encode electronic states of different magnetic quantum numbers in order to implement many-body systems with an enhanced degree of symmetry, characterized by SU(N) symmetric Hamiltonians. However, and playing devil's advocate, let us note here that this would allow the realization and study of arbitrary SU(N) models is a rather optimistic expectation. While Feshbach resonance allows to tune scatterings lengths to mimic the full spectrum of microscopic models [273], many-body collisions and losses represent the most challenging obstacles. This (almost) limits realizable Coulomb terms to local (onsite) interactions.

5.8. Conclusions

We investigated the phase diagram of the half-filled SU(N) unconstrained Heisenberg model on the honeycomb lattice for system sizes up to $L = 18$. For the limit $N \to \infty$ we solved the saddle point equations obtained from a Hartree Fock mean-field Ansatz self-consistently. In this large N limit the t-J model undergoes a QPT from a semimetal at small J/t to a VBS, where the lattice symmetry is broken spontaneously into a Kekule pattern at large J/t. Using PQMC we reproduced the mean-field results first for $N = 10$. It turns out that the dimerized phase is robust down to $N = 4$, where correlations start to strongly affect the order for small system sizes. In accordance with the dimerization we detected the simultaneous opening of a spin and single-particle gap. Only at $N = 2$ the picture changes as correlations are strong enough to break the spin-symmetry and the insulating phase for large J/t is antiferromagnetically ordered. Also, there is no direct transition from a semimetal to an insulator: a single-particle gap opens before the system acquires magnetization. We find an intermediate gapped phase which lacks obvious order and presents a potential spin liquid. Thus, we are able to reproduce the spin-liquid phase found in the SU(2) Hubbard model in the vicinity of the AF Mott insulator.

In the large-N limit the fluctuations induced by the infinite number of degrees of freedom allow to interpret a singled out site as if living in an effective mean field. As N decreases one can expect fluctuations to decrease and correlations to increase. The low coordination number on the honeycomb lattice upholds the fluctuations, supporting the mean field behavior over a large range of N. The persistence of the large-N VBS phase down to $N = 4$ implies that even sophisticated $1/N$ corrections would be still too small to accurately reproduce the SU(2) ground state, hence $N = 4$ can be considered a *large* number. This shows the inefficiency of large-N approaches to describe SU(2) quantum

antiferrogmagnets by means of $1/N$ corrections.

In a follow-up we test whether the SU(2) spin liquid phase, which is more dominant in the Hubbard model, extends to higher symmetries $N > 2$. Setting $J/t = 0$ we obtained first results at SU(4) which indicate the onset of an insulating phase prior to the crystallization into a VBS. This first sign of a possible intermediate phase, which separates the semimetal from the VBS, is the subject of an ongoing investigation.

Magnetic field induced Mott transition on the honeycomb lattice

6

Graphene, or the physics of electrons on the honeycomb lattice, has recently received tremendous attention due to its semimetallic nature with low-energy quasiparticles behaving as massless Dirac spinors; for a recent review see Ref. [1]. A crucial point, is the stability of this semimetallic phase to particle-hole pairing. In particular, research activities have been devoted to the investigation of magnetic-field-induced transitions as a function of magnetic fields [274, 275, 276] and electronic correlations [184, 185, 277].

In this project we show that the semimetallic state of the two-dimensional honeycomb lattice with a point-like Fermi surface is unstable towards a canted antiferromagnetic (AF) insulator upon application of an in-plane magnetic field. The magnetic field shifts the up and down spin cones in opposite directions, thereby generating a finite density of states at the Fermi surface and perfect nesting between the up and down spin Fermi sheets. This triggers a canted AF insulating state. The mechanism behind this instability can be understood already at the mean-field level [278, 279]. We show that those mean-field arguments indeed capture the correct physics, since exact quantum Monte-Carlo simulations on the honeycomb lattice with up to 12×12 unit cells compare favorably with those mean-field results. Details have been published in Refs. [240, 5].

6.1. SU(2) Hubbard model subjected to a magnetic field

Our starting point is the Hubbard model on the honeycomb lattice (cf. Fig. 6.1) $H = H_0 + H_U + H_B$, where

$$\begin{aligned} H_0 &= -t \sum_{\mathbf{i},\mathbf{r},\sigma} \left(a^\dagger_{\mathbf{i},\sigma} b_{\mathbf{i}+\mathbf{r},\sigma} + b^\dagger_{\mathbf{i}+\mathbf{r},\sigma} a_{\mathbf{i},\sigma} \right) , \\ H_U &= U \sum_{l=a,b} \sum_{\mathbf{i}} \left(n_{\mathbf{i},l,\uparrow} - 1/2 \right) \left(n_{\mathbf{i},l,\downarrow} - 1/2 \right) , \\ H_B &= \frac{g}{2} \mu_{\mathrm{B}} B \sum_{l=a,b} \sum_{\mathbf{i},\sigma} p_\sigma n_{\mathbf{i},l,\sigma} . \end{aligned} \tag{6.1}$$

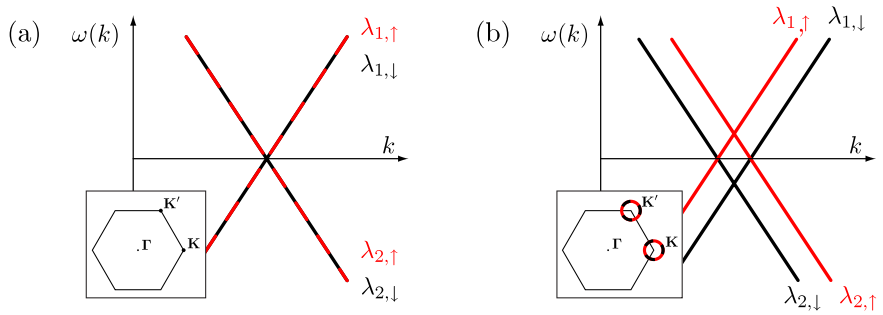

Fig. 6.1.: The nesting of the spin-up and spin-down Fermi surface for (a) $B = 0$, where the spin bands collapse onto each other, whereas for (b) $B > 0$ the bands are shifted by virtue of the magnetic field.

The electron operator $a^\dagger_{\mathbf{i},\sigma}$ ($b^\dagger_{\mathbf{i},\sigma}$) creates an electron on the orbital a (b) in the unit cell $\mathbf{i}$ and the associated electron density operator is $n^l_{\mathbf{i},\sigma} = a^\dagger_{\mathbf{i},\sigma} a_{\mathbf{i},\sigma}$ ($b^\dagger_{\mathbf{i},\sigma} b_{\mathbf{i},\sigma}$), for $l = a(b)$. Owing to the bipartite nature of the lattice, hopping with matrix element t, occurs only between the a- and b-orbitals of unit cells related by the lattice vector $\mathbf{r} = \{\mathbf{0}, \mathbf{a}_1 - \mathbf{a_2}, -\mathbf{a_2}\}$. The on-site electron-electron repulsion is denoted by $U > 0$ and $p_\sigma = \pm 1$ for $\sigma = \uparrow, \downarrow$. In the following, we set $(g/2)\mu_\mathrm{B} \equiv 1$. For comparison with experiments, we only consider setups with magnetic field orientations parallel to the lattice plane. The Hamiltonian H_0 gives rise to two bands, $\lambda_n(\mathbf{k}) = p_n \left| t \sum_{\mathbf{r}} e^{-i\mathbf{k}\cdot\mathbf{r}} \right|$, with $\lambda_{n,\sigma}(\mathbf{k}) = \lambda_n(\mathbf{k}) + p_\sigma B$ and $p_n = \pm 1$ for $n = 1, 2$ respectively, the latter being single particle states of $H_0 + H_B$. At half-band filling the Fermi surface consists of two points, K, K' in Fig. 6.1. At zero magnetic field the nesting instability is cut off by the vanishing density of states (cf. Sec. 1.1). At $B > 0$ the spin degeneracy is lifted and the bands shift. The low energy density of states becomes finite leading to the nesting relation $\lambda_{1,\uparrow}(\mathbf{k}) = -\lambda_{2,\downarrow}(\mathbf{k})$.

Given the above instability, a mean-field ansatz is derived by assuming the magnetization $\mathbf{m}$ to be alternating on the sublattices: $\mathbf{m}_l = \big(m_\parallel, \quad m_\perp(-1)^l, \quad 0\big)$, with the index $l = 0, 1$ referring to the orbitals in the unit cell. That is, the magnetization m has a constant component $m_\parallel$ parallel to the field axis and a staggered component $m_\perp$ in the plane perpendicular to the field. Neglecting fluctuations we can derive the gap-equations and solve them self-consistently. Our mean-field results are plotted in Figs. 6.2, 6.4a–c. At zero magnetic field, we observed as a function of U/t the expected transition from the semimetallic state ($\mathbf{m} = 0$) at $U < U_c$ to the AF Slater insulator characterized by $|m_\perp| > 0$. The semimetallic state at $B = 0$ is characterized by the spin degenerate dispersion relation, $\lambda_{n,\sigma}(\mathbf{k})$, as shown in Fig. 6.4. Ramping up the magnetic field lifts this degeneracy, thereby producing nested Fermi sheets of opposite spin indices. Hence, and irrespective of the magnitude of $U < U_c$, energy can be gained by ordering the spins in a canted antiferromagnet. The dispersion relation of this canted AF state is plotted

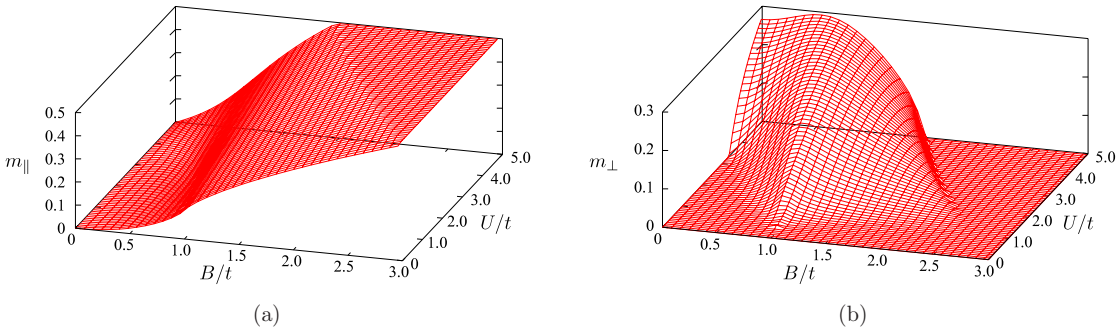

Fig. 6.2.: Parallel magnetization $m_\parallel$ (a) and staggered magnetization $m_\perp$ (b) vs. U and B.

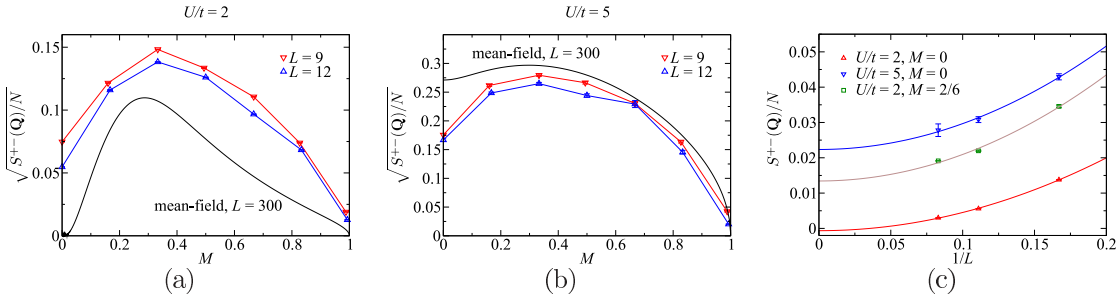

Fig. 6.3.: Staggered magnetization $\sqrt{S^{+-}(\mathbf{Q})/N}$ below (a) and above (b) the critical interaction strength. (c) Finite size extrapolation of $S^{+-}(\mathbf{Q})/N$. In the semimetallic phase, $U/t = 2$, the data is consistent with the onset of transverse staggered order at finite magnetization M. For comparison, we have plotted the $U/t = 5$ data in the absence of a magnetic field, but in the AF Mott insulating state.

in Fig. 6.4c. To compare at best with the QMC simulations we consider the quantity

$$A^{\uparrow}(\mathbf{k},\omega) = -\frac{1}{\pi}\mathrm{Im}\left(G^{\uparrow}_{aa}(\mathbf{k},\omega) + G^{\uparrow}_{bb}(\mathbf{k},\omega)\right) \ , \tag{6.2}$$

with a finite broadening. As apparent, the features with dominant weight follow the dispersion relation $\lambda_{1,\uparrow}(\mathbf{k})$ and $\lambda_{2,\uparrow}(\mathbf{k})$ and a gap at the Fermi level is apparent. Due to the transverse staggered moment, mixing between the up and down dispersion relations occurs, thereby generating shadow features following the dispersion relations of $\lambda_{1,\downarrow}(\mathbf{k})$ and $\lambda_{2,\downarrow}(\mathbf{k})$. The intensity of the shadow features tracks $m_\perp$. As apparent from Fig. 6.2 the growth of $m_\perp$ as a function of the magnetic field is countered by the polarization of the spins along the magnetic field. It is interesting to note that irrespectively of U/t the maximal value of $m_\perp$ and hence of the magnetic field induced gap is at $B = 1$. This corresponds to an energy scale matching the position of the Van-Hove singularity in the non-interacting density of states. At this point a maximal amount of energy can be gained by the opening of the gap.

To confirm our mean-field results, we have carried out projector auxiliary field QMC

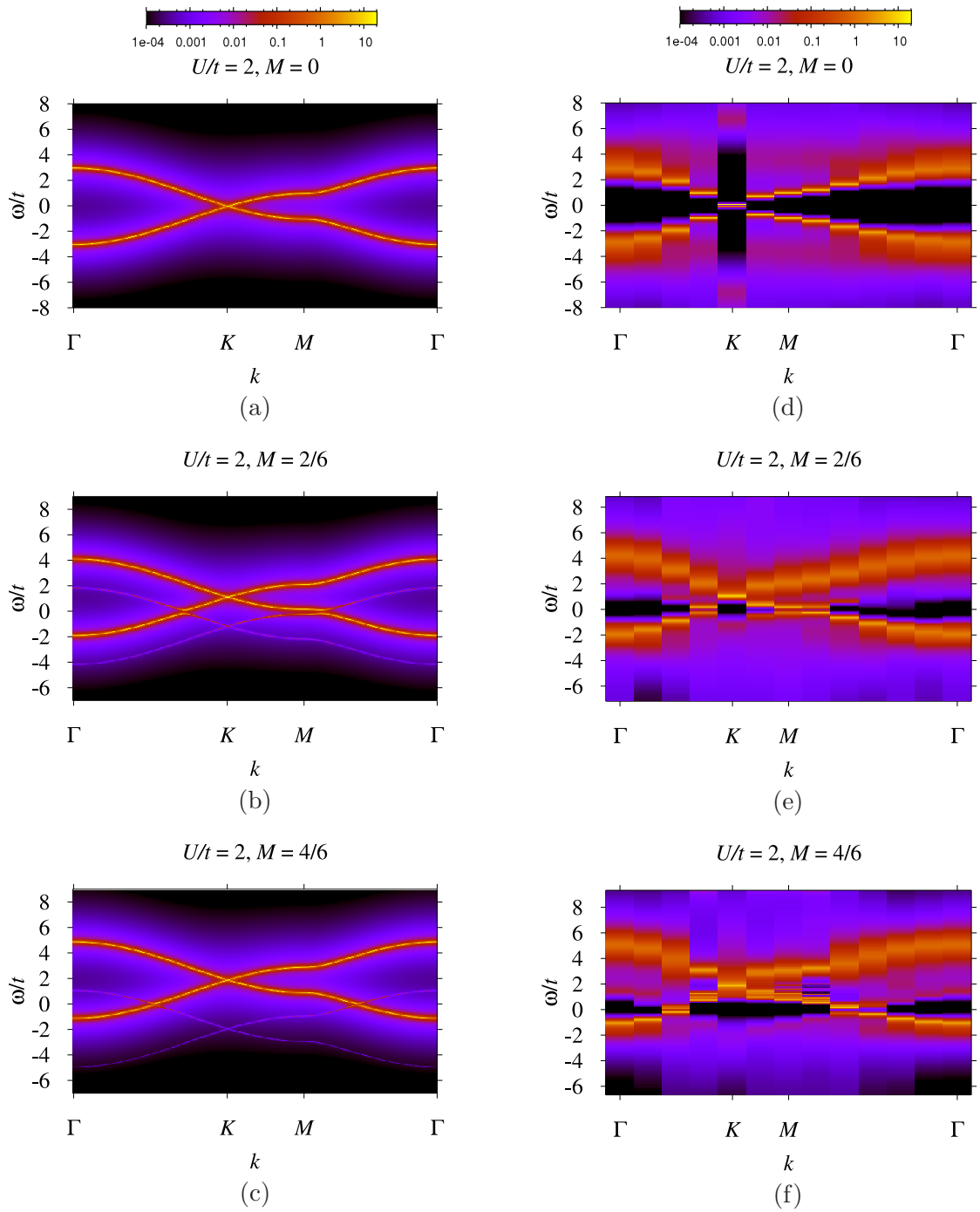

Fig. 6.4.: Single-particle spectral function $A^{\uparrow}(\mathbf{k},\omega)$ at $U/t = 2$, based on the mean-field (left) and the QMC calculations (right), respectively. The magnetization M takes the values 0, 2/6, and 4/6 (from top to bottom). For the QMC calculations, the lattice size was set to 12×12 unit cells.

calculations (cf. Sec. 1.2 and Ref. [10]). In this canonical approach, we fix the magnetization $M = \frac{N_\uparrow - N_\downarrow}{N_\uparrow + N_\downarrow}$ rather than the magnetic field. N_σ corresponds to the total number of electrons in the spin sector σ. Furthermore, due to the particle-hole symmetry which locks in the signs of the fermionic determinants in both spin sectors one can avoid the so-called negative sign problem irrespectively of the choice of the magnetization. In practice, for each finite system, we choose a value of the projection parameter θ, large enough such as to guarantee convergence within statistical uncertainty.

To detect transverse staggered magnetic order under an applied magnetic field, we have computed the spin-spin correlation functions (here defined for sublattice a),

$$S^{+-}(\mathbf{q}) = \frac{1}{N} \sum_{\mathbf{i},\mathbf{j}} e^{-\imath \mathbf{q}(\mathbf{i}-\mathbf{j})} \langle S_a^+(\mathbf{i}) S_a^-(\mathbf{j}) - S_a^+(\mathbf{i}) S_a^-(\mathbf{j}) \, , \tag{6.3}$$

with $\lim_{N\to\infty} S^{+-}(\mathbf{Q})/N = (m_\perp^{\mathrm{QMC}})^2$. We have computed this quantity on 6×6, 9×9 and 12×12 lattices, and our results are plotted in Fig. 6.3 both for $U < U_c$ and $U > U_c$. At $U/t = 2 < U_c/t$ and zero magnetization, $M = 0$, our results are consistent with $m_\perp^{\mathrm{QMC}} = 0$ whereas at $M = 2/6$, $m_\perp^{\mathrm{QMC}}$ takes a finite value. Although we cannot reproduce the essential singularity of the mean-field calculation at $U < U_c$, the overall form of the transverse staggered magnetization compares favorably with the mean-field results (see Fig. 6.3a,b) both at $U < U_c$ and $U > U_c$. Our mean-field value for $U_c/t \approx 3.3$, which agrees well with previous results obtained by Sorella and Tossati [184]. They employ a mean-field decoupling in the S^z component of the spin resulting in a $U_c/t \approx 2.2$, which differs by the factor 3/2 from our value where all spin components have been taken into account.

Within the PQMC, the zero temperature single particle Green function along the imaginary time axis can be computed efficiently with methods introduced in [23]. From this quantity, we can obtain the spectral function of Eq. (6.2) with the use of a stochastic formulation of the Maximum Entropy method [220, 221]. The so obtained results for $A^\uparrow(\mathbf{k}, \omega)$ are plotted in Fig. 6.4b,d,f. As apparent, the features in the QMC calculation which are associated with substantial spectral weight are well reproduced by the mean-field calculation. The particle-hole transformation, $\hat{a}^\dagger_{\mathbf{i},\sigma} \to \hat{a}_{\mathbf{i},-\sigma}$ and $\hat{b}^\dagger_{\mathbf{i},\sigma} \to -\hat{b}_{\mathbf{i},-\sigma}$, leads to the relation $A^\uparrow(\mathbf{k}, \omega) = A^\downarrow(\mathbf{k}, -\omega)$. At finite magnetic fields or equivalently at finite magnetizations, the staggered transverse order leads to a gapless Goldstone mode of which the quasiparticle can spin-flip scatter. As a consequence, and as already observed in the mean-field calculation, the features of the down spectral function should be visible in $A^\uparrow(\mathbf{k}, \omega)$. Upon close inspection of Fig. 6.4 one will observe that for each dominant low energy peak at $\omega(\mathbf{k})$ in $A^\uparrow(\mathbf{k}, \omega)$ a shadow feature at $-\omega(\mathbf{k})$ is present.

6.2. Discussion and outlook

Experimentally, such a transition could be observed by magneto resistance measurements. The transition to the canted antiferromagnet breaks a U(1) symmetry and hence occurs at finite temperatures, T_{KT}, in terms of a Kosterlitz-Thouless transition. Below T_{KT} the power-law decay of the transverse spin-spin correlation function should suffice to produce a visible pseudo-gap in the charge sector and hence an increase of the resistivity as a function of decreasing temperature. The primary issue to observe the transition is the magnitude of the required magnetic field such as to obtain a visible gap. With $t \approx 2.5\mathrm{eV}$ and $U \approx 5 - 12\mathrm{eV}$ [280] one can readily see that very large magnetic fields will be required to obtain charge gaps in the meV region. In particular, we can predict from our calculations that values of the order of $B \propto 10^2 - 10^3\mathrm{T}$ are required to obtain an acceptable gap.

In conclusion, we have carried out mean-field calculations and projective QMC simulations for the Hubbard model with the Zeeman spin coupling on the honeycomb lattice in a magnetic field oriented parallel to the lattice plane [240]. Our results show the inherent instability of the semimetallic state to a canted antiferromagnet upon application of the magnetic field.

7 Conclusion

All chapters have their own section with conclusion, discussion and outlook, so we refer to these for a summary of the individual projects. Nonetheless, let us comment the common themes throughout this thesis – the honeycomb lattice and quantum Monte Carlo.

The honeycomb lattice and its unique features have been discussed in Sec. 1.1. The relativistic dispersion and the vanishing density of states of electrons on the honeycomb lattice make the system resistant against instabilities. We have seen that many consequences of a local Coulomb interaction may be successfully captured in a simple mean field approach (Ch. 6), and the mean field ground states are very robust against the introduction of fluctuations (Ch. 5). At the same time, the low coordination number drives fluctuations which, in interplay with the sparse energy density around the Fermi level, suggests that correlations should be taken into account. Indeed, in Chapters 4 and 5 we have seen that in the intermediate coupling regime an unforeseen quantum spin liquid emerges, which is one of the most sought-after quantum phenomena in materials as well as realistic models. The rich physics on hexagonal lattices, or lattices with a dispersion relation similar to the honeycomb lattice, also play a dominant role in the booming fields of topological insulators and graphene electronics. It sets the ground for more unexpected and exciting discoveries in the future.

Our method of choice in these investigations is quantum Monte Carlo (Sec. 1.2, Ch. 2). Coming with its own complications and limitations like any method, quantum Monte Carlo has one compelling advantage: it is correct within error bars. Without uncontrolled approximations this method yields the true answer – within error bars! As seen in Chapters 4 and 5, quantum Monte Carlo yields results beyond the reach of mean field approximations, and most probably beyond the reach of perturbative approaches. A power which is invaluable when studying the complex interplay of interactions.

While the projects in Chapters 2, 3 and 6 are essentially completed, the projects in Chapters 4 and 5 brought up a number of questions, which we want to persue in the future. Especially the discovery of a quantum spin liquid in an model accessible by means of QMC leaves a bunch of loose strings, which need to be tied. However, let us mention

that although it seems to be a straightforward task to do more simulations, on larger lattices, at finite temperature, or looking into dynamical correlations more closely, each of them presents a huge undertaking by themselves. The computational effort to obtain the results in Ch. 4 already scratched the limits of nowadays computing resources. Going to even larger supercomputers requires an extended improvement and further specialization of the code. Nevertheless, we are convinced that further characterization of that exotic phase and exploring its consequences will prove to be a worthwhile investment.

Follow-up

A

A.1. The Suzuki-Trotter decomposition in detail

The decomposition used in Sec. 1.2 is presented for a sum of two non-commuting operators. If the commutator of two operators A and B vanishes, we can simply decompose into the exact product

$$\mathrm{e}^{(A+B)} = \mathrm{e}^{A}\,\mathrm{e}^{B}, \qquad \text{for } [A,B]=0\,. \tag{A.1}$$

In general, the two operators do *not* commute, which introduces the error R of the decomposition

$$\mathrm{e}^{-\beta(A+B)} = \mathrm{e}^{-\beta A}\,\mathrm{e}^{-\beta B} + R\,. \tag{A.2}$$

Expanding both sides in Taylor series for the first three terms yields

$$\mathrm{e}^{-\beta\,(A+B)} = 1-\beta\,(A+B)+\frac{\beta^2}{2}(A^2+B^2+2AB+[B,A])+\mathcal{O}(\beta^3)\,, \tag{A.3}$$

$$\begin{aligned}\mathrm{e}^{-\beta A}\,\mathrm{e}^{-\beta B} &= (1-\beta A+\frac{\beta^2}{2}A^2)\cdot(1-\beta B+\frac{\beta^2}{2}B^2)\\ &= (1-\beta\,(A+B)+\frac{\beta^2}{2}(A^2+B^2+2AB)+\mathcal{O}(\beta^3)\,,\end{aligned} \tag{A.4}$$

for left-hand side and right-hand side, respectively. Comparing these equations the error can be estimated with $\mathcal{O}(\beta^3)$. It is the product of the two operators A and B times $\beta^2/2$. Let t_A and t_B denote the order of magnitude of the operators the error can be written as

$$R \approx \frac{\beta^2}{2}\,\mathcal{O}(t_A\,t_B)\,. \tag{A.5}$$

In case of the Hubbard Hamiltonian t_A and t_B correspond to t and U. Using the lowest order Trotter decomposition, the error is proportional to $\Delta\tau^2$, under the condition that

the relevant operators are simultaneously real representable (Hermitian) [281]. In order to reduce this problem an improved form is given by a symmetric decomposition

$$\mathrm{e}^{-\beta\,(A+B)} = \mathrm{e}^{-\frac{\beta}{2}A}\,\mathrm{e}^{-\beta B}\,\mathrm{e}^{-\frac{\beta}{2}A} + \frac{\beta^3}{24}\,\mathcal{O}(t_A\,t_B\max(t_a,t_b))\;. \tag{A.6}$$

Note, there exists a variety of higher order decompositions, however they are numerical more expensive.

Whereas the product $\Delta\tau L$ defines the projection parameter (inverse temperature) of the simulation the right choice of $\Delta\tau$ and L depends on the observables one is interested in. In general this discretization determines the physics, hence time-steps should be reasonably small $U\Delta\tau < 1$ and checked by extrapolation $\Delta\tau \to 0$.

A.2. Trace over the fermions

We show that the trace over fermionic degrees of freedom can be expressed in form of a determinant. A Hamiltonian, bilinear in its fermion operators, can be straightforwardly diagonalized [8, 16]

$$H = \sum_\alpha a_\alpha\, c_\alpha^\dagger c_\alpha\;, \tag{A.7}$$

where we used the operators $c_\alpha = \sum_i \langle\alpha|i\rangle\, c_i$, $c_\alpha^\dagger = \sum_i \langle i|\alpha\rangle\, c_i^\dagger$, which result from the unitary transformation to the basis of N-particle states $|\alpha\rangle$ in which H is diagonal. The trace over the fermions can then be written as a determinant

$$\mathrm{Tr}\,\mathrm{e}^{-H} = \mathrm{Tr}\,\mathrm{e}^{-\sum_\alpha a_\alpha c_\alpha^\dagger c_\alpha} = \mathrm{Tr}\prod_\alpha \mathrm{e}^{-a_\alpha c_\alpha^\dagger c_\alpha} = \prod_\alpha \sum_{n_\alpha=0,1} \mathrm{e}^{-a_\alpha n_\alpha} = \prod_\alpha (1+\mathrm{e}^{-a_\alpha})\;. \tag{A.8}$$

We see that the evolution of the N-particle state is the superposition of the propagation of each particle independently. This holds for any linear superposition of the eigenstates of H and any product of matrices (in a basis where they can be represented in bilinear (orthogonal) form). Therefore, we can write

$$\begin{aligned}\mathrm{Tr}\,\mathrm{e}^{-H} &= \mathrm{Tr}\,\mathrm{e}^{-\sum_{ij} c_i^\dagger A_{ij} c_j}\,\mathrm{e}^{-\sum_{ij} c_i^\dagger B_{ij} c_j} = \mathrm{Tr}\,\mathrm{e}^{-\sum_\nu \gamma_\nu n_\nu} \\ &= \prod_\nu \sum_{n_\nu=0,1} \mathrm{e}^{-\gamma_\nu c_\nu^\dagger c_\nu} = \prod_\nu \left(1+\mathrm{e}^{-\gamma_\nu}\right) = \det\left(\mathbf{1}+\mathrm{e}^{-\mathbf{A}}\mathrm{e}^{-\mathbf{B}}\right)\;.\end{aligned} \tag{A.9}$$

A.3. Peierls phase factors & boundary conditions

Here we introduce the notion of Peierls phase factors, which are a prerequisite for App. A.4. Consider the kinetic Hamiltonian

$$H = \sum_{\langle ij\rangle} c_i^\dagger\, t_{ij}\, c_j\;, \tag{A.10}$$

and introduce a general (gauge invariant) magnetic field

$$H(\mathbf{A},\phi) = \sum_{\langle ij\rangle} \mathrm{e}^{\frac{2\pi \mathrm{i}}{\Phi_0}\int_{\mathbf{i}}^{\mathbf{j}} d\boldsymbol{\ell}\mathbf{A}(\mathbf{x},t)} c_i^\dagger\, t_{ij}\, c_j + e\sum_i c_i^\dagger c_i\, \phi(\mathbf{i},t)\ , \tag{A.11}$$

where $\Phi_0 = hc/e$ being the flux quanta and $\mathbf{i}$, $\mathbf{j}$ are the positions of the sites i, j. Using this definition gauge invariance is guaranteed, e.g., the general gauge transformation $\mathbf{A}'(\mathbf{x},t) = \mathbf{A}(\mathbf{x},t) + \boldsymbol{\nabla}\chi(\mathbf{x})$, $\phi'(\mathbf{x},t) = \phi(\mathbf{x},t)$ leaves the Hamiltonian (A.11) invariant up to an energy shift

$$\begin{aligned} H(\mathbf{A}',\phi') &= \sum_{\langle ij\rangle} \mathrm{e}^{\frac{2\pi \mathrm{i}}{\Phi_0}\int_{\mathbf{i}}^{\mathbf{j}} d\boldsymbol{\ell}\mathbf{A}(\mathbf{x},t)+\chi(\mathbf{j})-\chi(\mathbf{i})} c_i^\dagger\, t_{ij}\, c_j + e\sum_i c_i^\dagger c_i\, \phi(\mathbf{i},t) \\ &= \sum_{\langle ij\rangle} \underbrace{\mathrm{e}^{-\frac{2\pi \mathrm{i}}{\Phi_0}\chi(\mathbf{i})} c_i^\dagger}_{\tilde{c}_i^\dagger}\, t_{ij}\, \underbrace{\mathrm{e}^{\frac{2\pi \mathrm{i}}{\Phi_0}\chi(\mathbf{j})} c_j}_{\tilde{c}_j}\, \mathrm{e}^{\frac{2\pi \mathrm{i}}{\Phi_0}\int_{\mathbf{i}}^{\mathbf{j}} d\boldsymbol{\ell}\mathbf{A}(\mathbf{x},t)}\, c_j + e\sum_i n_i\, \phi(\mathbf{i},t)\ . \end{aligned} \tag{A.12}$$

Absorbing the phases into the creation (annihilation) operators leaves Eq. (A.12) equivalent to $H(\mathbf{A},\phi)$, but for a different choice of gauge.

Homogeneous magnetic field

The introduction of these so-called Peierls factors allows to, e.g., introduce a magnetic field $\mathbf{B} = (0,0,B) = \boldsymbol{\nabla}\times\mathbf{A} \to \mathbf{A} = (-y,x,0)B/2$, such that on a square lattice with periodic boundary conditions

$$c_i^\dagger c_j \mathrm{e}^{\frac{2\pi \mathrm{i}}{\Phi_0}\int_{\mathbf{i}}^{\mathbf{j}} d\boldsymbol{\ell}\mathbf{A}(\boldsymbol{\ell})} \overset{!}{=} c_{\mathbf{i}+L\mathbf{a}_\mu}^\dagger c_{\mathbf{j}+L\mathbf{a}_\mu} \mathrm{e}^{\frac{2\pi \mathrm{i}}{\Phi_0}\int_{\mathbf{i}+L\mathbf{a}_\mu}^{\mathbf{j}+L\mathbf{a}_\mu} d\boldsymbol{\ell}\mathbf{A}(\boldsymbol{\ell})}\ , \tag{A.13}$$

where $\mathbf{a}_\mu$ stands for the primitive vectors $\mathbf{a}_x$, $\mathbf{a}_y$. Shifting the integration boundaries $\boldsymbol{l}' = \boldsymbol{l} - L\mathbf{a}_\mu$ yields

$$\int_{\mathbf{i}+L\mathbf{a}_\mu}^{\mathbf{j}+L\mathbf{a}_\mu} d\boldsymbol{\ell}\mathbf{A}(\boldsymbol{\ell}) = \int_{\mathbf{i}}^{\mathbf{j}} d\boldsymbol{\ell}'\,\mathbf{A}(\boldsymbol{\ell}'+L\mathbf{a}_\mu) = \int_{\mathbf{i}}^{\mathbf{j}} d\boldsymbol{\ell}'\left(\mathbf{A}(\boldsymbol{\ell}') + \boldsymbol{\nabla}\chi_\mu(\boldsymbol{\ell})\right)\ , \tag{A.14}$$

with

$$\chi_x(\mathbf{x}) = \frac{B}{2}Ly\ , \qquad \chi_y(\mathbf{x}) = -\frac{B}{2}Lx\ , \tag{A.15}$$

such that

$$\begin{aligned} c_i^\dagger c_j \mathrm{e}^{\frac{2\pi \mathrm{i}}{\Phi_0}\int_{\mathbf{i}}^{\mathbf{j}} d\boldsymbol{\ell}\mathbf{A}(\boldsymbol{\ell})} &= c_{\mathbf{i}+L\mathbf{a}_\mu}^\dagger c_{\mathbf{j}+L\mathbf{a}_\mu} \mathrm{e}^{\frac{2\pi \mathrm{i}}{\Phi_0}\int_{\mathbf{i}}^{\mathbf{j}} d\boldsymbol{\ell}(\mathbf{A}(\boldsymbol{\ell})+\nabla\chi_\mu(\boldsymbol{\ell}))} \\ &= c_{\mathbf{i}+L\mathbf{a}_\mu}^\dagger \mathrm{e}^{-\frac{2\pi \mathrm{i}}{\Phi_0}\chi_\mu(\mathbf{i})}\, c_{\mathbf{j}+L\mathbf{a}_\mu} \mathrm{e}^{\frac{2\pi \mathrm{i}}{\Phi_0}\chi_\mu(\mathbf{j})}\ . \end{aligned} \tag{A.16}$$

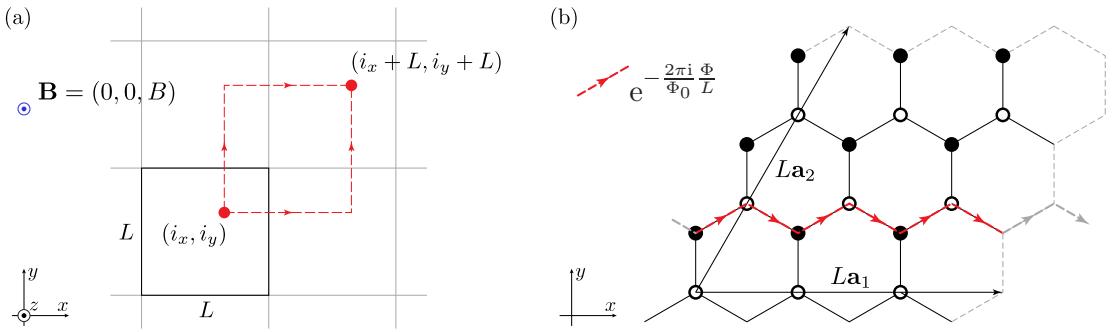

Fig. A.1.: Illustration of the gauge invariance of two paths through the periodic lattice (a) and a path along one lattice direction, picking up portions of phase leading to twisted boundary conditions (b).

The boundary condition reads

$$c^\dagger_{i+L} = e^{\frac{2\pi i}{\Phi_0}\chi_\mu(\mathbf{i})} c^\dagger_i \,. \tag{A.17}$$

The quantization of the magnetic field arises naturally from the requirement that the wave function must be single-valued, hence independent paths between two points must give the same phase (cf. Fig. A.3a)

$$\begin{aligned} e^{\frac{2\pi i}{\Phi_0}\frac{B}{2}\chi_x(\mathbf{i})} e^{\frac{2\pi i}{\Phi_0}\chi_y(\mathbf{i}+L\mathbf{a}_x)} &= e^{\frac{2\pi i}{\Phi_0}\frac{B}{2}\chi_y(\mathbf{i})} e^{\frac{2\pi i}{\Phi_0}\chi_x(\mathbf{i}+L\mathbf{a}_x)} \\ e^{\frac{2\pi i}{\Phi_0}\frac{B}{2}L(i_x+L)+Li_y} &= e^{\frac{2\pi i}{\Phi_0}\frac{B}{2}L(i_y+L)+Li_x} \,. \end{aligned} \tag{A.18}$$

This implies

$$\exp(2\pi i \frac{BL^2}{\Phi_0}) = 1 \quad \rightarrow \quad \frac{BL^2}{\Phi_0} = n \in \mathbb{N} \,, \tag{A.19}$$

such that the total magnetic field penetrating the lattice has to be a multiple integer of the flux quanta $\Phi_0 \approx 2.067 \times 10^{-15}\mathrm{Tm}^2$ (Wb). The magnetic field brings the advantage that degeneracies on the finite size energy spectrum are split, hence finite size gaps in the density of states become filled in, leading to a denser spectrum. Therefore finite size effects are reduced and the magnetic field may serve as an additional parameter in which finite-*size* scaling can be performed [282].

Twisted boundary conditions

The right choice of the vector potential also allows to impose a twist in the periodic boundary conditions, e.g., along the $\mathbf{a}_1$-, or x-direction

$$\mathbf{A}(\mathbf{x}) = \frac{\Phi}{L}\mathbf{e}_x \,, \qquad c^\dagger_{i+L} = c^\dagger_i \,, \tag{A.20}$$

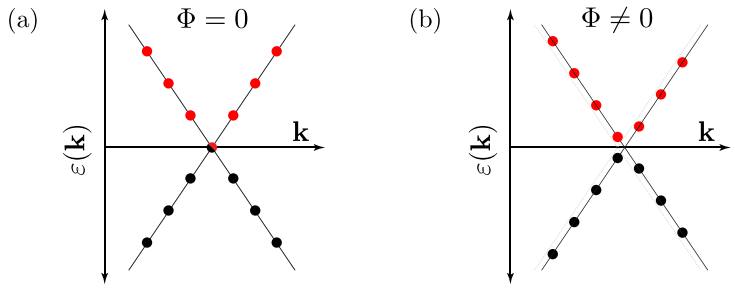

Fig. A.2.: Band degeneracy close to the Fermi level in the case of no flux (a) and finite flux Φ (b) traversing the lattice. Nonzero flux shifts the energies such that the degeneracy at the K-point is lifted.

such that

$$\begin{aligned} H &= \sum_{\langle ij \rangle} c_i^\dagger \, t_{ij} \, c_j \, \mathrm{e}^{\frac{2\pi \mathrm{i}}{\Phi_0} \frac{\phi}{L} (\mathbf{j}-\mathbf{i}) \cdot \mathbf{e}_x} \\ &= \sum_{\langle ij \rangle} \underbrace{c_i^\dagger \, \mathrm{e}^{-\frac{2\pi \mathrm{i}}{\Phi_0} \frac{\Phi}{L} i_x}}_{\tilde{c}_i^\dagger} \, t_{ij} \, \underbrace{c_j \, \mathrm{e}^{\frac{2\pi \mathrm{i}}{\Phi_0} \frac{\Phi}{L} j_x}}_{\tilde{c}_j} \, . \end{aligned} \tag{A.21}$$

The absorption of the phase factors into the operators allows to remove the magnetic field contribution from the Hamiltonian such that they show up in the boundary conditions since

$$\tilde{c}_{i+L}^\dagger = \mathrm{e}^{-\frac{2\pi \mathrm{i}}{\Phi_0} \frac{\Phi}{L} (i_x + L)} \underbrace{c_{i_x+L}^\dagger}_{c_i^\dagger} = \mathrm{e}^{-\frac{2\pi \mathrm{i}}{\Phi_0} \frac{\Phi}{L} L} \underbrace{c_i^\dagger \, \mathrm{e}^{-\frac{2\pi \mathrm{i}}{\Phi_0} \frac{\Phi}{L} i}}_{\tilde{c}_i^\dagger} = \mathrm{e}^{-\frac{2\pi \mathrm{i} \Phi}{\Phi_0}} \tilde{c}_i^\dagger \, . \tag{A.22}$$

Hence running along the x-axis one picks up portions of $\exp(-\frac{2\pi \mathrm{i} \Phi}{\Phi_0 L})$ such that going once through the lattice the acquires the phase twist $\exp(-\frac{2\pi \mathrm{i} \Phi}{\Phi_0})$ defined by the flux Φ (cf. Fig. A.3b). A twist may be used to lift the degeneracy in the bands of the free system as illustrated in Fig. A.3. This is one method to setup a non-degenerate trial wave function starting from the non-interacting Hamiltonian.

A.4. Flux quantization

Flux quantization denotes the phenomenon, predicted by London [283], in which the magnetic field is quantized in units of $h/2e$. This occurs in Type II superconductors subjected to a magnetic field. While below a critical field all magnetic flux inside the superconductor is suppressed according to the Meissner effect, up to a second critical field value flux can penetrate the superconducting bulk in discrete units – the flux quanta.

Flux quantization is used synonymously for the measurement of the phase structure in a numerical model, wherefrom its superconducting properties can be determined

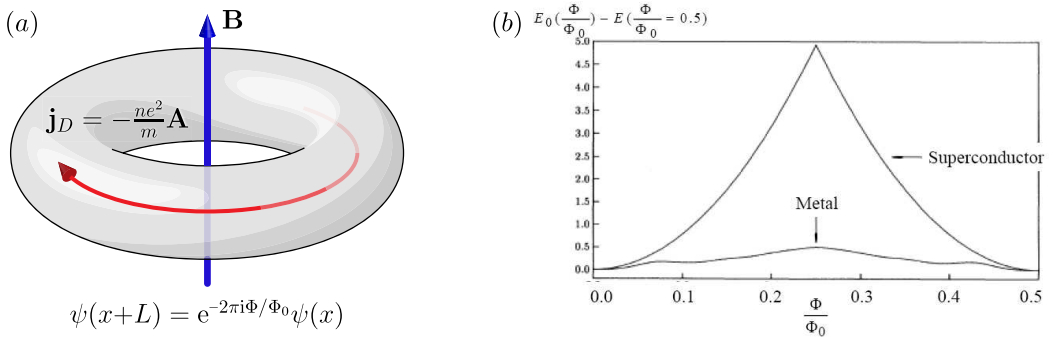

Fig. A.3.: Flux through the centre of a torus on which the lattice lies when using periodic boundary conditions (a). The macroscopic energy difference $E_0(\Phi/\Phi_0) - E_0(\Phi/\Phi_0 = 1/2)$ (b) for free bosons and fermions on a 64×64 lattice, taken from Ref. [190]. The curve for the fermions scales to zero in the thermodynamic limit.

independent of the pairing symmetry [192, 284, 190, 191]. In the flux quantization measurement, a magnetic flux Φ, in units of the flux quantum Φ_0 is thrusted through the centre of a torus on which the lattice of the model lies (when using periodic boundary conditions) shown in Fig. A.4a. From the functional form of the ground state energy with respect to the flux, $E_0(\Phi/\Phi_0)$, we can distinguish between normal and superconducting ground states. In a regular metal the total energy must not depend on the flux and the macroscopic energy difference $E_0(\Phi/\Phi_0) - E_0(\Phi/\Phi_0 = 1/2)$, which scales in the thermodynamic limit to a flat line as shown in Fig. A.4b. The remaining structure in Fig. A.4b is due to the finite lattice used.

Byers and Yang have shown that in the thermodynamic limit, $E_0(\Phi)$ exhibits local minima at quantized values of Φ, separated by is 1/n, which denotes the sum of charges in the basic group [192] (e.g., $n = 2$ for Cooper-pairs). These local minima in $E_0(\Phi)$ must be separated by a finite energy barrier and are related to the existence of super-currents which are trapped in the metastable states (cf. Fig. A.4b). This phenomenon is known as anomalous flux quantization. The superconducting state corresponds to a system spanning, macroscopic wave function and would hence *feel* the energy barrier which traps the super-current and stops it from dribbling away. For an insulating state the wave function is localized (decaying exponentially), hence it does not span around the torus is thus not influenced by the flux-barrier. Note, that the existence of anomalous flux quantization is only an indication of pairing, not a sufficient in itself to imply a superconducting state. Additionally needed is a finite superfluid density

$$\rho_s = \frac{1}{L^{d-2}} \frac{\partial^2 E_0(\Phi)}{\partial \Phi^2}\Big|_{\Phi=0} , \tag{A.23}$$

which corresponds to the curvature of the envelope of $E_0(\Phi/\Phi_0) - E_0(\Phi/\Phi_0 = 1/2)$. This quantity should approach a finite constant as $L \to \infty$ in a superconducting or perfectly

conducting metallic state. The existence of superconductivity is proven by an anomalous flux quantization and a simultaneously finite superfluid density.

A.5. Excitation spectra for the half-filled SU(2) Hubbard model

In Fig. A.4 and Fig. A.5 we show the intensity maps and energy distribution curves for a, $L = 15$ system. The spectral function $A(\mathbf{k}, \omega) = -\mathrm{Im}G(\mathbf{k}, \omega)/\pi$ is obtained from the stochastic analytic continuation of the one-particle Green's function to the real axis [220, 221]. The momentum resolved spectra run along the high symmetry path Γ-M-K-Γ for the values of $U/t = 3.5$, 4.0, 4.5 and 5.0. The spectra show a smooth transition from the renormalized Dirac liquid at $U/t = 3.5$ to the strong coupling regime $U/t = 5.0$. For $U/t = 3.5$ shadow bands appear in the one particle Green's function $A(\mathbf{k}, \omega)$ at higher energy, separated approximately by $2t$. Note that the intensity scale is logarithmic and hence emphasizes even small contributions. For all values of U/t the dominant excitation is located at K, the point closest to the Fermi level. As the system enters the intermediate phase, a Hubbard band forms at and close to the nesting vector at Γ and a gap opens. As U/t is increased even further the Hubbard bands are pushed to higher energies and the bandwidth of the lower branch becomes smaller.

The spin susceptibility $\chi_s(\mathbf{k}, \omega)$ shows a spin-wave like feature for all values of U/t which becomes smaller, and will asymptotically approach zero as U/t increases. In the QSL phase at $U/t = 4.0$ one can guess the existence of a finite spin gap. However, these spectra a for finite size system ($L = 15$), such that finite size gaps are always present. For larger U/t the lowest excitations increase in intensity and are closer to zero as one would expect from the formation of a Goldstone mode. In the intermediate phase the predicted excitation continuum of, e.g., deconfined spinons, cannot be seen. Indeed, the quasi-particle excitations appear well defined, such that we can identify the dominant peaks as the singlet-triplet excitations. The excitations above the gap might be of low intensity, vanishing in the statistical noise.

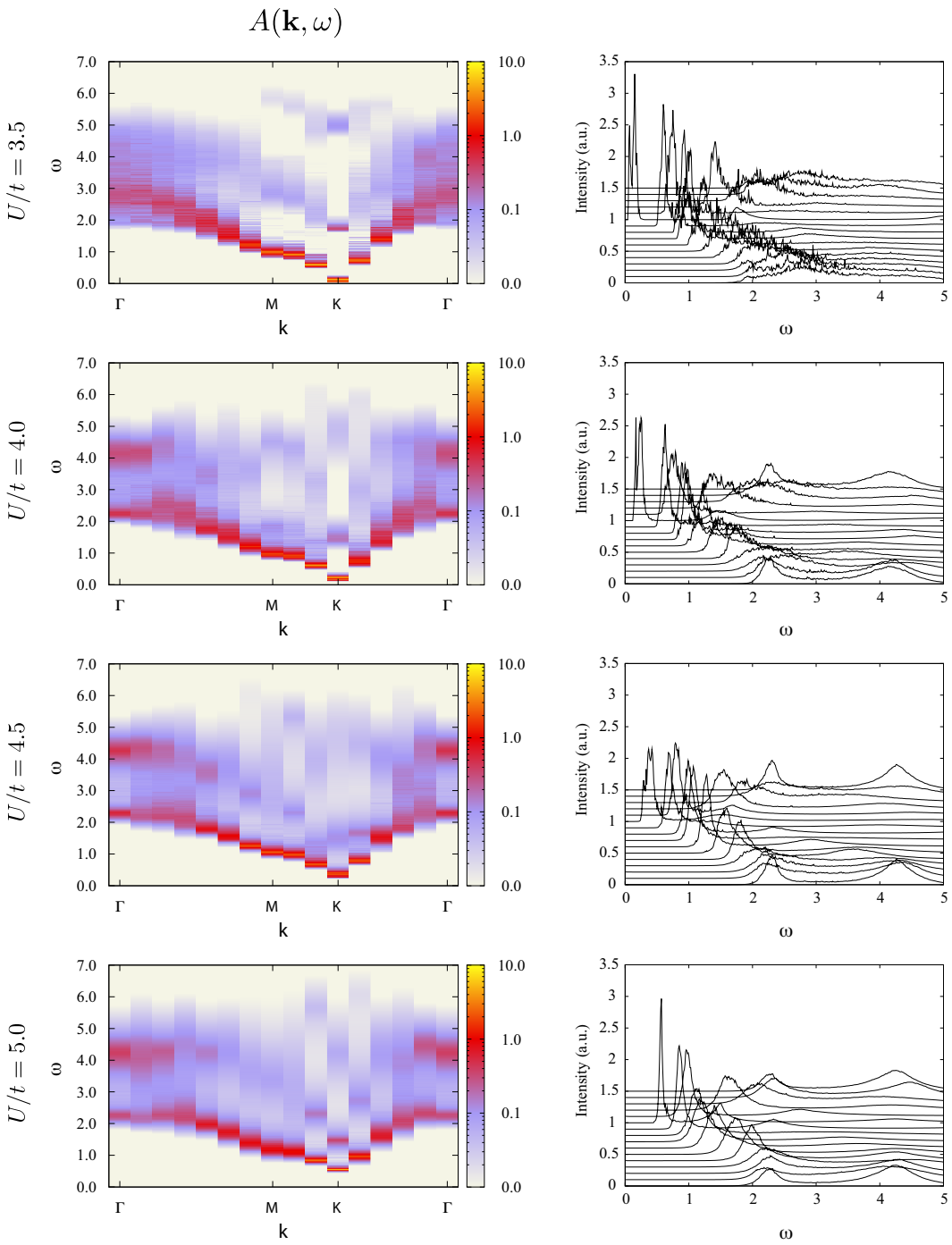

Fig. A.4.: Momentum resolved one particle Green's function spectra as intensity map (left) and energy distribution curves (right) along the high symmetry path Γ-M-K-Γ for the values of $U/t = 3.5$, 4.0, 4.5 and 5.0. The spectra show a smooth transition from the renormalized free case at $U/t = 3.5$ to the strong coupling regime $U/t = 5.0$.

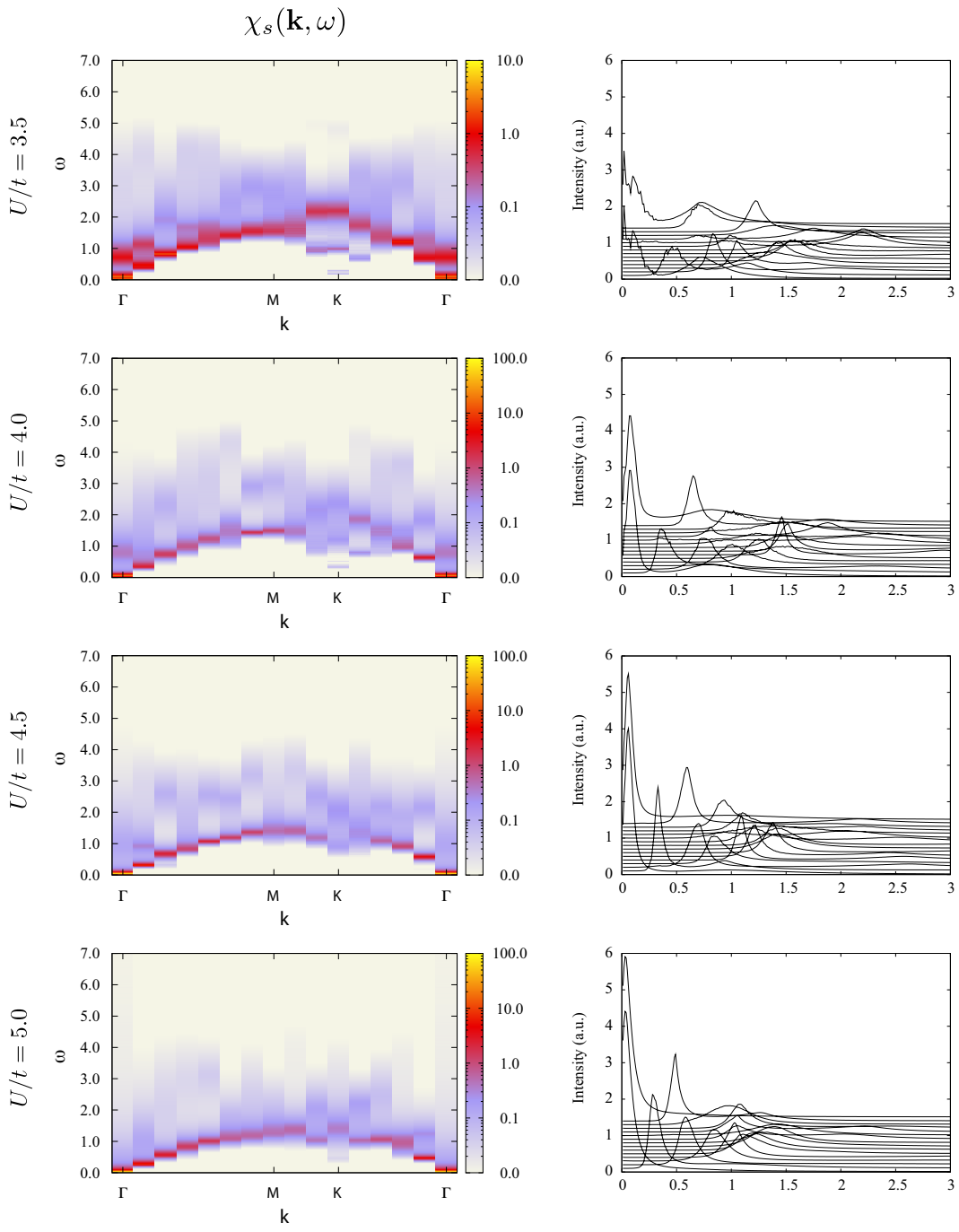

Fig. A.5.: Momentum resolved one particle spin susceptibility spectra as intensity map (left) and energy distribution curves (right) along the high symmetry path Γ-M-K-Γ for the values of $U/t = 3.5$, 4.0, 4.5 and 5.0. The spectra show a smooth transition from the renormalized free case at $U/t = 3.5$ to the strong coupling regime $U/t = 5.0$.

Bibliography

[1] A. H. C. Neto, F. Guinea, N. M. R. Peres, K. S. Novoselov, and A. K. Geim. The electronic properties of graphene. *Rev. Mod. Phys.* **81**, 109 (2009).

[2] P. R. Wallace. The Band Theory of Graphite. *Phys. Rev.* **71**, 622 (1947).

[3] J. C. Slonczewski and P. R. Weiss. Band Structure of Graphite. *Phys. Rev.* **109**, 272 (1958).

[4] G. W. Semenoff. Condensed-Matter Simulation of a Three-Dimensional Anomaly. *Phys. Rev. Lett.* **53**, 2449 (1984).

[5] M. Bercx. *Magnetic field induced semimetal-to-canted-antiferromagnet transition on the honeycomb lattice*. Master's thesis, Universität Würzburg (2008).

[6] N. Metropolis, A. W. Rosenbluth, M. N. Rosenbluth, A. H. Teller, and E. Teller. Equations of state calculations by fast computing machines. *J. Chem. Phys.* **21**, 1087 (1953).

[7] D. P. Landau and K. Binder. *A Guide to Monte Carlo Simulations in Statistical Physics*. Cambridge Univ. Press (2000).

[8] R. Blankenbecler, D. J. Scalapino, and R. L. Sugar. Monte Carlo calculations of coupled boson-fermion systems. I. *Phys. Rev. D* **24**, 2278 (1981).

[9] D. J. Scalapino and R. L. Sugar. Monte Carlo calculations of coupled boson-fermion systems. II. *Phys. Rev. B* **24**, 4295 (1981).

[10] F. F. Assaad and H. G. Evertz. World-line and Determinantal Quantum Monte Carlo Methods for Spins, Phonons and Electrons. *Lect. Notes Phys.* **739**, 277 (2008).

[11] T. C. Lang. *Dynamics & Charge Order in a quarter-filled ladder system coupled to the lattice*. Master's thesis, Technische Universität Graz (2005).

[12] M. Suzuki. *Comm. Math. Phys.* **51**, 183 (1976).

[13] M. Suzuki, S. Miyashita, and A. Kuroda. Monte Carlo Simulation of Quantum Spin Systems. I. *Prog. Theor. Phys.* **58**, 1377 (1977).

[14] H. F. Trotter. On the product of semi-groups of operators. *Proc. Amer. Math. Soc.* **10**, 545 (1959).

[15] J. Hubbard. Calculation of Partition Functions. *Phys. Rev. Lett.* **3**, 77 (1959).

[16] J. E. Hirsch. Two-dimensional Hubbard model: Numerical simulation study. *Phys. Rev. B* **31**, 4403 (1985).

[17] A. Muramatsu. *Quantum Monte Carlo Methods in Physics and Chemistry: Quantum Monte Carlo for Lattice Fermions.* M. P. Nightingale and C. J. Umrigar (Eds.), NATO Science Series Vol. :343-373, Kluwer Academic, Dordrecht (1999).

[18] F. F. Assaad. SU(2)-spin Invariant Auxiliary Field Quantum Monte Carlo Algorithm for Hubbard models. *arXiv*:cond-mat/9806307 (1998).

[19] F. F. Assaad. Phase diagram of the half-filled two-dimensional SU(N) Hubbard-Heisenberg model: A quantum Monte Carlo study. *Phys. Rev. B* **71**, 075103 (2005).

[20] G. D. Mahan. *Many-particle physics.* Plenum Press (1981).

[21] A. L. Fetter and J. D. Walecka. *Quantum Theory of Many-Particle Systems.* McGraw-Hill (1971).

[22] J. W. Negele and H. Orland. *Quantum Many-Particle Physics.* Perseus Books (1998).

[23] M. Feldbacher and F. F. Assaad. Efficient calculation of imaginary-time-displaced correlation functions in the projector auxiliary-field quantum Monte Carlo algorithm. *Phys. Rev. B* **63**, 073105 (2001).

[24] A. M. Tsvelik. *Quantum Field Theory in Condensed Matter Physics.* Cambridge Univ. Press (1996).

[25] M. Troyer and U.-J. Wiese. Computational Complexity and Fundamental Limitations to Fermionic Quantum Monte Carlo Simulations. *Phys. Rev. Lett.* **94**, 170201 (2005).

[26] R. W. Floyd. Nondeterministic Algorithms. *Journal ACM* **14**, 636 (1967).

[27] S. Chandrasekharan and U.-J. Wiese. Meron-Cluster Solution of Fermion Sign Problems. *Phys. Rev. Lett.* **83**, 3116 (1999).

[28] W. Janke. *Statistical Analysis of Simulations: Data Correlations and Error Estimation.* J. Grotendorst and A. Muramatsu (Eds.), NIC Series Vol. 10, Jülich (2002).

[29] A. D. Sokal and L. E. Thomas. Exponential convergence to equilibrium for a class of random walk models. *J. Stat. Phys.* **54**, 797 (1989).

[30] H. G. Evertz. The Loop Algorithm. *Adv. Phys.* **52**, 1 (2003).

[31] J. Hubbard. Electron Correlations in Narrow Energy Bands I. *Proc. R. Phys. Soc. London Series A* **276**, 238 (1963).

[32] J. Hubbard. Electron Correlations in Narrow Energy Bands II. *Proc. R. Phys. Soc. London Series A* **277**, 237 (1963).

[33] J. Hubbard. Electron Correlations in Narrow Energy Bands III. *Proc. R. Phys. Soc. London Series A* **281**, 401 (1963).

[34] E. H. Lieb and F. Y. Wu. Absence of Mott Transition in an Exact Solution of the Short-Range, One-Band Model in One Dimension. *Phys. Rev. Lett.* **20**, 1445 (1968).

[35] M. Karbach and G. Muller. Introduction to the Bethe Ansatz I. *Comput. Phys.* **11**, 36 (1997).

[36] M. Karbach, K. Hu, and G. Muller. Introduction to the Bethe Ansatz II. *Comput. Phys.* **12**, 565 (1998).

[37] M. Karbach, K. Hu, and G. Muller. Introduction to the Bethe Ansatz III. *arXiv*:cond-mat/0008018 (2000).

[38] F. Gebhard. *The Mott Metal-Insulator Transition.* Springer, Berlin Heidelberg (1997).

[39] A. Auerbach. *Interacting Electrons and Quantum Magnetism.* Springer, New York (1994).

[40] S. Watanabe and M. Imada. Thermodynamic Relations in Correlated Systems. *J. Phys. Soc. Jpn.* **73**, 3341 (2004).

[41] C. N. Yang and S. Z. Zhang. SO(4) symmetry in a Hubbard model. *Mod. Phys. Lett. B* **4**, 759 (1990).

[42] M. Feldbacher. *Hubbard and Kondo lattice models in two dimensions: A QMC study.* Ph.D. thesis, Bayerische Julius-Maximiliam-Universität Würzburg (2003).

[43] M. Hamermesh. *Group theory and its application to physical problems.* Addison-Wesley (1962).

[44] S. Sachdev. *Quantum phase transitions.* Cambridge Univ. Press (2001).

[45] M. Vojta. Quantum phase transitions. *Rep. Prog. Phys.* **66**, 2069 (2003).

[46] J. Goldstone. Field Theories With 'Superconductor' Solutions. *Nuovo Cim.* **19**, 154 (1961).

[47] J. Goldstone, A. Salam, and S. Weinberg. Broken Symmetries. *Phys. Rev.* **127**, 965 (1962).

[48] N. D. Mermin and H. Wagner. Absence of ferromagnetism or antiferromagnetism in one-or twodimensional isotropic Heisenberg models. *Phys. Rev. Lett.* **17**, 1133 (1966).

[49] T. Koma and H. Tasaki. Symmetry breaking and finite size effects in quantum

many-body systems. *J. Stat. Phys.* **76**, 745 (1994).

[50] F. F. Assaad and T. C. Lang. Diagrammatic Determinantal methods: projective schemes and applications to the Hubbard-Holstein model. *Phys. Rev. B* **76**, 035116 (2007).

[51] A. N. Rubtsov, V. V. Savkin, and A. I. Lichtenstein. Continuous-time quantum Monte Carlo method for fermions. *Phys. Rev. B* **72**, 035122 (2005).

[52] P. Werner, A. Comanac, L. de' Medici, M. Troyer, and A. J. Millis. Continuous-Time Solver for Quantum Impurity Models. *Phys. Rev. Lett.* **97**, 076405 (2006).

[53] E. Gull, P. Werner, A. Millis, and M. Troyer. Performance analysis of continuous-time solvers for quantum impurity models. *Phys. Rev. B* **76**, 235123 (2007).

[54] J. E. Hirsch and R. M. Fye. Monte Carlo Method for Magnetic Impurities in Metals. *Phys. Rev. Lett.* **56**, 2521 (1986).

[55] D. J. Luitz. *Anwendung der Diagrammatischen Monte Carlo Methode auf den Josephson Strom durch einen Kondo-Quantenpunkt.* Master's thesis, Universität Würzburg (2008).

[56] M. Feldbacher, K. Held, and F. F. Assaad. Projective Quantum Monte Carlo Method for the Anderson Impurity Model and its Application to Dynamical Mean Field Theory. *Phys. Rev. Lett.* **93**, 136405 (2004).

[57] M. I. Katsnelson. Comment on "Projective Quantum Monte Carlo Method for the Anderson Impurity Model and Its Application to Dynamical Mean Field Theory". *Phys. Rev. Lett.* **96**, 139701 (2006).

[58] M. Feldbacher, K. Held, and F. F. Assaad. Feldbacher, Held, and Assad Reply:. *Phys. Rev. Lett.* **96**, 139702 (2006).

[59] P. Werner and A. J. Millis. Efficient Dynamical Mean Field Simulation of the Holstein-Hubbard Model. *Phys. Rev. Lett.* **99**, 146404 (2007).

[60] J. E. Hirsch, R. L. Sugar, D. J. Scalapino, and R. Blankenbecler. Monte Carlo simulations of one-dimensional fermion systems. *Phys. Rev. B* **26**, 5033 (1982).

[61] F. F. Assaad and D. Würtz. Charge and spin structures in the one-dimensional t-J model. *Phys. Rev. B* **44**, 2681 (1991).

[62] W. Koller, D. Meyer, Y. Ōno, and A. C. Hewson. First- and second-order phase transitions in the Holstein-Hubbard model. *Europhys. Lett.* **66**, 559 (2004).

[63] T. Maier, M. Jarrell, T. Pruschke, and M. H. Hettler. Quantum cluster theories. *Rev. Mod. Phys.* **77**, 1027 (2005).

[64] E. Gull, P. Werner, O. Parcollet, and M. Troyer. Continuous-time auxiliary-field Monte Carlo for quantum impurity models. *Europhys. Lett.* **82**, 57003 (2008).

[65] K. Mikelsons, A. Macridin, and M. Jarrell. Relationship between Hirsch-Fye and weak-coupling diagrammatic quantum Monte Carlo methods. *Phys. Rev. E* **79**, 057701 (2009). PMID: 19518603.

[66] F. F. Assaad. Spin, charge, and single-particle spectral functions of the one-dimensional quarter filled Holstein model. *Phys. Rev. B* **78**, 155124 (2008).

[67] F. Goth. *A Quantum Monte Carlo Method for Systems Out of Equilibrium.* Master's thesis, Universität Würzburg (2009).

[68] P. Werner, T. Oka, and A. J. Millis. Diagrammatic Monte Carlo simulation of nonequilibrium systems. *Phys. Rev. B* **79**, 035320 (2009).

[69] M. Eckstein, M. Kollar, and P. Werner. Thermalization after an Interaction Quench in the Hubbard Model. *Phys. Rev. Lett.* **103**, 056403 (2009).

[70] L. Hulthén. *Ark. Mat. Astron. Fys. A* **26**, 1 (1938).

[71] B. Sutherland. Systems with resonating-valence-bond ground states: Correlations and excitations. *Phys. Rev. B* **37**, 3786 (1988).

[72] S. Liang, B. Doucot, and P. W. Anderson. Some New Variational Resonating-Valence-Bond-Type Wave Functions for the Spin-1/2 Antiferromagnetic Heisenberg Model on a Square Lattice. *Phys. Rev. Lett.* **61**, 365 (1988).

[73] G. Rumer. *Göttingen Nachr. Tech.* **1932**, 377 (1932).

[74] L. Pauling. The Calculation of Matrix Elements for Lewis Electronic Structures of Molecules. *J. Chem. Phys.* **1**, 280 (1933).

[75] C. K. Majumdar and D. K. Ghosh. On Next-Nearest-Neighbor Interaction in Linear Chain. I. *J. Math. Phys.* **10**, 1388 (1969).

[76] B. S. Shastry and B. Sutherland. Exact ground state of a quantum mechanical antiferromagnet. *Physica B+C* **108**, 1069 (1981).

[77] I. Affleck, T. Kennedy, E. H. Lieb, and H. Tasaki. Rigorous results on valence-bond ground states in antiferromagnets. *Phys. Rev. Lett.* **59**, 799 (1987).

[78] P. W. Anderson. Resonating valence bonds: A new kind of insulator? *Mater. Res. Bull.* **8**, 153 (1973).

[79] P. Fazekas and P. W. Anderson. On the ground state properties of the anisotropic triangular antiferromagnet. *Philos. Mag.* **30**, 432 (1974).

[80] S. Liang. Existence of Néel order at T=0 in the spin-1/2 antiferromagnetic Heisenberg model on a square lattice. *Phys. Rev. B* **42**, 6555 (1990).

[81] S. Liang. Monte Carlo calculations of the correlation functions for Heisenberg spin chains at T=0. *Phys. Rev. Lett.* **64**, 1597 (1990).

[82] G. Santoro, S. Sorella, L. Guidoni, A. Parola, and E. Tosatti. Spin-Liquid Ground

State in a Two-Dimensional Nonfrustrated Spin Model. *Phys. Rev. Lett.* **83**, 3065 (1999).

[83] K. Beach and A. W. Sandvik. Some formal results for the valence bond basis. *Nucl. Phys. B* **750**, 142 (2006).

[84] K. S. D. Beach. Master equation approach to computing RVB bond amplitudes. *Phys. Rev. B* **79**, 224431 (2009).

[85] M. Barma and B. S. Shastry. Classical equivalents of one-dimensional quantum-mechanical systems. *Phys. Rev. B* **18**, 3351 (1978).

[86] J. J. Cullen and D. P. Landau. Monte Carlo studies of one-dimensional quantum Heisenberg and XY models. *Phys. Rev. B* **27**, 297 (1983).

[87] B. B. Beard and U. Wiese. Simulations of Discrete Quantum Systems in Continuous Euclidean Time. *Phys. Rev. Lett.* **77**, 5130 (1996).

[88] N. V. Prokof'ev, B. V. Svistunov, and I. S. Tupitsyn. Exact quantum Monte Carlo process for the statistics of discrete systems. *JETP Lett.* **64**, 911 (1996).

[89] A. W. Sandvik. Stochastic series expansion method with operator-loop update. *Phys. Rev. B* **59**, R14157 (1999).

[90] O. F. Syljuåsen and A. W. Sandvik. Quantum Monte Carlo with directed loops. *Phys. Rev. E* **66**, 046701 (2002).

[91] A. W. Sandvik. Evidence for Deconfined Quantum Criticality in a Two-Dimensional Heisenberg Model with Four-Spin Interactions. *Phys. Rev. Lett.* **98**, 227202 (2007).

[92] A. W. Sandvik and K. S. D. Beach. Monte Carlo Simulations of Quantum Spin Systems in the Valence Bond Basis. *Computer Simulation Studies in Condensed-Matter Physics XX* (2008).

[93] K. Beach. Simulating quantum spin systems in the valence bond basis. *Presentation, private communication* (2006).

[94] R. G. Melko and R. K. Kaul. Scaling in the Fan of an Unconventional Quantum Critical Point. *Phys. Rev. Lett.* **100**, 017203 (2008).

[95] A. W. Sandvik and H. G. Evertz. Loop updates for variational and projector quantum Monte Carlo simulations in the valence-bond basis. *Phys. Rev. B* **82**, 024407 (2010).

[96] A. W. Sandvik. Ground State Projection of Quantum Spin Systems in the Valence-Bond Basis. *Phys. Rev. Lett.* **95**, 207203 (2005).

[97] J. Lou and A. W. Sandvik. Z_4-U(1) crossover of the order parameter symmetry in a two-dimensional valence-bond-solid. *arXiv*:0811.0837 (2008).

[98] A. Banerjee and K. Damle. Generalization of the singlet sector valence bond loop algorithm to antiferromagnetic ground states with total spin $S_{tot} = 1/2$. *arXiv*:1006.2598 (2010).

[99] K. S. D. Beach, F. Alet, M. Mambrini, and S. Capponi. SU(N) Heisenberg model on the square lattice: A continuous-N quantum Monte Carlo study. *Phys. Rev. B* **80**, 184401 (2009).

[100] F. Alet, S. Capponi, N. Laflorencie, and M. Mambrini. Valence Bond Entanglement Entropy. *Phys. Rev. Lett.* **99**, 117204 (2007).

[101] A. B. Kallin, I. González, M. B. Hastings, and R. G. Melko. Valence Bond and von Neumann Entanglement Entropy in Heisenberg Ladders. *Phys. Rev. Lett.* **103**, 117203 (2009).

[102] M. B. Hastings, I. González, A. B. Kallin, and R. G. Melko. Measuring Renyi Entanglement Entropy in Quantum Monte Carlo Simulations. *Phys. Rev. Lett.* **104**, 157201 (2010).

[103] D. Schwandt, F. Alet, and S. Capponi. Quantum Monte Carlo Simulations of Fidelity at Magnetic Quantum Phase Transitions. *Phys. Rev. Lett.* **103**, 170501 (2009).

[104] A. F. Albuquerque, F. Alet, C. Sire, and S. Capponi. Quantum critical scaling of fidelity susceptibility. *Phys. Rev. B* **81**, 064418 (2010).

[105] N. Read and S. Sachdev. Some features of the phase diagram of the square lattice SU(N) antiferromagnet. *Nucl. Phys. B* **316**, 609 (1989).

[106] N. Read and S. Sachdev. Spin-Peierls, valence-bond solid, and Néel ground states of low-dimensional quantum antiferromagnets. *Phys. Rev. B* **42**, 4568 (1990).

[107] T. Senthil, A. Vishwanath, L. Balents, S. Sachdev, and M. P. A. Fisher. Deconfined Quantum Critical Points. *Science* **303**, 1490 (2004).

[108] T. Senthil, L. Balents, S. Sachdev, A. Vishwanath, and M. P. A. Fisher. Quantum criticality beyond the Landau-Ginzburg-Wilson paradigm. *Phys. Rev. B* **70**, 144407 (2004).

[109] R. Moessner, S. L. Sondhi, and P. Chandra. Phase diagram of the hexagonal lattice quantum dimer model. *Phys. Rev. B* **64**, 144416 (2001).

[110] A. Vishwanath, L. Balents, and T. Senthil. Quantum criticality and deconfinement in phase transitions between valence bond solids. *Phys. Rev. B* **69**, 224416 (2004).

[111] P. Ghaemi, A. Vishwanath, and T. Senthil. Finite-temperature properties of quantum Lifshitz transitions between valence-bond solid phases: An example of local quantum criticality. *Phys. Rev. B* **72**, 024420 (2005).

[112] D. S. Rokhsar and S. A. Kivelson. Superconductivity and the Quantum Hard-Core

Dimer Gas. *Phys. Rev. Lett.* **61**, 2376 (1988).

[113] P. W. Anderson. The Resonating Valence Bond State in La_2CuO_4 and Superconductivity. *Science* **235**, 1196 (1987).

[114] C. Zeng and C. L. Henley. Zero-temperature phase transitions of an antiferromagnetic Ising model of general spin on a triangular lattice. *Phys. Rev. B* **55**, 14935 (1997).

[115] R. K. Kaul and R. G. Melko. Large-N estimates of universal amplitudes of the CP^{N-1} theory and comparison with a S=1/2 square-lattice model with competing four-spin interactions. *Phys. Rev. B* **78**, 014417 (2008).

[116] A. W. Sandvik and R. Melko. Nature of the antiferromagnetic to valence-bond-solid quantum phase transition in a 2D XY-model with four-site interactions. *arXiv*:cond-mat/0604451 (2006).

[117] F. Jiang, M. Nyfeler, S. Chandrasekharan, and U. Wiese. From an antiferromagnet to a valence bond solid: evidence for a first-order phase transition. *J. Stat. Mech: Theory Exp.* page P02009 (2008).

[118] V. N. Kotov, D. Yao, A. H. C. Neto, and D. K. Campbell. Quantum phase transition in the four-spin exchange antiferromagnet. *Phys. Rev. B* **80**, 174403 (2009).

[119] A. W. Sandvik. Continuous Quantum Phase Transition between an Antiferromagnet and a Valence-Bond Solid in Two Dimensions: Evidence for Logarithmic Corrections to Scaling. *Phys. Rev. Lett.* **104**, 177201 (2010).

[120] S. L. Sondhi, S. M. Girvin, J. P. Carini, and D. Shahar. Continuous quantum phase transitions. *Rev. Mod. Phys.* **69**, 315 (1997).

[121] P. Sengupta, R. T. Scalettar, and R. R. P. Singh. High-energy magnon dispersion in the half-filled Hubbard model: A comparison with La_2CuO_4. *Phys. Rev. B* **66**, 144420 (2002).

[122] R. Coldea *et al.* Spin Waves and Electronic Interactions in La_2CuO_4. *Phys. Rev. Lett.* **86**, 5377 (2001).

[123] A. Läuchli, J. C. Domenge, C. Lhuillier, P. Sindzingre, and M. Troyer. Two-Step Restoration of SU(2) Symmetry in a Frustrated Ring-Exchange Magnet. *Phys. Rev. Lett.* **95**, 137206 (2005).

[124] A. W. Sandvik. Finite-size scaling of the ground-state parameters of the two-dimensional Heisenberg model. *Phys. Rev. B* **56**, 11678 (1997).

[125] J. Oitmaa, C. J. Hamer, and Z. Weihong. Quantum magnets on the honeycomb and triangular lattices at T=0. *Phys. Rev. B* **45**, 9834 (1992).

[126] J. D. Reger, J. A. Riera, and A. P. Young. Monte Carlo simulations of the spin-1/2

Heisenberg antiferromagnet in two dimensions. *J. Phys.: Condens. Matter* **1**, 1855 (1989).

[127] E. V. Castro, N. M. R. Peres, K. S. D. Beach, and A. W. Sandvik. Site dilution of quantum spins in the honeycomb lattice. *Phys. Rev. B* **73**, 054422 (2006).

[128] J. Fouet, P. Sindzingre, and C. Lhuillier. An investigation of the quantum J_1-J_2-J_3 model on the honeycomb lattice. *Eur. Phys. J. B* **20**, 241 (2001).

[129] A. W. Sandvik and D. J. Scalapino. Order-disorder transition in a two-layer quantum antiferromagnet. *Phys. Rev. Lett.* **72**, 2777 (1994).

[130] A. Mulder, R. Ganesh, L. Capriotti, and A. Paramekanti. Spiral order by disorder and lattice nematic order in a frustrated Heisenberg antiferromagnet on the honeycomb lattice. *Phys. Rev. B* **81**, 214419 (2010).

[131] P. Zhou, J. E. Drumheller, G. V. Rubenacker, K. Halvorson, and R. D. Willett. Novel lowdimensional spin 1/2 antiferromagnets: Twohalide exchange pathways in A_2CuBr_4 salts. *J. Appl. Phys.* **69**, 5804 (1991).

[132] Y. Singh and P. Gegenwart. Antiferromagnetic Mott insulating state in single crystals of the hexagonal lattice material Na_2IrO_3. *arXiv*:1006.0437v1 (2010).

[133] A. A. Tsirlin, O. Janson, and H. Rosner. β-$Cu_2V_2O_7$ - a spin-1/2 honeycomb lattice system. *arXiv*:1007.1646v1 (2010).

[134] G. L. Flem, R. Brec, G. Ouvard, A. Louisy, and P. Segransan. Magnetic interactions in the layer compounds MPX3 (M = Mn, Fe, Ni; X = S, Se). *J. Phys. Chem. Solids* **43**, 455 (1982).

[135] K. Kurosawa, S. Saito, and Y. Yamaguchi. Neutron Diffraction Study on MnPS3 and FePS3. *J. Phys. Soc. Jpn.* **52**, 3919 (1983).

[136] P. A. Joy and S. Vasudevan. Magnetism in the layered transition-metal thiophosphates MPS_3 (M=Mn, Fe, and Ni). *Phys. Rev. B* **46**, 5425 (1992).

[137] Z. Y. Meng, T. C. Lang, S. Wessel, F. F. Assaad, and A. Muramatsu. Quantum spin-liquid emerging in two-dimensional correlated Dirac fermions. *Nature* **464**, 847 (2010).

[138] X.-G. Wen. *Quantum Field Theory of Many-Body Systems.* Oxford Univ. Press (2004).

[139] S. A. Kivelson, D. S. Rokhsar, and J. P. Sethna. Topology of the resonating valence-bond state: Solitons and high-Tc superconductivity. *Phys. Rev. B* **35**, 8865 (1987).

[140] M. Hermele *et al.* Stability of $U(1)$ spin liquids in two dimensions. *Phys. Rev. B* **70**, 214437 (2004).

[141] S.-S. Lee and P. A. Lee. U(1) Gauge Theory of the Hubbard Model: Spin Liquid states and possible application to κ-(BEDT-TTF)$_2$Cu$_2$(CN)$_3$. *Phys. Rev. Lett.* **95**, 036403 (2005).

[142] P. A. Lee. Lecture Notes. *Boulder Summer School for Condensed Matter and Material Physics* (2010).

[143] X.-G. Wen, F. Wilczek, and A. Zee. Chiral spin states and superconductivity. *Phys. Rev. B* **39**, 11413 (1989).

[144] L. Balents. Spin liquids in frustrated magnets. *Nature* **464**, 199 (2010).

[145] W. Rantner and X.-G. Wen. Spin correlations in the agebraic spin liquid: Implications for high T$_c$ superconductors. *Phys. Rev. B* **97**, 144501 (2002).

[146] P. A. Lee, N. Nagaosa, and X.-G. Wen. Doping a Mott insulator: Physics of high-temperature superconductivity. *Rev. Mod. Phys.* **97**, 17 (2006).

[147] T. Mizusaki and M. Imada. Gapless quantum spin liquid, stripe, and antiferromagnetic phases in frustrated Hubbard models in two dimensions. *Phys. Rev. B* **74**, 014421 (2006).

[148] R. Moessner, S. L. Sondhi, and E. Fradkin. Short-ranged resonating valence bond physics, quantum dimer models, and Ising gauge theories. *Phys. Rev. B* **65**, 024504 (2001).

[149] R. Moessner and K. S. Raman. Quantum dimer models. *arXiv*:0809.3051 (2008).

[150] R. Moessner and S. L. Sondhi. Resonating Valence Bond Phase in the Triangular Lattice Quantum Dimer Model. *Phys. Rev. Lett.* **86**, 1881 (2001).

[151] E. Fradkin, D. A. Huse, R. Moessner, V. Oganesyan, and S. L. Sondhi. Bipartite Rokhsar-Kivelson points and Cantor deconfinement. *Phys. Rev. B* **69**, 224415 (2004).

[152] X.-G. Wen. Quantum orders and symmetric spin liquids. *Phys. Rev. B* **65**, 165113 (2002).

[153] Y.-M. Lu and Y. Ran. Spin liquids on a honeycomb lattice: Projective Symmetry Group study of Schwinger fermion mean-field theory. *arXiv*:1005.4229v1 (2010).

[154] B. J. Powell and R. H. McKenzie. Quantum frustration in organic Mott insulators: from spin liquids to unconventional superconductors. *arXiv*:1007.5381v1 (2010).

[155] X.-G. Wen. Mean-field theory of spin-liquid states with finite energy gap and topological orders. *Phys. Rev. B* **44**, 2664 (1991).

[156] M. Hermele, T. Senthil, and M. P. A. Fisher. Algebraic spin liquid as the mother of many competing orders. *Phys. Rev. B* **72**, 104404 (2005).

[157] M. Hermele. SU(2) gauge theory of the Hubbard model and application to the

honeycomb lattice. *Phys. Rev. B* **76**, 035125 (2007).

[158] M. Z. Hasan and C. L. Kane. Topological Insulators. *arXiv*:1002.3895 (2010).

[159] X. Qi and S. Zhang. Topological insulators and superconductors. *arXiv*:1008.2026 (2010).

[160] E. Lieb, T. Schultz, and D. Mattis. Two soluble models of an antiferromagnetic chain. *Annals of Physics* **16**, 407 (1961).

[161] I. Affleck and E. H. Lieb. A proof of part of Haldane's conjecture on spin chains. *Lett. Math. Phys.* **12**, 57 (1986).

[162] I. Affleck. Spin gap and symmetry breaking in CuO_2 layers and other antiferromagnets. *Phys. Rev. B* **37**, 5186 (1988).

[163] M. B. Hastings. Lieb-Schultz-Mattis in higher dimensions. *Phys. Rev. B* **69**, 104431 (2004).

[164] B. Nachtergaele and R. Sims. A Multi-Dimensional Lieb-Schultz-Mattis Theorem. *Comm. Math. Phys.* **276**, 437 (2007).

[165] M. B. Hastings. Sufficient conditions for topological order in insulators. *Europhys. Lett.* **70**, 824 (2005).

[166] W. LiMing, G. Misguich, P. Sindzingre, and C. Lhuillier. From Néel long-range order to spin liquids in the multiple-spin exchange model. *Phys. Rev. B* **62**, 6372 (2000).

[167] S. Cheong and C. L. Henley. Correlation density matrix: An unbiased analysis of exact diagonalizations. *Phys. Rev. B* **79**, 212402 (2009).

[168] M. Levin and X. Wen. Detecting Topological Order in a Ground State Wave Function. *Phys. Rev. Lett.* **96**, 110405 (2006).

[169] A. Kitaev and J. Preskill. Topological Entanglement Entropy. *Phys. Rev. Lett.* **96**, 110404 (2006).

[170] S. Furukawa and G. Misguich. Topological entanglement entropy in the quantum dimer model on the triangular lattice. *Phys. Rev. B* **75**, 214407 (2007).

[171] S. Weinberg. *The Quantum Theory of Fields, Vol. 1: Foundations*. Cambridge University Press (2005).

[172] K. S. Novoselov *et al.* Two-dimensional gas of massless Dirac fermions in graphene. *Nature* **438**, 197 (2005).

[173] Y. Zhang, Y.-W. Tan, H. Stormer, and P. Kim. Experimental observation of the quantum Hall effect and Berry's phase in graphene. *Nature* **438**, 201 (2005).

[174] H. Zhang *et al.* Topological insulators in Bi_2Se_3, Bi_2Te_3 and Sb_2Te_3 with a single Dirac cone on the surface. *Nat. Phys.* **97**, 438 (2009).

[175] Y. L. Chen *et al.* Experimental Realization of a Three-Dimensional Topological Insulator, Bi_2Te_3. *Science* **438**, 178 (2009).

[176] J. E. Drut and T. A. Lähde. Critical exponents of the semimetal-insulator transition in graphene: A Monte Carlo study. *Phys. Rev. B* **79**, 241405 (2009).

[177] R. Jordens, N. Strohmaier, K. Gunter, H. Moritz, and T. Esslinger. A Mott insulator of fermionic atoms in an optical lattice. *Nature* **455**, 204 (2008).

[178] U. Schneider *et al.* Metallic and Insulating Phases of Repulsively Interacting Fermions in a 3D Optical Lattice. *Science* **322**, 1520 (2008).

[179] S. Raghu, X.-L. Qi, C. Honerkamp, and S.-C. Zhang. Topological Mott Insulators. *Phys. Rev. Lett.* **100**, 156401 (2008).

[180] C. L. Kane and E. J. Mele. Quantum spin Hall effect in Graphene. *Phys. Rev. Lett.* **95**, 226801 (2005).

[181] B. Uchoa and A. H. Castro Neto. Superconducting States of Pure and Doped Graphene. *Phys. Rev. Lett.* **98**, 146801 (2007).

[182] S. Cahangirov, M. Topsakal, E. Aktürk, H. Şahin, and S. Ciraci. Two- and One-Dimensional Honeycomb Structures of Silicon and Germanium. *Phys. Rev. Lett.* **102**, 236804 (2009).

[183] L.-M. Duan, E. Demler, and M. Lukin. Controlling Spin Exchange Interactions of Ultracold Atoms in Optical Lattices. *Phys. Rev. Lett.* **91**, 090402 (2003).

[184] S. Sorella and E. Tosatti. Semi-metal-Insulator Transition of the Hubbard Model in the Honeycomb Lattice. *Europhys. Lett.* **19**, 699 (1992).

[185] T. Paiva, R. T. Scalettar, W. Zheng, R. R. P. Singh, and J. Oitmaa. Ground-state and finite-temperature signatures of quantum phase transitions in the half-filled Hubbard model on a honeycomb lattice. *Phys. Rev. B* **72**, 085123 (2005).

[186] N. Furukawa. Antiferromagnetism of the Hubbard Model on a Layered Honeycomb Lattice - Is MgB2 a Nearly-Antiferromagnetic Metal? *J. Phys. Soc. Jpn.* **70** (Furukawa - J. Phys. Soc. J. 70, 1483 (2001)).

[187] K. L. Lee *et al.* Attractive Hubbard model on a honeycomb lattice: Quantum Monte Carlo study. *Phys. Rev. B* **80**, 245118 (2009).

[188] S. Ryu, C. Mudry, C.-Y. Hou, , and C. Chamon. Masses in graphene-like two-dimensional electronic systems: topological defects in order parameters and their fractional exchange statistics. *Phys. Rev. B* **80**, 205319 (2009).

[189] F. D. M. Haldane. Model for a Quantum Hall Effect without Landau Levels: Condensed-Matter Realization of the 'Parity Anomaly'. *Phys. Rev. Lett.* **61**, 2015 (1988).

[190] F. F. Assaad, W. Hanke, and D. J. Scalapino. Flux quantization in the two-dimensional repulsive and attractive Hubbard models. *Phys. Rev. Lett.* **71**, 1915 (1993).

[191] F. F. Assaad, W. Hanke, and D. J. Scalapino. Temperature derivative of the superfluid density and flux quantization as criteria for superconductivity in two-dimensional Hubbard models. *Phys. Rev. B* **50**, 12835 (1994).

[192] N. Byers and C. N. Yang. Theoretical Considerations Concerning Quantized Magnetic Flux in Superconducting Cylinders. *Phys. Rev. Lett.* **7**, 46 (1961).

[193] L. Pauling. *The Nature of the Chemical Bond*. Cornell University Press (1960).

[194] A. Andreev and I. Grishchuk. Spin nematics. *Sov. Phys. JETP* **60**, 267 (1984).

[195] E. H. Lieb. Two theorems on the Hubbard model. *Phys. Rev. Lett.* **62**, 1201 (1989).

[196] A. Keren *et al.* Muon spin relaxation measurements in kagomé lattice system $SrCr_8Ga_4O_{19}$. *Hyperfine Interact.* **85**, 181 (1994).

[197] Y. Okamoto, H. Yoshida, and Z. Hiroi. Vesignieite $BaCu_3V_2O_8(OH)_2$ as a Candidate Spin-1/2 Kagome Antiferromagnet. *J. Phys. Soc. Jpn.* **78**, 033701 (2009).

[198] M. J. Lawler, A. Paramekanti, Y. B. Kim, and L. Balents. Gapless Spin Liquids on the Three-Dimensional Hyperkagome Lattice of Na_4Ir_3O_8. *Phys. Rev. Lett.* **101**, 197202 (2008).

[199] H. Ikegami, R. Masutomi, K. Obara, and H. Ishimoto. Low-Temperature Magnetization of Submonolayer^3He Adsorbed on HD Preplated Graphite. *Phys. Rev. Lett.* **85**, 5146 (2000).

[200] O. I. Motrunich. Variational study of triangular lattice spin- 1/2 model with ring exchanges and spin liquid state in kappa-(ET)_2Cu_2(CN)_3. *Phys. Rev. B* **72**, 045105 (2005).

[201] L. F. Tocchio, A. Parola, C. Gros, and F. Becca. Spin-liquid and magnetic phases in the anisotropic triangular lattice: The case of kappa -(ET)_2X. *Phys. Rev. B* **80**, 064419 (2009).

[202] Y. Shimizu, K. Miyagawa, K. Kanoda, M. Maesato, and G. Saito. Spin Liquid State in an Organic Mott Insulator with a Triangular Lattice. *Phys. Rev. Lett.* **91**, 107001 (2003).

[203] Y. Kurosaki, Y. Shimizu, K. Miyagawa, K. Kanoda, and G. Saito. Mott Transition from a Spin Liquid to a Fermi Liquid in the Spin-Frustrated Organic Conductor $\kappa - (ET)_2Cu_2(CN)_3$. *Phys. Rev. Lett.* **95**, 177001 (2005).

[204] M. Yamashita *et al.* Thermal-transport measurements in a quantum spin-liquid state of the frustrated triangular magnet κ-(BEDT-TTF)$_2$Cu$_2$(CN)$_3$. *Nat. Phys.*

5, 44 (2009).

[205] S. Yamashita *et al.* Thermodynamic properties of a spin-1/2 spin-liquid state in a κ-type organic salt. *Nat. Phys.* **4**, 459 (2008).

[206] J. M. Ziman. *Electrons and Phonons.* Oxford Univ. Press (1960).

[207] T. Itou, A. Oyamada, S. Maegawa, M. Tamura, and R. Kato. Quantum spin liquid in the spin-1/2 triangular antiferromagnet $EtMe_3Sb[Pd(dmit)_2]_2$. *Phys. Rev. B* **77**, 104413 (2008).

[208] T. Itou, A. Oyamada, S. Maegawa, M. Tamura, and R. Kato. ^{13}C NMR study of the spin-liquid state in the triangular quantum antiferromagnet $EtMe_3Sb[Pd(dmit)_2]_2$. *J. Phys. Conf. Ser.* **145**, 012039 (2009).

[209] M. Yamashita *et al.* Highly Mobile Gapless Excitations in a Two-Dimensional Candidate Quantum Spin Liquid. *Science* **328**, 1246 (2010).

[210] J. E. Drut and T. A. Lähde. Is Graphene in Vacuum an Insulator? *Phys. Rev. Lett.* **102**, 026802 (2009).

[211] J. E. Drut and T. A. Lähde. Lattice field theory simulations of graphene. *Phys. Rev. B* **79**, 165425 (2009).

[212] K. I. Bolotin, F. Ghahari, M. D. Shulman, H. L. Stormer, and P. Kim. Observation of the fractional quantum Hall effect in graphene. *Nature* **462**, 196 (2009).

[213] K. S. Novoselov *et al.* Electric Field Effect in Atomically Thin Carbon Films. *Science* **306**, 666 (2004).

[214] H. Scedilahin *et al.* Monolayer honeycomb structures of group-IV elements and III-V binary compounds: First-principles calculations. *Phys. Rev. B* **80**, 155453 (2009).

[215] H. Nakano *et al.* Soft Synthesis of Single-Crystal Silicon Monolayer Sheets. *Angew. Chem.* **118**, 6451 (2006).

[216] G. D. Simoni *et al.* Delocalized-localized transition in a semiconductor two-dimensional honeycomb lattice. *arXiv*:1007.3168v1 (2010).

[217] R. Coldea, D. A. Tennant, and Z. Tylczynski. Extended scattering continua characteristic of spin fractionalization in the two-dimensional frustrated quantum magnet Cs_2CuCl_4 observed by neutron scattering. *Phys. Rev. B* **68**, 134424 (2003).

[218] H. Katsura, N. Nagaosa, and P. A. Lee. Theory of the Thermal Hall Effect in Quantum Magnets. *Phys. Rev. Lett.* **104**, 066403 (2010).

[219] M. R. Norman and T. Micklitz. How to Measure a Spinon Fermi Surface. *Phys. Rev. Lett.* **102**, 067204 (2009).

[220] A. W. Sandvik. Stochastic method for analytic continuation of quantum Monte

Carlo data. *Phys. Rev. B* **57**, 10287 (1998).

[221] K. S. D. Beach. Identifiying the maximum entropy as a special limit of stochastic analytic continuation. *arXiv*:cond-mat/0403055 (2004).

[222] A. P. Ramirez. Strongly geometrically frustrated magnets. *Annu. Rev. Mater. Sci.* **24** (1994).

[223] J. T. Chayes, L. Chayes, and S. A. Kivelson. Valence bond ground states in a frustrated two-dimensional spin-1/2 Heisenberg antiferromagnet. *Commun. Math. Phys.* **123**, 53 (1989).

[224] A. H. MacDonald, S. M. Girvin, and D. Yoshioka. $\frac{t}{U}$ expansion for the Hubbard model. *Phys. Rev. B* **37**, 9753 (1988).

[225] A. H. MacDonald, S. M. Girvin, and D. Yoshioka. Reply to "Comment on 't/U expansion for the Hubbard model"'. *Phys. Rev. B* **41**, 2565 (1990).

[226] M.-S. Nam, A. Ardavan, S. J. Blundell, and J. A. Schlueter. Fluctuating superconductivity in organic molecular metals close to the Mott transition. *Nature* **449**, 584 (2007).

[227] N. B. Kopnin and E. B. Sonin. BCS superconductivity of Dirac electrons in graphene layers. *Phys. Rev. Lett.* **100**, 246808 (2008).

[228] T.-P. Cheng and L.-F. Li. *Gauge Theory of Elementary Particle Physics*. Oxford Univ. Press (2000).

[229] M. E. Peskin and D. V. Schroeder. *An Introduction to Quantum Field Theory*. Addison-Wesley (1995).

[230] W. Pfeifer. *The Lie Algebras su(N)*. Birkhäuser (2000).

[231] H. J. Lipkin. *Lie Groups for Pedestrians*. North-Holland Publishing Co. (1965).

[232] J. E. Humphreys. *Introduction to Lie Algebras and Representation Theory*. Springer (1972).

[233] I. Affleck and J. B. Marston. Large-n limit of the Heisenberg-Hubbard model: Implications for high-Tc superconductors. *Phys. Rev. B* **37**, 3774 (1988).

[234] J. B. Marston and I. Affleck. Large-n limit of the Hubbard-Heisenberg model. *Phys. Rev. B* **39**, 11538 (1989).

[235] I. Affleck, D. P. Arovas, J. B. Marston, and D. A. Rabson. SU(2n) quantum antiferromagnets with exact C-breaking ground states. *Nucl. Phys. B* **366**, 467 (1991).

[236] A. M. Perelomov and V. M. Popov. Casimir operators for the unitary group. *JETP Lett.* **1**, 160 (1965).

[237] C. C. Nishi. Simple derivation of general Fierz identities. *Am. J. Phys.* **73**, 160

(2005).

[238] E. Akkermans, G. Montambaux, J. Pichard, and J. Zinn-Justin, editors. *Fermi liquids and non-Fermi liquids*. Proceedings of Les Houches Summer School LXI (1995).

[239] C.-Y. Hou, C. Chamon, and C. Mudry. Electron Fractionalization in Two-Dimensional Graphenelike Structures. *Phys. Rev. Lett.* **98**, 186809 (2007).

[240] M. Bercx, T. C. Lang, and F. F. Assaad. Magnetic field induced semimetal-to-canted-antiferromagnet transition on the honeycomb lattice. *Phys. Rev. B* **80**, 045412 (2009).

[241] C. Honerkamp and W. Hofstetter. Ultracold Fermions and the SU(N) Hubbard Model. *Phys. Rev. Lett.* **92**, 170403 (2004).

[242] I. Bloch, J. Dalibard, and W. Zwerger. Many-body physics with ultracold gases. *Rev. Mod. Phys.* **80**, 885 (2008).

[243] S. Giorgini, L. P. Pitaevskii, and S. Stringari. Theory of ultracold atomic Fermi gases. *Rev. Mod. Phys.* **80**, 1215 (2008).

[244] A. V. Gorshkov *et al.* Two-orbital SU(N) magnetism with ultracold alkaline-earth atoms. *Nat. Phys.* **6**, 289 (2010).

[245] M. Hermele, V. Gurarie, and A. M. Rey. Mott Insulators of Ultracold Fermionic Alkaline Earth Atoms: Underconstrained Magnetism and Chiral Spin Liquid. *arXiv*:0906.3718v2 (2009).

[246] C. Xu. Zoo of Liquids in multi-orbital SU(N) Magnets with Ultracold Alkaline Earth Atoms. *arXiv*:0906.3727v2 (2009).

[247] M. A. Cazalilla, A. F. Ho, and M. Ueda. Ultracold Gases of Ytterbium: Ferromagnetism and Mott States in an SU(6) Fermi System. *arXiv*:0905.4948v3 (2009).

[248] M. M. Boyd *et al.* Optical Atomic Coherence at the 1-Second Time Scale. *Science* **314**, 1430 (2006).

[249] A. J. Daley, M. M. Boyd, J. Ye, and P. Zoller. Quantum Computing with Alkaline-Earth-Metal Atoms. *Phys. Rev. Lett.* **101**, 170504 (2008).

[250] A. V. Onufriev and J. B. Marston. Enlarged symmetry and coherence in arrays of quantum dots. *Phys. Rev. B* **59**, 12573 (1999).

[251] K. I. Kugel and D. I. Khomskii. Crystal structure and magnetic properties of substances with orbital degeneracy. *Sov. Phys. JETP* **37**, 725 (1973).

[252] D. P. Arovas and A. Auerbach. Tetrahis(dimethylamino)ethylene-C_60: Multicomponent superexchange and Mott ferromagnetism. *Phys. Rev. B* **52**, 10114 (1995).

[253] Y. Q. Li, M. Ma, D. N. Shi, and F. C. Zhang. SU(4) Theory for Spin Systems

with Orbital Degeneracy. *Phys. Rev. Lett.* **81**, 3527 (1998).

[254] S. K. Pati, R. R. P. Singh, and D. I. Khomskii. Alternating Spin and Orbital Dimerization and Spin-Gap Formation in Coupled Spin-Orbital Systems. *Phys. Rev. Lett.* **81**, 5406 (1998).

[255] Y. Tokura and N. Nagaosa. Orbital Physics in Transition-Metal Oxides. *Science* **288**, 462 (2000).

[256] D. Huse. Lecture Notes. *Boulder Summer School for Condensed Matter and Material Physics* (2010).

[257] D. J. Wineland, R. E. Drullinger, and F. L. Walls. Radiation-Pressure Cooling of Bound Resonant Absorbers. *Phys. Rev. Lett.* **40**, 1639 (1978).

[258] W. Neuhauser, M. Hohenstatt, P. Toschek, and H. Dehmelt. Optical-Sideband Cooling of Visible Atom Cloud Confined in Parabolic Well. *Phys. Rev. Lett.* **41**, 233 (1978).

[259] B. D. Esry, C. H. Greene, and J. P. Burke. Recombination of Three Atoms in the Ultracold Limit. *Phys. Rev. Lett.* **83**, 1751 (1999).

[260] M. Greiner, O. Mandel, T. Esslinger, T. W. Hansch, and I. Bloch. Quantum phase transition from a superfluid to a Mott insulator in a gas of ultracold atoms. *Nature* **415**, 39 (2002).

[261] K. L. Lee, B. Grémaud, R. Han, B.-G. Englert, and C. Miniatura. Ultracold fermions in a graphene-type optical lattice. *Phys. Rev. A* **80**, 043411 (2009).

[262] G. Grynberg, B. Lounis, P. Verkerk, J.-Y. Courtois, and C. Salomon. Quantized motion of cold cesium atoms in two- and three-dimensional optical potentials. *Phys. Rev. Lett.* **70**, 2249 (1993).

[263] R. Ciuryło, E. Tiesinga, and P. S. Julienne. Optical tuning of the scattering length of cold alkaline-earth-metal atoms. *Phys. Rev. A* **71**, 030701 (2005).

[264] P. Naidon and P. S. Julienne. Optical Feshbach resonances of alkaline-earth-metal atoms in a one- or two-dimensional optical lattice. *Phys. Rev. A* **74**, 062713 (2006).

[265] T. Köhler, K. Góral, and P. S. Julienne. Production of cold molecules via magnetically tunable Feshbach resonances. *Rev. Mod. Phys.* **78**, 1311 (2006).

[266] K. M. Jones, E. Tiesinga, P. D. Lett, and P. S. Julienne. Ultracold photoassociation spectroscopy: Long-range molecules and atomic scattering. *Rev. Mod. Phys.* **78**, 483 (2006).

[267] S. Wessel, F. Alet, M. Troyer, and G. G. Batrouni. Quantum Monte Carlo simulations of confined bosonic atoms in optical lattices. *Phys. Rev. A* **70**, 053615 (2004).

[268] N. Gemelke, X. Zhang, C. Hung, and C. Chin. In situ observation of incompressible Mott-insulating domains in ultracold atomic gases. *Nature* **460**, 995 (2009).

[269] W. S. Bakr *et al.* Probing the Superfluid-to-Mott Insulator Transition at the Single-Atom Level. *Science* **329**, 547 (2010).

[270] J. F. Sherson *et al.* Single-atom-resolved fluorescence imaging of an atomic Mott insulator. *Nature* **467**, 68 (2010).

[271] I. Bloch. Quantum coherence and entanglement with ultracold atoms in optical lattices. *Nature* **453**, 1016 (2008).

[272] M. M. Boyd *et al.* Nuclear spin effects in optical lattice clocks. *Phys. Rev. A* **76**, 022510 (2007).

[273] J. P. Kestner and L.-M. Duan. Effective single-band models for strongly interacting fermions in an optical lattice. *Phys. Rev. A* **81**, 043618 (2010).

[274] I. L. Aleiner, D. E. Kharzeev, and A. M. Tsvelik. Spontaneous symmetry breaking in graphene subjected to an in-plane magnetic field. *Phys. Rev. B* **76**, 195415 (2007).

[275] H. Kempa, H. C. Semmelhack, P. Esquinazi, and Y. Kopelevich. Absence of metal-insulator transition and coherent interlayer transport in oriented graphite in parallel magnetic fields. *Solid State Commun.* **125**, 1 (2003).

[276] D. E. Kharzeev, S. A. Reyes, and A. M. Tsvelik. Spin density wave formulation in graphene facilitated by the in-plane magnetic field. *arXiv*:cond-mat/0611251 (2006).

[277] I. F. Herbut. Interactions and Phase Transitions on Graphene's Honeycomb Lattice. *Phys. Rev. Lett.* **97**, 146401 (2006).

[278] I. Milat, F. Assaad, and M. Sigrist. Field induced magnetic ordering transition in Kondo insulators. *Eur. Phys. J. B* **38**, 571 (2004).

[279] K. S. D. Beach, P. A. Lee, and P. Monthoux. Field-Induced Antiferromagnetism in the Kondo Insulator. *P* **92**, 026401 (2004).

[280] T. A. Gloor and F. Mila. Strain induced correlation gaps in carbon nanotubes. *Eur. Phys. J. B* **38**, 9 (2004).

[281] R. M. Fye. New results on Trotter-like approximations. *Phys. Rev. B* **33**, 6271 (1986).

[282] F. F. Assaad. Depleted Kondo lattices: Quantum Monte Carlo and mean-field calculations. *Phys. Rev. B* **65**, 115104 (2002).

[283] F. London. On the Problem of the Molecular Theory of Superconductivity. *Phys. Rev.* **74**, 562 (1948).

[284] C. M. Varma and A. Sudbo. Flux-quantization in one-dimensional copper-oxide models. *J. Phys. I France* **3**, 585 (1993).

Curriculum Vitae

Thomas Christoph Lang
born in Graz, November 4$^{\text{th}}$ 1979
Austrian, married

Education

[10/2006 – 09/2010]	Doctoral-study of theoretical physics at the Institut für Theoretische Physik und Astrophysik, Würzburg; advisor Fakher F. Assaad.
[10/2005 – 09/2006]	Visiting scholar at Boston University, MA; advisor Anders W. Sandvik.
[10/2002 – 09/2005]	Diploma-study of physics at the Institute of Theoretical Physics at Graz University of Technology, Diploma thesis *Dynamics and charge order in a quarterfilled ladder system coupled to the lattice*; advisor Hans Gerd Evertz.
[10/2001 – 09/2002]	Diploma-study of physics at University of Regensburg (Germany) participating ERASMUS student-exchange program.
[10/1999 – 10/2002]	Diploma-study of physics at Karl-Franzens University of Graz
[06/1998]	High school (A-level) graduation at BG/BRG Seebachergasse, exam paper (Fachbereichsarbeit) in computer-science and physics *Simulation of fluids and gases aided by cellular automata.*
[09/1990 – 05/1998]	BG/BRG Seebachergasse (high school).

Würzburg, 20. September 2010

Thomas C. Lang

List of publications

The listed publications have been printed in peer-reviewed journals and proceedings:

[1] Z. Y. Meng, TCL, S. Wessel, F. F. Assaad and A. Muramatsu. Quantum spin liquid emerging in two-dimensional correlated Dirac fermions. *Nature* **464**, 847 (2010).

[2] M. Bercx, TCL and F. F. Assaad. Magnetic field induced semimetal-to-canted-antiferromagnet transition on the honeycomb lattice. *Phys. Rev. B* **80**, 045412 (2009).

[3] TCL, M. Bercx, D. J. Luitz, G. Li, F. F. Assaad and W. Hanke. QMC Studies of Strongly Correlated Electron Systems. *HPC in Science and Engineering Garching/Munich 2009*, to appear (2010).

[4] S. Hochkeppel, TCL, C. Brünger, F. F. Assaad and W. Hanke. QMC Studies of Strongly Correlated Electron Systems. *HPC in Science and Engineering Garching/Munich 2007*, 669 (2008).

[5] M. Hohenadler and TCL. Autocorrelations in quantum Monte Carlo simulations of electron-phonon models. *Lect. Notes Phys.* **739**, 357 (2008).

[6] F. F. Assaad and TCL. Diagrammatic determinantal quantum Monte Carlo methods: Projective schemes and applications to the Hubbard-Holstein model. *Phys. Rev. B* **76**, 035116 (2007).

[7] C. Gabriel, E. Sherman, TCL, M. Aichhorn, and H. G. Evertz, Finite-temperature investigation of quarter filled ladder systems. *Physica B* **359**, 1400 (2005).

These papers are in preparation:

[1] TCL, Z. Y. Meng, S. Wessel, F. F. Assaad and A. Muramatsu. Phase diagram of the SU(N) Hubbard-Heisenberg model on the honeycomb lattice: a QMC study. To be submitted to *Phys. Rev. B*.

[2] TCL, F. F. Assaad, and A. W. Sandvik. Breakdown of a valence bond solid in a Heisenberg model with four-spin exchange on the honeycomb layers. To be submitted to *Phys. Rev. B*.

[3] Z. Y. Meng, H. Feldner, TCL, A. Honecker, S. Wessel, F. F. Assaad Correlations in graphene nano-ribbons: a QMC study. To be submitted to *Phys. Rev. B*.

Versicherung an Eides statt

Hiermit versichere ich, Thomas C. Lang geboren am 4. November 1979 in Graz, Österreich, an Eides statt, dass ich die vorliegende Arbeit eigenständig, d.h. insbesondere ohne Hilfe eines kommerziellen Promotionsberaters angefertigt habe. Es wurden keine anderen als in der Arbeit angegebenen Quellen und Hilfsmittel benutzt. Diese Arbeit liegt nicht in gleicher oder anderer Form in einem anderen Prüfungsfach vor.

Würzburg, 20. September 2010

Thomas C. Lang

Acknowledgments

I am indebted to many people for their long-lasting support and encouragement which was invaluable for the successful completion of this research work. In the following lines I hope to express my gratitude and respect for those who were the most influential.

First and foremost, I would like to thank my thesis advisor Prof. Dr. Fakher F. Assaad! Your support, your guidance and motivating discussions throughout these years are much appreciated. I have learnt a great deal from you, and your appreciation of my own assessment in discussions encouraged me to pursue my passion for physics in the future.

I greatly appreciate the very fruitful and enjoyable collaboration with Zi Yang Meng, Stefan Wessel and Alejandro Muramatsu from the University of Stuttgart. Special thanks to my colleague Zi Yang for talk beyond physics and the joined forces against the frustration and lows during the long struggle until publication.

I would like to thank my colleagues and friends within the department: Lee Martin, Christian Brünger, Martin Bercx, Jutta Ortloff, David Luitz, Florian Goth, Martin Hohenadler, Julia Wernsdorfer, Maximilian Aulbach and Jan Werner for discussions and support. Special thanks to Martin B. and Florian for proof reading! Thanks to Judith Stahl for ensuring a smooth running department and thanks to all members of the department for the kind environment!

I also most sincerely thank my family, especially my darling Magdalena, for your love and ongoing encouragement.

Thanks to my good friend caffeine!